

**HYBRID 3D BIOPRINTING OF FUNCTIONALIZED
STRUCTURES FOR TISSUE ENGINEERING**

by

SEYEDEH FERDOWS AFGHAH

Submitted to the Graduate School of Engineering and Natural Sciences

in partial fulfillment of

the requirements for the degree of

Doctor of Philosophy

Sabanci University

December 2020

HYBRID 3D BIOPRINTING OF FUNCTIONALIZED STRUCTURES FOR TISSUE ENGINEERING

APPROVED BY:

[REDACTED]

[REDACTED]

[REDACTED]

[REDACTED]

[REDACTED]

DATE OF APPROVAL: 25.12.2020

© Seyedeh Ferdows Afghah 2020

All Rights Reserved

HYBRID 3D BIOPRINTING OF FUNCTIONALIZED STRUCTURES FOR TISSUE ENGINEERING

SEYEDEH FERDOWS AFGHAH

Ph.D. Dissertation, December 2020

Supervisor: Prof. Dr. Bahattin Koc

ABSTRACT

Keywords: Hybrid Bioprinting, Melt electrospinning Writing (MEW), Extrusion Printing, Tissue Engineering, Scaffold

Tissue engineering is an interdisciplinary field of research aiming at developing methods and technologies for regenerating damaged tissues. It relies on a combinatory platform of biomaterials with cells and bioactive molecules to resemble the human microenvironment to stimulate tissue constructs. Hence, numerous factors, including biochemical, biophysical, and mechanical aspects of the host tissue, have to be taken into account for developing a successful tissue replacement. Skin replacements caused by traumas, injuries, and burns are a burden to the healthcare system globally. The human body cannot fully regenerate the tissue with all the functionalities and features in severe wounds or skin loss. Poor mechanical properties, scarring, delayed cell and biomolecules infiltration, and non/poor vascularization are the main challenges yet to be addressed.

Three-dimensional (3D) bioprinting, also known as additive manufacturing (AM), a layer-by-layer fabrication method, is regarded as a gold standard technique with the ability of

controlled deposition of biomaterials in the desired geometry by using computer-aided design (CAD) models. Together with the development of biomaterials and architecture design, 3D bioprinting could ease the long and complicated journey towards functional tissue regeneration. In this context, the fabrication of small fibers mimicking natural extracellular matrix (ECM), selection of functional material with good mechanical and biochemical properties, the inclusion of bioactive molecules to enhance functionality, and printability are prerequisite factors of successful scaffold fabrication.

In this work, novel hybrid 3D bioprinting approaches have been developed for functionalized structures, mainly for skin tissue engineering. Within this framework, we first optimized the effect of printing parameters on fiber diameter for Melt Electrospinning Writing (MEW), a special 3D printing process, using response surface methodology (RSM) as a predictive tool. Then we copolymerized polycaprolactone (PCL) with polypropylene succinate to improve its degradation rate and hydrophilicity and functionalized it with silver nitrate to induce antibacterial properties, and finally, it was 3Dprinted using an extrusion-based printer. For preparing hybrid 3D bioprinting, we used a composite support-bath system based on Pluronic PF127 was formulated with the inclusion of Laponite RDS and calcium chloride as rheological modifier and stabilizer, respectively. The rheological characterization of support-bath showed thixotropic behavior with a high degree of recoverability which facilitated bioprinting of complex hydrogel structures within the support-bath through an extrusion system. Then, we fabricated a polymer-hydrogel construction using MEW-casting for skin tissue substitute. In this context, we first investigated the geometrical effect of melt electrowritten scaffolds on cord-like structure formation for pre-vascularization. Mesh scaffolds with 0-90and 60-120 degree orientations and honeycomb shape were explored and cell-laden gelatin hydrogels were infiltrated inside those PCL scaffolds, and the results suggested the potential of honeycomb structure for better mechanical and invitro properties. In the final stage, a functionalized hybrid MEW-hydrogel scaffold for wound healing was fabricated. A functionalized mesh structure of PCL-bioactive glass was created via MEW, and a gelatin hydrogel comprising basic fibroblast and vascular endothelial growth factors was cast within the mesh scaffold. *In vivo* implantation of hybrid scaffolds showed promising results for accelerating and functionality of the healed parts according to wound closure and histological evaluation.

ÖZET

Anahtar kelimeler: Hibrid biyobasım, Eriyik elektroyazdırma (MEW), Ekstrüzyon tabanlı basım, Doku mühendisliği, Doku iskelesi

Doku mühendisliği, hasarlı dokuları yenilemek için yöntem ve teknolojiler geliştirmeyi amaçlayan disiplinler arası bir araştırma alanıdır. Doku oluşumunun uyarılması için insan mikro ortamında bulunan hücreler ve biyoaktif moleküllerin kullanılmasına dayanan birleşik bir biyomateryal platformudur. Bu nedenle, fonksiyonel bir doku eşleniği geliştirmek için konakçı dokunun biyokimyasal, biyofiziksel ve mekanik yönleri dahil olmak üzere çok sayıda faktör dikkate alınmalıdır. Travmalar, yaralanmalar ve yanıkların neden olduğu ciddi yaralarda veya deri kaybında insan vücutu dokuyu tüm işlevsellik ve özelliklerle tam olarak yenileyemez. Bu nedenlere gereksinim duyulan deri nakilleri, küresel olarak sağlık sistemi için bir yüktür. Zayıf mekanik özellikler, yara izi, gecikmiş hücre ve biyomolekül infiltrasyonu ve vaskülarizasyonun olmaması, deri yenilenmesi için halen ele alınması gereken ana zorluklardır.

Üç boyutlu (3B) biyobasım, yani eklemeli imalat (AM) olarak da bilinen katmanlı imalat yöntemi, biyomalzemelerin bilgisayar destekli tasarım (CAD) modelleri kullanılarak istenen geometride kontrollü olarak yerleştirilebilmesi ile altın standart bir teknik olarak kabul edilir. Biyomalzemelerin seçilmesi ve mimari tasarımın geliştirilmesi ile birlikte, 3D biyobasım, fonksiyonel doku rejenerasyonuna doğru uzun ve karmaşık yolculuğu kolaylaştırabilir. Bu bağlamda, doğal hücre dışı matrisi (ECM) taklit eden küçük liflerin üretimi, iyi mekanik ve biyokimyasal özelliklere sahip işlevsel malzeme seçimi, işlevselliği artırmak için biyoaktif moleküllerin malzemeye dahil edilmesi ve bu malzemenin basılabilirliği, başarılı iskele üretiminin ön koşul faktörleridir.

Bu çalışmada, özellikle cilt dokusu mühendisliği için işlevselleştirilmiş yapılar için yenilikçi hibrit 3B biyo-basım yöntemleri geliştirildi. Bu çerçevede, ilk olarak, özel bir 3B basım işlemi olan eriyik-elektron basım (3B-MEW) parametrelerinin fiber çapı üzerindeki etkisini, yanıt yüzey metodolojisini (RSM) tahmin aracı olarak kullanarak optimize edildi. Daha sonra polikaprolaktonu (PCL) biyobozunma oranı ve hidrofilikliğini artırmak için polipropilen süksinat ile kopolimerize edildi ve antibakteriyel özelliklerini indüklemek için gümüş nitrat eklandı ve son olarak ekstrüzyon tabanlı bir yazıcı kullanılarak 3 boyutlu yazdırıldı. Karmaşık yapıda hidrojel iskelelerinin 3D biyo-basım hazırlamak için, sırasıyla reolojik modifiye edici ve stabilizatör olarak Laponite RDS ve kalsiyum klorürün dahil edilmesiyle formüle edilen Pluronic PF127'ye dayalı bir kompozit destek banyosu sistemi kullanıldı. Destek banyosunun reolojik özellikleri, destek banyosu içine bir ekstrüzyon sistemi aracılığıyla karmaşık hidrojel yapılarının biyo-basım yapılmasını ve yüksek derecede geri kazanılabilirliğini kolaylaştırın tiksotropik davranış gösterdi. Ardından, deri eşlenik dokusu için hibrit MEW-hidrojel iskele yapısı üretildi. Bu bağlamda ilk olarak MEW ile üretilen iskelelerinin geometrisinin damarlanma için kordon benzeri yapı oluşumuna etkisi 0-90 ve 60-120 derece yönelimlere ve bal peteği şekline sahip farklı ağ iskeleleri kullanılarak araştırıldı. Üretilen PCL iskelelerinin içine hücre yüklü jelatin hidrojeller sızdırılarak hibrit yapı oluşturuldu ve sonuçlar, daha iyi mekanik ve in vitro özellikler için petek yapısının potansiyelini ortaya koydu. Son aşamada, yara iyileşmesi için işlevselleştirilmiş bir hibrit MEW-hidrojel iskelesi üretildi. PCL-biyoaktif camın işlevselleştirilmiş bir ağ yapısı, MEW aracılığıyla yaratıldı ve fibroblast ve vasküler endotel büyümeye faktörlerini içeren bir jelatin hidrojel, ağı yapı iskelesi içine dökülerek çapraz bağladı. Hibrit yapı iskeletlerinin in vivo implantasyonu, yara kapanması ve histolojik değerlendirmeye göre iyileşmiş parçaların hızlanması ve işlevselliği için umut verici sonuçlar gösterdi.

ACKNOWLEDGEMENT

Hereby, I wish to thank the people who supported me to pursue my goals in life and without whom this journey would not be possible.

Firstly, I would like to express my sincere gratitude to my supervisor, Prof. Dr. Bahattin Koc for his trust, guidance and continuous support in these years that made it possible for me to pass through this tough and at the same time enjoyable time of my life. He gave me courage to seek new ideas, and not to restrain myself.

Special thanks go to the faculty members, lab specialists, and technicians of the department of Engineering and Natural Sciences of Sabanci University for their helps and supports.

I am so lucky to have such wonderful, kind, and helpful lab members Ali Nadernezhad, Dr. Mine Altunbek, Anil Ahmet Acar, Ozum Sehnaz Caliskan, Ezgi Bakirci, Caner Dikyol, and other group members that make me feel at home.

Special thanks to my dear friends at Sabanci University, Farzaney Jalalypour, Pouya Yousefi Louyeh, and Taha Behroozi Kohlan whom I could rely on and had many unforgettable memories with.

I am grateful to the Scientific and Technological Research Council of Turkey (TUBITAK) for providing financial support under grant numbers 213M687 and 217M254 Awarded for Assoc. Prof. Dr. Burcu Saner Okan and Prof. Dr. Bahattin Koc.

Finally, I owe my deepest appreciation to my family members for their spiritual support and love during my whole life. Their wonderful and consistent motivations kept me going regardless of the challenges that I faced in my lifetime.

Contents

1	Chapter 1. Introduction and motivatoin	1
2	Chapter 2: Biomimicry in Bio-Manufacturing: Developments in Melt Electrospinning Writing Technology Towards Hybrid Biomanufacturing	7
2.1	Background	8
2.2	Principles and Challenges of MEW	11
2.3	Opportunities for MEW in Tissue Engineering	13
2.4	Hybrid Melt Electrospinning Writing-Fiber Reinforcement of Hydrogel Constructs	16
2.4.1	Reinforcement Mechanism in Melt Electrowritten Fiber-Hydrogel Composites	17
2.4.2	Biological and Mechanical Aspects of Reinforced Composites in Different Tissue Engineering Applications.....	22
2.5	Other Hybrid Approaches with MEW	29
2.6	Summary and Future Perspective.....	33
3	Chapter 3: 3D printing of silver-doped polycaprolactone-poly(propylene succinate) composite scaffolds for skin tissue engineering	36
3.1	Introduction	38
3.2	Materials and methods	40
3.2.1	Materials	40
3.2.2	Synthesis of polycaprolactone	40
3.2.3	Synthesis of poly(1, 3 propylene succinate)	41
3.2.4	Synthesis of PCL-PPSu block copolymers	42
3.2.5	Contact angle measurement	43
3.2.6	Enzymatic degradation.....	43
3.2.7	Hydrolytic degradation	44
3.2.8	Analysis of silver ion release and silver distribution	44
3.2.9	3D printing process	45
3.2.10	Biocompatibility evaluation	46
3.2.11	Antibacterial activity of block copolymer impregnated with silver nitrate	47
3.2.12	Statistical analysis	48
3.3	Results and Discussion.....	48
3.3.1	Structural analysis of PCL-PPSu block copolymer	48
3.3.2	Thermal behavior and 3D printing of PCL-PPSu block copolymers.....	50
3.3.3	Degradation behavior	53

3.3.4	Silver release and surface characterization of polymer films	57
3.3.5	Cell viability assessment.....	58
3.3.6	Antibacterial activity of block copolymer impregnated with AgNO ₃	59
3.4	Conclusion.....	62
3.5	Supplementary document.....	63
4	Chapter 4. Modeling 3D melt electrospinning writing by response surface methodology	66
4.1	Introduction	67
4.2	Materials and Methods	69
4.2.1	Materials	69
4.2.2	3D Melt electrospinning direct writing process	69
4.2.3	Determination of the experimental parameters	70
4.2.4	Experimental design and measurement.....	71
4.3	Results and Discussion.....	73
4.3.1	Regression model analysis	73
4.3.2	Relationship between process parameters and fiber diameter	77
4.3.3	Process parameter optimization	79
4.3.4	Validation of the model by printing a 3D scaffold	81
4.4	Conclusion.....	83
5	Chapter 5: Preparation and characterization of nanoclay-hydrogel composite support-bath for bioprinting of complex hollow structures	84
5.1	Introduction	85
5.2	Results and discussion.....	88
5.2.1	Rheological characterization of the support-bath.....	88
5.2.2	Effect of PF concentration	89
5.2.3	Effect of CaCl ₂ concentration	93
5.2.4	Printability of overhanging and complex structures in PF-RDS support-bath.....	98
5.2.5	Bioprinting of cell-laden alginate hydrogel in support-bath	103
5.3	Conclusion.....	105
5.4	Methods.....	106
5.4.1	Preparation of PF-RDS support-bath and characterization	106
5.4.2	Rheological measurements	106
5.4.3	CAD design of complex structures and 3D printing inside support-bath	107
5.4.4	Bioprinting of cell-laden alginate in PF-RDS support-bath.....	108
5.4.5	Evaluation of in-gel bioprinting biocompatibility.....	109
5.4.6	Statistical Analysis.....	109

6 Chapter 6. 3D printing of hybrid scaffolds for skin tissue engineering: an investigation on the scaffold's geometry in a hybrid design and its influence on mechanical behavior, cell alignment and morphology.....	110
6.1 Introduction	111
6.2 Materials and Methods	114
6.2.1 Materials	114
6.2.2 CAD modeling and scaffold fabrication via MEW.....	114
6.2.2.1 Sodium hydroxide treatment for enhancing hydrophilicity.....	116
6.2.3 Mechanical testing	116
6.2.4 Cell-laden hydrogel preparation.....	117
6.2.5 Hybrid scaffolds preparation.....	117
6.2.6 Morphological and structural characterization.....	118
6.2.7 Cell viability and morphology	119
6.2.7.1 Statistical analysis	119
6.2.8 Results and discussion	120
6.2.8.1 MEW of scaffolds with various geometries	120
6.2.8.2 Mechanical analyses of the scaffolds	120
6.2.8.3 Morphological observations of the scaffolds	123
6.2.8.4 Cell viability and morphological analysis	125
6.3 Conclusion.....	129
7 Chapter 7: 3D Fiber Reinforced Hydrogel Scaffolds by Melt Electrowriting and Gel Casting as a Hybrid Design for Wound Healing	130
7.1 Introduction	131
7.2 Results and Discussion.....	134
7.2.1 Mechanical Properties and swelling behavior.....	135
7.2.2 Bioglass characterization	138
7.2.3 <i>In vitro</i> cytotoxicity.....	138
7.2.4 Evaluation of wound healing <i>in vivo</i>	139
7.2.4.1 Gross anatomical evaluation.....	139
7.2.4.2 Histological evaluation	141
7.3 Conclusion.....	145
7.4 Experimental sections	146

7.4.1	Materials	146
7.4.2	Fabrication of thermoplastic meshes.....	147
7.4.2.1	Synthesis of bioactive glass (BG).....	147
7.4.2.2	Preparation of PCL-bioactive glass composite.....	148
7.4.2.3	Fabrication of melt electrowritten scaffolds.....	148
7.4.3	GF delivery microparticles and hydrogel matrices	148
7.4.3.1	Preparation of gelatin microspheres	148
7.4.3.2	Impregnation of bFGF and VEGF into GMS	149
7.4.3.3	Hydrogel matrices	150
7.4.4	Characterization	151
7.4.4.1	BG characterization	151
7.4.4.2	Mechanical testing	151
7.4.4.3	Swelling behavior	152
7.4.5	<i>In vitro</i> cytotoxicity evaluation.....	152
7.4.6	<i>In vivo</i> study.....	153
7.4.6.1	Implantation of scaffolds	153
7.4.6.2	Macroscopic evaluation of wound closure percentage.....	154
7.4.6.3	Necroscopy and removal of tissues	154
7.4.6.4	Histology	154
7.4.6.5	Statistical analysis	155
7.4.7	Supplementary documents	155
8	Conclusions and future works.....	158
9	References.....	161

List of Figures

Figure 2-1: Schematic representation of solution electrospinning (left), and melt electrospinning writing (right).....	10
Figure 2-2. The effect of collector speed (A) on final structure at constant pressure, and (B) on fiber diameter at different air pressures [82]	13
Figure 2-3. Different hybrid manufacturing approaches by employing MEW.....	17
Figure 2-4. General modeling overview for continuum and micro-finite element (FE) models.	20
Figure 2-5. Schematic view of the designed composite for cartilage application tissue having a different composition, geometry, and mechanical properties.	22
Figure 2-6. (A) Viability and (B) morphology of cardiac progenitor cells (CPCs) in collagen hydrogel infiltrated in squared and rectangular bare-PCL and blended-PCL scaffolds.....	26
Figure 2-7. Attachment of HUVECs on the fibronectin coated PCL fiber networks with different pore size	31
Figure 2-8. Hybrid setup of melt electrospinning writing-solution electrospinning (MEW-SE) for manufacturing of composite PCL/collagen structure.....	32
Figure 3-1. Reaction routes of (A) PPSu, and (B) PCL-PPSu block copolymer	41
Figure 3-2. (A) Schematic view of the custom-made 3D printer, (B) real image of the printing setup during the scaffold printing.....	46
Figure 3-3. FTIR spectra of PCL-PPSu block copolymer, PCL and PPSu polymers.....	49
Figure 3-4. (A) $^1\text{H-NMR}$ and (B) $^{13}\text{C-NMR}$ spectra of PPSu, PCL and PCL-PPSu block copolymer .	50
Figure 3-5. DSC curves of the PCL-PPSu and PCL	51
Figure 3-6. SEM images of 3D printed copolymer impregnated with silver nitrate scaffolds at different magnifications.....	53
Figure 3-7. Wettability and degradation of PCL-PPSu and PCL in different media	54
Figure 3-8. Cytotoxicity of the extracts of the components to HDF cells in vitro.....	56
Figure 3-9. Zone of inhibition for PCL-PPSu and PCL-PPSu/ AgNO_3 polymer films against different microorganisms	60

Figure 3-10. Analysis of microorganisms' adhesion on the PCL-PPSu and PCL-PPSu/AgNO ₃ films.	62
Figure 4-1 3D melt electrospinning direct writing printer	70
Figure 4-2. Normal probability plot of residual at 95% of confidence interval	76
Figure 4-3. Estimated fiber diameters versus actual fiber diameters	76
Figure 4-4. Residual versus fitted values	77
Figure 4-5. 3D response surfaces and contour plots of fiber diameter with respect to process parameters	78
Figure 4-6. Contour plots of fiber diameter with respect to process parameters for optimized model	81
Figure 4-7. SEM images of printed scaffolds with randomly selected parameters from the contour plot	82
Figure 5-1. Temperature and time sweep measurements of the support-bath showing storage and loss moduli over time for different concentrations of PF	88
Figure 5-2. Dynamic rheological characterization of the support-bath representing the effect of PF concentration on flow behavior and recoverability of the structure at 37 °C	90
Figure 5-3. Dynamic rheological characterization of the support-bath representing the effect of CaCl ₂ concentration on network characteristics, flow behavior and recoverability at 37 °C	94
Figure 5-4. Characterization of PF-RDS support-bath for printability of tubular structures in various angular configurations	100
Figure 5-5. Fabrication of 3D complex constructs. CAD models of (a) star shape, (b) grid-pattern, (c) branched vascular structure, and (d) nose shape	103
Figure 5-6. Fabrication of cell-laden alginate constructs using PF-RDS support-bath	104
Figure 6-1. A schematic representation of melt electrowriting of structures with different geometries	115
Figure 6-2 Schematic representation of scaffold fabrication; From MEW of PCL scaffold to hybrid structure	118
Figure 6-3. Mechanical properties of the fabricated scaffolds	121
Figure 6-4. Digital images of the scaffolds	124

Figure 6-5. Images of the melt electrowritten scaffolds	125
Figure 6-6. Representative confocal images of 0-90 mesh, 60-120 mesh, and honeycombs hybrid scaffolds stained for Calcein-AM (green) and PI (red).....	126
Figure 6-7. Fluorescence images of 0-90 mesh, 60-120 mesh, and honeycomb structures stained for F-actin (phalloidin: red) and nuclei (DAPI: blue)	128
Figure 7-1. Illustration showing an overview of the study	135
Figure 7-2. A) Tensile properties and B) Swelling behavior at different time intervals in PBS	137
Figure 7-3. Toxicity assay against HDF cells in vitro	139
Figure 7-4. Time-dependent variation of the wound closure percentage	140
Figure 7-5. Evaluation criteria in secondary wound healing based on histological analysis of different sample groups	143
Figure 7-6. Hematoxylin and Eosin (H&E) staining of histological sections of two scaffold groups at Day 7	144
Figure 7-7. Hematoxylin and Eosin (H&E) staining of histological sections of treatment groups at Day 21	145

1 Chapter 1. Introduction and motivation

Tissue engineering has gone through a revolution from traditional xenograft and autograft implantation to the efforts of fabrication and substitution of a functional structure that resembles the native tissue regarding geometry, mechanical, physiochemical, and biological properties [1]. In principle, tissue engineering comprises of three main components as follows: scaffold, cells, and bioactive molecules/growth factors. The scaffold provides a substrate where cells could hold-on to and spread over. It should mimic the natural microenvironment of the cells in such a way that they would be able to proliferate and secrete their own extracellular matrix (ECM). In this regard, scaffold's design and material's selection play important roles in guidance and stimulation of the cells [2]. In the last few decades three-dimensional (3D) printing has received considerable attention due to its potential for fabrication of complex porous constructs with interconnected pores in a layer-by-layer fashion at high precision. It is capable of realization of complex architecture designs which enable to obtain desired mechanical, physical, and biological properties. In addition, interconnected porosity would assist nutrients and waste transport more efficiently [3,4]. Extrusion printing is one of the most common printing techniques owing to its ease of use, low cost, high materials deposition precision with the aid of computer aided design (CAD) models, and a wide range of available biomaterials. However, reaching low filaments sizes mimicking natural human ECM, especially for thermoplastic polymers, is a limitation that needs to be overcome [5]. Melt electrospinning writing (MEW) is an additive manufacturing (AM) method which is a combination of solution electrospinning and extrusion printing. The print head is connected to a computer that moves according to the designed path, as in extrusion printing. In contrast to solution electrospinning, no toxic solvent is needed, thus toxicity risk is diminished, and material is printed in molten phase with higher viscosity which results in better control over its deposition [6]. Hence, MEW offers the precision of extrusion printing and at the same time is capable of obtaining filaments with much smaller than the nozzle diameter even to sub-microns. In addition, the final fabricated structure would possess a more flexible structure with more similar size to the human tissue ECM like skin.

Skin is the largest organ in the body acting as a barrier which protects internal organs from physiochemical, mechanical, and thermal hazards of the external environment. Additionally,

it is responsible for maintaining thermoregulation and hemostasis, sensation, and prevention of excess water loss [7,8]. The skin is comprised of epidermis, dermis, and subcutaneous tissue layers and the functioning is mainly coming from the cells and structures of the outer two layers [9]. If an injury happens, a consecutive cascades phases occur as following: hemostasis, inflammation, proliferation, and remodeling. For small-sized skin loss (< 1cm), wound closure happens spontaneously. However, this is not the case for large skin losses or chronic wounds which needs extra medical care [10]. The gold standard for treating large skin loss is autografting, despite its drawbacks such as limited donor sites, scarring the donor part, and long treatment duration [11]. Alternatively, 3D printing techniques could be used instead of conventional approaches, with the capability of fabricating patient specific skin substitutes with various cell sources and biomaterials according to the demand. Several materials from natural and synthetic sources are utilized for 3D printing of scaffolds for tissue engineering applications. They can be categorized in metals, ceramics, hydrogel, and thermoset/thermoplastic polymers. According to the tissue of interest, poly (lactide -co-glycolide) (PLG), polycaprolactone (PCL), Poly (lactic acid) (PLA), and poly (glycerol sebacate) (PGS) are widely used materials showing biodegradability, biocompatibility, and good mechanical properties. However, they mostly have hydrophobic surfaces with very low degradation rate [12]. Hydrogels, on the other hand possess water-rich structure with more cell friendly nature suitable for cell attachment and nutrient flow, but with poor mechanical properties and printability. On these bases, 3D printing of hybrid structures could be a promising approach for getting the advantage of both materials categories [13].

The main objective of this thesis was to investigate on candidate methodologies and materials based on 3D printing techniques including MEW and extrusion printing for manufacturing of hybrid structures for skin regeneration and wound healing application. In this context, we first provided a literature review of current state of research in additive manufacturing with focus on MEW and its potential for hybrid manufacturing. We discussed about the principles, challenges, and advantages of MEW among other additive manufacturing techniques. The discussion was followed by the effect of hybrid manufacturing approaches on mechanical and cellular properties of the final product and future perspective of hybrid MEW processes. Using MEW as a powerful tool for scaffold fabrication, we implemented a mathematical model for studying the effect of printing parameters on the

filament's diameter which could be used to predict the fiber diameter according to process parameters. To do so, Response Surface Methodology (RSM) method was implemented and at the end, a very simple and practical model was obtained.

PCL is a favorable polymer used in tissue engineering for many applications. Its biocompatibility, biodegradability, good mechanical properties, and melt processability with relatively low melting temperature makes it one of the most common polymers in scaffold fabrication via additive manufacturing techniques. However, its slow degradation kinetics and hydrophobic properties create a barrier for its clinical application. Copolymerization is an alternative approach to overcome these drawbacks. In this context, we synthesized poly propylene succinate (PPSu) and copolymerized it with PCL which resulted in higher degradation rate, improved hydrophilicity, and lower melting point compared to neat PCL. Additionally, the copolymer was doped with silver nitrate and the results showed enhanced antibacterial properties with no negative effect on cells according to *in vitro* characterization. The composite was 3D printed via extrusion printing to fabricate a 3D mesh structure. The findings showed that this composite could be utilized for skin tissue engineering applications.

Other than stiff polymeric materials like PCL, PLA, PLGA hydrogels are another appealing polymeric material for tissue engineering due to having high water content, bioactive molecules, and possessing similar structures to that of natural ECM [14]. Bioprinting of hydrogels namely bioinks is regarded as a challenging process in biofabrication of tissue substitutes because of their poor mechanical characteristics, showing shear-thinning properties, narrow temperature range for printability, and low shape fidelity. Hence the demand on development of new bioprinting approaches are increasing for fabrication of complex structures that could be used for soft tissue engineering applications such as skin substitutes and vascular structures. On this basis, we prepared and characterized a support-bath system for bioprinting of hydrogels called as in-gel printing technique. Different compositions based on the complexes of Pluronic PF127, nanoclay (Laponite RDS) and calcium chloride were prepared, and the rheological properties of the formulations were investigated. Series of complex geometries were bioprinted by in-gel technique with cell-laden alginate as a sample hydrogel. The results confirmed the successful preparation of

support-bath that allowed bioprinting of complex structures possessing their shape fidelity. The findings of this section could be used for various hydrogels depending on the targeted tissue.

Despite the significant developments of 3D printing techniques, vascularization is still a challenge especially for thick structural substitutes. Geometrical features strongly govern the cellular behavior. Proper morphological alignments of cells would lead to formation of cord-like structures that could further assist the vascularization process. In this basis, hybrid structures in a combination of hydrogel and thermoplastic polymer were fabricated to obtain enhanced mechanobiological features for the application in skin tissue engineering. With that in mind, we aimed to explore the effect of different architectural design of the melt electrowritten scaffolds on cellular response. The algorithms of three different geometries for mesh structures of 0-90 and 60-120 degree orientations and a honeycomb construct were written and G-codes were generated for MEW path planning. Melt electrowritten scaffolds were fabricated and filled with cell-laden gelatin hydrogel and photocrosslinked using visible light in the presence of metallic complex photocrosslinker. Skin tissue cellular components human skin fibroblasts (HSFs) and human umbilical vein endothelial cells (HUVECs) were co-cultured in gelatin hydrogel. The cellular response in different designs were studied and honeycomb structure showed more potential in aligning the cells and the ability to guide the formation of lumen structures. Mechanical properties of honeycomb structure also revealed that they represented high storage of elastic energy in tensile test and at the same time possessed high elastic modulus. The findings of this section could indicate the possible role of geometrical aspects in a hybrid design in controlling biomechanical properties of the fabricated substitute.

Wound healing includes a cascade of consecutive events that happen in a sequence of specific timing. For severe and/or chronic wounds, the healing processes could be slowed down which could increase the infection risk. A natural way to prevent the infection, is the formation of a connective tissue namely “scar” formation. This process will delay further recovery and functionality of the original tissue. In this context, the last chapter was designated to manufacturing of composite hybrid structure consisting of thermoplastic polymer/hydrogel via MEW and gel casting for wound healing application. Bioactive glass

(BG) containing silver was synthesized and added to PCL to induce healing stimulation and antibacterial properties. Melt electrowritten PCL-BG mesh was fabricated by MEW and infiltrated with gelatin hydrogel and crosslinked with visible light. Gelatin microspheres, as growth factor delivery vehicles, were synthesized and selectively impregnated with basic fibroblast growth factor (bFGF) and vascular endothelial growth factor (VEGF) to locally enhance healing and vascularization through selective casting of the hydrogel matrix within the 3D mesh matrix. Hybrid scaffolds were implanted in Sprague Dawley rat *in vivo* and the results showed enhanced healing of large skin defects in terms of wound closure time, vascularization, fibroblast-collagen amount, and epithelial formation.

The second chapter of this thesis entitled “Biomimicry in bio-manufacturing: developments in melt electrospinning writing technology towards hybrid biomanufacturing” [15] is the literature review for MEW and its potential for hybrid manufacturing.

The third chapter presents “3D printing of silver-doped polycaprolactone-poly(propylene succinate) composite scaffolds for skin tissue engineering” [16] for copolymerization of PCL with PPSu and its functionalization with silver nitrate.

Chapter 4 discusses Modeling 3D melt electrospinning writing by response surface methodology [17] showing the response of printing parameters on fiber diameter for MEW.

Chapter 5 explains preparation and characterization of nanoclay-hydrogel composite support-bath for bioprinting of complex hollow structures [18] where hydrogel bioprinting in a composite support-bath system and its characterization, bioprinting precision, and cell viability results are presented.

Chapter 6 describes 3D printing of hybrid scaffolds for skin tissue engineering: an investigation on the scaffold’s geometry in a hybrid design and its influence on mechanical behavior, cell alignment and morphology. This chapter also investigates geometrical cues on mechanical and cellular behavior for the formation of cord-like structure in vascularization path.

The seventh chapter “3D fiber reinforced hydrogel scaffolds by melt electrowriting and gel casting as a hybrid design for wound healing” discusses the fabrication of hybrid functionalized scaffold and it’s *in vivo* characterization for wound healing.

The result of each chapter is published/submitted to a peer-reviewed journal.

2 Chapter 2: Biomimicry in Bio-Manufacturing: Developments in Melt Electrospinning Writing Technology Towards Hybrid Biomanufacturing

This chapter was published in the journal of Applied Sciences as a review article [15].

Melt electrospinning writing has been emerged as a promising technique in the field of tissue engineering, with the capability of fabricating controllable and highly ordered complex three-dimensional geometries from a wide range of polymers. This three-dimensional (3D) printing method can be used to fabricate scaffolds biomimicking extracellular matrix of replaced tissue with the required mechanical properties. However, controlled, and homogeneous cell attachment on melt electrospun fibers is a challenge. The combination of melt electrospinning writing with other tissue engineering approaches, called hybrid biomanufacturing, has introduced new perspectives and increased its potential applications in tissue engineering. In this chapter, principles and key parameters, challenges, and opportunities of melt electrospinning writing, and particularly, recent approaches and materials in this field are introduced. Subsequently, hybrid biomanufacturing strategies are presented for improved biological and mechanical properties of the manufactured porous structures. An overview of the possible hybrid setups and applications, future perspective of hybrid processes, guidelines, and opportunities in different areas of tissue/organ engineering are also highlighted.

Keywords: melt electrospinning writing, hybrid biomanufacturing, three-dimensional scaffold, tissue engineering

2.1 Background

Scaffolds are considered as one of the key elements in tissue engineering (TE), providing a porous three-dimensional (3D) support structure for cells [2,19–21]. The interconnected porosity assists cell migration and nutrients and oxygen flow within the structure [22,23]. The fabricated scaffold must meet the principle criteria of a non-toxic, biocompatible structure with controlled biodegradability while maintaining sufficient mechanical properties that are comparable to native tissue to hold the structure's integrity [3,24,25]. In recent years, additive manufacturing (AM), also known as 3D-printing, has been widely used to fabricate well-defined structures with necessary environmental factors to enhance cell adhesion, proliferation, differentiation, and extracellular matrix (ECM) secretion [26–28]. This technique leads to the production of user-defined geometries with highly controlled porous complex macro-structures in a layer-by-layer approach that was based on the computer-aided design (CAD) model. AM techniques benefit from several technological advantages, among which reproducibility of the process, a broad range of choices in materials, and lower cost as compared to the other conventional methods are highlighted [29–31]. There are numerous approaches in AM, and the most common ones are extrusion-based printing or fused deposition modeling (FDM) [32,33], stereolithography (SLA) [34], ink-jet printing [35], and selective laser sintering (SLS) [36].

Electrospinning is a very popular technique, in which the material is deposited on a collector by the aid of a strong electric field through a fine nozzle. This technique shows great potential in the field of TE, owing to its simplicity, low cost of apparatus, and the ability to combine different polymers with improved properties [37]. Among the main approaches in electrospinning, solution electrospinning (SE) is a well-known method that has been used to fabricate 3D porous scaffolds for several decades in the field of TE [38–44]. SE setup has different parts as a syringe connected to a fine nozzle, a syringe pump that applies pressure, a high voltage supplier, and a collector. In principle, a continuous jet of polymer solution would be formed while using applied electrical field from the nozzle to the collector, while the solvent will be removed during or after deposition by self-evaporation. The polymer jet is narrowed due to a balance between the electrostatic repulsions of the ions and the surface tension that willing to minimize the surface charges. By a further increase of the applied

voltage, the filament at the spinneret tip turns into a conical shape jet stream called Taylor cone [45–47]. Several challenges, such as toxicity of solvents, solubility, and miscibility of polymers, instability of mass flow, and evaporation rates of the solvents have been already addressed in the literature [45,48–50]. It should be noted that some attempts have been made to address the instability challenge of SE and, hence, to control the filament placement, including near-field electrospinning [51], focused electrical field [52], using rotating disc collector [53] and high speed cylindrical collector [54], patterning the collector's conductivity [55], and direct-write electrospinning [56]. However, the issue of using toxic solvents is yet to be addressed. In addition, the fabrication of an aligned 3D structure with large dimensions is still a challenge due to the accumulation of residual electrical charges in the deposited filaments [57].

Melt electrospinning (ME) is a green, solvent-free method with a higher surface quality of the resultant filament as compared to solution electrospinning. By this means, no ventilation and further recovery and the removal of the toxic solvent is required, which reduces the cost of the process. Moreover, the toxicity concerns caused by toxic solvents would be eliminated. In addition, some polymers that cannot be dissolved in any solvent can be processed by ME. It also provides the opportunity of using multimaterials at once that either is not possible to find a common solvent, or it will cause difficulties for electrospinning [58]. Similar to SE, the polymer jet is subjected to pulling (electrostatic Columbic and gravitational) and resistive (surface tension and viscoelastic) forces at spinneret tip [6,59]. However, the polymer melt with much higher viscosity and lower conductivity lead to more stable jet during the deposition that makes it easier to obtain a controlled-shape filament. This would often result in larger fiber diameters and porosities in ME compared with SE, which can be positively considered in special cases since small pore size of electrospun fibers from SE might be a challenge for cell adhesion and cell migration [60].

Based on the above, melt electrospinning could be a promising method for 3D scaffolds fabrication. The polymer melt extruding through a nozzle will solidify rapidly without whipping in the air until reaches the collector [61,62]. With an integration of computer-controlled head, the same as AM processes, it enables the deposition of highly ordered fibers of layer-by-layer assembly, so-called melt electrospinning writing (MEW) or melt

electrospinning direct writing (MEDW) [63]. Figure 2-1 illustrates a schematic view of SE and MEW setups. Scaffolds that were fabricated with this method are appropriate candidates for TE and, owing to their high surface to volume ratio, they would assist in cell attachment and proliferation [57]. The scaffold's structure, porosity, size, and shape for different tissues and applications could be adjusted, so they can provide a porous environment with desired porosity and pore sizes for cell infiltration, cell binding, blood flow, and vascularization [20,63,64].

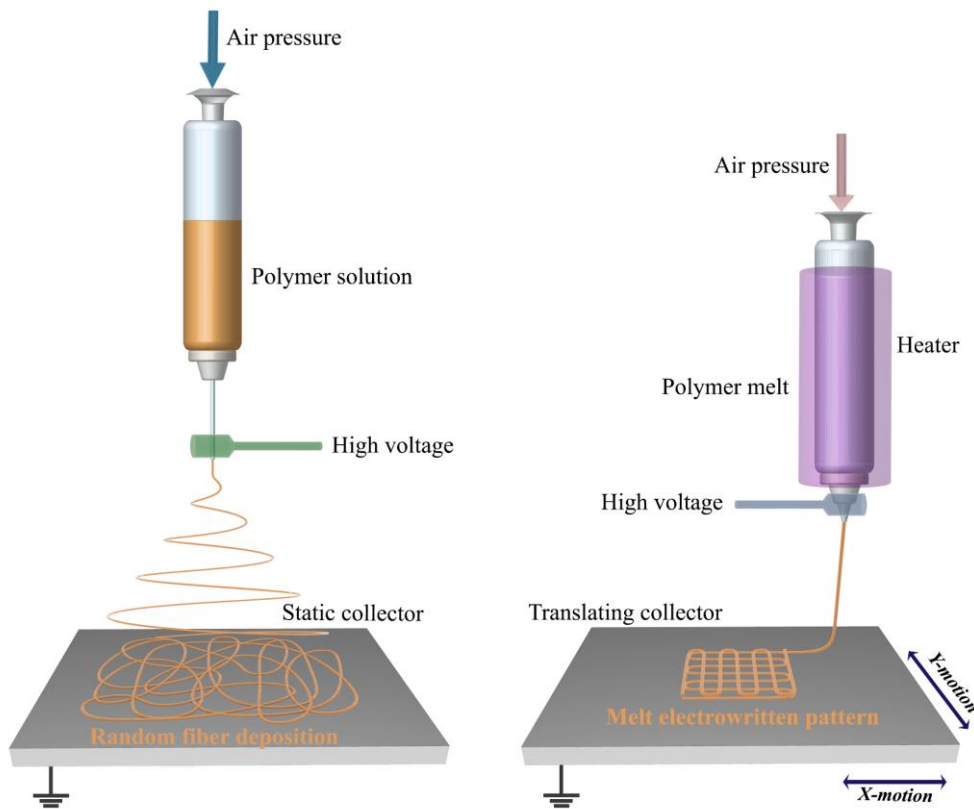


Figure 2-1: Schematic representation of solution electrospinning (left), and melt electrospinning writing (right)

Next sections present a summary of the principles, challenges, and recent updates of MEW in tissue engineering applications. In this context, the necessity of implementation of MEW as a part of a hybrid approach and its potential for scaffold fabrication is also discussed.

2.2 Principles and Challenges of MEW

The general MEW setup includes a high voltage supply, back pressure, material reservoir, and a collector. A heating system that is mostly grounded is integrated as an additional element compared to SE setup. The syringe or nozzle is heated and connected to a high voltage generator [65,66]. Electrical force, applying pressure, and surface tension are the forces applied to the molten polymer jet. By increasing the voltage difference and reaching a threshold value, it will be extruded continuously to the collector with a much smaller diameter than the nozzle [67]. For example, this method could reduce the fiber diameter from tens of microns down to 820 nm [62]. The collector or the syringe head could be movable in different directions [17,65]. One of the complexities of MEW setup is exposing heating element to high voltage electric field and how to put an insulator shield between the heating system and the syringe connected to high voltage to prevent any electrical interference [17,68]. Another challenge of applying high voltage to polymer melt is to fabricate a well-ordered structure as the tip-to-collector distance increases. The charge accumulation on the deposited fibers would cause fiber repulsion which results in structural distortion [69]. However, researchers have melt electrospun scaffolds with 100 layers of filaments [62] and recently Wunner and his coworkers [57] performed a numerical analysis to overcome the repulsion of depositing fiber issue that is caused by the accumulation of excess charge. They could achieve a high-volume structure of more than 7 mm. A further key factor in MEW is the heat and charge distribution in the syringe and nozzle, and between the collector and nozzle, respectively which determines the viscosity of the polymer and the electric force behavior [6,59,70]. In order to get a highly ordered filament deposition as “writing”, many parameters as printer’s head/collector speed, electric field, back pressure, temperature, and tip-to-collector distance must be in harmony. It is noteworthy to mention that the MEW setup itself plays an important role and since the process is in its infancy, many efforts have provided setup modifications for better control and feasibility of the process to reach perfect structures. Heating components other than electrical heating jackets can be classified into heating guns [71,72], lasers [73,74], and circulating fluids (water and oil) [75] that were used to circumvent possible difficulties of electrical shortcuts between the heater and electrical fields[57]. In order to apply pressure, the majority of studies used a pneumatic system in their setup with higher control on the applying force [66], rather than that syringe pump [76], screw-extruding, and mechanical feeding

[61,77]. Collectors are also divided into two general categories as static [17] and rotating [6]. The rotating cylindrical collectors enable various types of geometries like tubular structures [20,78,79]. In addition, some pattern shaped collectors were defined to guide the filament deposition in a porous hollow assembly [80].

So far, other setups for ME have been proposed to overcome technical issues or improve the system. For instance, Fang *et al.* [81] prepared a needleless melt electrospinning setup to avoid the corona discharge issue with the ability to increase the voltage difference up to 90 kV. In order to reduce the fiber diameter, Morikawa and coworkers [82] established a new setup as wire melt electrospinning and a down-stream non-isothermal heating method as an extra heating source for melt electrospinning [83]. Another method called bubble melt electrospinning was proposed by Li *et al.* [84] to eliminate the needle and reduce the fiber diameter. Besides, a research group prepared an umbellate spinneret for mass production reason rather than applying multiple nozzles [85].

Based on previously mentioned information, the processing parameters, such as collector speed and air pressure, significantly affect final structure and fiber diameter, as represented in Figure 2-2 [86]. The scaffold's architecture directly controls its mechanical and biological properties [17,87–89]. Therefore, a significant amount of research in the literature has been focused on adjusting, understanding, and predicting the influence of process parameters on fiber diameter, experimentally, and numerically [17,58,76,87,90–93].

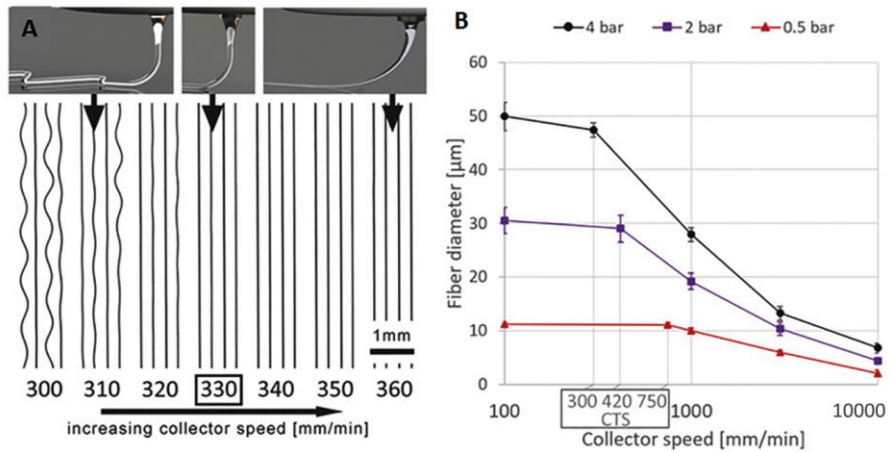


Figure 2-2. The effect of collector speed (A) on final structure at constant pressure, and (B) on fiber diameter at different air pressures [86]

2.3 Opportunities for MEW in Tissue Engineering

MEW is a recent milestone in additive manufacturing techniques for scaffold fabrication. Applying different biocompatible and biodegradable materials enables great opportunities for a wide range of applications in tissue engineering [21,94] including scaffolds for soft tissues like skin [95], endosteum [96], nerve [97], and cardiac tissue engineering [98]. Tubular structures that showed promising results for different tissues from bone, neural, and vascular applications were also fabricated with MEW method [78,79].

A wide range of polymers has been used in ME for tissue engineering applications. Polycaprolactone (PCL) [65,80], polylactic acid (PLA) [99], poly-L-lactic acid (PLLA) [100], poly (ethylene glycol) (PEG) [76], polyurethane (PU) [101], polymethyl methacrylate (PMMA) [102], polypropylene (PP) [103], and their blends are the most commonly reported materials. So far, some novel polymers were implemented in this field as well to address the disadvantages of mostly used polymers like hydration and hydrophobicity. However, polymers in exposure to water-containing environments as culture medium would absorb a considerable amount of water and consequently lose their mechanical properties. To address this issue, Chen *et al.* [104] synthesized poly(L-lactide-co-ε-caprolactone-co-acryloyl carbonate) (poly(LLA-ε-CL-AC)), a photo-crosslinkable terpolymer. Bertlein *et al.* coated PCL with a hydrophilic hydrogel that increased its hydrophilicity for a long-term duration in a

pH-independent strategy [105]. Hochleitner and coworkers [106] manufactured melt electrospun scaffolds from a hydrophilic class of polymers, so-called poly(2-oxazoline)s (POx). They synthesized poly(2-ethyl-2-oxazoline) (PEtOx) and revealed its potential for scaffold fabrication by MEW. Melt electrospinning writing was implemented for another polymer with piezoelectric properties. Florczak *et al.* [107] applied Poly(vinylidene difluoride) (PVDF) for a melt electrospun fibrous mesh structure with the manipulation of process parameters to achieve a perfect highly-ordered structure.

To date, the number of studies working on MEW with new approaches is significantly increasing [50,108]. Wunner *et al.* demonstrated the scale-up ability of MEW by integration of multi-print heads to their setup [109]. Eichholz and Hoey [110] studied the effect of scaffold's architecture on human skeletal stem cell behavior after optimizing their MEW setup. Different scaffold structures were fabricated in random orientation and controlled fiber patterns. The patterned structures were formed by depositing the fibers with an angle of 90, 45, and 10 degrees of every second layers. The effect of scaffold morphology on mechanical strength and cellular behavior were monitored. The results indicated that structure with 90° showed better mechanical properties, as well as cell spreading and osteogenic differentiation.

Hrynevich *et al.* [86] regulated the pressure and collector speed in their MEW setup during printing and achieved multimodal and multiphasic gradient scaffolds. Cell spheroids seeded in the scaffold's porosities attached and formed aggregates due to the low fiber diameter of the gradient scaffold and proper interconnectivity. In another study by McMaster and colleagues [111], cell spheroids from adipose-derived stromal cells were seeded on a mesh-like structure. Some ultra-fine threading was printed at the bottom of the scaffold by manipulating the processing parameters in order to hold the cell spheroids. The melt electrowritten scaffold induced the adipogenic lineage differentiation, and it provided an environment to obtain a sheet-like structure. In another study, Hochleitner and colleagues [112] performed melt electrospinning writing to fabricate box-shaped scaffolds for tendon and ligament application. The parameters were adjusted to achieve sinusoidal filaments to resemble the crimped structure of collagen I present in tendons and ligaments. An increase in tensile strength, elastic modulus, and elasticity as compared to straight fibers were observed. Besides these applications, Zeng *et al.* [113] fabricated microfluidic channels via melt electrospinning

writing method. A master mold of PCL as a sacrificial layer was melt electrospun, followed by casting polydimethylsiloxane (PDMS) on the patterned PCL structure and further curing. Afterward, the PDMS layer was removed and inlet and outlet holes were punched. Another PDMS microchannel was bonded to the first layer by applying a hot press. By means of this method, they achieved a microfluidic channel in a straightforward and cost-effective manner with the ability to adjust width and depth of the channels.

The current state of literature highlights the great potential of MEW in different areas of tissue engineering and scaffold fabrications, from hard to soft tissues with a wide range of materials according to the desired properties. Mechanical properties and biological response to the scaffolds could be simply tuned with adjusting the internal architecture. Moreover, since no toxic solvent is used, *in situ* fabrication of scaffolds for applications, such as wound dressings and bandages, could be realized [71]. The possibility of the incorporation of multi-nozzle setups could also be considered. Expansion of materials library, innovative hardware designs, and hence the ability to deliver more structural diversity make MEW a versatile approach to fabricate microstructures with controlled and desired properties.

The balance between processability, mechanical properties of the scaffolds, and their biocompatibility can be considered as one of the main challenges in the further development of MEW. In this respect, the utilization of other established fabrication technologies together with MEW as a hybrid approach could be a promising strategy to overcome the shortfalls of MEW and broadening its potential. By the aid of a hybrid method, one can fabricate hierarchical structures in order to satisfy cellular and mechanical demand and fulfill the requirements for tissue engineering constructs, while other application criteria, such as mechanical durability and/or processing challenges of specific materials, could be addressed. By this way, a handful of techniques that are based on surface modification and/or inclusion of hydrogels within stiff polymer structures fabricated by MEW would make new opportunities in the field of scaffold fabrication. Although the application of MEW as a part of a hybrid bio-manufacturing strategy is not widely explored at the moment, a critical review on the current state of research in this area can provide insight on the possibilities for development of sophisticated multifunctional structures.

2.4 Hybrid Melt Electrospinning Writing-Fiber Reinforcement of Hydrogel Constructs

MEW exhibits numerous advantages with the ability to fabricate flexible and highly-controlled geometries at sub-micron levels from several polymeric materials [53,95,114], yet, there are considerable issues to be addressed for their effective use in tissue engineering and regenerative medicine (RM). The main limitation is due to the hydrophobic nature of polymers causing the hindrance of controlled cell-scaffold interaction and organization. The examples of post-processing of scaffolds by plasma or sodium hydroxide (NaOH) treatments have been reported to improve hydrophilicity, but the non-specific adsorption of proteins on the construct still restricts the controlled and hierarchical alignment and thus cellular behavior [79,115–117].

Controlling and tuning the mechanical properties of fabricated scaffold via AM techniques that are comparable to native tissue is another pivotal challenge. For example, complex tissues, such as heart, muscle, cartilage, skin, etc., are soft and flexible structures, but they are tough enough to withstand high stresses without any destruction.

Utilizing MEW in a hybrid fashion has introduced new perspectives and enhanced its potential in terms of mechanical properties and biocompatibility. The hybrid constructs of the MEW scaffolds can be prepared with different approaches, as represented in Figure 2-3.

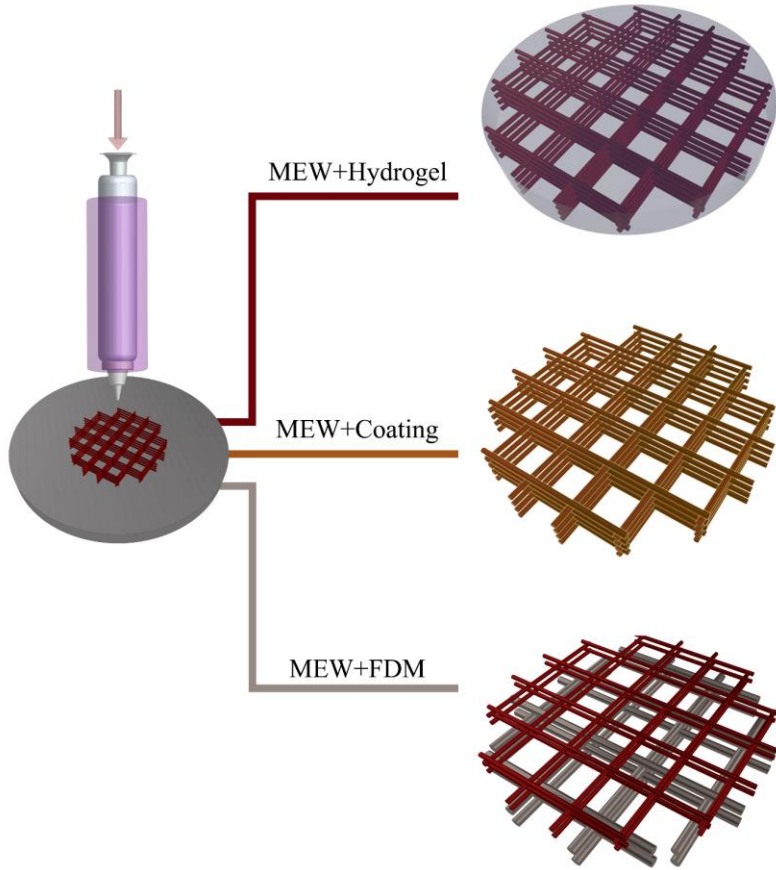


Figure 2-3. Different hybrid manufacturing approaches by employing MEW

2.4.1 Reinforcement Mechanism in Melt Electrowritten Fiber-Hydrogel Composites

Hydrogels are excellent candidates for scaffold fabrication with the potential for resembling the microenvironments of human body and encapsulation of different cells in their highly hydrated structures. Their tunable physicochemical properties, such as growth and differentiation factor ingredients, could strongly affect cellular behavior [14,118–120]. However, their structures are not as mechanically strong as the ECM of soft tissues, including fibrous proteins. Their lack of mechanical instability also limits the proper cellular functionality. The enhancement of mechanical strength can be achieved by increasing the concentration of polymer content or the crosslinking degree in the hydrogel, which may negatively affect cell viability, proliferation, migration, and differentiation [14,118–121]. The incorporation of a hydrogel within geometrically varied micro-fibers produced by MEW has fulfilled the required mechanical properties to mimic the function of fibrous ECM of soft

tissues [98,122–129]. Mainly, the construction procedure of hybrid hydrogel-MEW composites has two steps, which are the fabrication of fibers via MEW and infiltration of hydrogel in manufactured fibers [98,122–130].

The mechanism behind reinforcement of hydrogel matrices by melt electrowritten fibers was investigated in different studies with several hypotheses. Visser et al. [122] elucidated the reinforcement mechanism while using gelatin methacrylate (GelMA) hydrogel infiltrated into highly arranged networks of PCL microfibers. The composite was manufactured for musculoskeletal tissue engineering application, and the reinforced structure showed a significant increase in stiffness compared to hydrogel structure. It was revealed that the reinforced structure's mechanical strength was similar to that of native cartilage tissue. The hydrogel reinforced with fiber structure showed higher stiffness, rather than hydrogel scaffold and, interestingly, higher than the fiber scaffold without hydrogel. This result demonstrated the synergistic effect of reinforcing the composites. Mainly, lateral expansion of the hydrogel leads to the conversion of axial loads into lateral loads, which can be covered by fiber networks as tension in hybrid composites. Therefore, an increase in stiffness of the composite was correlated with horizontal expansion of the hydrogels while applying stress to the neighboring fibers under tension. Moreover, comparing the compressive loading responses also assessed the effect of fiber diameter on the stiffness of the composites. Low and high fiber diameter networks were manufactured via MEW and FDM, respectively. The composite structure with high fiber diameter showed similar stiffness with the structure without hydrogel. This means that the axial loads did not cause an elongation of the thick fibers. On the other hand, for the composites with thin fibers, the fibers that were elongated as a response to axial loading and hydrogel supported the structural integrity. In addition, the stiffness difference was observed between the groups of fiber networks with and without hydrogels. These observations indicated that a synergistic reinforcement effect was only observed only in the composites with small fiber diameters that were manufactured via MEW. The stiffness of the composite after compressive loading was further demonstrated through a mathematical model [122]. To calculate construct stiffness, fiber radius, the number of fibers and elastic modulus of the polymer were used as directly proportional variables, while the axial strain of fiber and composite and construct radius were used as reversely proportional ones. The mathematical model revealed that hydrogel expands with axial compressive loading

and causes exposure of the MEW fibers to tensile loads. However, theoretical stiffness value was calculated larger than the experimental one. It demonstrates the complexity of theoretical modeling of polymer-hydrogel composites, which demands more in-depth studies.

Bas et al. stated a similar hypothesis for reinforcement mechanism of hydrogels by MEW fiber network [63]. As stiffness of the composite relies on the MEW fiber networks, a detailed study was performed by controlling fiber spacing of 400 μm and 800 μm , and grid patterns with 0–90° and 0–60–120° orientations. The constructed melt electrowritten PCL fiber networks were infiltrated with GelMA, and GelMA/hyaluronic acid-methacrylamide (HAMA) hydrogels and the stiffness of the structures were evaluated. It was proposed that the hydrogels had significant lateral to axial strain ratio due to high Poisson's ratio values. However, the composites showed low Poisson's ratio, since highly organized fiber networks suppressed lateral deformation of the hydrogels. This synergistic reinforcement mechanism was the same as that reported by Visser et al. [122].

In another study, the high order finite element method was used to simulate the mechanical characteristics and elastic modulus of composites [123]. Composites with varying fiber spacing were used for the analysis. Simulation analysis revealed that decreasing the fiber spacing increased the compressive moduli of the composite due to higher reinforcing filler ratio, which was a similar synergistic reinforcement mechanism with the aforementioned studies [63,122]. The simulation results presented higher stiffness value for fiber networks as compared to experimental data, although the experimental and theoretical data for hydrogel alone and fiber-reinforced hydrogel samples were similar.

Castilho et al. performed two different finite element (FE) analyses in order to investigate the mechanism behind the reinforcement of hydrogel through fiber networks [124], as summarized in Figure 2-4. In this regard, melt electrowritten PCL network with different fiber spacing and GelMA hydrogel were manufactured. Subsequently, a compression test was performed to obtain stress-strain data that were used as an input for FE analysis. Afterward, a melt electrowritten fiber network was manufactured, and GelMA hydrogel was infiltrated into its gaps, and the FE analysis results were validated with experimental data. In the first analysis, continuum FE model was examined by employing the idealized geometry of the composite, which is unidirectional lamina. Continuum FE model exhibited the expansion of

hydrogel inside the composite. Besides, the diminishing effect of fiber network on hydrogel movement was observed. For individual hydrogel and fiber network structures, continuum the FE model results were similar to the experimental data in terms of compressive stress-strain behaviors. However, theoretical stiffness of the composite with higher fiber volume fraction was significantly lower than the experimental data in this model, although the stiffness values for composites with lower fiber volume fraction were similar.

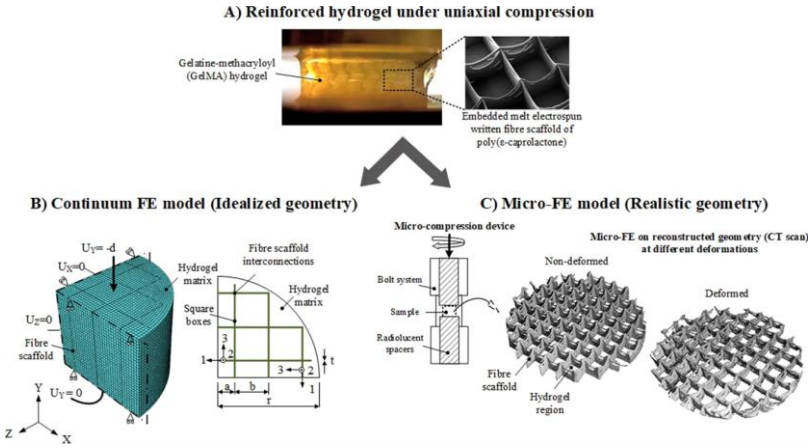


Figure 2-4. General modeling overview for continuum and micro-finite element (FE) models. (A) Uniaxial compression test for the investigation of reinforcement mechanism of the composite. (B) Continuum FE model on a quarter of an idealized composite architecture (C) Schematic μ -CT representation of the micro-FE model for the real composite architecture at different deformation levels [124]

In second analysis, micro-FE model was performed by employing the micro-computed tomography (μ -CT) images of the composite's geometry. The micro-FE model presented similar results with the experimental data in terms of deformation of fiber scaffold and composites. The results indicated that addition of hydrogel into fiber scaffold increased stiffness of the overall composite several folds due to the prevention of fiber network buckling through the resistance of hydrogels. Several inferences were made from those FE models. Continuum FE model stated that the reinforcement of the composites with low fiber fraction volume was governed by lateral expansion of the hydrogel, which put the fibers under tension. This hypothesis was similar to the previously mentioned studies. However, those studies did not consider different fiber spacing while explaining the mechanism. On the other hand, micro-FE model underlined the significance of load transfer through the interconnecting

regions of the fibers. Reinforcement of the composites with high fiber volume fraction through buckling inhibition by the resistance of hydrogels was also highlighted. Thus, FE analysis would be effective in optimizing the structure's architecture based on desired mechanical properties.

As an alternative to the heuristic approach, which relies on experimental trials, numerical modeling could be employed for design of the architecture and optimization of manufacturing parameters. In this regard, Bas et al. introduced the design of soft network composite with different mechanical and biological characteristics by modeling and manufacturing the composite, accordingly [125]. By provided compressive modulus and Poisson's ratio value of the hydrogel as an input to numerical model, compressive modulus of the composite was calculated. Based on the numerical results, 0-90° grid patterns with varying pore size and fiber thickness were determined for the fiber network design. Theoretical compressive modulus value obtained from the numerical model was validated by comparing the experimental results with that of different zones of the articular cartilage tissue model having different mechanical features. For this aim, the PCL fiber network with different fiber thicknesses and pore size was manufactured via MEW, and GelMA hydrogel was filled within the scaffold gaps, as shown in Figure 2-5. The initial layers of scaffold were printed with the PCL fibers, including hydroxyapatite nanoparticles (nHA), in order to mimic calcified zone, which is present between the native articular cartilage tissue and subchondral bone. Reinforcement of the hydrogels by fiber network was determined through uniaxial compression test. Compressive modulus values obtained by numerical modeling were in agreement with the experimental mechanical testing results.

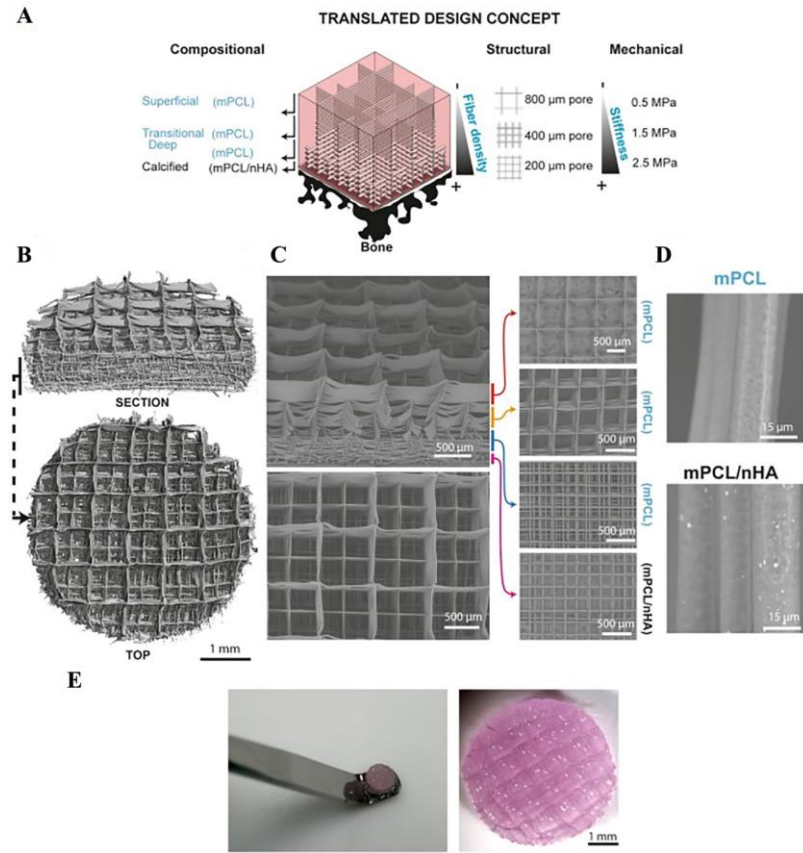


Figure 2-5. (A) Schematic view of the designed composite for cartilage application tissue having a different composition, geometry, and mechanical properties. (B) Micro-CT images of PCL fiber networks. (C) Scanning electron microscopy (SEM) images showing different zones of the composite scaffold. (D) SEM images of polycaprolactone (PCL) fibers with and without nHA. (E) General view of the composite structure [125]

2.4.2 Biological and Mechanical Aspects of Reinforced Composites in Different Tissue Engineering Applications

Depending on mechanical requirements of the target tissue, such as stress-strain relations, anisotropy, viscoelasticity, and flexibility, different improvements have been made on the MEW fiber-hydrogel composite. Within this framework, fiber networks with varying polymer types, fiber thicknesses, fiber spacing, and geometries have been designed and combined with several hydrogels for different tissue engineering applications.

In a simple approach, MEW PCL scaffold's porosity and crosslinking degree of GelMA was evaluated based on the composite stiffness and recovery for articular cartilage tissue

[122]. Chondrocytes that were encapsulated within GelMA hydrogel were homogeneously distributed throughout the PCL construct. The cells kept their spherical morphology and showed enhanced viability within the reinforced GelMA hydrogels. According to quantitative reverse transcriptase-polymerase chain reaction (PCR) analysis, a physiological compressive loading of 20% strain and 1 Hz induced the up-regulation of expression of genes encoding the ECM proteins of chondrocyte.

In another study, to recapitulate viscoelastic and stress relaxation characteristics of the articular cartilage, high negatively charged star-shaped poly(ethylene glycol)/heparin (sPEG/Hep) was used as hydrogel and then reinforced with the PCL fiber network having a 0°–90° grid pattern with different pore sizes that emulated collagen fibers in terms of anisotropic and nonlinear features [123]. Treating the surface with NaOH treatment increases the wettability of the fiber network.

When compared to alone sPEG/Hep hydrogel and MEW fiber network, the compressive modulus was several folds higher in fiber-reinforced hydrogel composite. Since the compressive modulus of the composite was measured as being higher than the summation of compressive modulus of hydrogel and fiber network alone, which indicated the synergistic reinforcement effect. Moreover, composite structure exhibited similar viscoelastic nature of the articular cartilage. Similar to the results of compressive modulus, only the fiber-reinforced hydrogel composite exhibited similar stress-relaxation behavior with the human articular cartilage, and the enhancement of ECM protein expression under hydrostatic pressure was observed [123].

Another study that was related to articular cartilage tissue engineering was conducted by employing reinforcement of hydrogels through melt electrowritten bi-layered microfiber network [126]. Different zones of articular cartilage tissue were resembled by two layers designed with different fiber patterning strategy in order to obtain zonal mechanical characteristics of the native cartilage tissue. The GelMA hydrogel was cast into the PCL fiber network, which was made up of dense structure with 0–45–90–135° crossed diagonal pattern mimicking a superficial tangential zone (STZ) and uniform 0–90° box structure mimicking middle and deep zone (MDZ) of the articular cartilage. A significant mechanical strength difference was observed between the reinforced and non-reinforced hydrogel structures. The

presence of a STZ layer enhanced the compressive modulus several folds as compared to the composite without STZ layer as the presence of STZ layer provided distribution of compressive load to the whole composite uniformly. Human chondrocytes encapsulated in GelMA hydrogel reinforced with bi-layered PCL fibers were tested under two different conditions: static conditions with chondrogenic differentiation factor and mechanical strength induced condition without addition of any differentiation factor. The results revealed that both conditions showed cartilage differentiation by the similar production of sulfated glycosaminoglycan (GAG) and collagen II, which indicated the activation of signaling factors under proposed mechanical condition.

The reinforcement of hydrogel by fiber networks was also used for a variety of other soft tissues. Fiber networks with different geometries have been constructed to meet the requirements of different mechanical properties of soft tissues. For instance, since soft tissues function under high tensile loads, a flexible soft tissue bearing high tensile loads were manufactured by embedding stretchable curvy PCL fiber networks into a hydrogel for tensile load-bearing, mechanical anisotropy, and flexibility [127]. A combination of poly (ethylene glycol) diacrylate (PEGDA), GelMA, and alginate were employed as hydrogel matrix. Since the transfer of the applied loads depends on the interaction between soft matrix and reinforcing fibers, the surface of the fibers was functionalized by photo-crosslinkable acryl groups, which provided covalent bonding between fiber network and PEGDA and GelMA hydrogels. The maximum tensile strain value that the composite could handle before irreversible deformation was recorded as being similar to the values of native soft tissues. After yielding point, manufactured fiber network elongated rather than being ruptured. Stiffness of the composite was several folds higher than the stiffness of hydrogel without reinforcement. Encapsulating human bone-marrow-derived mesenchymal precursor cells (hBMPCs) into the hydrogel assessed the biocompatibility of the soft network system. The encapsulated cells infiltrated into the curvy PCL MEW fibers were found to be viable after 72 h of incubation period.

Cardiac tissue is another complex soft tissue with a highly organized fibrillar structure and mechanical strength. MEW manufacturing method offers great potential to establish an environment with a highly organized structure for cardiac tissue engineering by providing

sufficient mechanical strength. Based on this idea, Castilho et al. systematically investigated the effect of hydrophobicity and the morphology of melt electrowritten PCL fibers on collagen reinforcement and the response of cardiac progenitor cells (CPCs) for potential therapeutic applications [98]. Due to the drawbacks of PCL, such as hydrophobic nature and slow degradation, hydroxyl-functionalized polyester, (poly (hydroxymethylglycolide-co- ϵ -caprolactone) (pHMGCL) was employed. Fiber scaffolds with rectangle and square geometries were manufactured while using two different formulations of polymers, which are PCL and pHMGCL-PCL blend. The fibrous scaffolds were evaluated with and without hydrogel forms. In case of fibrous networks without hydrogel, the tensile modulus of the blended-PCL scaffold was lower than that of scaffolds manufactured from PCL, but both types of scaffolds were in the similar range with the tensile modulus of human myocardium. However, those scaffolds showed different tensile modulus values that were based on their shapes. The rectangular shape exhibited anisotropic behavior of the native cardiac tissue. Even though tensile modulus and anisotropy of the scaffold showed almost similar mechanical characteristics to the native cardiac tissue, long-term mechanical features need to be investigated by employing cyclic tensile loading and other mechanical tests. In the case of composite structures, both blended and bare-PCL scaffold allowed collagen matrix infiltration in a uniform distribution, while collagen hydrogel with no support of PCL fiber scaffold remodeled into a clumped form. The analysis of CPCs in collagen hydrogel within both of the fiber scaffolds that were made up of PCL with and without blending with pHMGCL showed that the cells were 99% viable, regardless of the geometry and hydrophobicity of the fibers. However, cellular alignment and morphology changed, depending on geometry of the scaffold. Cells were randomly arranged in squared geometry scaffolds while the alignment of the cells was more regular, particularly in a preferential direction on rectangular ones. The number of aligned cells on the blended-PCL scaffold was found more than PCL scaffold, as shown in Figure 2-6. The nucleus of CPC's in the rectangular blended-PCL composites promoted less circular shape when compared to those in the square-shaped ones. In addition, it was observed that the interconnected porous structure also allowed the interaction of the cells between the compartments. This study revealed that hydrophobic nature of fibers and geometry of the scaffold strongly affect the interference between matrix and reinforcing fibers, which is reflected by cellular behavior. The authors also noted that pHMGCL might

change the electrical stimulation on the fibers, which can also have a positive effect on CPC's response.

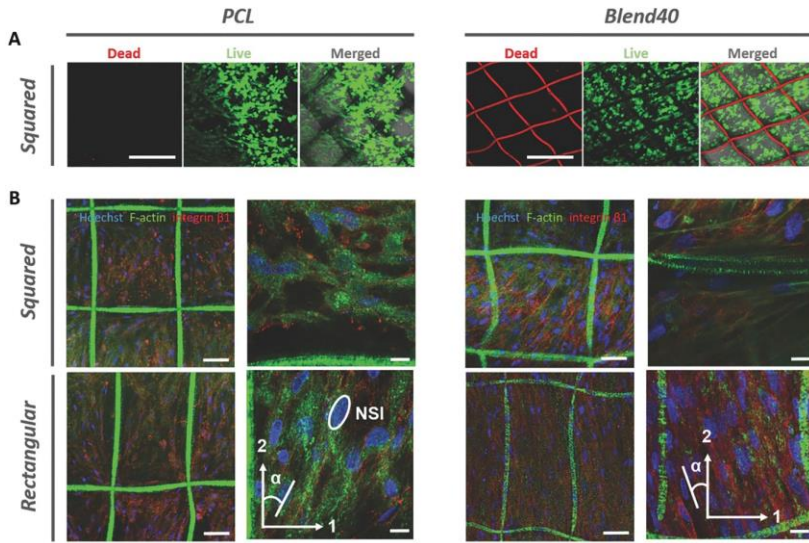


Figure 2-6. (A) Viability and (B) morphology of cardiac progenitor cells (CPCs) in collagen hydrogel infiltrated in squared and rectangular bare-PCL and blended-PCL scaffolds [98]

A physiologically relevant 3D environment that was fabricated from melt electrowritten fibrous composite could be considered for treatment of myocardial regeneration. Generally, the treatment can be followed by replacement of the dead cells during myocardial infarction with the healthy cells. Since induced-pluripotent stem cells (iPSCs) have the capability of generating large numbers of human cardiomyocytes, they are the target for direct transplantation, which showed promising results in non-human primates. However, they are not effective due to limited contractility and electrical instability.

Complex fibrillar architecture and mechanical characteristics of myocardial tissue were intended to be recapitulated for the production of heart patch in another study of Castilho et al. [128]. For this purpose, fiber networks with the hexagonal and rectangular structure were manufactured via MEW and then seeded with human induced pluripotent stem cell-derived cardiomyocytes (iPSC-CM), which was encapsulated within a collagen-based hydrogel matrix. Under in-plane tensile loading conditions, biaxial deformation characteristic of the hexagonal fiber scaffold was found to be superior to the rectangular-shaped scaffold.

Although the results were better than the rectangular fiber scaffold, deformation, and fatigue behavior of the hexagonal fiber network was poor in the y-direction. The fatigue behavior of the hexagonal fiber scaffold after cyclic tensile loading was more promising than the one in the case of the rectangular fiber network. iPSCs encapsulated in a collagen-based hydrogel were used to monitor the effect of different geometrical composite structures on cellular behavior. The cells were aligned through the fibers and they showed synchronous contractions throughout the scaffold. The cells in the hexagonal fiber network showed faster contractions and maturation of contractile myocytes. In vivo studies followed by injection of the matured cardiac patch onto a beating, the porcine heart did not reveal harmful effects on cell viability and on integrity of the engineered construct. It was proposed that fabrication of PCL fiber network with hexagonal microstructure improved the biaxial deformation and compliance.

Another different biomimetic design and fabrication strategy was proposed for heart valve tissue engineering (HVTE) in the study carried out by Saidy et al. [129]. The biomechanical characteristics of heart valve leaflets were aimed to be achieved by highly organized wavy-like PCL melt electrowritten fiber scaffold to mimic the collagen fibers that are present in the structure of the heart valve. Human vascular smooth muscle cells (HUVSMCs) were seeded to the scaffold either directly onto the scaffold or by encapsulating in fibrin hydrogel, followed by casting to the scaffold. The mechanical features of the manufactured construct showed similar results with native tissue in terms of J-shaped stress-strain curve behavior, anisotropy, and viscoelasticity. HUVSMC in the homogenously formed composite sustained the viability and exhibited the biochemical and mechanical properties of the main ECM component of native heart valve leaflet with the enhanced synthesis of collagen type I and type III. In the aforementioned studies on cardiac tissue engineering, uniaxial tensile tests were only performed on the fiber scaffolds without hydrogel matrix. Although it would be speculated that the main contributor to the mechanical properties of the composite is fiber network, investigation of the fiber network with hydrogel matrix due to the synergistic effect of the hybrid structure would reveal valuable understanding.

There are other reports that consist of melt electrowritten fibers and hydrogel composites. In those studies, although their potential to recapitulate tissue functions was reported, their mechanical properties were not explored. For example, Hutmacher et al. presented an

approach for periosteum regeneration [131]. Periosteum, which is the reservoir for vascular components, and bone-forming cells has a critical role in the regeneration of complex multiphasic system. The periosteum is mechanosensitive tissue that is exposed to shear and traction loads during movement and based on the subjected force it regulates cell proliferation and differentiation. This multiphasic structure was mimicked as in a composite of melt electrowritten PCL tubular scaffold seeded with human bone marrow mesenchymal stem cells (BM-MSCs) and sPEG/Hep hydrogel system that was loaded with HUVECs as a target for large bone defect repair. BM-MSCs were used as bone-forming cells, while the HUVECs cells were utilized for vessel formation. sPEG/Hep hydrogels were modified with RGD and loaded with VEGF. After the hydrogel infiltration in the tubular PCL scaffold, the cells were cultured in angiogenic conditions for seven days of in vitro culturing. Subsequently, the composites were implanted in femur side of mice. The explanted constructs after 30 days from implantation showed that HUVEC cells were not proliferated but formed capillary-like structures and BM-MSC kept proliferation without differentiation. In addition, it was observed that the implanted human cells were gradually replaced by the host cells. This study demonstrated the efficiency of multiphasic hybrid design with a combination of different human cell types in the periosteum tissue engineering concept.

In another study, the effect of the composition of soft matrix component and photoinitiator type for crosslinking within PCL microfibers on the re-differentiation of chondrocyte was investigated [132]. GelMA type A or type B that were mixed with hyaluronic acid (HA) were photocrosslinked with either lithium acylphosphinate (LAP-visible light; 405 nm) or Irgacure 2929 (IC2929-at UV light; 365 nm). Interestingly, it was found that PCL fiber reinforcement increased the expression of ECM components of chondrocytes in hydrogel constructs. GelMA from type B photocrosslinked with IC2929 enhanced the formation of cartilage-like tissue as compared to others through promoting increased GAG production, which showed similar compressive strength as native articular cartilage.

The MEW-hydrogel hybrid manufacturing approach has also allowed for the development of 3D in vitro tissue models, such as neural and tumor cultures [130,133]. For example, Glycine receptor transfected (GTR; ligand-gated ion channel) Ltk-11 cells encapsulated in Matrigel reinforced with melt electrowritten PCL scaffold. This model provided information

regarding the functioning of the ion channels with electrophysiological measurements from a physiologically similar 3D system [133]. In another study, patient-derived ovarian cancer cells were encapsulated in PEG hydrogel infiltrated into PCL fiber scaffold. It was used to mimic the tissue environment for the investigation of malignant behavior and tumor-promoting signals [130]. Designed models showed clinically similar gene expression of ovarian cancer with the samples that were obtained from a high-grade serous ovarian cancer patient. These models may be helpful for screening the possible medicines or a combination of therapies and design for other clinical trials.

It is clear that the MEW-hydrogel hybrid system is a promising technique for RM, TE, and disease models, yet two-step fabrication of the hybrid structures limits the control over-structure design and fiber writing. To overcome this limitation, Ruijter et al. assessed a single-step construction approach by MEW of PCL and extrusion bioprinting of eMSC-laden GelMA hydrogel [119]. This approach allowed for the precise deposition of cells in a mechanically stable composite with controlled porosity and pore shape. It was confirmed that the applied high voltage during construction did not affect either the cell viability and metabolic activity or the ability to differentiate toward multiple lineages of eMSC.

2.5 Other Hybrid Approaches with MEW

Melt electrowritten fibers post-processed with other materials could be classified as hybrid manufacturing. This approach relies on the initial production of MEW scaffold, which is tuned into relatively hydrophilic surface by plasma, NaOH treatment, or polymer coating. Subsequently, these microfibers are basically coated with cell attractive biomaterials, such as calcium phosphate (CaP), collagen, and fibronectin. For example, NaOH treatment to PCL scaffolds causes the formation of carboxyl and hydroxyl groups, which allows for the reproducible CaP coating. CaP coated fibers showed successful attachment of cells, and the results were found promising for bone tissue engineering [96,134]. Thibaudeau et al. proposed the utilization of the CaP coated PCL melt electrowritten fibers to develop a human bone environment in a murine host model to monitor the metastasis of human breast tumor to bone tissue [134]. The primary human osteoblast cells (hOB) successfully attached on the hybrid structure for seven days, which was then successfully implanted into immunodeficient mice. Afterwards, the formation of humanized bone ossicles in mice was confirmed. After the

injection of human breast cancer cells into blood circulation of the mice, it was observed that the cancer cells metastasized and formed lesions on bone tissues. This proposed model system was suggested to be useful for investigating the mechanism of human breast cancer metastasis to human bone in a murine host. In another study, the formation of endosteal bone-like tissue, which has an important role in hematopoietic stem cell proliferation, migration, and differentiation found in the inner wall of long bones surrounding bone cavity on CaP coated MEW PCL scaffolds were demonstrated [96]. The expression of endosteal and osteogenic specific markers of both primary human osteoblasts and placenta-derived mesenchymal stem cells under non-osteogenic and osteogenic conditions demonstrated a realistic design of tissue engineering strategies with physiologically relevant 3D porous ECM microenvironment for the generation of tissue-specific niches.

Bertlein et al. [105,135] fabricated melt electrowritten PCL composites by further coating with proteins and monitored the enhancement of cell attachment and cell functioning. Besides, the relation between the pore size and formation of neovascular like structures was analyzed while using melt electrowritten structures with 100, 200, and 350 μm pore size coated with fibronectin [135]. Figure 2-7 shows HUVECs attachment on the coated fiber networks after one day incubation period. The formation of a neovascular structure was observed after one week incubation of HUVEC cells on 350 μm pore size scaffolds. In the other study, collagen-functionalized star-shaped polyethylene oxide based prepolymers (sP(EO-stat-PO)) coated PCL scaffolds showed decreased cell attachment, due to a decrease in the non-specific protein adsorption on the surface [105].

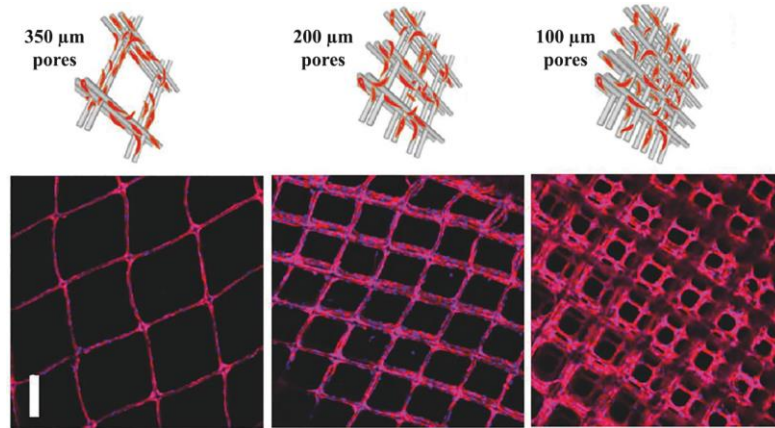


Figure 2-7. Attachment of HUVECs on the fibronectin coated PCL fiber networks with different pore size. Scale bar represents 200 μm [135]

MEW is used in combination with other scaffold generation methods to enhance their biological and mechanical properties. It was combined with FDM to generate a roughened surface that enhanced initial attachment, proliferation, and Ca^{2+} deposition of the osteoblast-like cells [136]. In another study, melt electrowritten structures with different geometries were designed for attachment of osteoblasts on one side, and keratinocytes and connective tissues on the other side. The fibrous structures were combined with a core PCL film that was prepared via casting to prevent possible infections for applications of oral and maxillofacial surgery [137]. In this study, the design of construct was found cytocompatible with improved cell proliferation and showed bacteria-tightness over two weeks.

Melt electrospun scaffolds could be functionalized by integrating with solution electrospinning [138,139]. In the study of Park et al., they combined MEW with solution electrospinning to acquire micro-nano fibers, mimicking the ECM structure for further application in tissue engineering [138]. PCL was utilized for MEW process to manufacture a mesh-like structure, and a PCL/collagen blend was used for SE, as shown in Figure 2-8. The hybrid MEW-SE scaffold was fabricated in a two-step manner. The patterned microlayers were melt electrospun, and PCL/collagen nanofibers were deposited between the layers by electrospinning. Three different combinations of MEW and SE were used with varying the number of PCL/collagen layers. Afterwards, bovine chondrocytes were seeded, and cell adhesion and proliferation were investigated for 10 days of incubation on different hybrid

scaffold designs. The results demonstrated that the scaffolds containing more layers of PCL/collagen had 2.5 folds higher cell attachment and 2.7 times more cell number than the melt electrospun PCL scaffold. The amide groups of PCL/collagen nanofibers with improvement in its hydrophilicity with the help of its rough surface and higher surface area enhanced the cell attachment, and the ECM like architecture of the hybrid structure enhanced its cell proliferation.

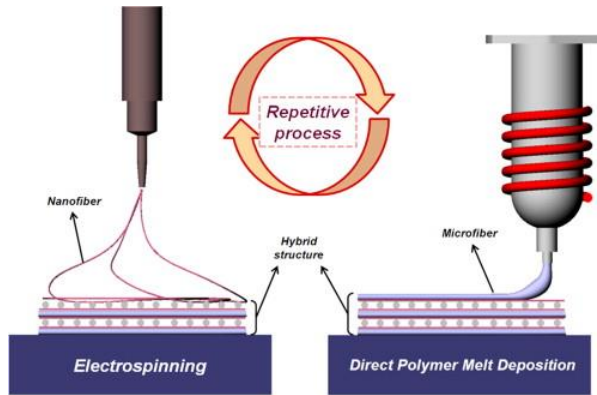


Figure 2-8. Hybrid setup of melt electrospinning writing-solution electrospinning (MEW-SE) for manufacturing of composite PCL/collagen structure [138]

Another study was performed by developing a hybrid MEW-SE setup for neural applications. Khadem Mohtaram et al. [139], melt electrospun two different micro-patterns of PCL as loop mesh and biaxial aligned structures and functionalized them with retinoic acid (RA) encapsulated PCL while using SE. The scaffolds were then seeded with neural progenitors that were derived from human induced pluripotent stem cells (iPSCs). The promotion and differentiation of iPSCs were evaluated, and the effect of different geometries was explored as well. Cell viability, immunohistochemistry, neurite extension, and real-time quantitative PCR analysis were performed. Electrospinning of RA encapsulated PCL increased cell attachment due to expanding the available surface area for cells to adhere. The cells were able to adhere, align, and migrate along the fibers in the loop mesh scaffolds with lower fiber diameters. Biaxial aligned fibers showed more promising results in terms of cell viability, proliferation, elongation, and neurite outgrowth. In general, melt electrospun structures induced the expression of neural markers in the cells, and hybrid structures showed the highest expression of neural markers as compared to loop mesh and biaxial aligned

scaffolds. Melt electrospinning could be favorable for neural tissue engineering, since the geometry of the fabricated structure strongly influences the cell alignments and cell response. Moreover, by integrating it with other techniques, it can serve as a promising strategy to fulfill the requirements of the designed scaffold. The modification of melt electrospun structures by solution electrospinning utilizing benign solvents or water with a variety of polymers encapsulated with drugs, nanoparticles, and biomolecules could enrich its application for different tissue engineering purposes.

2.6 Summary and Future Perspective

The ability to utilize a large number of polymers and their blends has led to an increasing number of studies that are related to MEW in recent years. Computer-controlled nature of the melt electrospinning writing process facilitates design and fabrication of the structures with great control over mechanical properties and, subsequently, cellular responses. Owing to the elimination of solvent in comparison with the solution electrospinning, this method reduces the cost of the process, with respect to the solvent removal and recycling, toxicity and miscibility, and ventilation system. The feasibility of inclusion of several types of nanoparticles and active biomaterials, such as bioactive glasses, carbon nanotubes, drugs, and antibiotics within the polymers has resulted in further expansion of the application of MEW in tissue engineering. Despite the highlighted advantages of MEW, progressive development in material libraries, and establishment of innovative hardware, some requirements are yet to be addressed. For instance, the fiber diameter could not be obtained as low as natural ECM diameter. In addition, most of the polymers that were processed by this method possess hydrophobic surfaces with low control over cell attachment and protein adsorption. Although mechanical properties can be tuned by controlling the structure's architecture and porosity, high stiffness values, and low elasticities as compared to human tissues are major concerns in further applications. Moreover, the thermoplastic polymers which could be utilized at elevated temperatures are also limited. To address these challenges, the integration of MEW with other techniques as a hybrid process could indeed offer a promising strategy. This integration would, in turn, provide the possibility to include cell-laden hydrogels, heat-sensitive drugs, or bioactive molecules, and to functionalize the polymers with other AM techniques combined with MEW. The reinforcement of hydrogels by well-ordered melt electrospun structures is

one of the most common hybrid approaches presented in the literature, which is mainly used for soft tissue regeneration applications. The implementation of rigid polymer meshes within less stiff hydrogels showed significant improvements in composite stiffness. This improvement is explained with the synergistic reinforcement effects with several hypotheses. In general, the residual tensile stress in the fibers due to the expansion of the hydrogel in the compressive loading, enhanced load transfer within the fiber network, and the role of hydrogels in the prevention of buckling have been emphasized. It should be noted that most of the mechanical tests were conducted under compressive loading conditions. However, no investigation on the reinforcement mechanism under other loading conditions (i.e., tensile and shear loading) has been conducted, although they significantly contribute to the mechanical behavior of native tissues. This approach holds high potential in the case of several areas of research, including cartilage, cardiac, neural, skin and bone tissue engineering, and wound healing applications, not only for improving the mechanical properties, but also maintaining a hydrated environment at the same time for cells to attach, migrate, and differentiate. By further development of materials and architectures, we foresee extensive progress in hybrid systems to utilize a wide variety of polymers and hydrogels with several biomolecules, cells, and nanoparticles.

Hybrid approaches are not limited to fiber-reinforced composites. Other approaches, like functionalization or coating of the melt electrospun structures with calcium phosphate, sodium hydroxide, and plasma treatment, were also employed. This would improve the surface properties and tune the functionality of melt electrospun structures for better cell-scaffold interactions. Some researchers developed a hybrid system with other AM or conventional techniques by the incorporation of FDM, solution electrospinning, and casting, into the melt electrowriting setup. This would result in a mechanically strong hydrophilic scaffold with the higher surface area.

As a conclusion, the adjustment of mechanical properties of multiphasic composites can be considered as a key factor in hybrid printing. More comprehensive experimental and numerical modeling studies are needed to better understand the mechanical properties and optimize the properties of hybrid MEW structures. Although elastic modulus and Poisson's ratio of the components of the hybrid structure would be considered as the main parameters

for the modeling studies, other biomechanical features of the components and the mutual interactions of the components should be taken into account to improve the accuracy of modeling.

In addition to the consideration of proper mechanical testing protocols, there exists a gap in the literature regarding the assessment of degradation kinetics of the composites and counterbalance between the extent of degradation and the mechanical and structural integrity. Degradation kinetics and the rate of new tissue formation/integration would play a crucial role in the determination of the interactions between the implanted construct and surrounding tissue after the implantation.

3 Chapter 3: 3D printing of silver-doped polycaprolactone-poly(propylene succinate) composite scaffolds for skin tissue engineering

This chapter was published in the journal of Biomedical Materials as a research article [16].

Scaffold-based tissue engineering approaches have been commonly used for skin regeneration or wound healings caused by diseases or trauma. For an ideal complete healing process, scaffold structures need to meet the criteria of biocompatibility, biodegradability, and antimicrobial properties, as well as to provide geometrical necessities for the regeneration of damaged tissue. In this study, design, synthesis and characterization of a three dimensional (3D) printable copolymer based on polycaprolactone-block-poly(1,3-propylene succinate) (PCL-PPSu) including anti-microbial silver particles is presented. 3D printing of PCL-PPSu copolymers provided a lower processing temperature compared to neat PCL, hence, inclusion of temperature-sensitive bioactive reagents into the developed copolymer could be realized. In addition, 3D printed block copolymer showed an enhanced hydrolytic and enzymatic degradation behavior. Cell viability and cytotoxicity of the developed copolymer were evaluated by using human dermal fibroblast (HDF) cells. The addition of silver nitrate within the polymer matrix resulted in a significant decrease in the adhesion of different types of microorganisms on the scaffold without inducing any cytotoxicity on HDF cells in vitro. The results suggested that 3D printed PCL-PPSu scaffolds containing anti-microbial silver particles could be considered as a promising biomaterial for emerging skin regenerative therapies, in the light of its adaptability to 3D printing technology, low-processing temperature, enhanced degradation behavior and antimicrobial properties.

Keywords: polycaprolactone-poly(propylene succinate) block copolymer, 3D printing, scaffolds, antimicrobial properties, skin tissue engineering.

3.1 Introduction

The skin plays a crucial role as the largest tissue in the body, which acts as a thermal, mechanical, and bacterial barrier. Severe skin injuries caused by burns, traumas or wounds may not heal by themselves and require skin tissue substitutes [140–143]. To mimic the network topology of the extracellular matrix (ECM) of the skin, a highly porous 3D structure with interconnected pores is essential to support cell migration and proliferation, nutrient and waste transport, and vascularization [22,33,144,145]. Control over the structural and geometrical features of 3D scaffolds, as well as the identification of candidate materials with acceptable biocompatibility and similarity of physical and mechanical properties with host tissue, have yet to be addressed [33,144,146]. Moreover, the degradation behavior of scaffolds can be tuned with respect to the requirements of tissue engineering applications. In this respect, novel fabrication strategies can play a significant role in producing desired scaffold architectures with tunable material properties [20,95].

AM, also known as 3D printing, is one of the most promising scaffold fabrication strategies due to its ability to produce complex structures with customized geometries by utilizing CAD models [3,147,148]. Among the AM processes, extrusion-based 3D printing is a popular and widely used technique since it can produce polymeric scaffolds with customized geometries with ease and low-cost [149–151].

PCL is a semicrystalline polymer widely used for tissue engineering applications due to its biodegradability, non-toxicity, ease of thermal processing, high decomposition temperature, excellent mechanical properties, and the possibility of its incorporation as a composite, physical blend, or copolymer with other biomaterials [152,153]. However, some challenges such as low degradation rate due to a high degree of crystallinity, hydrophobicity, and relatively high melting temperature, might limit the application of PCL [154]. A common way of addressing these limitations is to blend or copolymerize PCL with other appropriate polymers to tune the rate of degradation and its hydrophilicity, as well as to lower the melting point [154]. Bio-based polymers with monomers from renewable sources have attracted a great deal of attention because of their advantages such as conservation of limited resources, low toxicity, biodegradability, availability and environmental friendliness [155,156]. Among them, PPSu, a biodegradable polyester, is a promising candidate to be copolymerized with

PCL since it has a low melting point of around 44 °C and a glass transition temperature of around -36 °C with a fast degradation rate. Previous studies showed that the addition of PPSu to PCL increased the enzymatic degradation rate and its hydrophilicity [156–159].

Infection is one of the significant healing hindrances for the skin repair procedure. The functionalities of utilized scaffold such as antimicrobial activity, could significantly affect the healing process during post-implantation. Hence, the scaffolds which possess antimicrobial characteristics in addition to the desired geometrical and physicochemical properties would be advantageous [160–162]. To date, different strategies in skin tissue regeneration and wound healing applications have been implemented, including the incorporation of various types of antibiotics and silver compounds [162–166]. Due to the development of the strains of antibiotic-resistant bacteria and the environmental concerns about using antibiotics, alternatives such as incorporating silver into the biopolymers are used in skin regeneration therapies [167,168].

Furthermore, the effectiveness of antibiotics is usually restricted to certain bacteria, while silver-containing components have shown promising results against a broad spectrum of microorganisms including fungi, viruses, and some Gram-negative and Gram-positive bacteria. Silver, in both metallic and ionic forms, possesses strong antibacterial and anti-inflammatory properties and has been used in many applications such as cosmetics, wound dressing, medical products, and wound healing scaffolds. In addition, it shows low systemic toxicity and can enhance the epithelialization of the wounds and reduce surface inflammation [169–175].

To date, there are numerous attempts at the utilization of PCL and its blends and copolymers with biodegradable polyesters for 3D printing applications [176–178]. To the best of our knowledge, there is only one study about the preparation of poly(butylene succinate)/polylactide blends and further processing by fused deposition modeling (FDM) printing [179]. In this context, this study is the first attempt at the development of 3D printable PCL-PPSu block copolymer with silver-induced biocidal properties, enhanced degradation and a relatively low-processing temperature compared to neat PCL. In this paper, a block copolymer of PCL-PPSu with different molar fractions and composites containing silver nitrate was synthesized and characterized to be used for skin tissue engineering and

wound healing applications. The printability of the resultant composites was further investigated, and an ideal composition was used for 3D printing of well-defined porous scaffolds. Degradation behavior and hydrophilicity of the selected copolymer were investigated by enzymatic/hydrolytic degradation studies and contact angle measurements, respectively. Biocompatibility of the composition was evaluated by viability analysis of HDF cells *in vitro*. Furthermore, the antimicrobial activities of the scaffolds were analyzed with microbial cell attachment and zone of inhibition test for *C. albicans*, *P. aeruginosa*, *E. coli*, and *S. aureus* microorganisms.

3.2 Materials and methods

3.2.1 Materials

Succinic acid (98%) and sodium nitrate (99.5%) were purchased from Fluka. Stannous octoate, ϵ -caprolactone (97%), 1, 3-propanediol (99%), tetrabutyl titanate (TBT, 97%), methanol (99%), chloroform (97%), sodium chloride (NaCl), silver nitrate (AgNO_3), yeast extract, peptone from casein, pancreatic digest, ethanol ($\geq 99.8\%$), Lipase *Pseudomonas cepacia*, and dimethyl sulfoxide (DMSO) were obtained from Sigma-Aldrich. Chloroform, nitric acid (HNO_3), and sodium borohydride were purchased from Merck. HDF cells and all the microorganisms used in the antibacterial studies were purchased from ATCC (UK). Dulbecco's modified Eagle medium (1X DMEM, 4.5 g l⁻¹ D-Glucose, L-glutamine, sodium pyruvate), fetal bovine serum (FBS), HyClone phosphate-buffered saline (10 X PBS, w/o calcium, magnesium), and Pen-Strep (10 000 Units ml⁻¹ penicillin, 10,000 μg ml⁻¹ streptomycin) were obtained from Gibco (UK). Cell proliferation reagent WST-1 was purchased from Roche. PBS tablets were obtained from MP Biomedicals, LLC (France).

3.2.2 Synthesis of polycaprolactone

PCL was synthesized via ring-opening polymerization of ϵ -caprolactone. Briefly, ϵ -caprolactone (50 g) and stannous octoate (20 μl) monomers were placed in a round bottom flask and heated to 180 °C and maintained for 24 h. After completion of the reaction, the product was dissolved in chloroform (50 ml) and precipitated in cold methanol. Then, the

solution was kept at -20°C overnight and followed by a filtration process. The product was dried in a vacuum oven for two days for solvent removal.

3.2.3 Synthesis of poly(1, 3 propylene succinate)

PPSu was synthesized based on a two-stage melt polycondensation polymerization method. In the first step, succinic acid (30 g, 0.254 mol) and 1, 3-propanediol (20.24 g, 0.2794 mol) were charged into a reactor in the presence of TBT (26 μl , 76.2 μmol) as the catalyst. The reaction mixture was heated up to 180°C under nitrogen atmosphere through refluxing for 90 min. During this step, succinic acid monomers were esterified to form oligomers. In the second stage, the reaction temperature was increased up to 200°C while a low vacuum (0.8 bar) was applied for 1 h and then a high vacuum (1.5 mbar) was used for 2 h at 220°C . The reaction was kept overnight at 230°C under a low vacuum (0.8 bar) to complete the second stage of the reaction and obtain PPSu polymer. The reaction product was dissolved into 200 mL methanol and placed at 4°C for 24 h. The white solid precipitates were separated from the solvent by filtration and dried for 2 d under vacuum. Figure 3-1(A) depicts the reaction route of PPSu polymerization, and Table 3-1 summarizes the reaction conditions and molecular weight of PPSu.

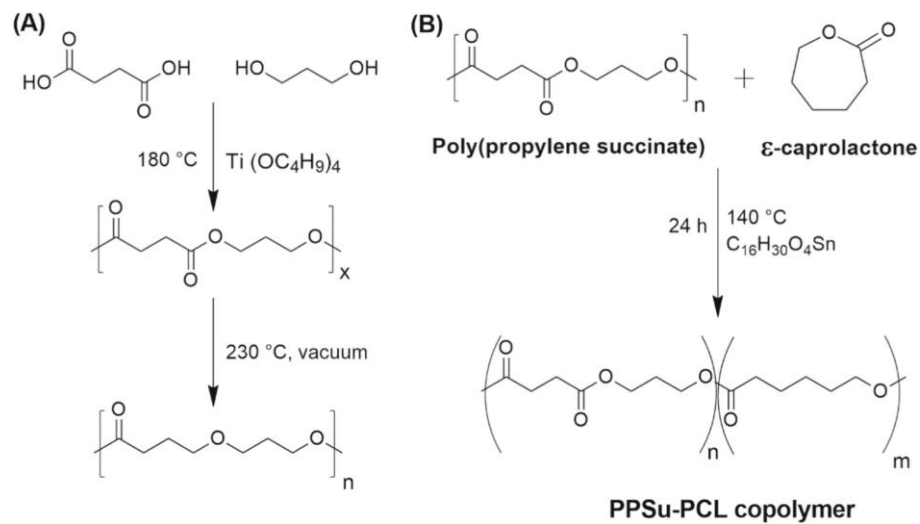


Figure 3-1. Reaction routes of (A) PPSu, and (B) PCL-PPSu block copolymer

Table 3-1. The number of reactants in the polymer synthesis and molecular weight of PPSu

Polymer type	Succinic acid (g)	1, 3-propanediol (g)	Ti(OBu) ₄ (μl)	Yield (%)	M _w (g/mol)	M _n (g/mol)
PPSu	30	20.24	26	54	4201	3388

3.2.4 Synthesis of PCL-PPSu block copolymers

PCL-PPSu block copolymer was synthesized through a bulk polymerization technique. PPSu to ϵ -caprolactone monomer was in the weight ratio of 1:10 by using 2 g of PPSu and 20 g of ϵ -caprolactone monomers in the presence of stannous octoate (0.05 wt% of ϵ -caprolactone) at 140 °C for 24 h. Afterward, the resultant product was dissolved into chloroform (50 mL) and was precipitated by adding cold methanol (300 mL). The resultant polymer was separated from the solvent and unreacted monomers were removed by filtration and then the material was kept drying in vacuum for three days at room temperature. In addition to 1:10 weight ratio, PPSu was undergone polymerization with ϵ -caprolactone monomer in the ratio of 1:5. PPSu-PCL having 1:10 weight ratio showed better printing behavior due to the differences in number average molecular weight and polydispersity index (PDI) of these two synthesized polymers. The details about experimental conditions and characterization results are given in Table S3-1 and S3-2 in the supplementary document.

Functional groups of the polymers were investigated by Nicolet iS 10 Fourier transform infrared spectroscopy (FTIR). FTIR spectra were obtained in %Transmittance mode in the spectral region of 400 to 4000 cm⁻¹ using a resolution of 2 cm⁻¹ and 32 co-added scans. ¹H- and ¹³C- nuclear magnetic resonance spectroscopy (¹H-NMR and ¹³C-NMR) were used to evaluate the composition and structure of the synthesized polymers (Varian Unity Inova, 500 MHz spectrometer). The thermal behavior of the polymers was analyzed by differential scanning calorimetry (DSC) using a TA-Q2000 instrument within the temperature range of -50 to 100 °C at heating and cooling ramp of 10 °C min⁻¹ under nitrogen atmosphere. The molecular weight and PDI of polymers were determined by Viscotek-VE2001 gel permeation chromatography (GPC) in DMF. Among all the combinations of the synthesized copolymers,

the initial printability tests were performed to screen the suitable candidate material for 3D printing (data not shown). The addition of PPSu at higher fractions resulted in increased elasticity of copolymer, which resulted in poor printability. For 3D printing, antibacterial and in vitro experiments, the copolymer with PPSu:PCL ratio of 1:10 was selected.

3.2.5 Contact angle measurement

Apparent change in the wettability of the copolymers compared with PCL was assessed using water contact angle measurements (Terra Lab, Turkey). Samples of PCL and PCL-PPSu were prepared by solution casting, and a deionized water droplet was placed onto the surface of polymer films (4 samples per each polymer), and the calculated contact angle values were presented as mean \pm SD.

3.2.6 Enzymatic degradation

PCL and PCL-PPSu based polymeric films with the same size and mass were prepared by casting. PBS (0.01 M, 1 \times) with a pH of 7.4 and 1X concentration was prepared by dissolving tablets in Milli Q water. Lipase *Pseudomonas cepacia* enzyme was dissolved in PBS at the concentration of 0.15 mg/mL of PBS, and the enzyme concentration for the polymer was 0.4 unit/mg.

Degradation tests were conducted in two different groups of PCL and PCL-PPSu copolymer films. Samples were kept in vials containing medium and were incubated at 37 °C at 100 rpm for up to 10 d. The medium was changed every 3 d. At specific time points, the polymer films were removed from the media and washed three times with deionized water followed by drying in a vacuum oven at room temperature until reaching a constant weight. Each sample was weighed before and after soaking in media. The percentage mass loss of the samples was calculated using equation. 1 as an indicator of the degree of biodegradability, where M_i and M_f are the initial and the final mass of the samples, respectively.

$$\text{Mass Loss (\%)} = \frac{M_i - M_f}{M_i} \times 100 \% \quad (1)$$

The surface morphology of the polymer films at different time points was observed using Zeiss Leo Supra VP 35 field emission scanning electron microscope (FE-SEM) at 4 kV acceleration voltage. Samples were sputter-coated with a thin layer of gold-palladium by a Denton Vacuum Desk V sputter before SEM imaging.

3.2.7 Hydrolytic degradation

Films of PCL and PCL-PPSu block copolymer were prepared by solution casting with prolonged drying time to ensure complete solvent removal. Hydrolytic degradation tests were conducted in two different mediums, including PBS, with a pH of 7.4 and DMEM cell culture media. Polymer films with the same dimensions were kept at an equal amount of media and maintained at 37 °C with constant shaking of 180 rpm in an incubator shaker for up to 21 d. On specific days, the polymer films were removed from the media and washed with deionized water and dried in a vacuum oven at 30 °C. The same protocol as mentioned in section 2.6 was followed to measure the degree of degradability.

3.2.8 Analysis of silver ion release and silver distribution

Silver release behavior of PCL-PPSu/AgNO₃ composites was studied by soaking them in PBS at 37 °C and shaking a rate of 50 rpm over 21 d. The samples were selected at the same size and shape to eliminate the effect of their size and shape for ionic release. PBS solution was not changed during the analysis to measure the cumulative release amount. At specific time points, silver ion concentration was measured by inductively coupled plasma optical emission spectrometry (ICP-OES) (Agilent Technologies, model 5110). Polymer samples used for these measurements were impregnated with 1% (wt/wt) silver nitrate.

Both copolymer films and solutions were characterized to measure the amount of silver released in PBS solution and total silver within the polymer. Acid digestion was performed for sample preparation. Briefly, copolymer films were dissolved in 5 mL of HNO₃ and kept on a hot plate for 10 min for complete dissolution. Afterward, the solution was diluted with a 20-fold dilution factor and filtered for further analysis. The same protocol was followed for

PBS solutions with a dilution factor of 20. To evaluate the homogeneity of silver distribution in the polymer matrix, samples were analyzed with FE-SEM equipped with energy dispersive x-ray spectroscopy (EDS). Polymer films were sputter-coated with gold-palladium before imaging.

3.2.9 3D printing process

A custom-built computer numerical control (CNC) 3D printer setup was utilized in this work explained elsewhere [180]. Briefly, the motorized printer head was connected to a computer and controlled by MACH3 CNC software. Rhinoceros 5 (Robert McNeel & Associates) was used to generate G-codes for desired printing patterns. The printer head mounted on the z-axis consisted of a 10-mL metal syringe and a nozzle with an inner diameter of 150 μm (Musashi Engineering Inc., Japan) heated by a heating jacket (New Era Pump Systems, Inc. NY, USA). A pneumatic dispensing system (Nordson EFD Performus V) was connected to the syringe. Figure 3-2 represents a schematic view of the 3D printer machine and the printing setup during printing. The printing temperature was selected based on thermal properties obtained by DSC measurements. The synthesized copolymer impregnated with silver nitrate was printed at 55 °C (the selection of temperature was based on the offset temperature of melting point in DSC data and the corresponding viscosity) while the samples were thermally equilibrated at 55 °C for 2 h prior printing. The applied pressure and print speed were set as 2 bars and 210 mm. min^{-1} , respectively. The extruded molten polymer was solidified on a collector at room temperature by the aid of a small cooling fan with the current of 80 mA placed 2.5 cm far from the nozzle. Cuboid structures with dimensions of 10 × 10 × 2 mm (15 consecutive layers) and gap size of 350 μm were 3D printed. Increments along the Z-axis of each layer was selected the same as the nozzle size (150 μm). Morphology of the printed scaffolds was investigated by FE-SEM. Pore size, filament diameter, and the variation of deposition profiles and shape fidelity of the printed samples were analyzed by using ImageJ software on the obtained SEM images. Measurements were done from 20 random regions of the scaffolds at different layers of each SEM picture. The data were reported as mean \pm standard deviation.

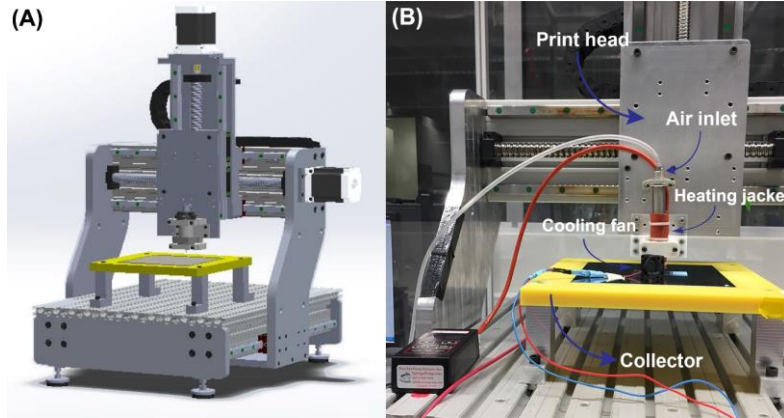


Figure 3-2. (A) Schematic view of the custom-made 3D printer, (B) real image of the printing setup during the scaffold printing

3.2.10 Biocompatibility evaluation

Cell viability and biocompatibility of the 3D printed constructs was evaluated by cell viability and morphology analysis after treatment of HDF cells with the extracts of the scaffolds. The extract samples were prepared based on the instructions at ISO 10993–12 with small modifications. Briefly, a 20 mg/mL of the 3D printed PCL, PCL/AgNO₃, PCL-PPSu, and PCL-PPSu/AgNO₃ scaffolds were incubated in fibroblast basal media for 72 h at 37 °C at 150 rpm. After the incubation period, the liquid portion was taken and filtered through a 0.22 µm filter. Previous studies showed that embedding 5% of AgNO₃ into polymer scaffolds improved the antibacterial properties of the scaffolds with no significant cytotoxic effect on the cells [181,182]. The optimum concentration was assessed by incorporation of 5% (wt/wt) AgNO₃ in the polymer matrix and further examination of cell viability.

HDF cells were cultured in fibroblast basal media (ATCC, PCS-201-030) containing fibroblast growth kit-serum-free (ATCC, PCS-201-040) and 1% Penicillin-Streptomycin Ampicillin (PSA). The cells were maintained at 37 °C under an atmosphere composed of 95% air and 5% CO₂. Cells were seeded in 96-well plate at a density of 5 × 10³ cells/well and incubated for 24 h. After the incubation period, several dilutions of the extracts (100%, 50%, 25%, 12.5%, 6.2%, 3.1%, 1.6%, 0.8% and 0.4%) were added into the cell culture followed by incubation for 24 h. Fibroblast basal media including 5% PBS and 5% DMSO were used as negative and positive controls, respectively. At the end of the incubation, the media was

removed, and cells were rinsed with PBS. Cell viability was determined using the WST-1 colorimetric assay.

For morphological characterization, cells were seeded in 24-well plate (25×10^3 cells/well) and incubated for 24 h. Dilution of the extracts of the 3D printed samples with concentrations of 100%, 50%, and 25% were added into the wells and were incubated for 24 h. Morphological changes were monitored using a Zeiss PrimoVert light microscope.

3.2.11 Antibacterial activity of block copolymer impregnated with silver nitrate

The synthesized PCL-PPSu copolymer and PCL were dissolved in chloroform, and the solution of AgNO_3 in ethanol was added with final concentrations of 1% and 2.5% (wt/wt). Concentrations of AgNO_3 were selected based on in vitro cytotoxicity assessments. Antimicrobial activities of rectangular 5×5 mm polymer films were determined by examining the zone forming potential through diffusion using model microorganisms including Gram-negative *P. aeruginosa* and *E. coli*, Gram-positive bacteria *S. aureus*, and yeast *C. albicans*. A 200 μl of microorganism cultures grown overnight were added by spreading on lysogeny broth (LB) agar Petri dishes and then, rectangular polymer materials with/without AgNO_3 were placed on LB agar Petri dishes and incubated at 37 °C overnight. Antimicrobial activity was determined by observing the presence of the zone of inhibition around the copolymer films after the incubation period and the diameter of each inhabitation zone was measured and reported in mm.

Adhesion of microorganisms on the copolymer surfaces was investigated. Briefly, the overnight microorganism cultures were seeded onto the PCL-PPSu and PCL-PPSu/ AgNO_3 copolymer films and incubated at 37 °C for 3 h. Incubation was continued overnight at 80 rpm with the addition of fresh LB medium. At the end of the incubation time, copolymer films were removed from the medium and subjected to washing with 0.9% NaCl (three times). The copolymer films taken from the saline solution (0.9% NaCl) were sonicated for 3 min to release the bacteria into the saline solution. 100 μL of saline solutions were spread on LB agar Petri dishes and incubated at 37 °C overnight. After incubation, the growth densities on LB agar Petri dishes were monitored.

3.2.12 Statistical analysis

The statistical evaluations for cell viability were performed using t-test, and cell viability data, hydrolytic and enzymatic degradation values and silver ion concentrations were expressed as the means \pm SD with at least three experiments. Those with p values <0.01 were considered as significant differences.

3.3 Results and Discussion

3.3.1 Structural analysis of PCL-PPSu block copolymer

FTIR spectra of PCL, PPSu, and PCL-PPSu block copolymer are illustrated in Figure 3-3. PCL exhibited a sharp peak at 1720 cm^{-1} , which is due to carbonyl stretching, while the two weak peaks at 2944 cm^{-1} and 2863 cm^{-1} correspond to the asymmetric and symmetric $-\text{C}-\text{H}$ stretching. Additionally, the peak at 1176 cm^{-1} is assigned to the $-\text{C}-\text{O}$ stretching [183]. In the PPSu spectra, the peak at 1715 cm^{-1} indicates the presence of the carbonyl group in the polymer structure [184]. The weak peak at 2971 cm^{-1} corresponds to the stretching of $-\text{C}-\text{H}$ bond related to the ester group. Furthermore, 1150 cm^{-1} is attributed to the bending of $-\text{C}-\text{O}-$ ester bond [185,186]. The presence of characteristic peaks of both PPSu and PCL in the spectrum of PCL-PPSu block copolymer confirms the formation of the copolymer structure with both PPSu and PCL segments.

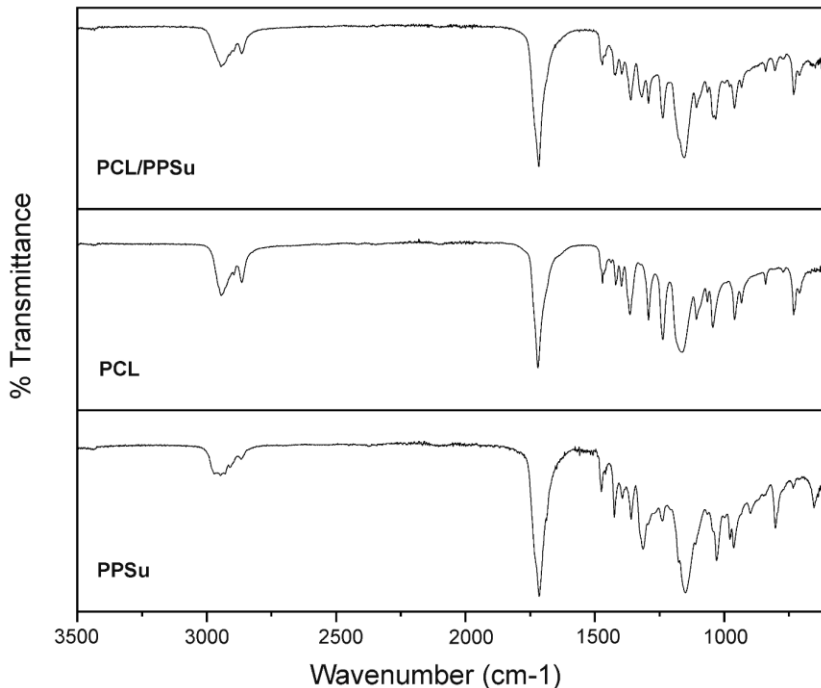


Figure 3-3. FTIR spectra of PCL-PPSu block copolymer, PCL and PPSu polymers

NMR analysis was used to identify the molecular structure of the synthesized polymers. Figure 3-4(A) represents the $^1\text{H-NMR}$ spectra of PCL, PPSu, and PCL-PPSu polymers. In the $^1\text{H-NMR}$ spectrum of PPSu polymer, the quintuple peak at 1.94–2.01 ppm corresponds to a methylene group (c) of the 1, 3-propanediol fragment. The characteristic peak at 4.1–4.2 ppm is attributed to the protons of two similar methylene groups (a) while the protons of two methylene groups on succinic acid monomer (a) appear as a single peak at 2.6 ppm. On the other hand, PCL gives a triple peak because of protons on the methylene group in the neighbor of oxygen (j) at 4.05–4.1 ppm. The protons of methylene group (h, h') appear as multiple peaks at 1.6–1.7 ppm. The (i) group protons is identified by a quintuple peak at 1.4 ppm, while (g) protons appear as a triple peak at 2.25 ppm [157]. $^1\text{H-NMR}$ spectrum of PCL-PPSu showed peaks in the same regions without any significant shift confirming the presence of both segments in the structure of the copolymer. At 3.63 ppm, a small triple peak corresponds to methylene protons of hydroxyl terminated ends ($-\text{CH}_2\text{OH}$) of polyesters which also exists in the copolymer [186]. The changes are remarkable in the peak area which corresponds to the molar fraction of the two polymers of PCL and PPSu with the same ratio of

1:10 for PPSu:PCL [157]. The peak integral values and normalized values to (c) peak are summarized in Table S3-3 in the supplementary document.

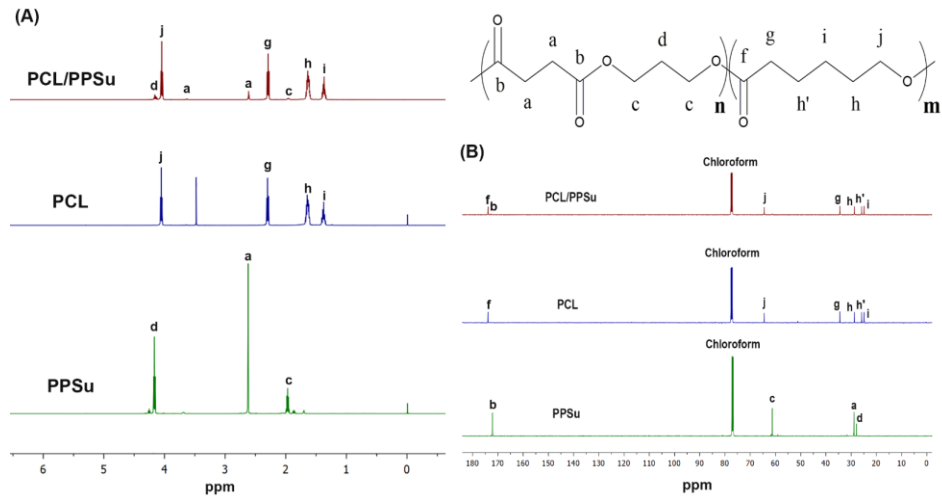


Figure 3-4. (A) ^1H -NMR and (B) ^{13}C -NMR spectra of PPSu, PCL and PCL-PPSu block copolymer

^{13}C -NMR spectra of the synthesized polymers are presented in Figure 3-4(B). ^{13}C -NMR spectrum of PPSu showed a peak at 172.3 ppm which attributes to the carbonyl carbon in the polymer structure (b), the peak at 61.4 ppm is assigned to the (c) carbon in PPSu molecular structure. In addition, the peaks at 29.1 and 28.9 ppm correspond to methylene carbons of succinic acid fragment (a), and the methylene group of 1,3-propanediol (d) fragment, respectively [187]. In the ^{13}C -NMR spectrum of PCL, the peak at 173.7 ppm is attributed to carbonyl group (f), 64.2 ppm peak is assigned to (j) carbon, the peak at 34.2 ppm corresponds to methylene group adjacent to carbonyl group (g), 27.9, 25.6, and 24.6 ppm peaks correspond to methylene groups (h), (h') and (i), respectively [188]. However, overlapping of PPSu and PCL peaks and the dominance of PCL peaks in ^{13}C -NMR spectra limits the ability of structural identification of PCL-PPSu through ^{13}C -NMR.

3.3.2 Thermal behavior and 3D printing of PCL-PPSu block copolymers

DSC curves for the heating and cooling cycles of PCL and PCL-PPSu copolymer are presented in Figure 3-5. Both polymers underwent crystallization during corresponding

cooling cycles. The onset of the crystallization peak for PCL was at 38 °C (T_c), and the maximum value was at 32 °C. On the other hand, the crystallization of PCL-PPSu started at 28 °C, and the maximum value was set at 23 °C. The heat of crystallization (ΔH_c) obtained from cooling cycles showed the state of the crystallization and its kinetics. The heat of crystallization (ΔH_c) for PCL was 72 J/g while the heat released during the crystallization of the copolymer was 32 J/g. The higher crystallization of PCL stems from its higher PDI providing higher chain mobility compared to PCL-PPSu block copolymer [189]. The copolymer's melting point in the second heating cycle occurred at a lower temperature than in the PCL sample (42 °C and 50 °C for the copolymer and PCL, respectively). The PCL-PPSu graph represents a semicrystalline behavior with a double melting point in the first heating cycle which could be attributed to the different blockchains of the copolymer [157]. In addition, the heat of melting (ΔH_m) showed a similar trend as ΔH_c as presented in Table S3-2, due to the difference in kinetics of crystallization of PCL-PPSu.

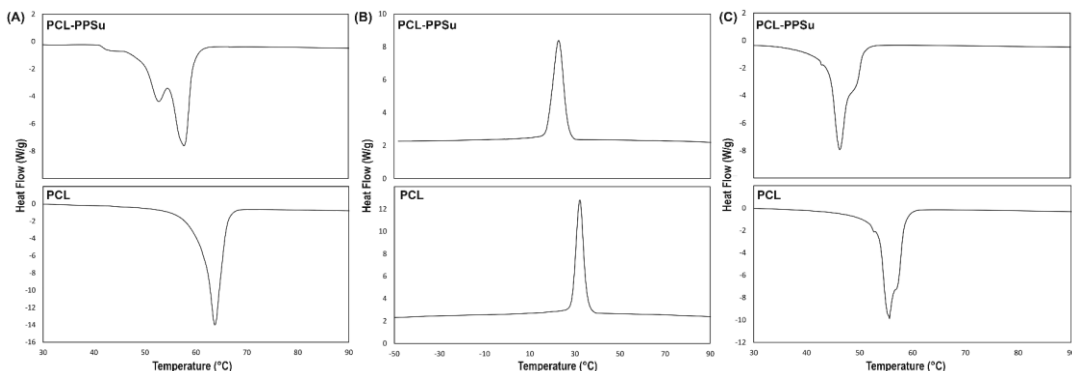


Figure 3-5. DSC curves of the PCL-PPSu and PCL; (A) the first heating cycle, (B) the first cooling cycle, (C) the second heating cycle. The heating and cooling cycles were conducted with a rate of 10 °C/min

Processing temperature plays a critical role in the 3D printing of materials in the melt phase. The mutual dependence of melt viscosity and chemical stability of the polymers on process temperature have been already discussed in several studies [60,189,190]. The processing temperature of the thermoplastics would also impact the thermal degradation and accordingly, chemical stability of the polymer would be compromised upon increasing the temperature [191]. On the other hand, the feasibility of embedding drugs and nanoparticles in

the polymer is strongly affected by the temperature in which the inclusions could be utilized without degradation and any further effect on the drug release [192]. Hence, lowering the temperature could broaden the application of the candidate drugs and nanoparticles. Moreover, the lower processing temperature during 3D printing would extend the lifetime of the embedded drugs. In the last few decades, many studies have been done to investigate the thermal stability of the drugs, and they are categorized as resistant to low, moderate, high temperatures, or non-heat resistant [192,193]. However, these studies have mostly explored the effect of temperature for a short period of time [194]. In this respect, lower melting temperature observed in PCL-PPSu copolymer compared to PCL might be an advantage in extending the stability and application window of both the polymer and possibly the embedded drugs.

The heating and cooling profiles during 3D printing were designed by considering DSC results. In this way, polymer melt in the syringe reservoir was slowly cooled down below the crystallization temperature between each run to allow the complete development of a crystalline structure. Uniformity of the flow properties and repeatability of the 3D printing process significantly depend on thermal history and the processing conditions. The development of a fully crystalline structure in the syringe reservoir before each printing trial minimized the alteration of flow profile at the same processing conditions.

The structure and morphology of the 3D printed scaffolds were observed using FE-SEM (Figure 3-6). The interconnected porous structure and structural uniformity of a 3D printed scaffold are of great importance. Hence, to evaluate the structural uniformity and the material's printability, filament diameter, and inter-layer gap distance of the printed structures were measured from SEM images using ImageJ software. The samples were cut in the z-axis and the gap distance were measured form different layers. Each measurement was reported as an average of 20 random locations in the 3D printed scaffold. The structure stability was assessed by the determination of standard deviation (SD) of the calculated values. The measured printed filament diameter was $272.40 \mu\text{m} \pm 5.89$ (SD), and the inter-layer gap distance was calculated as $330.80 \mu\text{m} \pm 4.04$ (SD). The low values of the standard deviations demonstrated that 3D printed scaffolds possessed structural uniformity in terms of filament diameter and pore size. This indicates that the selection of process parameters based on the

physical characteristics of the synthesized copolymer resulted in good adaptation with the 3D printing process. Designed gap size was selected to be 350 μm and due to filament expansion during printing, it reduced to 330 μm . By selecting a low pressure with a high print speed, we could optimize the resulting structure in terms of filament length and gap distance. Figure 3-6(D) represents a cross-section image of the scaffold to evaluate the interconnectivity of the pores. SEM images and the subsequent image analysis showed that the synthesized copolymer composite could be 3D printed with high structural uniformity and controlled geometry at the examined process conditions. It has been shown that interconnected porous structure of the 3D printed scaffolds can provide proper nutrient and oxygen flow for the seeded cells and support the formation of new tissue upon implantation.

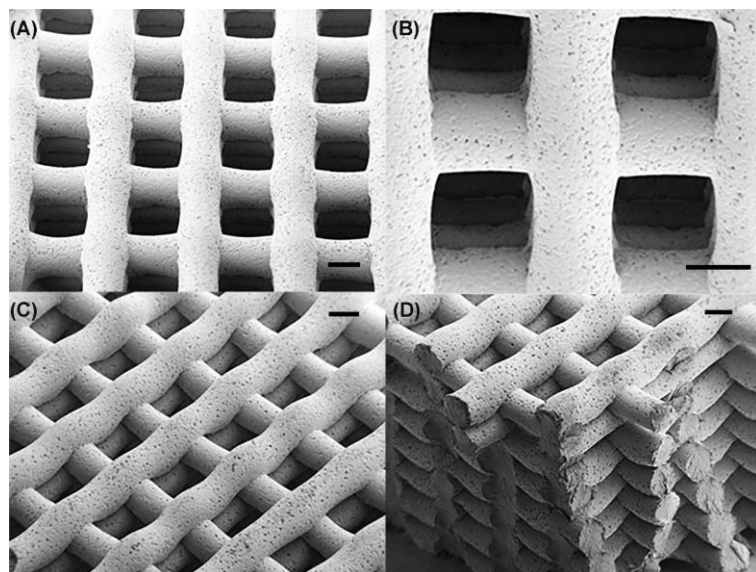


Figure 3-6. SEM images of 3D printed copolymer impregnated with silver nitrate scaffolds at different magnifications; scale bars: 200 μm

3.3.3 Degradation behavior

Surface wettability and the degree of hydrophilicity of a biomaterial is correlated with its cell attachment properties and possibly the hydrolytic degradation behavior [195]. Results of the water contact angle measurement for PCL and PCL-PPSu showed a significant increase in the wettability of copolymer compared with PCL. The measured contact angle values for PCL and PCL-PPSu samples were $87.43^\circ \pm 4.7$ and $61.23^\circ \pm 3.5$, respectively (Figure 3-7(A)). As

the Figure implies, the wettability and hence the hydrophilicity of the copolymer enhanced significantly in comparison with pure PCL.

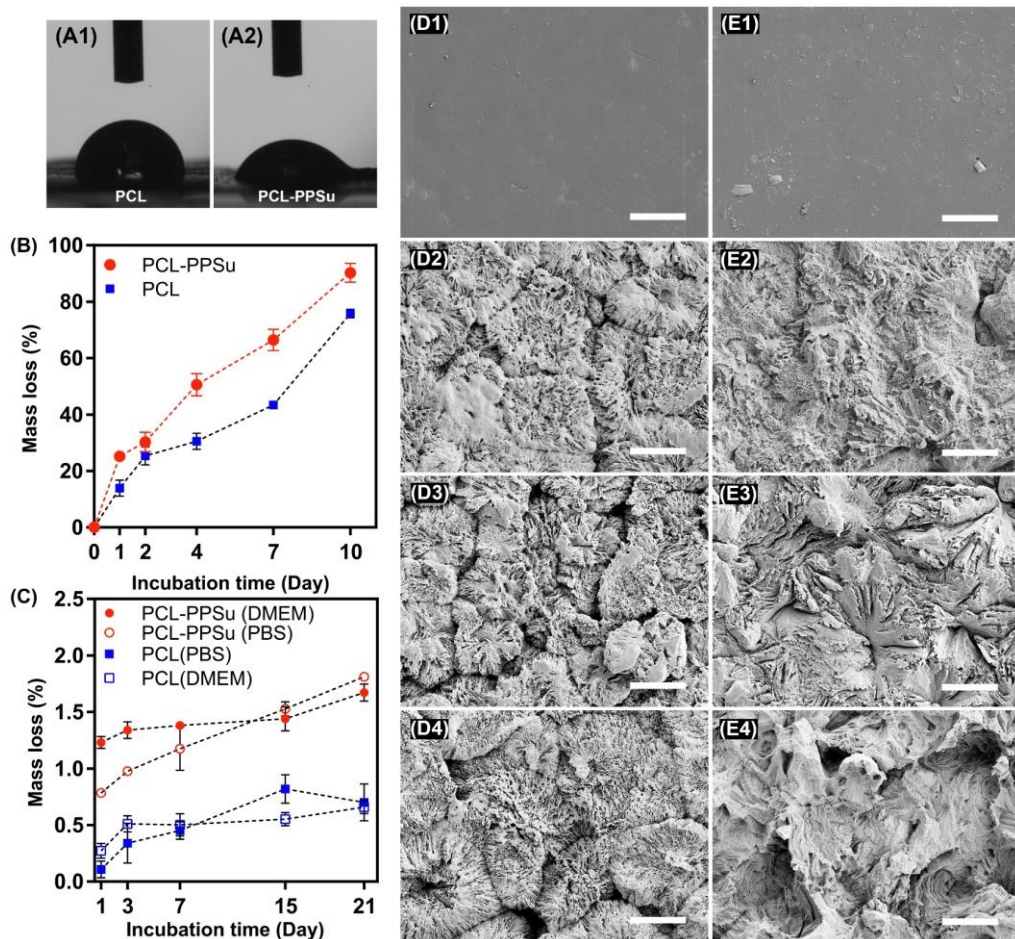


Figure 3-7. Wettability and degradation of PCL-PPSu and PCL in different media. Water contact angle measurements for (A1) PCL and (A2) PCL-PPSu. (B) Enzymatic degradation as a function of incubation time at 37 °C for PCL-PPSu and PCL. (C) Hydrolytic degradation as a function of incubation time at 37 °C for PCL-PPSu and PCL in PBS and DMEM. SEM micrographs of degraded PCL-PPSu films (D1–D4) and PCL films (E1–E4) at day 0, day 2, day 7, and day 10 of enzymatic degradation; scale bars: 20 μ m

Enzymatic hydrolysis of the PCL and PCL-PPSu samples in PBS solutions containing *Pseudomonas cepacia* lipase, which degrades polyesters by breaking the ester bonds [155,196], at 37 °C were investigated by monitoring mass loss and morphology of the samples during 10 d. The percentage of mass loss versus time shows much higher values of mass loss with a steeper slope for the copolymer compared with PCL (Figure 3-7(B)). After 1

d incubation, the mass loss percentage for the copolymer was 25.19%, while this value was almost half (13.90%) for the PCL. The values of mass loss percentage for PCL-PPSu copolymer and PCL after 10 d were 90.2% and 75.8%, respectively. The same behavior was observed, as the incubation of copolymer samples more than 10 d resulted in complete physical destruction and since the accurate measurement of mass loss was not further possible, this point was considered as the 100% degradation state. The copolymer was completely degraded after 11 d while the corresponding time for PCL was at day 14 (data for 100% degradation was not shown in the graph). The extent of degradation at every time points and also the slope of the graph were both higher for the copolymer compared with PCL which is in agreement with previous studies [159,197].

The cleavage of ester end groups of the PCL and PCL-PPSu samples during enzymatic degradation would be affected by the degree of crystallinity. Due to the greater number of ester groups in the copolymer, more available sites for bond cleavage would be expected [196,198,199]. Knowing the fact that the degree of crystallinity is related to the polymer's molecular weight, the lower degradation rate of PCL compared to PCL-PPSu was in conformity with the molecular weight data obtained from GPC [200]. The number of methylene groups between the ester groups is another important key factor in the hydrolysis of polyesters, and as it rises, degradability increases [201]. This was in agreement with the observed higher degradation rate of PCL-PPSu copolymer.

Figure 3-7(D) and (E) illustrate SEM images of surface morphology of the polymer films before and after hydrolysis at different time points. Before the experiments, the polymer films demonstrated smooth surfaces (Figure 3-7(D1) and (E1)). Further incubation resulted in the formation of a flower-like morphology in PCL-PPSu surface (Figure 3-7(D2)–(D4)) corresponding to spherulites formation during crystallization [202]. After 2 d of hydrolysis and attaching the lipase to polyester surfaces [155], portions of these spherulites were seemed to be degraded and dissolved in the solution which is suggested to be related to the amorphous regions, while the crystalline segments remained intact (Figure 3-7(D2)) [200,202]. By further increasing the hydrolysis time, increased surface roughness was observed in both PCL and copolymer samples. Enzymatic degradation is a heterogeneous process that initiates from the surface, and the crystallinity of the polymer plays a vital role in localized degradation

progress, which was observed in both samples. Higher crystallinity of PCL samples resulted in slower rates of hydrolysis at the same time intervals, which was evident in morphological features of degraded samples as well as mass loss values throughout the incubation.

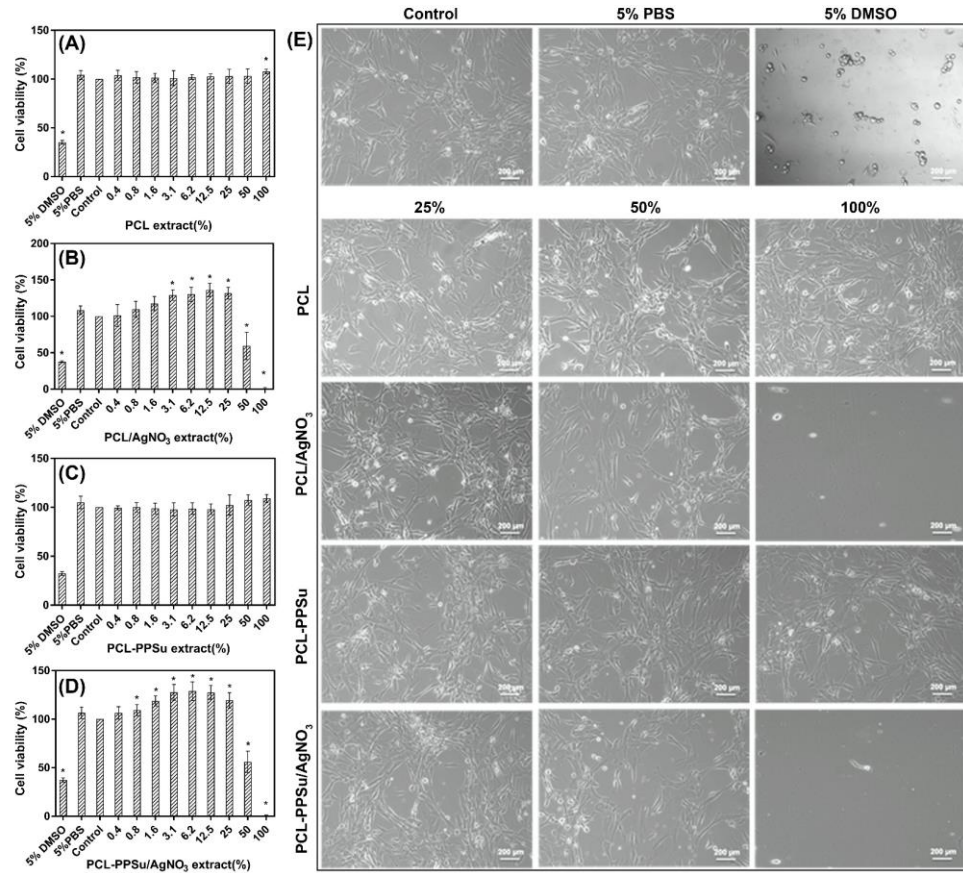


Figure 3-8. Cytotoxicity of the extracts of the components to HDF cells in vitro. Negative controls: PBS. Positive control: 5% DMSO in PBS. Control: Cells without scaffolds. Cytotoxicity of leachates derived from (A) PCL, (B) PCL/AgNO₃, (C) PCL-PPSu and (D) PCL-PPSu/AgNO₃ (*p < 0.01). Bright-field microscopy images of HDF cells after being exposed to leachates are provided in panel (E)

Biocompatibility of PCL has been a subject of debate due to the slow rate of hydrolytic degradation which can easily span over a year [203]. As well as the higher rate of enzymatic degradation in copolymer samples, the apparent increase in wettability and the higher chance of ester cleavage in PPSu containing copolymer might have a significant impact on hydrolytic degradation. Hydrolytic degradation of the PCL and PCL-PPSu samples in DMEM and PBS media were examined by monitoring mass loss at different time points up to 21 d. The

percentage of mass loss versus time shows higher values of mass loss for the copolymer compared with PCL in both media (Figure 3-7(C)). The values of mass loss percentage for PCL-PPSu copolymer after 21 d of immersion in DMEM and PBS were 1.67% and 1.81%, respectively, while the corresponding values for PCL samples were decreased by more than half. The calculated mass loss percentage at day 21 for PCL in DMEM and PBS were 0.66% and 0.70%, respectively. A small difference in the degradation of samples in different mediums was observed. However, samples incubated in PBS showed higher mass change from the first day to the last day of the experiments. The samples incubated in DMEM medium showed a relatively high mass loss at day 1 while the rate of degradation was slower throughout the experiments. Regardless of the sample type and the medium, the mass loss percentage increased with sample incubation time.

The degree of crystallinity directly influences the hydrolytic degradation rate, which is mainly due to the cleavage of ester bonds. Since the number of ester groups in the copolymer is higher compared to PCL, the observed increase in the rate of hydrolysis was expected [198]. Considering the apparent increase in wettability of copolymers, the mutual effects of more available cleavage bonds, and the more hydrophilic nature of copolymer resulted in faster degradation rates. The reported mass loss during the three-week period might seem to be negligible. However, considering the very slow rate of hydrolytic degradation of PCL which might be over several months, the observed 50% increase in the mass loss of copolymers during the short period of experiments would be promising.

3.3.4 Silver release and surface characterization of polymer films

The concentration of silver ion released from PCL-PPSu/AgNO₃ soaked in PBS was measured by ICP-OES for 21 days of incubation. Moreover, the released ion content at each time point was compared with the total amount of silver within the bulk of the samples (Table 3-2). The reported data belongs to the average value of 4 replicates with the corresponding standard deviations. The results demonstrate a very low released silver ions (about 4.5–7.5 mg kg⁻¹), whereas the silver content within the bulk of the samples were almost one thousand times higher. This confirms the hypothesis that the amount of released silver ions during the incubation period stayed below the cytotoxic level [204].

Table 3-2. Silver amount in PBS solutions and PCL-PPSu/AgNO₃ measured with ICP-OES
(The values are reported in ppm)

Incubation time	Day 1	Day 3	Day 7	Day 14	Day 21
Sample	Silver content (ppm)				
PBS solution	4.35 ± 1.18	5.41 ± 1.92	6.32 ± 0.48	7.45 ± 1.50	7.56 ± 1.40
Copolymer	5581.99 ± 8.5	4707.92 ± 5.3	4396.48 ± 7.4	4344.17 ± 6.5	4210.50 ± 4.5

It is worth mentioning that low standard deviation of silver content in bulk samples indicates a homogeneous silver distribution throughout the polymer.

Figure S3-1(B) shows EDS (map) of PCL-PPSu/AgNO₃ EDS, which demonstrates a uniform distribution of silver on the surface of the sample.

3.3.5 Cell viability assessment

Cytotoxicity of PCL, PCL-PPSu, and the corresponding AgNO₃ containing composites on HDF cells were investigated by using WST-1 colorimetric assay. Exposure of the extracts of PCL and PCL-PPSu samples did not affect cell viability on cultured cells compared with control groups (Figure 3-8(A) and (C)). The results of viability assessments after exposure of several dilutions of the extracts from composite samples containing 5% (wt/wt) AgNO₃ are presented in Figure 3-8(B) and (D). The high concentration of AgNO₃ caused a dramatic loss of viability, which can be due to the release of toxic Ag⁺ ions from the scaffold to the medium [181]. However, further dilutions of the extracts from the samples resulted in a gradual increase in the viability. Regardless of the polymer matrix, a significant increase in the viability of cells treated with 25% and less diluted media was observed.

The images in Figure 3-8(E) show the morphology of HDF cells exposed to the polymer extracts after 24 h. Morphological characterization was performed using 100%, 50%, and 25% diluted media since no toxic effect was observed for other tested concentrations. Cells

treated with PCL and PCL-PPSu extracts maintained their characteristic morphology for all tested concentrations. However, the highest concentration of PCL/AgNO₃ and PCL-PPSu/AgNO₃ extracts resulted in a significant loss of cell morphology and detachment of the cells from the surface due to the cytotoxic effect of Ag⁺ released in the medium. Although a few cells seen lost their morphology and detached from the surface, diluted extracts to 50% and 25% maintained the cell morphology. Therefore, the concentrations of AgNO₃ were decreased to 2.5% and 1% in the composites for further antibacterial activity experiments.

3.3.6 Antibacterial activity of block copolymer impregnated with AgNO₃

Antimicrobial properties of silver ions, which exhibit a high level of toxicity for a broad range of microorganisms, are promising in medical terms [171]. The polymeric structure, incorporated with AgNO₃ showed an improvement in biocidal properties [175,182]. The concentration of AgNO₃ was commonly selected below 5% and both in vitro and in vivo studies possessed good antimicrobial activity with no noticeable toxicity effects [181,182].

Antimicrobial properties of PCL-PPSu and PCL-PPSu/AgNO₃ were determined by zone of inhibition test using *E. coli*, *P. aeruginosa*, *S. aureus*, and *C. albicans* pathogens, which are related to infections seen in implants or burn wound areas [175]. The microorganism strains were seeded on LB agar Petri dishes by spreading from overnight cultures. Then, the copolymer films with/without AgNO₃ were placed carefully on the LB agar.

After overnight incubation, no evidence of antimicrobial effects against *E. coli*, *P. aeruginosa*, *S. aureus*, and *C. albicans* strains was observed in copolymer samples (Figure 3-9). However, copolymers impregnated with AgNO₃ exhibited antimicrobial activity against all the tested microorganisms. Evident inhibition zones were observed around the copolymer films with varying sizes corresponding to different microorganisms. As shown in Figure 3-9, PCL-PPSu/AgNO₃ films showed positive antimicrobial activity against *C. albicans*, a harmless member of the human microbiome which can lead to life-threatening infections under certain conditions. Similar antimicrobial activities for *P. aeruginosa*, *E. coli* and *S. aureus* pathogens were observed but to a lesser extent compared to *C. albicans*. Inhibition

zones formed around the PCL-PPSu films with/without AgNO₃ are presented in Table 3-3. Data are represented as mean \pm SD with 3 replicates.

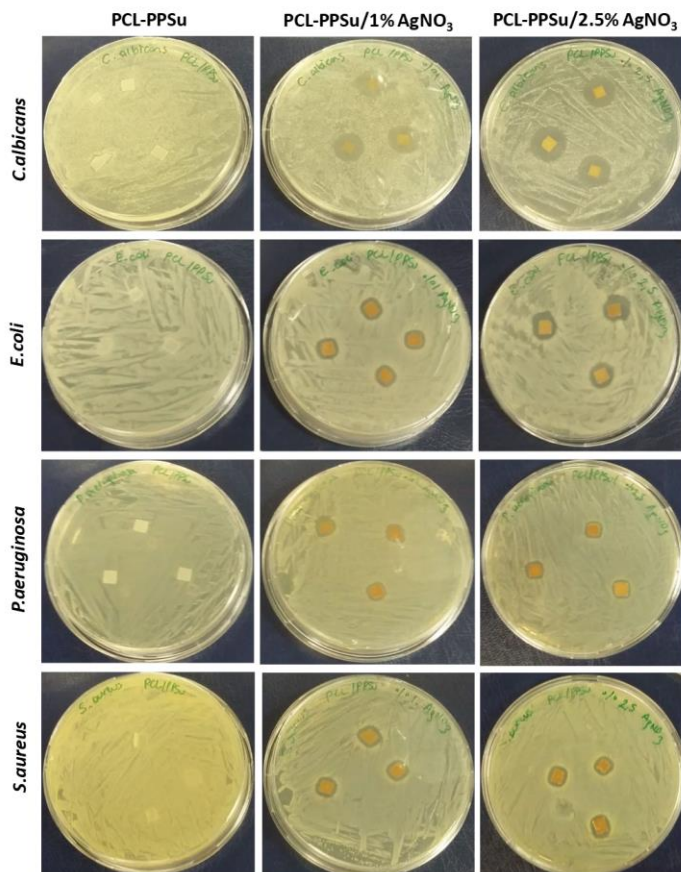


Figure 3-9. Zone of inhibition for PCL-PPSu and PCL-PPSu/AgNO₃ polymer films against different microorganisms

Table 3-3. Diameter of zone of inhibition diameter (mm) for samples with varying concentrations of AgNO₃ against different microorganisms

Sample	Zone of inhibition diameter (mm)			
	<i>C. albicans</i>	<i>E. coli</i>	<i>S. aureus</i>	<i>P. aeruginosa</i>
PCL	0	0	0	0
PCL + 1% AgNO ₃	16.3 \pm 1.2	9.6 \pm 0.6	9.3 \pm 0.6	8.2 \pm 0.1

PCL + 2.5% AgNO ₃	17 ± 1.4	10.4 ± 0.6	10.3 ± 1.2	9 ± 0.1
PCL-PPSu	0	0	0	0
PCL-PPSu + 1% AgNO ₃	14.7 ± 1.5	10 ± 0.1	9.7 ± 0.6	7.9 ± 0.6
PCL-PPSu + 2.5% AgNO ₃	15.3 ± 1.4	12.6 ± 1.2	10.3 ± 0.6	8.2 ± 0.6

As shown in Table 3-3, for both PCL and PCL-PPSu composite incorporated with AgNO₃, the zone of inhibition diameters are as the following: *C. albicans* > *E. coli* > *S. aureus* > *P. aeruginosa*. Adhesion of microorganisms on the copolymer film surfaces was also analyzed. The results showed that the microorganism's density on PCL-PPSu copolymer films was quite high for all microorganisms (Figure 3-10). In addition, LB medium incubated with the films became blurry due to the growth of microorganisms. However, no growth was observed in Petri dishes belongs to PCL-PPSu/AgNO₃ film surfaces incubated with *E. coli* and *P. aeruginosa*, while the density of *C. albicans* and *S. aureus* decreased compared to their control groups (Figure 3-10). Moreover, no visible turbidity in the LB media was observed.

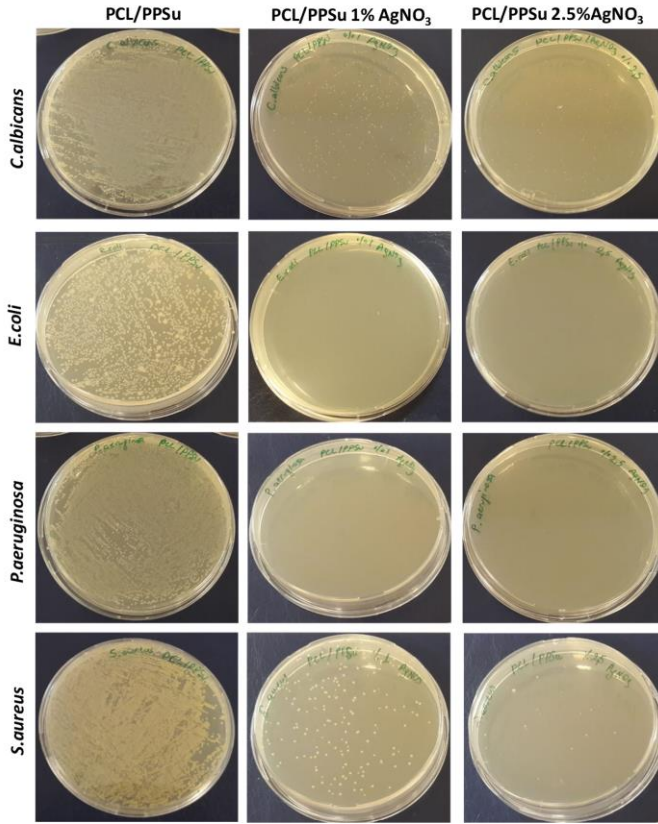


Figure 3-10. Analysis of microorganisms' adhesion on the PCL-PPSu and PCL-PPSu/AgNO₃ films

3.4 Conclusion

In this chapter, a 3D printable block copolymer of PCL-PPSu with the adjusted composition was synthesized and characterized in detail. The effect of incorporation of PPSu within the PCL as a candidate material for skin tissue engineering applications was investigated. The assessment of structural uniformity of 3D printed structures showed that the selection of process parameters based on physical properties of synthesized copolymer resulted in 3D printing of porous structures with well-defined interconnected porosity, which could support nutrient and oxygen flow in vitro. Moreover, the synthesized PCL-PPSu copolymer showed higher enzymatic and hydrolytic degradation rates and improved hydrophilicity compared to PCL, which can be employed in designing skin regenerative scaffolds with controlled degradation behavior. To provide the antibacterial properties, silver nitrate was incorporated within the copolymers with different concentrations, and its

cytotoxicity level was investigated by cell viability assay. Assured that our composite scaffolds did not show any cytotoxicity for the composition of 1% (wt/wt) silver nitrate with silver releasing a very little amount of silver in the media, antimicrobial activity was utilized to investigate the effect of this antibacterial agent. It was shown that the incorporation of silver nitrate to the copolymer significantly reduced microbial cell adhesion for all microorganisms investigated. The zone of inhibition test results demonstrated that silver nitrate was more effective for *E. coli* and *C. albicans* rather than *P. aeruginosa* and *S. aureus*. We have shown that by combining the improved degradation behavior, low-processing temperature, antimicrobial properties, and adaptability with the 3D printing process, composites based on PCL-PPSu could be an attractive biomaterial for emerging skin tissue engineering and wound healing applications.

3.5 Supplementary document

Reaction materials and their initial ratios for copolymerization with different concentrations are presented in Table S3-1.

Table S3-1. Reaction conditions of PPSu-PPCL block copolymers with different PCL ratios

Polymer type	PPSu/ ϵ -caprolactone (w/w)	PPSu (g)	ϵ -caprolactone (g)	Sn(oct) ₂ (ml)
PPSu-PCL (1:5)	1:5	3	15	0.73
PPSu-PCL (1:10)	1:10	2	20	0.97

The summary of DSC and GPC tests as well as the yield percentages of the polymerization of the PCL and PCL-PPSu are presented in Table S3-2.

Table S3-2. Characterization results of PPSu-PPCL block copolymers with different PCL ratios

Polymer type (w/w)	T _m (°C)	ΔH _m (J/g)	T _c (°C)	ΔH _c (J/g)	M _w (g/mol)	M _n (g/mol)	PDI	Yield (%)
PCL	49	71	38	72	28008	18494	1.51	80
PPSu-PCL (1:5)	41	52	31	52	16500	8300	1.99	88
PPSu-PCL (1:10)	42	33	28	32	15600	13300	1.17	63

Integral values of ¹H-NMR and ¹³C-NMR peaks for PCL-PPSu copolymer were calculated and presented in Table S3-3.

Table S3-3. Results of 1H-NMR and ¹³C-NMR spectroscopy for PCL-PPSu block copolymer

Symbol	Polymeric segment type	Shift (ppm)	Integral values for PCL-PPSu	Normalized integral value to (c) PCL-PPSu
a	PPSu	2.6	2.73847	0.86
d	PPSu	1.96-2.01	1.81143	0.57
c	PPSu	4.1-4.2	3.16995	1
j	PCL	4.05-4.1	18.1258	5.7
g	PCL	2.25	18.9198	5.97
h, h'	PCL	1.6-1.7	37.1879	11.73
i	PCL	1.4	18.0466	5.69

Figure S3-1 shows the distribution of silver through the surface of PCL-PPSu doped with 1% AgNO₃ which demonstrates the homogeneity and complete distribution of silver within the sample.

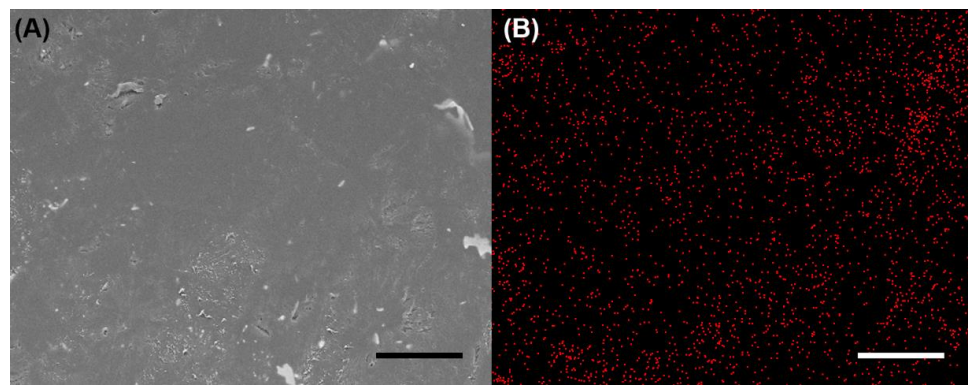


Figure S3-1. Surface analysis of PSL-PPSu composite doped with AgNO₃. (A) SEM image of composite film, and (B) elemental dot map scanned by EDS showing silver distribution within the composite; Images are taken at 1KX magnification and scale bars are 50 μm

4 Chapter 4. Modeling 3D melt electrospinning writing by response surface methodology

This chapter was published in the journal of Materials and Design as a research article [17].

Three-dimensional melt electrospinning writing is a promising technique for 3D printing of porous scaffolds with well-defined geometrical features. The diameter of electrospun fibers strongly affect the achievable resolution and consequently several other physical, mechanical, and structural properties of the fabricated scaffold. However, there are a few process parameters which significantly affect the size of electrospun fibers. In this study, response surface methodology (RSM) was used to investigate the critical and optimized process parameters and their interaction effects on the desired fiber diameter. Four process parameters, including collector speed, tip-to-collector distance, applied pressure, and voltage were studied considering their practical ranges. The results showed that all the parameters except the applied voltage had a significant effect on the printed fiber diameters. A generalized model for the interaction effects of the parameters was introduced which can be used as a framework for selecting the process parameters to achieve the desired fiber diameter. The developed model was validated by choosing random process parameters and printing three-dimensional scaffolds. The results confirm that the predicted fiber diameters match closely with the actual fiber diameters measured directly from the printed scaffold.

Keywords: 3D melt electrospinning writing, Response surface methodology, Three-dimensional scaffold printing, Parameter optimization.

4.1 Introduction

The demand for additive manufacturing processes is on the rise due to its unrivaled design freedom and ability to directly manufacture highly complex and customized geometries with various materials [3,148,205–207]. In recent years, additive manufacturing processes have been used to fabricate three-dimensional (3D) scaffolds for tissue engineering applications [150,208]. Because of their availability and accurate control of the porosity and fiber diameter, deposition based additive manufacturing processes are commonly used for tissue engineering applications [20,49,75,80]. Due to the high viscosity of the biomaterials used, the fiber diameter in deposition based additive manufacturing processes is mainly limited by the larger nozzle sizes [98,209,210].

Electrospinning is a fast-emerging technique to produce ultrafine fibers from a wide range of polymers. This technique can be used with both solution and melt phases of polymers depending on the application. In conventional electrospinning processes, polymer solutions turn into continuous polymer jets in the presence of an electric field applied between a nozzle and a collector. Solution based techniques have been widely used due to the low cost and simplicity of the hardware used, and the ease of adaptation to a wide variety of polymers. However, the major drawbacks of the solution based techniques for medical applications are related to uncontrolled nature of spun fibers and the use of toxic solvents which may not evaporate completely during the process [49,108,211]. To address these challenges, some innovative approaches like near-field electrospinning [51], direct-write electrospinning [56,212], and focused electrical field [52] have been used to produce structures with more controlled features. However, these methods still require solvents throughout the process. In contrast, melt electrospinning is an alternative technique which does not rely on any solvents and can produce highly ordered fiber depositions. Moreover, polymer melts usually have a higher viscosity than the solutions, which result in the formation of more stable polymer jets with better control and higher precision. This enables direct writing of structures with desired patterns [45,47,49,62,65,79,205].

Polymers with high viscosity and low conductivity can be used for 3D melt electrospinning writing to produce well-ordered 3D patterned structures consisting of multiple layers of deposited fibers [45,62]. Hence, porous structures with interconnected pores and ultra-fine

details can be fabricated by using this technique. However, controlling the shape, morphology and fiber diameter is challenging due to the complexity of the mutual effects of the process parameters. Since fiber diameter and porosity can directly affect the scaffold properties, determining those parameters is of great interest to a range of applications [213–215].

The main effective parameters of MEW are collector speed, pressure, tip-to-collector distance, temperature, and applied voltage. In the literature, there are number of studies considering the effects of different process parameters on the fiber diameter and the shape fidelity of electrospun structures [77,93,214,216,217]; however, a few explored their counter-influence and interactions. Hence, determining the influence of process parameters on the shape and the diameter of the deposited fibers is crucial in predicting the relevant set of process parameters to achieve the desired fiber diameter.

In the literature, response surface methodology (RSM) has been used to investigate the interaction effects of not only the process parameters but also material properties and experimental conditions. The current studies in the literature have mainly applied this statistical approach to solution-based electrospinning techniques [89,213–216,218–224] . There have been recent studies in which a similar but limited statistical classification methods were employed in determining the interaction of parameters on the structural properties of electrospun structures for melt electrospinning [58,77,87,93,219,225–227]. Among them, a few papers were dedicated to determine fiber diameter and morphology in melt electrospinning and melt electrospinning writing [58,77,87,217,226–228]. These studies indicated several process parameters as the most significant ones such as temperature [58,226,228], applied voltage [227], and laser power (in the case of laser melt electrospinning) [217,227], and material parameters such as molecular weight [77,225] and structure [58,77]. Despite the differences in identification of most influential parameters on fiber diameter, these methods were similar in choosing an orthogonal design of experiments. Only two research work used RSM for melt electrospinning process [93,225]. Implementation of the orthogonal design of experiments in the mentioned studies let the authors sort out the impact of each parameter on the diameter of deposited fibers. However, a detailed statistical analysis of 3D melt electrospinning writing by identification of interaction effects on fiber diameter and construction of a model equation for the process is of great importance. With an

emphasis on 3D MEW for fabrication of well-organized structures rather than the melt electrospinning processes, to the best of our knowledge, there is no report in the literature considering the effect of process parameters on fiber diameter. In this respect, the aim of this study was to investigate the effect of individual process parameters and their mutual interactions on the fiber diameter by using design of experiments (DOE) and a linear regression model for 3D melt electrospinning writing processes. Moreover, a generalized model for prediction of fiber diameter based on the process parameters was developed and validated experimentally.

4.2 Materials and Methods

4.2.1 Materials

Polycaprolactone (PCL) pellets (CAPA 6400) with a molecular weight of 37,000 g/mol was purchased from CAPA (Perstorp Ltd., UK) and stored in vacuum to prevent any degradation and eliminate the unwanted effects on the process caused by the atmospheric humidity.

4.2.2 3D Melt electrospinning direct writing process

An overview of the experimental setup is shown in Figure 4-1. A custom-made Computer Numerical Control (CNC) 3D melt electrospinning direct writing printer was developed for the experiments. The 3D printer is controlled with a software-based CNC controller, MACH3 software (Newfangled Solutions LLC, ME, USA). The head of the melt electrospinning writing printer consisted of a 10-mL metal syringe as a material reservoir connected to a high precision nozzle with an inner diameter of 250 μm (Musashi Engineering Inc.). A high voltage DC power supply (ES30, Gamma High Voltage Research, FL) is connected to the tip of the nozzle. A pneumatic air dispenser (EFD Performus V, Nordson) is used for extruding material. An Arduino Mega microcontroller with shield RAMPS 1.4 is used for controlling two heating elements for the bed and the nozzle, which is protected from any possible sparks with an isolator.

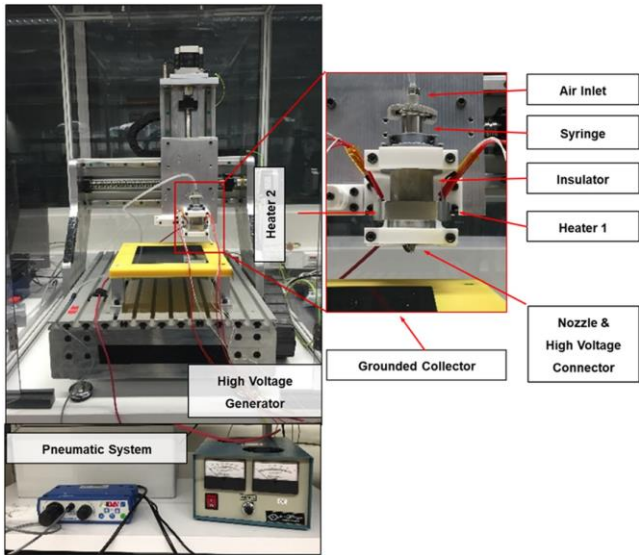


Figure 4-1 3D melt electrospinning direct writing printer

4.2.3 Determination of the experimental parameters

Based on the thermal characterization and rheological properties of PCL (data not shown), the working temperature for all experiments was set at 70 °C, and the polymer melt was equilibrated at the working temperature for 3 h before conducting the experiments.

For 3D melt electrospinning printing process, PCL pellets were melted inside the syringe and printed on an indium-tin-oxide coated conductive glass placed on the collector. Several process parameters affect the structure, shape and consequently the fiber diameter. However, some of them play more important roles such as voltage difference between the nozzle tip and the collector, tip-to-collector distance, applied pressure, and collector speed.

As a general framework to investigate the influence of each parameter on the dimensions of the deposited filament, the first step was to define the stable printing criteria. Stable printing was defined as obtaining stable designed shape fiber between the polymer jet and the collector with an acceptable lag and the other possible deposition morphologies such as sinusoidal shapes, figure eight loops, and coiling were considered as non-acceptable morphologies. In 3D melt electrospinning writing, a substantial aspect is how the applying parameters are affecting the shape of the fiber to control the desired architecture of the final structure. Different structures can be obtained during the deposition depending on the

interactive influence of process parameters. For instance, if the driving forces and collector speed do not match, one possible result is whipping instability of the polymer jet which results in bending and stretching of the fiber on the collector [98,205,229]. Therefore, minimum and maximum values of each process parameter were separately investigated to identify whether the set values would contribute to stable printing, and the shape of deposited fibers. This step has been done continuously to reach a range of all parameters according to the previous methods [205]. The selection of parameter domains was based on two criteria, the possibility of deposition of a straight fiber within the range of the given variable, and the synchronization of deposition rate and collector speed to eliminate the spatial lag in deposition. Moreover, the limitations of hardware in acceleration during linear motions were also considered in the selection of parameter ranges.

To obtain a stable Taylor cone [49] and to reach a proper fiber formation, the deposited polymer jet was stabilized at a specified tip-to-collector distance, voltage, and pressure for 50 seconds before moving the printer head. The values of the parameters are shown in Table 4-1.

Table 4-1. Process parameters and the corresponding levels

Parameters	Code	Levels		
		-1	0	1
Collector speed (mm/min)	x_1	310	355	400
Distance (mm)	x_2	7	10	13
Pressure (bar)	x_3	0.6	0.8	1
Voltage (kV)	x_4	5.5	6.2	7

4.2.4 Experimental design and measurement

Response surface methodology integrates the statistical and mathematical techniques to investigate the individual effects of the parameters and interaction effects of the independent factors on the response. The resultant response is related to some independent factors. This would help to optimize the response and make a relation between response and independent factors. In this study, a Face-centered Central Composite Design (FCCD) was used because of its feasibility and relatively small number of experiment requirement. This design consists of axial points located on the centers of the faces of the cube, and each factor possesses at most

three levels. The total number of experiments was $2^k + 2k + n_c$, in which the number of factors is shown by k, and 2k and n_c represent the number of axial and center points, respectively. For this study, all the possible levels and center points for each factor were included in the DOE to enhance the precision of the model regarding calculation of residual error. This resulted in an FCCD array with 8 face and 7 center points. The implementation of FCCD design would also provide the benefit of using a second order polynomial equation for modeling the results, which enables the estimation of the effects of individual factors and the interaction effects on the response [220,230,231]. The four independent factors in this study were collector speed, tip-to-collector distance, applied pressure, and voltage while the response was the fiber diameter. Three levels of each parameter for the quadratic model were labeled as -1, 0, and +1 resulting in 31 experimental sets including seven sets for the central points. The model used in this study was a polynomial equation and it was evaluated with analysis of variance (ANOVA) and coefficients of determination (R^2). The significant parameters were determined by using F-value by calculating $F_{critical}$ and P-value with a 95% confident level ($\alpha = 0.05$). The quadratic polynomial equation was used for linear regression model to identify the curvature effects. The second order polynomial equation is as the following:

$$y = \beta_0 + \sum_{i=1}^k \beta_i x_i + \sum_{i=1}^k \beta_{ii} x_i x_i + \sum_{i < j} \sum \beta_{ij} x_i x_j \quad (1)$$

where y is the response (in this case fiber diameter) and x_i is the independent factor (inputs), k is the total number of factors, β is the regression coefficient. The calculations were performed using MINITAB R17 software.

To examine the fiber diameter, all the samples were evaluated by scanning electron microscopy (FE-SEM, Zeiss LEO Supra 35VP) after being sputter-coated with gold-palladium and taking images at $500\times$ and $750\times$ magnifications for the quantification of fiber diameters and the validation experiments, respectively. ImageJ software was utilized for the quantification of fiber diameters, and the average diameter was calculated based on 100 individual measurements for each fiber in corresponding images. The independent parameters are shown in Table 4-2 with their coded and real level values.

4.3 Results and Discussion

4.3.1 Regression model analysis

To investigate the model, a Face-centered Central Composite Design (FCCD) was used with four factors. A total of 31 experiments were conducted as shown in Table 4-2. The second order polynomial model was derived by using the experimental results. In this model, the regression coefficients were calculated by using the least square estimation method in MINITAB R17. The model equation with evaluated regression coefficients (β) is written as equation 2.

$$\begin{aligned} y = & 61.340 - 3.505 x_1 + 0.875 x_2 + 7.584 x_3 - 0.397 x_4 \\ & + 0.012 x_1 x_1 - 1.696 x_2 x_2 + 0.766 x_3 x_3 - 0.136 x_4 x_4 \\ & - 0.029 x_1 x_2 - 0.402 x_1 x_3 - 0.416 x_1 x_4 + 0.304 x_2 x_3 \\ & - 0.003 x_2 x_4 - 0.654 x_3 x_4 \end{aligned} \quad (2)$$

Table 4-2. Experimental results with coded and real data

#	Collector speed (mm/min)	Distance (mm)	Pressure (bar)	Voltage (kV)	x_1	x_2	x_3	x_4	Fiber Diameter (micron)	$\pm SD$
1	310	7	0.6	5.5	-1	-1	-1	-1	54.47	± 0.780
2	400	7	0.6	5.5	1	-1	-1	-1	49.99	± 0.632
3	310	13	0.6	5.5	-1	1	-1	-1	55.13	± 0.700
4	400	13	0.6	5.5	1	1	-1	-1	51.16	± 0.897
5	310	7	1	5.5	-1	-1	1	-1	71.94	± 0.627
6	400	7	1	5.5	1	-1	1	-1	63.94	± 0.700
7	310	13	1	5.5	-1	1	1	-1	75.12	± 0.616
8	400	13	1	5.5	1	1	1	-1	65.78	± 0.976
9	310	7	0.6	7	-1	-1	-1	1	56.06	± 0.548
10	400	7	0.6	7	1	-1	-1	1	48.31	± 0.570
11	310	13	0.6	7	-1	1	-1	1	58.31	± 1.588
12	400	13	0.6	7	1	1	-1	1	48.62	± 0.467
13	310	7	1	7	-1	-1	1	1	69.98	± 0.758
14	400	7	1	7	1	-1	1	1	61.33	± 0.536
15	310	13	1	7	-1	1	1	1	70.95	± 0.801
16	400	13	1	7	1	1	1	1	64.60	± 0.827
17	310	10	0.8	6.2	-1	0	0	0	63.22	± 0.720
18	400	10	0.8	6.2	1	0	0	0	58.39	± 0.562
19	355	7	0.8	6.2	0	-1	0	0	58.04	± 0.571
20	355	13	0.8	6.2	0	1	0	0	60.16	± 0.427
21	355	10	0.6	6.2	0	0	-1	0	54.11	± 0.379

22	355	10	1	6.2	0	0	1	0	69.02	± 0.585
23	355	10	0.8	5.5	0	0	0	-1	59.55	± 0.508
24	355	10	0.8	7	0	0	0	1	61.76	± 0.495
25	355	10	0.8	6.2	0	0	0	0	63.49	± 0.585
26	355	10	0.8	6.2	0	0	0	0	60.17	± 0.501
27	355	10	0.8	6.2	0	0	0	0	61.24	± 0.303
28	355	10	0.8	6.2	0	0	0	0	61.26	± 0.524
29	355	10	0.8	6.2	0	0	0	0	62.79	± 0.596
30	355	10	0.8	6.2	0	0	0	0	63.76	± 0.644
31	355	10	0.8	6.2	0	0	0	0	59.96	± 0.671

After evaluating the data from ANOVA table, the collector speed, tip-to-collector distance, and pressure had significant effects on fiber diameter. However, there is not enough statistical evidence to label the applied voltage and interaction parameters as significant parameters. The corresponding results are shown in Table 4-3.

Table 4-3. Regression analysis and the summary of model by ANOVA

Source	DOF	SS	MS	F-Value	P-Value
Regression	14	1299.85	92.85	40.04	0.00
Collector speed	1	221.09	221.09	95.34	0.00
Distance	1	13.77	13.77	5.94	0.03
Pressure	1	1035.31	1035.31	446.46	0.00
Voltage	1	2.83	2.83	1.22	0.29
Collector speed*Collector speed	1	0.00	0.00	0.00	0.99
Distance*Distance	1	7.46	7.46	3.22	0.09
Pressure*Pressure	1	1.52	1.52	0.66	0.43
Voltage*Voltage	1	0.05	0.05	0.02	0.89
Collector speed*Distance	1	0.01	0.01	0.01	0.94
Collector speed*Pressure	1	2.59	2.59	1.12	0.31
Collector speed*Voltage	1	2.77	2.77	1.20	0.29
Distance*Pressure	1	1.48	1.48	0.64	0.44
Distance*Voltage	1	0.00	0.00	0.00	0.99
Pressure*Voltage	1	6.85	6.85	2.95	0.11
Error	16	37.10	2.32		
Lack-of-Fit	10	22.78	2.28	0.95	0.55
Pure Error	6	14.32	2.39		
Total	30	1336.95			

The model's regression P-value of 0.00 indicates that at least one parameter had a significant effect on the model [220]. The coefficient of determination (R^2) is the measure for the evaluation of the total variation between the model and the experimental results. The obtained value of R^2 was equal to 0.9722, which indicates that 97.22% of the experimental data were in agreement with the predicted values by the model. Depending on the implemented design, R_{adj}^2 might be used for the evaluation of the model instead of R^2 . This is usually the case when additional variables are added to the regression model to enhance the precision. If non-significant variables are included in the model, R_{adj}^2 usually decreases [220]. For the current model, R_{adj}^2 was found to be 94.80%. These high values demonstrate the suitability of the model. Moreover, the P-value of lack of fit in the proposed model was 0.55, which meant that there was no evidence for lack of fit. In this respect, it can be deduced that the proposed model could be applied for prediction of the fiber diameter based on the studied process parameters. It should be noted that the given model equation is best suited for the selected studied intervals. By choosing parameter values outside the mentioned ranges, a new set of experiments should be performed, and the individual and interaction effects of the parameters should be re-evaluated to construct a proper model equation with enough statistical accuracy.

Anderson-Darling (AD) normality test results are demonstrated in Figure 4-2. The normal probability of residuals and the estimated fiber diameters were plotted against the actual fiber diameters in Figure 4-2, Figure 4-3. These graphs indicate that the model matched with the real experimental data. The P-value of the normal probability plot of residuals indicates a normal distribution, considering the P-value was at an acceptable level. Figure 4-4 illustrates that the residuals were randomly distributed and no biased or out-of-randomness errors occurred.

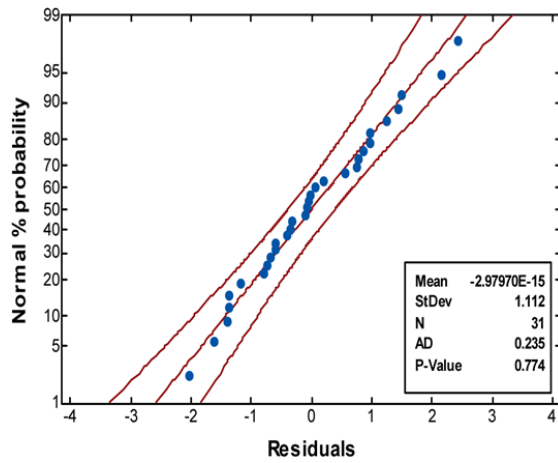


Figure 4-2. Normal probability plot of residual at 95% of confidence interval

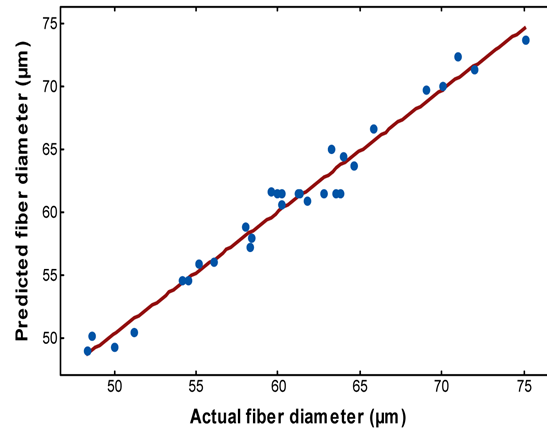


Figure 4-3. Estimated fiber diameters versus actual fiber diameters

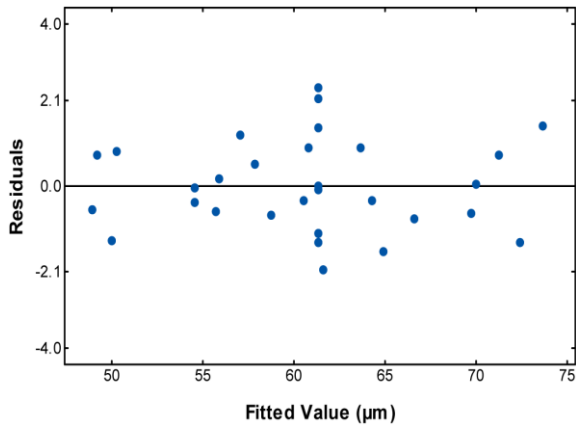


Figure 4-4. Residual versus fitted values

4.3.2 Relationship between process parameters and fiber diameter

The response surface graphs based on the derived model equation are plotted in Figure 4-5. The obtained data suggest that the smallest fiber diameter could be reached at a high collector speed, low pressure, high voltage, and short distance. Figure 4-5(a), (b), and (c) indicate that fiber diameter decreases dramatically as the collector speed increases. At a constant melt flow, the fiber gets thinner by increasing the collector speed. It is already shown in previous studies that by increasing the velocity, the pulling force increases so that fiber diameter decreases [215].

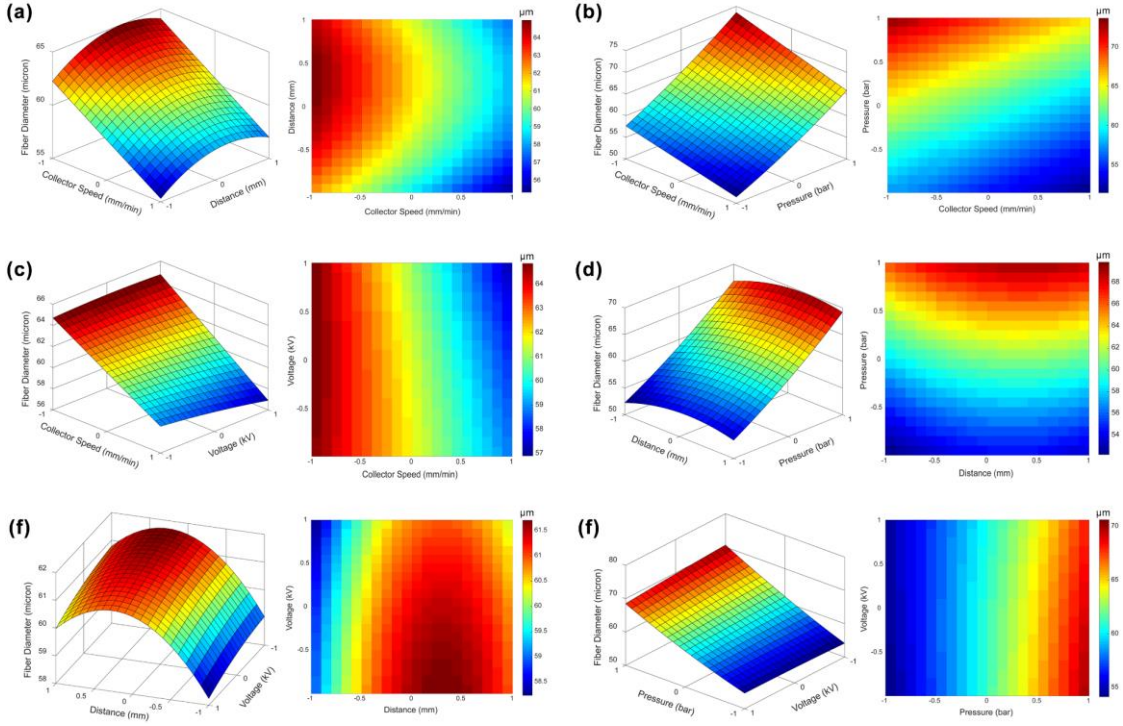


Figure 4-5. 3D response surfaces and contour plots of fiber diameter with respect to process parameters; (a) collector speed vs. distance (b) collector speed vs. pressure (c) collector speed vs. voltage (d) distance vs. pressure (e) distance vs. voltage (f) pressure vs. voltage. The rest of parameters in each plot were set to level 0

The effect of pressure on fiber diameter can be seen in Figure 4-5(b), (d), and (f). An increase in pressure, resulted in an increase in fiber diameter, which can be attributed to the effect of pressure on the material's flow [229].

For better understanding of the effects of tip-to-collector distance and applied voltage, the applied forces should be investigated. When there is no applied voltage and pressure, the equilibrium condition could be achieved by considering the relationships between the acting forces such as viscosity, surface tension, and gravitational forces. If gravitational force is smaller than surface tension, the droplet will remain unchanged at the tip of the nozzle. By applying a voltage, an electric field will be created with normal and tangential components. By increasing the intensity of electric field, the tangential electric stresses will also increase proportionally on the surface of the liquid. Subsequently, the shape of liquid material starts to form into a cone shape which is also called Taylor cone [49].

The changes in the distance had a curvature effect on fiber diameter as shown in Figure 4-5(a), (d) and (e). The general trend of the effect of distance on fiber diameter can be described as fiber diameter increases up to the center point and it decreases again after passing a threshold value. This behavior can be explained by considering the role of tangential electrical stresses by increasing the distance between tip and collector up to a threshold value (approximately 10.75 mm as observed during experiments). Under these circumstances, the tangential electrical stresses will decrease upon increasing the distance [92]. On the other hand, the fiber diameter decreases by an increase in the collector distance due to the increase in tensile forces and non-isothermal condition of the highly viscous jet. Hence, the balance between tangential electrical stresses and tensile forces for maintaining the inertia at a constant value results in a decrease in fiber diameter [49,92].

As illustrated in Figure 4-5, no significant effect was observed by changing the applied voltage within the experimental range. Although a minor influence of the applied voltage on the fiber diameter might be observed, it was dominated by the other parameters and not high enough to reach our pre-selected significance level. The same trend and behavior were reported in a previous study in which the applied voltage had negligible effects on fiber diameter [232].

The extent of the contribution of process parameters in the model equation is a good indicator to determine whether a parameter had a significant effect on the response at the first place, and how significant was the observed influence. In this way, the applied voltage was directly excluded from the model equation due to its nonsignificant effect on fiber diameter. By ordering the parameters for their significance level, their observed effects on the output can be deduced from the value of the corresponding coefficients in the model; the higher value implicates the higher impact on the output. Hence, the order of process parameters based on the significance of their contribution in the resulting fiber diameter can be sorted as pressure, collector speed, and tip-to-nozzle distance.

4.3.3 Process parameter optimization

To fully understand the effect of each process parameter on the spun fiber diameter, a significant number of experiments must be conducted. As seen in equation (1), the predicted model was very complex, but the nonsignificant variables with no evidence of their

contribution in the response could be eliminated to simplify the model. Hence, an analysis on the corresponding P-values in ANOVA table was performed, and the parameters or the interaction effects whose P-values were higher than the confidence level (0.05) were excluded from the equation to simplify the model. After the elimination of nonsignificant factors, the optimized model can be written as follows:

$$y = 60.728 - 3.505x_1 + 0.875x_2 + 7.584x_3 \quad (3)$$

In this model, R^2 , R_{adj}^2 , and the P-value of lack-of-fit were 95.01%, 94.45%, and 0.522, respectively. These results demonstrate that the model was well fitted and describes the experimental data with an acceptable error margin. The contour plots of the optimized model are presented in Figure 4-6, in which the corresponding process parameters for the resultant fiber diameters are shown.

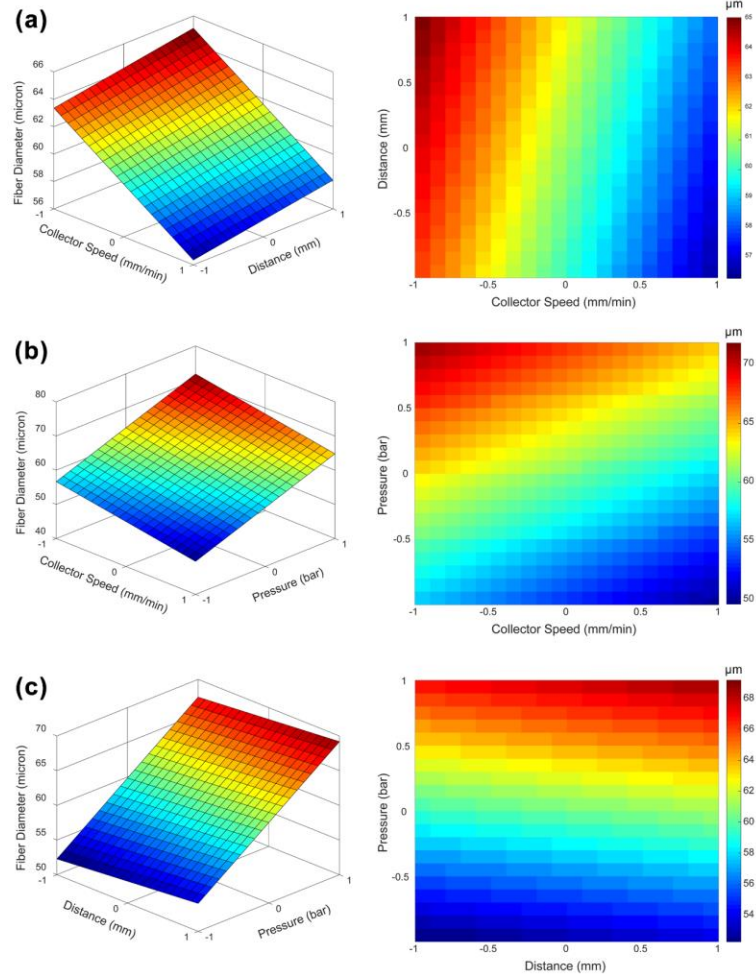


Figure 4-6. Contour plots of fiber diameter with respect to process parameters for optimized model and their mutual interactions on fiber diameter, (a) collector speed vs. distance (b) collector speed vs. pressure (c) distance vs. pressure. For each graph the other parameters were set to level 0

4.3.4 Validation of the model by printing a 3D scaffold

To validate the proposed model, a random set of variables from the plots in Figure 4-6a, b, and c were selected as the printing parameters ([collector speed, distance], [collector speed, pressure], [distance, pressure], respectively). Three-dimensional scaffolds of $4\text{cm} \times 4\text{cm}$ were printed with the set parameters with 6 layers of height and gap size of 700 μm . The corresponding images were acquired by SEM to observe their spatial alignment and measure the fiber diameters. The chosen coded parameters are listed in Table 4-4.

Table 4-4. Validation of model with random sets of variables adapted with the optimized model

#	Collector speed (mm/min)	Distance (mm)	Pressure (bar)	Voltage (kV)	x ₁	x ₂	x ₃	Predicted Fiber Diameter (μm)	Fiber Diameter (μm)	±SD
1	310	13	0.8	6.2	-1	1	0	65.11	67.54	0.642
2	400	7	0.6	6.2	1	0	-1	49.64	47.31	0.816
3	355	12.25	0.9	6.2	0	0.75	0.5	65.18	63.82	0.709
4	332	10	0.65	6.2	-0.5	0	-0.75	56.79	51.32	0.759

The resultant spun 3D structures are also shown in Figure 4-7. The results from the validation experiments showed that the measured fiber diameters were in good agreement with those predicted by the optimized model. Considering the randomness in selecting the set of parameter values during the validation step, it can be concluded that the proposed model could predict fiber diameters with a high accuracy. This would be significantly useful in determining melt electrospinning writing of 3D structures with dimensional accuracy required by the desired application.

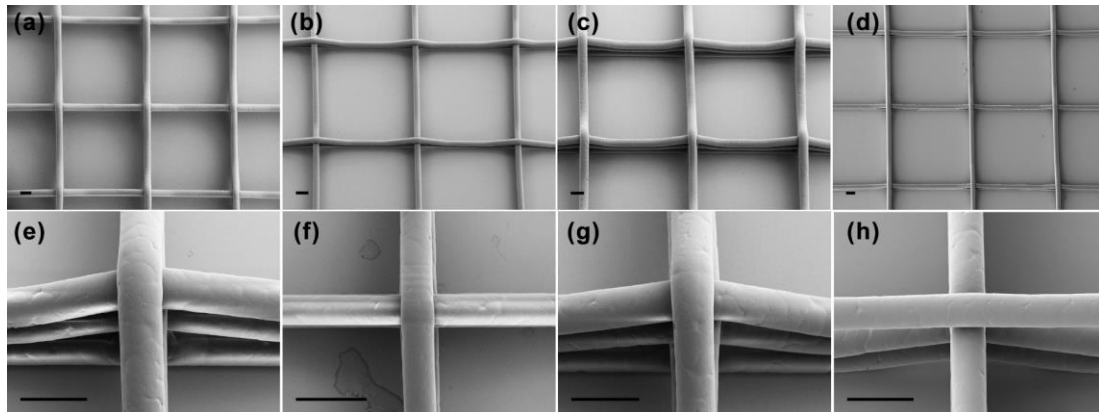


Figure 4-7. SEM images of printed scaffolds with randomly selected parameters from the contour plot according to Table 4-4, (a and e) experiment #1, (b and f) experiment #2, (c and g) experiment #3, and (d and h) experiment #4; Scale bars 100 μm

4.4 Conclusion

In this study, response surface methodology was used to investigate the effect of critical 3D melt electrospinning write process parameters (collector speed, tip-to-collector distance, pressure, and applied voltage) on the fiber diameter. First, a range of values for those process parameters resulting in perfect straight fiber was obtained. A face-centered central composite design (FCCD) of experiment was selected for design of experiment due to its applicability and simplicity. The model was fitted with a quadratic equation using a linear regression model. The process parameters are optimized by omitting the nonsignificant values. The resultant R^2 , R_{adj}^2 , and P-value of lack-of-fit were obtained as 95.01%, 94.45%, and 0.522, respectively, indicating that the fitted data and the experimental values were perfectly matching and there was no evidence for lack-of-fit. The analysis of the proposed model showed that collector speed, tip-to-collector distance, and pressure had significant effects on fiber diameter. The predicted model for fiber diameter of spun polycaprolactone was also validated using the actual values of fiber diameter acquired from the SEM images of the 3D printed scaffolds. The results suggest that the obtained model can be used as a framework for choosing process parameters in 3D melt electrospinning printing/writing to achieve the desired fiber diameter.

5 Chapter 5: Preparation and characterization of nanoclay-hydrogel composite support-bath for bioprinting of complex hollow structures

This chapter was published in the journal of Scientific Reports as a research article [18].

Three-dimensional bioprinting of cell-laden hydrogels in a sacrificial support-bath has recently been emerged as a potential solution for fabricating complex biological structures. Physical properties of the support-bath strongly influence the bioprinting process and the outcome of the fabricated constructs. In this section, we reported the application of a composite Pluronic-nanoclay support-bath including calcium ions as the crosslinking agent for bioprinting of cell-laden alginate-based hydrogels. By tuning the rheological properties, a shear-thinning composite support-bath with fast self-recovery behavior was yielded, which allowed continuous printing of complex and large-scale structures. The printed structures were easily and efficiently harvested from the support-bath without disturbing their shape fidelity. Moreover, the results showed that support-bath assisted bioprinting process did not influence the viability of cells encapsulated within hydrogel. The presented study demonstrates that Pluronic-nanoclay support-bath can be utilized for bioprinting of complex, cell-laden constructs for vascular and other tissue engineering applications.

5.1 Introduction

Three-dimensional (3D) bioprinting provides controlled deposition of hydrogels, biological matters or biomaterials to fabricate complex cell-laden structures in a layer-by-layer manner for various tissue engineering applications. Natural or synthetic biocompatible and biodegradable cell-laden hydrogels are commonly used to construct 3D environment with the ability to turn into gel at physiological conditions without impairing cell integrity and cell-to-cell interaction. Extrusion based bioprinting is one of the most common method to deposit cell-laden hydrogels in desired geometry with precise control in micrometer scale. The process requires gelation of liquid hydrogel either by physical, thermal or chemical crosslinking before, during, or after bioprinting. However, physical phase transition of hydrogels during extrusion might clog the nozzle and could disrupt the viability of the encapsulated cells [233,234]. In addition, due to low mechanical strength, the printed hydrogels may not be strong enough to hold overhanging structures. Integration of the subsequent layers is another challenge which needs proper adjustment of hydrogel gelation time with the printing process [235,236]. The level of humidity strongly affects cellular viability, which is not often preserved during in-air hydrogel extrusion bioprinting [237,238]. These limitations can arise due to both hydrogel properties such as viscosity and gelation time, and the printing parameters such as fabrication time, extrusion pressure and nozzle size. Among them, viscosity of the hydrogel has a pivotal role. Viscosity can be fine-tuned with increasing the concentration, which increases the hydrogel stiffness and subsequently might have an adverse effect on cell migration and functioning. A sacrificial secondary hydrogel with different gelation property, or a viscosity modifying biomaterial is generally introduced within the primary hydrogel to obtain a qualified structure during the extrusion based bioprinting process [239–242].

Direct free form writing of hydrogels in a fugitive and sacrificial support-bath has addressed aforementioned limitations. A support-bath with the Bingham plastic flow behavior can provide a rigid supporting matrix and at the same time, instantaneous yielding and rapid recovery during and after passage of the extruding nozzle, respectively [238,243–246]. In addition to the adequate flow behavior, the support-bath should quickly provide the necessary gelation to control the spreading of the extruded viscous bioink and let the printed layers to be

integrated, and concurrently avoiding nozzle clogging. This approach has been demonstrated by depositing liquid hydrogel precursors within self-healing support materials such as Carbopol, Laponite, gelatin, gellan, fumed silica particles, Pluronic and alginate [247–254]. However, the functionality of the support-bath materials is influenced by several parameters. In addition, the compatibility of the support-bath with the printed hydrogel has also a crucial role for a successful bioprinting [248–250,255,256]. For example, hydrophobic perfluorotributylamine fluid was employed for the bioprinting of agarose hydrogel due to its high buoyant density [249]. Since the approach of supporting is based on buoyancy, viscosity of the printed hydrogel might affect the structural resolution which limits the applicability of this support material in different types of hydrogels. In another study, two different types of hyaluronic acid which were modified with adamantane or β -cyclodextrin, respectively, were utilized as self-healing support material, by using their reverse assembly capability as host-guest interactions [256]. Although methacrylated gels were successfully printed, the possible reaction of adamantane or β -cyclodextrin ends would limit the utilization of this technique to be used with different materials. Due to their stress-yielding properties, Carbopol microgels and gelatin microparticles have also been studied [247,248]. However, ionic sensitivity of the Carbopol and, thermal instability and microparticle size-dependency of the gelatin slurry limit their use. Therefore, to address limitations and general requirements for bioprinting of hydrogels with various properties, new formulations of support-bath systems are needed.

Poly(ethylene oxide)-poly(propylene oxide)-poly(ethylene oxide) (Pluronic F127; PF) is one of the support-bath material candidates possessing concentration dependent-thermoreversible gelation property. It is in gel form at around body temperature (concentrations >18%) and turns into liquid below 10 °C [257]. Hence, it was implemented as support-bath or sacrificial fugitive ink at room temperature within the range of 25-40% concentrations [258,259]. However, viscoelastic modulus of the material was not strong enough for micrometer scale resolution in a long time printing processes due to mechanical weakness and tendency of quick dissolving in physiological conditions [257,259]. Sol-gel transition concentration of PF was modified by addition of Laponite [240,260]. Laponite is a layered synthetic nanoclay with chemical formula of $\text{Si}_8\text{Mg}_{5.45}\text{Li}_{0.4}\text{O}_{24}\text{Na}_{0.7}$ similar to hectorite. It exists as a 2D disc-like structure, 25 nm in diameter and 1 nm in thickness with negative charges distributed on the faces (OH^-) and positive charges on the edges (Na^+).

Due to its biocompatibility, low cost, availability, thermal stability, processability, ionic insensitivity, and anisotropic behavior, Laponite can be considered as a promising rheology-modifier, or used as mechanical reinforcing component and crosslinker with several hydrogel systems [261–263]. It was utilized in different applications of tissue engineering from composite hydrogel printing to support-bath material [180,246,264–266]. The gel-forming ability of Laponite involves a multi-step mechanism. When particles react with hydroxide ions in the water, phosphate ions dissolve. After the ion dissolution, the nanoclay particles start to interact with each other while the sodium ions diffuse towards the surfaces within the galleries, resulting in expanded thixotropic gel structure [267–269]. Laponite RDS, a category of Laponite family, possesses an extra peptizing agent of sodium pyrophosphate ($\text{Na}_4\text{P}_2\text{O}_7$) at the edges which ionically stabilizes the structures and prevent the face-edge bond formation between particles [270]. The pyrophosphates give a thixotropic behavior to the structure [270]. These properties of Laponite would make it a suitable support-bath material, but the printed hydrogels have high viscosity with stiff network which is a disadvantage for cellular activities like cell adhesion, migration and proliferation [271–273]. In addition, the removal procedure of the supporting gel is complicated, often resulting in damage to the printed structure due to being strongly adherent nanoclay particles [254].

In this chapter, we developed a composite support-bath based on the mixture of PF and Laponite (PF-RDS) in the presence of calcium ions, to be used in free form bioprinting of complex cell-laden hydrogel structures. Although both materials show unique properties and have been individually employed as sacrificial support gels, they showed limited capacities in bioprinting of low viscosity inks at low concentrations and also the ease and efficiency of removal procedure [236,246]. By combining two components as a composite support-bath, it would be possible to employ the distinct characteristics of each, namely the thermoresponsive gelation of PF and the thixotropic behavior of Laponite. We analyzed different formulations with varying concentrations of PF-RDS and calcium chloride (CaCl_2) to achieve optimum rheological properties. Sodium alginate was utilized as a precursor solution to evaluate printability of complex and hollow structures by *in situ* crosslinking within the support-bath. Finally, cell-laden hydrogel structures were bioprinted in the support-bath and the

cytocompatibility of the bioprinting process was analyzed by monitoring the viability and metabolic activity of cells after printing process.

5.2 Results and discussion

5.2.1 Rheological characterization of the support-bath

The weak interactions of the support-bath components play a critical role in the formation of network and its stability and hence the preservation of the printed hydrogel structures in overhanged and complex geometries [243–245]. In this research, thermoresponsive behavior of PF was combined with the thixotropic behavior of the Laponite to obtain yielding and easily removable support-bath structure. Laponite RDS is selected due to formation of a stable polymer-nanoclay complex with the presence of Ca^{2+} and possession of a neutral isoelectric point providing a biocompatible environment [269,270].

Thermoresponsive gelation behavior of the PF-RDS support-bath with different formulations was characterized through a typical temperature sweep test from 4 to 37 °C with a final dwelling time of 2 h by the evolution of storage (G') and loss (G'') moduli (Figure 5-1). By increasing temperature, G' and G'' moduli raised as a result of both liquid crystalline phase transition of PF in ionic media and the presence of Laponite particles [241,260,269]. Then, G' and G'' reached a steady state by further incubation at 37 °C.

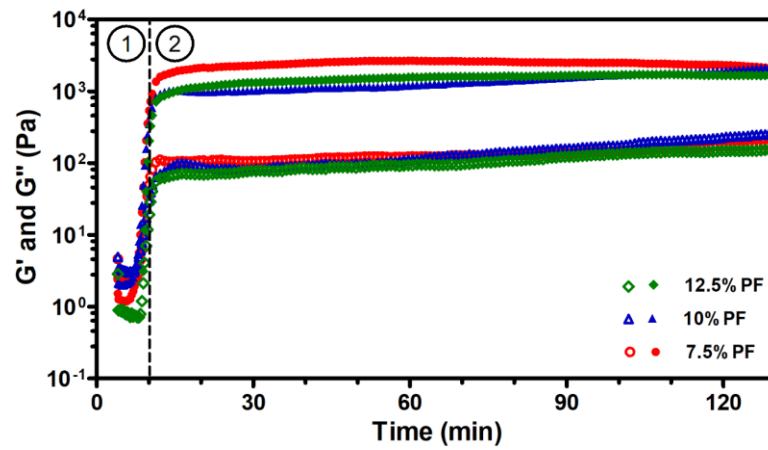


Figure 5-1. Temperature and time sweep measurements of the support-bath showing storage and loss moduli over time for different concentrations of PF. Laponite and CaCl_2 concentrations were set to 3% and 1%, respectively. Storage (G') modulus (filled symbols) and loss (G'') modulus (open symbols). Vertical dashed line separates two measurements.

Region (1) represents temperature sweep test from 4 to 37 °C and region (2) shows time sweep measurement at 37 °C for 2 h

5.2.2 Effect of PF concentration

Figure 5-2 represents rheological characterization of different concentrations of PF in the presence of Laponite-RDS and CaCl_2 at constant concentration. Dynamic moduli of composite containing 7.5, 10, and 12.5% of PF, and 3% Laponite RDS, and 1% CaCl_2 are plotted during the strain amplitude (Figure 5-2a) and angular frequency sweeps (Figure 5-2b). Strain amplitude graphs demonstrate the flow point of the materials at which a transition between elastic gel state ($G' > G''$) to viscous liquid-like state ($G'' > G'$) is observed [266,274]. At very low strain amplitudes, G' and G'' of the material show the linear viscoelastic behavior [275]. Increasing the concentration of PF from 7.5% to 10% in the composite resulted in an apparent increase in both moduli during constant strain amplitude loading, however further increase to 12.5% induced a significant decrease (Figure 5-2a). The value of storage moduli of 7.5 and 12.5% PF containing composites were observed to be almost the same while the corresponding value for 10% PF one was 1.5-fold higher. The interactions of PF and RDS are considered to be very complex and have not been completely known, however it is assumed that electrostatic interactions as well as hydrogen bonding are the dominant players in the final structural configuration[265,276]. Reversible adsorption and detachment of polymer chains on the charged surfaces of the Laponite nanodiscs would result in a physically crosslinked network which shows solid-like elastic or fluid-like viscous behavior depending on external forces. Furthermore, cluster formation of the clay nanodiscs and subsequent agglomeration with PF polymeric chains would contribute in observation of high yield behavior upon applied stress [274,277]. The density of charges at the edges of Laponite RDS is different associated with pyrophosphate ions, which will lead to face-face interaction in contrast to face-edge attraction [267,278]. The attraction between these bonds will further link more particles at the dace-edge orientation and create a network that forms the final “gel state” [274,279,280]. The observed developments in both G' and G'' by increasing the PF concentration can be attributed to the bridging effect of PF micelles and chains with their vicinal nanoclay particles which results in stabilization of the composite [265,281]. In this way, it is speculated that there would be a threshold for such interactions, which could be

translated to the surface capacity, and hence the mass quantity of the Laponite-RDS in such a system. A viscoelastic gel structure could be formed by increasing the PF concentration up to a certain value above which, the faces of the Laponite-RDS nanoclays would be already saturated by the adsorbed polymer. Further increase in the polymer concentration will not necessarily contribute in establishment of long-range elastic interactions between the two components of the system [260,282]. The mixtures of PF and CaCl₂ (Control 1) and Laponite-RDS and CaCl₂ (Control 2) were selected as control groups to identify the contribution of each individual component of the composite in development of the viscoelastic properties. It should be note that the exclusion of CaCl₂ from the mixture of PF-Laponite RDS resulted in the formation liquid-like composite, failing to form a viscoelastic gel network. Hence, this composition was not included in the set of experiments. Control 1 failed to show a detectable linear viscoelastic limit within the range of strain values 10⁻³ to 10³ (%). This can be explained by formation of clusters consisting of polymer chains at low concentration of PF as reported elsewhere [283]. Control 2 showed a linear viscoelastic range during strain amplitude sweeps, however the storage modulus values were much lower than the corresponding region in PF-RDS composites containing PF at the same CaCl₂ concentration [280]. Both control groups showed less elastic moduli, since Laponite acts as a physical cross-linker to PF polymer chains in the presence of CaCl₂ which is in agreement with previous study of Wu *et al* [240].

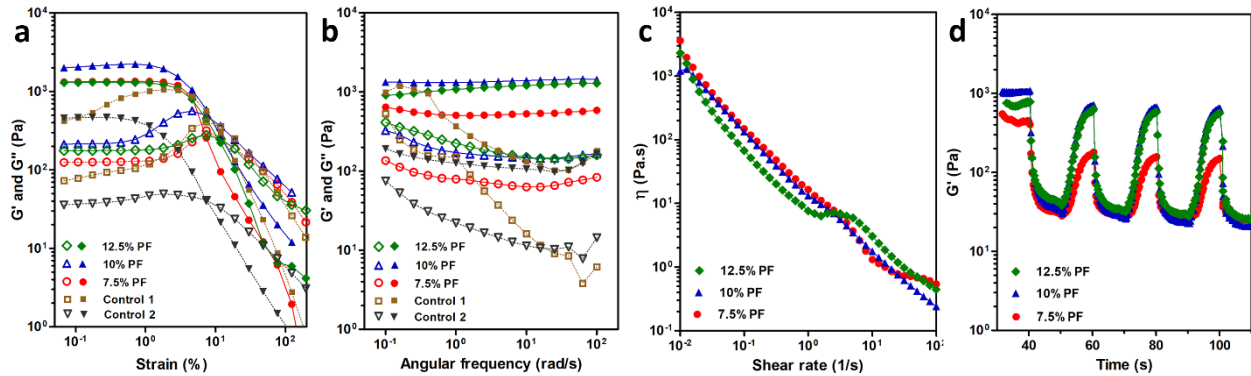


Figure 5-2. Dynamic rheological characterization of the support-bath representing the effect of PF concentration on flow behavior and recoverability of the structure at 37 °C (Laponite-RDS and CaCl₂ concentrations were constant at 3 and 1%, respectively except for control samples). Control 1 and control 2 included 10% PF, and 3%RDS, respectively. at constant 1% CaCl₂ (a) Strain amplitude sweep profiles of supporting mediums, (b) frequency sweep profiles within the linear viscoelastic range, (c) viscosity vs. shear rate plots revealing

the shear thinning behavior of the support material, (d) cyclic strain measurements at high (50%) and low (0.6%) strains showing storage (G') moduli of the samples in 4 cycles. Storage (G') modulus (filled symbols) and loss (G'') modulus (open symbols)

The dynamic viscoelastic properties of the formed networks of PF in the presence of Laponite-RDS and CaCl_2 were also probed by frequency sweep analysis (Figure 5-2b). The elastic features of the matrix were dominant throughout the whole measured frequencies, characterized by G' values higher than G'' values [274]. The elastic modulus value at 7.5% PF was considerably lower than the other two concentrations. By increasing the PF concentration to 10%, the interactions between PF and Laponite-RDS evolves from a viscoelastic-dominant gel state to a glassy state colloidal network, in which the elastic modulus is almost independent from the frequency of deformation. Further increase in PF concentration to 12.5% resulted in weakening of the elastic response of the system at low frequencies, an indication of the increased contribution of excess PF chains which are speculated to have no direct interactions with Laponite nanoparticles. The results demonstrate that concentration dependent interactions between polymer and clay nanoparticles allow the formation of suitable and stable network for support-bath [280,281,284]. Control 1 showed a strong dependency of both elastic and loss moduli to frequency values. It could be due to testing parameters which was not in a viscoelastic region. Control 2 showed glassy gel-like behavior with almost constant elastic modulus values at all frequencies, revealing the effect of calcium ions in the formation of House of Cards-like structure which was utilized as support-bath material in previous studies [246]. However, the value of storage modulus was much lower compared to the composite with PF which needs more viscous bioink to be able to provide enough mechanical strength to hold the structure during bioprinting process.

Shear thinning behavior and yield stress values of the composite support-bath materials were investigated by a shear rate sweep test (Figure 5-2c). As the graph implies, all the tested concentrations showed the same trend of viscosity drop but the sample with 7.5% PF had the highest decrease in its viscosity while the sample with 10% of PF had the lowest change. The Herschel-Bulkley model (equation 1) was used to fit the data and estimate the dynamic yield stress and flow index values [247,267].

$$\tau = \tau_y + K\gamma^n \quad (1)$$

where τ is shear stress, τ_y is yield stress, γ is shear rate, and K and n are consistency factor and flow index, respectively. The model's parameters are presented in Table 5-1.

Table 5-1. Herschel-Bulkley parameters for composite materials with different PF concentrations at constant concentrations of Laponite-RDS (3%), and CaCl₂ (1%)

PF concentration (%)	τ_y (Pa)	K	n
7.5	32.8 ± 3.5	6.78 ± 2.2	0.73 ± 0.1
10	42.6 ± 5.7	10.32 ± 1.3	0.47 ± 0.2
12.5	28.6 ± 4.3	5.4 ± 2	0.60 ± 0.17

Flow index (n) is the main indicator of the shear-thinning behavior. The indices of 7.5 and 12.5% PF were almost equal, showing the same behavior in viscosity drop, which can be also observed in Figure 5-2c. Yield stress values obtained from Herschel-Bulkley model are in agreement with the yield stress trends from strain sweep measurement. On the other hand, PF samples with 10% concentration showed an increase in yield stress, which could be attributed to the same saturation of polymer-particle interactions as mentioned previously. It should be noted that Control 2 samples did not show that much different values of viscosity vs. shear rate and Control 1 data was not reliable as mentioned in the previous part due to its non-linear viscoelasticity, therefore the graphs were not included.

Figure 5-2d shows recoverability of the composite throughout cyclic deformation. Due to the thixotropic characteristics, the disturbed matrix result in rebuilding of the interactions by forming the matrix network over time [236,266]. The so-called self-recovery property represents an essential feature of the composite matrix to be utilized as a support-bath material. Dynamic strain tests were performed at high (50%) and low (0.6%) strains. The strain cycles were repeated in 10 seconds intervals to monitor how fast the composite material could recover itself. Thixotropic behavior was monitored within 16 cycles (data was clipped to 4 cycles to enhance the legibility) and the recovery time and the extent of drop in storage moduli after 3rd cycle of deformation were almost constant. As shown in the graph, even in a

short time of 10 seconds the structures with 10 and 12.5% of PF could almost reach to their initial storage moduli. The composite with 7.5% of PF showed lower recovery in storage modulus compared with the starting point. This could be due to lower amount of polymer-chains which could not enhance the composite matrix stiffness [281]as the amount of PF was not enough to resist the high shear strain values to rapidly recover the physically crosslinked polymer chains attaching on the Laponite nanodiscs charged surfaces [274,277].

5.2.3 Effect of CaCl₂ concentration

The contribution of ionic content in the formulation to viscoelastic properties of the composite was systematically assessed by varying the CaCl₂ concentration with constant PF and Laponite-RDS which were set to 10 and 3%, respectively. We evaluated three different concentrations of 1, 0.5, and 0.25% for CaCl₂ in the formulation to provide a moderate crosslinking for dispensed liquid form of alginate and to obtain an integrated structure without diffusion into the support-bath [267,280,285]. It should be mentioned that the lowest concentration of Ca²⁺ were above the threshold of “gel” formation below which a “glass-colloid” would be formed as explained in the previous study[286]. Figure 5-3 shows the rheological properties of the composites with different CaCl₂ concentrations.

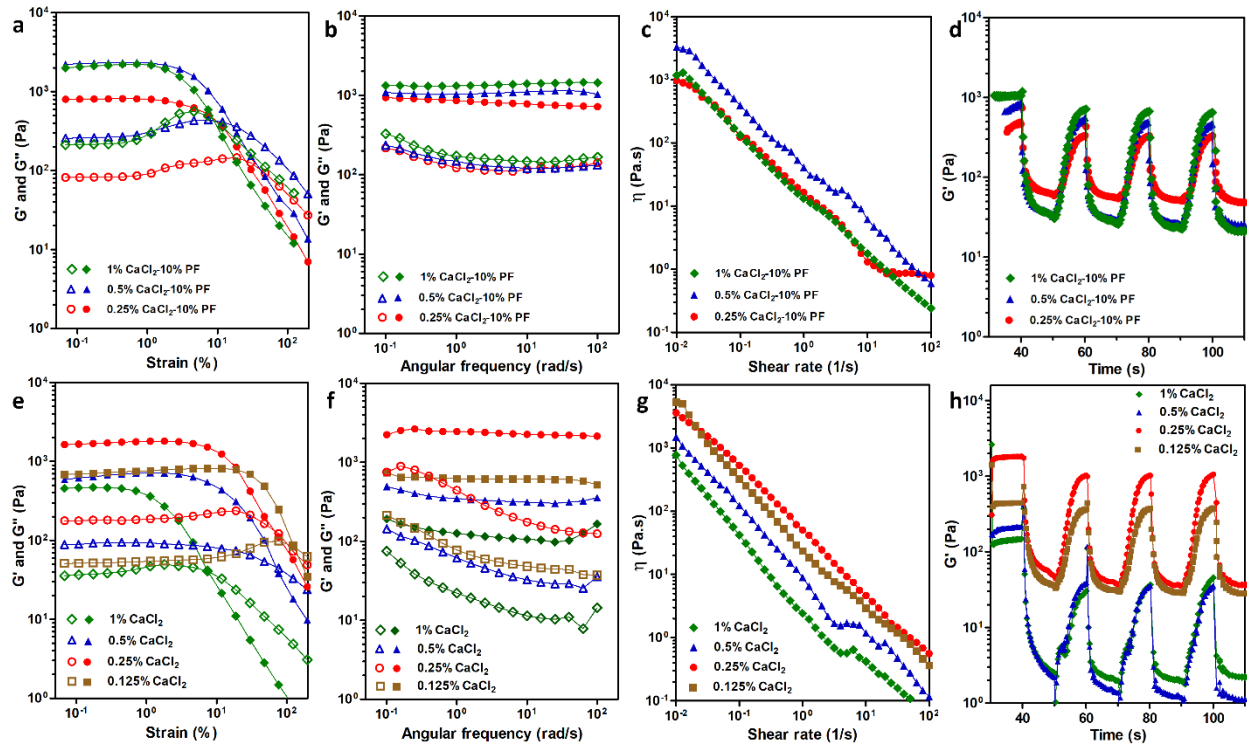


Figure 5-3. Dynamic rheological characterization of the support-bath representing the effect of CaCl₂ concentration on network characteristics, flow behavior and recoverability at 37 °C (a-d were included samples with constant PF and Laponite concentrations of 10 and 3%, respectively.) (e-f were included only 3% Laponite-RDS.) (a and e) Strain amplitude sweep profiles of supporting medium, (b and f) frequency sweep profiles within the linear viscoelastic range. (c and g) viscosity vs. shear rate plots revealing the shear thinning behavior of the support material, (d and h) cyclic strain measurements at high (50%) and low (0.6%) strains showing storage (G') moduli of the samples in four cycles. Storage (G') modulus (filled symbols) and loss (G'') modulus (open symbols)

Strain amplitude sweep (Figure 5-3a) shows the correlation of the extents of the linear viscoelastic region with three different CaCl₂ concentrations. At low strain values, storage moduli are higher than loss moduli demonstrating the solid-like elastic behavior of the structures [275]. By further increasing strain values, structure starts to breakdown and material starts to yield. Dynamic moduli of the sample containing 0.25% CaCl₂ was observed much lower than the other two concentrations since low ionic concentrations cannot lead to complete formation of aggregates [277,280]. Concentration of ions will change the net charge distribution of nanoclay particles in the composite matrix from edge to the surface and through the polymer chains [277]. The variation of surface charge in the composite gels with

lowest CaCl_2 content translates to the enhancement of Van der Waals forces compared to the ionic interactions. By increasing the salt content, the network formation will face a transition from repulsive clay-clay interactions to attraction of opposite charges and eventually forming a strong gel network [277]. The electrostatic attractive forces among nanoclay particles would correspond to material's yield stress [278]. In addition, enhanced exfoliation of nanoclays with the increased ion concentration will take place that might correspond to the phase separation of the matrix under stress [280,287]. It was evident by evaluation of the obtained rheological data that increasing the ion concentration resulted in a similar trend in increasing the storage modulus. Considering these data, it is concluded that the ionic content in the current experimental design was still below the threshold to induce any phase separation [269,279,280]. It should be also noted that presence of divalent Ca^{2+} ions would shift the equilibrium in balancing of the ionic interactions between nanoclay galleries, which the acclaimed House of Cards-like structure during network formation of pristine Laponite is due to exfoliation of nanodiscs in presence of monovalent Na^+ ions. In this way, formation of a long-ranged network due to exfoliation and collapse of nanoclay galleries in the absence of PF showed a threshold concentration of CaCl_2 above which, the dynamic moduli and cross-over points in strain sweeps decreased significantly. We speculated that at this critical concentration of divalent Ca^{2+} ions, the exfoliation of nanodiscs was to an extent that the formed network was completely dependent on ionic interactions and secondary forces like Van der Waals interactions between PF and Laponite nanodiscs could not significantly contribute to overall viscoelasticity of the composite.

All the formulations showed a glassy state with frequency independence of elastic moduli throughout a wide range (Figure 5-3b). The one order of magnitude ratio between G' than G'' indicated a stable network formation with no relaxation time within the probed range of frequencies [244]. The sample with 0.25% CaCl_2 showed more dependency of storage modulus to the frequency of deformation which is an indication of weaker and more viscous nanoclay-nanoclay and polymer-nanoclay interactions. It is speculated to be due to the contribution of Ca^{2+} in formation of the glassy House of Cards-like structure in PF-RDS [280].

Shear-thinning behavior of the samples with different ionic concentrations was explored through a shear rate sweep measurement (Figure 5-3c). Dynamic yield stress and flow index values were calculated by fitting the data to Herschel-Bulkley model (Table 5-2). For all the samples viscosity decreases by increasing shear rate expressing similar shear-thinning behavior regardless of their ionic concentration. However, the sample with 0.5% CaCl₂ showed higher values which could be due to bridging effect of Ca²⁺ that is the connection of two nanoclay particles from their negative surfaces that results in agglomeration of particles and possessing higher viscosity [280].

Table 5-2. Herschel-Bulkley parameters for composite materials with different CaCl₂ concentrations at constant concentrations of Laponite-RDS (3%), and PF (10%)

CaCl ₂ concentration (%)	τ_y (Pa)	K	n
0.25	26.3 ± 5	7.3 ± 3.6	0.58 ± 0.1
0.5	47.7 ± 4.2	11.39 ± 3	0.27 ± 0.15
1	42.6 ± 5.7	10.32 ± 2.3	0.47 ± 0.2

Cyclic strain measurements were performed and storage modulus vs. time was plotted to explore the recoverability of the structures for 10 seconds per cycle. (Figure 5-3d). Storage values dropped after first cycle and continued with almost the same values. The lowest CaCl₂ concentration showed less decrease and less recovery in storage modulus during the test. This phenomenon could be attributed to the fact that the ionic concentration was not enough to interact with nanoclay particles and hence not much gel-like structure was formed [246]. Initial storage modulus values were higher for samples with higher ionic concentration which is in agreement with aforementioned structural properties.

Based on previously published article which utilized a composite of CaCl₂-Laponite as a support-bath material [236], we selected four different formulations of CaCl₂ with 3% Laponite and explored how ionic concentrations would affect their rheological behavior. Fig. 3e represents flow behavior of the samples at different strain values. Interestingly, by increasing CaCl₂ concentration from 0.125 to 0.5%, G' increased and afterwards decreased and the formulation of 0.25% CaCl₂ showed higher storage modulus compared to other

samples. Based on visual observation, composites containing 0.125 and 0.5% concentrations of CaCl_2 formed stiffer gel-like structure than others. In addition, their flow points are at higher strain values which could be attributed to bridging effect [280]. Compared to composites containing PF, the agglomeration of nanoclay particles due to interaction of two negatively-charged surfaces happened at lower ionic concentrations. In other words, composites containing PF with 0.5% of CaCl_2 showed more viscous properties, whereas samples correspond to 0.25% of CaCl_2 without PF had higher viscosity and elastic moduli. This result demonstrates the effect of Ca^{2+} ions on Laponite nanoclay structure as shown in previous studies [246,251,280].

Almost the same behavior was observed for frequency sweep measurements (Figure 5-3f). The composites of CaCl_2 and Laponite act as a glassy colloid with no dependency of elastic moduli on frequency changes. Elastic moduli values repeated the same as for strain amplitude sweep test. The more the ionic concentration, the more possibility to shield the nanoclay charges and consequently damaging the House of Cards-like structure of Laponite [288].

Shear thinning behavior of the samples were monitored through a shear-rate measurement and their viscosity were plotted against shear rate values (Figure 5-3g). As the graph implies, all the formulations represented shear-thinning behavior and their viscosity dropped by increasing shear rate values.

Recoverability of the samples were investigated through a cyclic strain measurement (each cycle was 10 sec) and corresponding storage modulus values were recorded and plotted vs. time to mimic the nozzle translation in the support-bath. The composites containing 0.125 and 0.25% of CaCl_2 showed much higher G' values with almost constant values for each cycle revealing their ability to recover their structure rapidly. The other two formulations containing 0.5 and 1% of CaCl_2 had low storage moduli and their values drop too much after first cycle demonstrating that the composites are not capable of fast recovery. Compared to composites containing PF their storage moduli are extremely lower which is due to interaction of polymer molecular chains and nanoclay particles causing physical cross-linking [280]. This demonstrates that both thixotropic behavior of Laponite and thermoresponsive properties of PF contribute for the physical crosslinking and the formation of a viscoelastic support-bath.

It is noteworthy to mention that low concentrations of CaCl_2 showed promising behavior to be used as an electrolyte together with Laponite nanoclay. In this study, we selected 0.5% CaCl_2 since it was not only a structural modifier for Laponite, but also a cross-linker for alginate. Our aim was to utilize a low concentration cell-laden hydrogel (3% alginate) to provide a cell-friendly bioprinting process with the utilization of a relatively low pressure for extrusion of bioink in a moderate CaCl_2 concentration to obtain sufficient cross-linking density for structural integrity among the subsequently printed layers.

5.2.4 Printability of overhanging and complex structures in PF-RDS support-bath

The challenges of overhanging and tubular complex structure printing have been addressed with different approaches in the literature [289–294]. The principle of the printing mechanism of those tubular structures are based on one-step extrusion of hydrogel in air, which is cross-linked by the inclusion of cross-linker through a coaxial nozzle system. These techniques are capable of printing hollow vascular-like structures in small dimensions by employing different formulations of bioinks, whereas construction of complex shapes in a layer-by-layer manner may not be applicable for integration of the extruded subsequent layers.

Printing in support-bath has been an emerging approach utilized by extrusion of hydrogels in a liquid form to have an appropriate shape fidelity, as well as to provide a more cell-friendly process compared to in-air extrusion bioprinting [293]. Laponite support-bath was demonstrated as support bath for fabrication of overhanging and complex branched tubular structures for various hydrogel types with different cross-linking mechanism [246,295]. Although Laponite support bath was investigated individually with many aspects for printing, the extruded hydrogel concentration was very high which could affect living cell functionality [246]. The use of high concentration of hydrogel is expected due to the slow crosslinking kinetics of alginate in the presence of low concentration of CaCl_2 , which has a strong negative effect on viscoelastic properties of Laponite as it is demonstrated above.

Rheological characterization suggested that all the tested PF-RDS composites could be used as a support-bath for hydrogel printing. Three percent of alginate was used for printing inside the support-bath that has lower concentration compared to previous studies

[236,246,296]. Among PF concentrations, 10% showed better viscoelastic behavior in terms of storage modulus and self-recovery. Printability of alginate into the support-bath containing various CaCl_2 concentrations were investigated. In the previous report, concentration of CaCl_2 for the Laponite support-bath was 0.125% [236]. However, our initial experiments showed that even the CaCl_2 concentration of 0.25% was not enough to efficiently cross-link 3% of alginate hydrogel during printing. This concentration was much lower than the hydrogel that was used in the mentioned study (8% alginate). On the other hand, increasing the concentration of CaCl_2 to 1% resulted in fabrication of structures with non-integrated fibers and occurrence of staircase effect [246]. Hence, the support-bath with composition of 10% PF and 0.5% CaCl_2 was used. Moreover, Ding *et al.* increased CaCl_2 concentration to 0.5% in a 4% Laponite support bath, while they used a concentrated and more viscous hydrogel blend as the extruded bioink (3% alginate+10% gelatin) [246]. This could be correlated to the decreased self-recovery properties of Laponite support-bath in the presence of high CaCl_2 concentrations. It is worth mentioning that increasing the concentration of CaCl_2 above 0.125% causes the deterioration of the House of Cards-like structure and shear-thinning property of only Laponite support-bath. Formulation of the Laponite support bath with PF resulted in increased tolerance over the CaCl_2 content and allowed to dispense less viscous hydrogel with higher shape fidelity at low extrusion pressure, which would be a more cell friendly process.

A detailed overview of 3D printed overhanging hollow structures with different angular configurations before and after recovery from PF-RDS support-bath are demonstrated in Figure 5-4. Support-bathes were incubated at 37 °C in a humidified environment for two hours prior printing based on the rheological data explained above. Integrated and bended tubular structures perpendicular to the surface (90°) and with 60° and 45° angles and a conical structure with 60° angle were printed in 20 layers. The front views of the tubular structures in support-bath are presented in Figure 5-4-a, b, c, d. It is clearly seen that the angles of printed structures were the same as designed models. The front and top views of the printed structures after harvesting from support-bath demonstrated that structures were well-crosslinked with integrated layers and preserved angular configurations due to optimized concentration of CaCl_2 in the PF-RDS bath. The height of the printed structures were measured as 7.58 mm ± 0.9, 4.54 mm ± 0.08, and 3.88 mm ± 0.25 for tubular structures of 90°, 60°, and 45° angles,

respectively. Based on computer-aided design (CAD) models, all the printed structures should have the same height. During printing of the tubular structure with 90° angle, the nozzle moved through the same x-y coordinates for 20 times. In contrast, the movement patterns of the nozzle for the other angled structures were not as repetitive in the same coordinates. As a result, diffusion of the hydrogel ink during printing of the structure with 90° angle was more and the final structure had higher height. Angles of the bended structures after removing from support-bath were measured as follows: $85.9^\circ \pm 1.40$, $59.4^\circ \pm 2.33$, and $47.8^\circ \pm 5.34$, which indicates a high printing resolution for the overhanging CAD models in the PF-RDS bath. The printed structures of alginate with 3% concentration demonstrated that the support-bath had proper viscoelastic characteristics which allowed printing of liquid-like hydrogels with relative low viscosity in a defined geometry and *in situ* cross-linking while the shape fidelity of overhanging hollow structures were preserved.

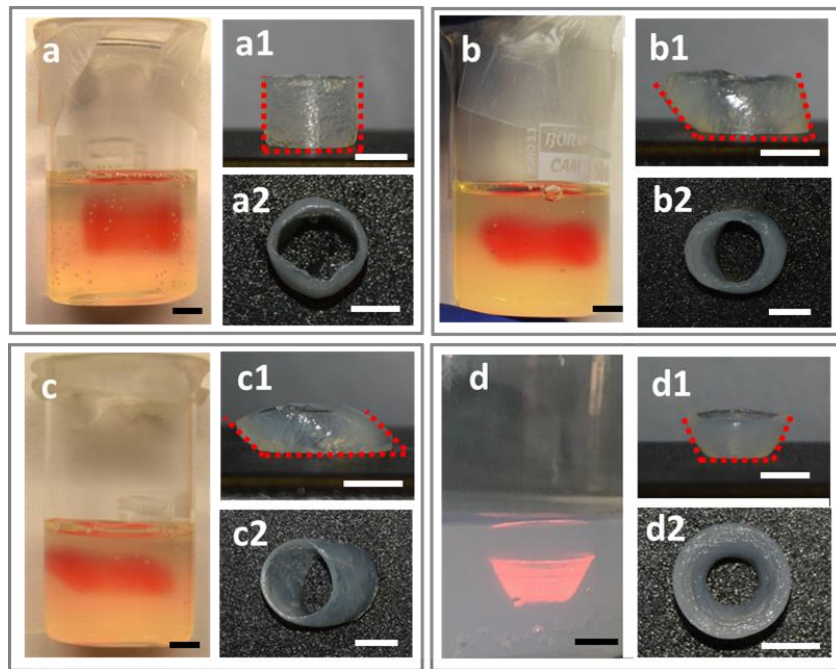


Figure 5-4. Characterization of PF-RDS support-bath for printability of tubular structures in various angular configurations. Digital images of the printed tubular alginate structures using 25-gauge nozzle in the support-bath angled at (a) 90° , (b) 60° and (c) 45° , and (d) a conical structure with 60° angle with respect to the surface. Digital images after removal of support-bath, from front and top views of (a1, a2) 90° , (b1, b2) 60° and (c1, c2) 45° bended tubular structures and (d1, d2) conical structure after removal from support-bath. Scale bars indicate 5 mm

Three different complex structures including star shape, grid and branched vascular structure were used to demonstrate printing capability of complex geometries with different scales inside the PF-RDS support-bath. Figure 5-5 shows the CAD models, top views of the printed structures before and after removal of the support-bath. Compared to reported Laponite support bath at which the sample was incubated for 6 h to obtain proper gelation [236], we could easily remove the printed constructs from the PF-RDS support bath just after printing. Increased concentration of CaCl_2 in support bath provided enough crosslinking density and ice-cold NaCl solution facilitated the removal of PF coated RDS. A star shape with an outer diameter of 2 cm was selected to demonstrate the precise deposition of extruded filaments with sharp corners (Figure 5-5-a1). Shape fidelity and its high resolution after the support-bath removal are demonstrated in Figure 5-5-a2. A small square grid structure with one cm length was chosen to explore the recoverability of the support medium in a repetitive pattern. CAD model of grid structure is depicted in Figure 5-5b. Despite the structural integrity and shape fidelity concerns for grid structure printing, the support-bath presented here allowed its fabrication (Figure 5-5-b1). The structure was harvested without disturbing shape fidelity during removal from the PF-RDS as shown in Figure 5-5-b2.

A vascular structure plays an important role for living tissues in oxygen and nutrients transportation, and metabolic removal. Fabrication of the vascular network is essential for the functional structures. A CAD model for a branched vascular structure with an overall length of ~ 3 cm and a width of ~ 2 cm was designed (Figure 5-5c). The vascular structure with a wall thickness of ~ 0.95 mm and 6 mm height was printed by three offsetted contours in each layer. Figure 5-5-c1 shows the printed branched structure inside the support-bath that was printed in 50 min. After gently removal of the support material from the lumen, interconnectivity of the hollow vascular structure was monitored by passing a food dye through it. The diffusion test demonstrated no leakage from the walls.

To demonstrate the capability of our support-bath for printing of anatomically relevant and 3D complex structures, a nose shape with an overall 2.7 cm length and 1.7 cm width was printed using 25 Gauge nozzle (Figure 5-5d). It is to be noted that the printing path strongly affects the final structure as it was demonstrated before[297]. When printing path started from the tip of nose inside the support-bath, we could obtain a smooth surface on the nose with

apparent nostrils as represented in Figure 5-5-d3. This result also verifies the applicability of our support-bath for bioprinting of liquid hydrogels in various complex and large scale structures.

The printed constructs demonstrated the feasibility of the support-bath for continuous and repeated retracing of the print-head. As stress-yielding phenomena happened around the local area where nozzle moves, overall rheological characteristics of the support-bath did not change and did not cause any disruption of the complex shapes, highlighting the stability of the support-bath for long-lasting printing procedures. Although printing speed is considered as a key parameter affecting the yielding properties of the support-bath [246,253], we printed with different print speeds and the support-bath revealed a consistent recovery. In addition, shape fidelity preservation after structure removal from the support-bath has demonstrated the sufficient integration between the consecutive layers.

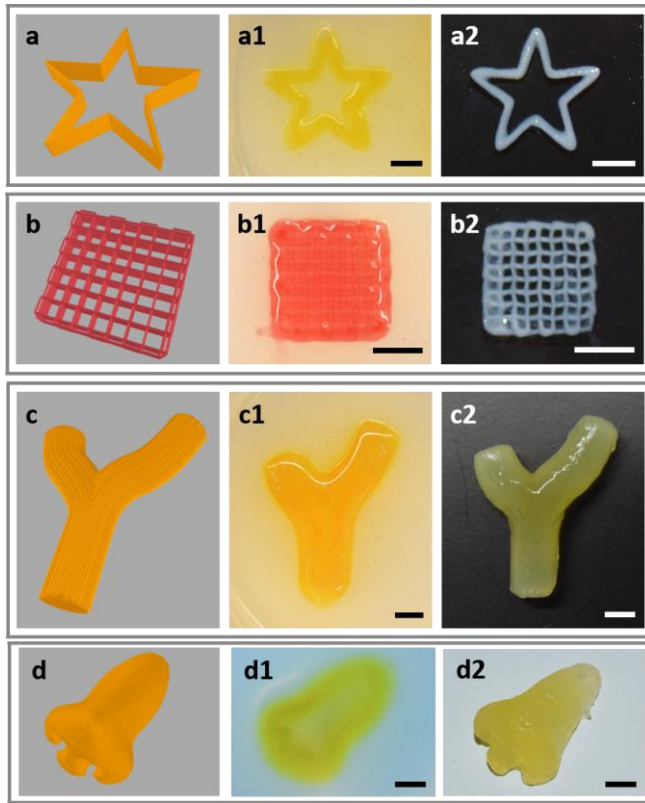


Figure 5-5. Fabrication of 3D complex constructs. CAD models of (a) star shape, (b) grid-pattern, (c) branched vascular structure, and (d) nose shape. Digital images of the fabricated structures (a1, b1, c1, d1) before and (a2, b2, c2, d2) after recovered from PF-RDS support-bath. Scale bars indicate 5 mm

5.2.5 Bioprinting of cell-laden alginate hydrogel in support-bath

Cell-laden hydrogels dispensed from a nozzle are being exposed to a shear stress, and followed by an invasive effect of cross-linking mechanism [293,298]. Therefore, fabrication process of cell-laden hydrogels inside the support-bath might affect the cellular integrity.

Since the nozzle size and feeding pressure for the extrusion of cell-laden hydrogel have an inverse relation, the use of small needle size might have more negatively effect on cell viability. We selected a small nozzle (30-Gauge) to investigate the effect of bioprinting process in support-bath in intense conditions. Compatibility of the bioprinting process was evaluated by monitoring cell viability after bioprinting. Alginate used to encapsulate the cells in this study is commonly employed in 3D bioprinting applications due to the biocompatibility and fast crosslinking in the presence of Ca^{2+} ions despite its bio-inert nature

and limited biodegradability. It is also used as a thickening hydrogel to enhance the bioprintability of the other, more bioactive hydrogels [236,246]. NIH-3T3 mouse fibroblast cells in a density of 1×10^6 cells/mL were encapsulated in 3% of alginate and bioprinted by feeding pressure of 0.5 bar and print speed of 150 mm/min. Well defined 3D hollow structure with a 5 mm diameter and average height of 0.6 mm was obtained by the integration of deposited four concentric fibers of cell-laden alginate. Figure 5-6 shows (a) bright field image of harvested bioprinted structure from the support-bath and (b) Calcein AM (green) and PI (red) stained, live and dead cells, respectively, in a complete bioprinted structure. The results demonstrated the structural integrity of the proposed structure for bioprinting and their efficient recovery from support-bath with high percentage of viable cells [236,246,254]. Live and dead cell numbers showed that $82.7 \pm 6.5\%$ cells in alginate hydrogel were viable after one day (Day 1) of incubation (Figure 5-6c). The percentage of viable cells did not change on Day 3 while the cell viability increased to $94.3 \pm 4.6\%$ at Day 7. The results indicated that extrusion pressure did not affect the cell viability significantly and the cells almost recovered at Day 7.

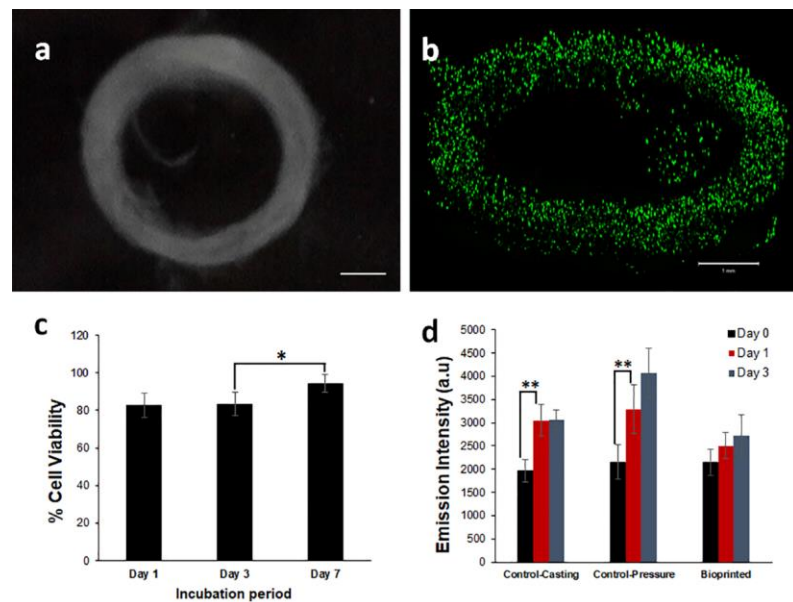


Figure 5-6. Fabrication of cell-laden alginate constructs using PF-RDS support-bath. (a) Image of harvested bioprinted tubular structure from support bath. (b) Confocal microscopy image of live/dead cells encapsulated in the alginate hydrogel in a complete 3D bioprinted hollow structure at Day 3 and the zoomed images of cells obtained on Day 1, Day 3, and Day 7. (c) Quantitative viability analysis of cells for Day 1, 3 and 7 after bioprinting. Two tail Students t-test was used to analyze the significant change in the cell-viability after bioprinting

process. P-values * < 0.05 were considered as significant. Scale bars indicate 1 mm for (a) and (b) and 0.5 mm for the zoomed images

5.3 Conclusion

We herein developed a composite gel based on PF-RDS as a sacrificial support material for in-gel printing of overhanging complex and hollow structures. Alginate was used as the printing bioink and CaCl_2 was utilized to enhance the viscoelastic properties of the polymer-nanoclay composite gel and as the crosslinking agent for alginate. The effect of different concentrations of PF and CaCl_2 on rheological properties including viscoelasticity, yield, and recoverability showed the potential of our composite structure to be utilized as a supporting material with the ability of long-term storage and reusability. Utilization of PF inside the support-bath resulted in increased tolerance of nanoclay discs over the CaCl_2 content and allowed to dispense less viscous hydrogel with higher shape fidelity at low extrusion pressure, which would be a more cell friendly process. Furthermore, it decreased the time of incubation period in the support-bath that provided enough crosslinking density before removing the fabricated construct. Compared to the previously published studies which used only Laponite for their support-bath[236,246], the printed structures could be harvested easier without significant residues of the support-bath adhered to the structures. Performance of the composite gel as support bath was validated by printing several alginate hydrogel structures. The measured dimension of the recovered hollow structures showed that the height and the angles were well defined. The support-bath did not only allow precise printing of different complex structures but also helped recovery of the structures with high resolution. A diffusion test assessed on a printed branched vascular structure also demonstrated structural integrity and interconnectivity of the channels. NIH-3T3 cell-laden alginate bioprinted inside the support-bath showed homogeneous distribution with above 80% viability within the hydrogel revealed the potential of the composite support structure for a cell friendly bioprinting process and to be further used for various tissue engineering applications.

5.4 Methods

5.4.1 Preparation of PF-RDS support-bath and characterization

PF-RDS support-bath was prepared by slowly adding equal volume of PF-CaCl₂ (Sigma Aldrich) solution into Laponite RDS (BYK Additives & Instruments) suspension. Briefly, PF solutions with 15%, 20% and 25% concentrations were prepared by dissolving in 0.5, 1 or 2% (w/v) CaCl₂ solution at cold room (4 °C) under continuous stirring. A 6% Laponite-RDS solution was prepared by suspending appropriate amount of dry Laponite-RDS powder in deionized (DI) water and vigorously stirring for minimum one hour at room temperature to allow fully exfoliation and dispersion of nanoclay particles with a transparent appearance [236,286]. Then, PF solution was added slowly into Laponite-RDS solution under continuous stirring at 4 °C to obtain final concentrations of 7.5, 10 and 12.5% for PF and 0.25, 0.5 and 1% of CaCl₂ with constant Laponite concentration of 3%. The mixture was further stirred for minimum one hour at 4 °C. The composite material was centrifuged at 4000 rpm for 3 min prior to incubation at 37 °C to remove the bubbles. It is worth to mention that final 2% of Laponite was also prepared and examined but the electrical repulsive forces were not enough to make an ordered array of particles. Hence, the matrix storage and recovery was not appropriate for printing [265,278,280] and it was omitted from further experiments (data not shown). The composite material was stable and could be stored at 4 °C for a long time with no changes in its properties [281]. Based on rheological data, 3% of Laponite-RDS, 10 % of PF, and 0.5% of CaCl₂ concentrations were selected for the support bath formulation.

5.4.2 Rheological measurements

All rheological characterizations were performed on a MCR302 (Anton Paar, Austria) equipped with a Peltier plate for temperature control. A stainless steel parallel plate of 25 mm diameter with a gap distance of 0.5 mm was utilized for all the experiments. A low viscosity silicon oil was used as the solvent trap during the measurements. Rotational and oscillatory measurements were performed to investigate the flow and viscoelastic behavior of the support-baths. Gel yield stresses and linear viscoelastic (LVE) regions were measured by strain sweep from 0.01-100% at a constant angular frequency of 10 rad/s. Oscillatory angular frequency sweeps were carried out within the LVE range (0.6% strain and angular frequency

of 0.1-100 rad/s) to monitor the dynamic rheological behavior. Temperature sweep experiments were conducted from 4-37 °C with 5 °C/min ramp to observe gelation temperature and evolution of the structure's moduli. To investigate the recovery behavior of the support-bath during hydrogel extrusion, cyclic strain test at low and high oscillatory strains of 0.6 and 50% at constant angular frequency of 10 rad/s and 10 s duration per cycle was performed. Shear rate sweeps were conducted to monitor the shear thinning behavior and viscosity changes of the formulations between 0.01-100 1/s.

Samples were incubated at 37 °C for 2 h with a pre-shear rate of 1/s prior to each run. Three measurements were taken for each sample and mean values were reported. The effect of different compositions of PF and CaCl₂ on flow behavior of the support material was investigated. Control groups were selected as CaCl₂-PF named as Control 1 and CaCl₂-Laponite RDS named as Control 2 with different concentrations of CaCl₂. Control 1 contained 10 and 1% for PF and CaCl₂, respectively to observe the effect of Laponite on rheological properties. Control 2 were included constant Laponite-RDS of 3% and 0.125, 0.25, 0.5, and 1% of CaCl₂.

5.4.3 CAD design of complex structures and 3D printing inside support-bath

A customized three axes 3D bioprinter controlled by MACH3 software (Newfangled Solutions) was used to print different structures. Hydrogel solution was loaded into a 10 mL material reservoir equipped with a double thread screwed plastic nozzle (Musashi Engineering, Japan) and material extrusion from the printing head was provided through a pneumatic dispensing unit (Nordson EFD Performus V). CAD models of the constructs were developed in Rhinoceros 6 (Robert McNeel & Associates, USA) and tool paths were generated and transformed into G-codes.

Star shape, grid pattern and branched vascular-like, and a nose shape structure in different scales were printed using 3% (w/v) sodium alginate (Sigma Aldrich) solution prepared in DI water. Star and grid-pattern structures were printed with a 25 Gauge nozzle and vascular-like, and nose shape were fabricated via a 23 Gauge nozzle. For star shape printing, 15 layers of hydrogels were deposited by setting parameters as 140 mm/min print speed and 0.7 bar

feeding pressure. The structure was formed by depositing two concentric contours without any gap in between them. The grid shape of 0-90° zigzag $10 \times 10 \text{ mm}^2$ deposition pattern including 9 stripes with 750 μm gap in between was extruded in each layer with 140 mm/min print speed and 0.7 bar feeding pressure. Branched vascular-like construct was printed at 150 mm/min print speed and 0.6 bar feeding pressure. Nose shape structure was printed with 2.7 cm length and 1.7 cm width using a 25 Gauge nozzle at 130 mm/min print speed and 0.5 bar feeding pressure by three offsetted counters.

Prior to support-bath removal, the structures were post-crosslinked in a 2% CaCl_2 solution for 10 min. Then, residual support-bath materials were removed from the beakers by pipetting 1% cold NaCl solution. To show the presence of lumen inside the structure and impermeability and its interconnectivity, diffusion test was performed by delivering blue food dye solution from one end of the branched vascular structure.

5.4.4 Bioprinting of cell-laden alginate in PF-RDS support-bath

All components of support-bath and alginate were sterilized by autoclaving. Dry powder of PF was sterilized at 105 °C for 30 min as suggested in the previous study to prevent rheological property changes[299]. CaCl_2 and Laponite-RDS were also autoclaved in their powder forms. Then, the support-bath was prepared as explained above. Alginate solution was prepared in 3% (w/v) concentration in 1×PBS and autoclaved at 121°C for 15 min before encapsulating the cells.

NIH-3T3 cells (ATCC) were grown in Dulbecco's Modified Eagle Medium (DMEM, Sigma) supplemented with 10% fetal bovine serum (FBS, Sigma) and 1% penicillin-streptomycin (Gibco) at humidified atmosphere containing 5% CO_2 at 37 °C. The cells with a 1×10^6 cells/mL density were prepared by suspension in 3% alginate solution at room temperature. A 0.5 bar pressure was applied to extrude cell-laden hydrogel from a 30 Gauge nozzle with 150 mm/min print speed. After printing, the alginate structures were washed with 1% ice-cold NaCl solution and DMEM. They were placed into 12 well-plate with fresh DMEM and incubated at the incubator.

5.4.5 Evaluation of in-gel bioprinting biocompatibility

The viability of 3T3 cells-encapsulated in the alginate was evaluated on Day 1, Day 3, and Day 7 after bioprinting. At the end of incubation points, the samples were transferred into glass bottom Petri dishes and washed with 1×PBS. Calcein AM/PI staining was used to evaluate live/dead cells. Briefly, cells were first stained with 1 μ M calcein-AM (Invitrogen, green fluorescence) for 30 min and then, with 0.75 μ M propidium iodide (Invitrogen, red fluorescence) for 5 min in 1×PBS at 37 °C, followed by washing in 1×PBS for three times. The viable cells were monitored with maximum excitation/emission wavelengths of 488/515 nm, respectively while the dead cells were monitored at maximum excitation/emission wavelengths of 561/625 nm, respectively, using inverted confocal microscope (Carl Zeiss LSM 710). 3D images were obtained using tiled z stacks with 5.00 μ m intervals and 2.77 μ m pixel size. The live/dead cells were analyzed quantitatively by using ImageJ 1.48v software.

5.4.6 Statistical Analysis

All values for cell viability and rheological assessments are presented as the mean \pm SD (n=3). Students t-test was used to analyze the significant difference. P values <0.05 and <0.01 are considered statistically significant.

6 Chapter 6. 3D printing of hybrid scaffolds for skin tissue engineering: an investigation on the scaffold's geometry in a hybrid design and its influence on mechanical behavior, cell alignment and morphology

Engineering thick skin tissue substitutes resembling the physiochemical and mechanical properties of the native tissue is a challenge. Vascularization plays a critical role in the success of any tissue scaffold. Melt electrowriting (MEW) is a powerful technique with the potential to fabricate ordered and desired structures with low fiber diameters resembling native tissues. Here, we first constructed three MEW porous structures of polycaprolactone (PCL)with different microstructures including 0-90 and 60-120 degree and a honeycomb-like orientation of fibers which were subsequently cast with gelatin hydrogel crosslinked by visible light, encapsulating human umbilical vain endothelial (HUVEC) and human skin dermal fibroblast (HSF) cells. Structures with various geometries were investigated mechanically and biologically. Mechanical tensile tests revealed that honeycomb microstructure of hybrid PCL/gelatin showed high elongation (121%) until failure and around 6 MPa of elastic modulus which could be used for skin tissues with high stretchability. Morphological observation of cells at different architectures showed that all the structures provided a cell-friendly environment which supported cell growth, distribution, and their metabolic activities. Among those, honeycomb geometry could guide the cells the most and led to the formation of vessel-like structures. The results of this initial study showed a great potential for further analysis of such hybrid designs as a promising candidate for full-thickness scaffolds for skin tissue engineering.

6.1 Introduction

Demands for skin tissue substitutes has increased significantly over the last few decades due to the vast majority of skin lost caused by burns, trauma and diabetic skin ulcers [144]. The possible solutions were initially focused on skin substitutes from xenografts to allografts sources and were followed by development of regenerative medicine with fabrication of skin equivalents from natural and synthetic materials to address the limitations of those traditional treatments [145]. Additive manufacturing technology, also referred to as three-dimensional (3D) printing has come into spotlight owing to its ability to fabricate 3D constructs in a layer-by-layer fashion mimicking native environment at relatively low cost through a rapid process. With this technology, bioengineering of intricate geometrical structures with high precision are fabricated in a reproducible manner [300,301]. A promising tissue scaffold must possess a stiff and fibrous structure mimicking extracellular matrix (ECM) [130] and hydrophilic surface for cells to spread, elongate, and proliferate with interconnected pores allowing transportation of nutrients and oxygen [302]. Although, 3D printing can fabricate scaffolds with highly ordered and controlled nature, the fiber diameters of scaffolds could be large to degrade in a shorter time to allow cells to replace the scaffold. Melt electrospinning writing (MEW) is a combination of extrusion printing, namely fused deposition modeling (FDM), and solution electrospinning [17]. This technique enables accurate control on fiber deposition of FDM by using computer aided design (CAD) modeling hence gives the freedom of adjusting fiber diameter and pore size and at the same time provides micron-scale fibers with the help of high voltage difference without usage of any solvent [45,146]. Besides, final structure will contain interconnected pores that assists nutrients and cell migration. Fabrication of scaffold with filaments at tens of microns resembles ECM structure of the skin and yields a substrate that would guide cells and provides a flexible structure which facilitates further integration with the surrounding tissue [95,303]. Many thermoplastic polymers have been used in MEW of scaffolds for different tissue engineering applications [15]. Polycaprolactone (PCL) is one of the most broadly used polymers because of its biocompatibility, low melting temperature, availability, and good mechanical properties [97] and was already used as a skin scaffold that supported fibroblast cells infiltration [95]. A study by Chong et al. [304] proved that MEW of PCL could provide a structure with high strength and enhanced elasticity suitable for skin tissue engineering. Interestingly, it was demonstrated that the density and stiffness of

structures also influence the vascularization and it was shown that decreasing the density and stiffness would result in enhancement of vascularization [305].

Mimicking the natural tissue microenvironment is an essential criterion for the success of any regenerative approach. Skin is a functional tissue consists of dermis, epidermis, and hypodermis layers with multiple cell types [306]. Numerous studies have worked on bioprinting of skin substitutes using different biomaterials and cells to resemble the skin tissue regarding its structure and mechano-physiological properties. Rimann and coworkers [307] fabricated a multi-layered skin tissue model using different bioprinting techniques. Lee and coworkers [308] biofabricated a functional skin construct using fibroblasts and keratinocytes in a collagen hydrogel in a transwell system that led to formation of stratum corneum. In another study Cubo *et al.* [141] bioprinted a bi-layered skin substitute comprised of human derived skin cells to ensure its functionality. Koch and colleagues [309] bioprinted a skin substitute with dermal and epidermal layer which finally formed a laminin layer at the layers interface. Although these studies revealed promising results for skin tissue engineering, however, they did not consider vascularization in their substitutes. Vascularization is one the most crucial and challenging aspects of 3D printed tissue constructs without which no oxygen, nutrient, and waste would flow. Thus it is impossible to develop thick structures which could survive and function for a long period of time [310,311]. A common approach for vascularization is to provide a pre-vascularized structure *in vitro* by using endothelial cells [312–314]. Studies showed that ordered deposition of endothelial cells would enhance the vascularization [315,316]. In this regard, Pourchet *et al.* [317] developed a full thickness bi-layered skin construct with 5 mm height. Human umbilical vein endothelial cells (HUVECs) were utilized to create vascular channel. Kim et al. [318] developed a perfusable vascularized skin model comprising of epidermis, dermis, and hypodermis component representing a complex skin substitute. A more recent study was done by Baltazar et al. [319] in the same manner of perfutable vascularized skin construct. In these studies, various hydrogels were used for cell encapsulation in a hybrid structure including collagen, blood plasma, alginate, gelatin, Gelatin Methacryloyl (GelMA), poly(ethylene) glycol (PEG) based hydrogel, and fibrin. Different crosslinking mechanisms are utilized corresponding to hydrogel structure. Among these, gelatin gained attention due to its biocompatibility, possessing peptide chains that resemble arginine-glycine-aspartic acid (RGD) amino acid sequences that are cell

adhesion sites which could enhance granulation tissue formation and epithelialization [132]. In addition, gelatin represents the ability to be photopolymerized in several ways showing various degradability and stiffness [7,140]. Crosslinking using radiation in visible light range in the presence of ruthenium (Ru) complex and sodium persulfate (SPS) is an emerging method that manifested favorable results in a non-invasive manner with tailorable crosslinking density and mechanical properties. Moreover, visible light penetration depth is higher compared to UV radiation [320–323]. In this photopolymerization technique, Ru and SPS act as photocatalyst and photoinitiator, respectively. Two mechanisms of crosslinking in such systems are proposed, which are based on generation of radicals from tyrosine groups in gelatin. In this context, Ru³⁺ ions formed through oxidative quenching of Ru complex initiate the radical formation [324]. Visible light crosslinking of gelatin hydrogels facilitates a more cell friendly application of photocrosslinking, with the potential to be integrated as a biofabrication strategy.

Microstructural design of the scaffolds is another key objective in scaffold's fabrication that is mostly being neglected. Although, several studies revealed that geometrical cues not only affect the mechanical properties, it also regulates biological responses such as cell alignment and signaling, cell fate and their functionalities [325–328]. However, most of these works are focused on bone and cartilage tissue engineering [329–331]. Regarding the effect of structural architecture on vascularization, Nikkhah et al. [332] showed that fabrication of various micropatterns of endothelial cells embedded within GelMA hydrogel guided their proliferation, alignment, and finally led to formation of a cord-like structure which is necessary for primary steps of vascularization. Similarly, Zhu et el. [333] reported a micro-aligned electrospun fibrous scaffold with a potential for blood vessel formation. A more recent study by Yao et al. [327] revealed the effect of structural architecture on morphogenesis of endothelial cells. They found that a honeycomb geometry could guide the cells to form tubular structure as prevascularization step. This phenomenon could be used to manipulate cellular behavior for desired applications.

Herein, in this study we aim to investigate the effect of various geometries including a 0-90 degree mesh-like, 60-120 degree mesh-like, and a honeycomb structure fabricated through melt electrowriting on cell alignment, morphology and vascularization as a preliminary study

of a thick and vascularized skin substitute. To do so, a hybrid structure of PCL/cell laden gelatin hydrogel was prepared and examined. Human skin fibroblasts (HSFs) and HUVECs were co-cultured within the hydrogel and it was cross-linked through type II photo initiation mechanism with two initiators of Ru and SPS in a visible light range. Moreover, melt electrowritten PCL scaffolds were treated with sodium hydroxide (NaOH) to improve its hydrophilicity. In addition, mechanical properties of the scaffolds with and without hydrogel were assessed. The results revealed that honeycomb structure enhanced cell alignment that could induce the formation of cord-like structures which in the presence of appropriate biochemical cues, would assist further vascularization. Honeycomb architecture had the most effect on cell orientation, followed by 60-120 and 0-90 mesh structures. However, all ordered structures could facilitate the formation of cord-like structures. Tensile test showed higher axial elastic modulus for 0-90 mesh structure, followed by honeycomb and with a drastic decrease, 60-120 mesh had the lowest value. Compared with the other mesh designs, the honeycomb structure demonstrated significantly higher elastic work with high elongation at break.

6.2 Materials and Methods

6.2.1 Materials

PCL Capa 6400 (molecular weight of 37,000 g/mol) was acquired from Capa Perstorp Ltd, UK. Sodium hydroxide (NaOH), gelatin type B, tris (2,2-bipyridyl) dichlororuthenium (II) hexahydrate (Ru), and SPS were purchased from Sigma-Aldrich. HUVECs, HSF, Eagle's Minimum Essential Medium (EMEM), basal culture medium were bought from ATCC. Pen-Strep (10,000 Units/ml penicillin, 10,000 µg/mL streptomycin) was obtained from Gibco, UK. Phosphate buffered saline (PBS) tablets were obtained from MP Biomedical, France.

6.2.2 CAD modeling and scaffold fabrication via MEW

Algorithms of continuous printing path for three different structures including mesh with 0-90 degree, and 60-120 degree orientations, and a honeycomb shape were developed and converted to G-codes using Python script. G-codes were loaded in MACH3 motion controller software (Newfangled Solutions). Melt electrowriting setup was a custom-made platform developed on the basis of a 3D-axis printer explained previously [17]. It consisted of two

heating units controlled with Arduino Mega microcontroller, and a 10 mL syringe and a 250 μm diameter nozzle mounted on the print head, an air dispensing system (Musashi Engineering Inc., Japan) and a high voltage generator (Gamma High Voltage Research, FL). The collector was grounded, and the nozzle was connected to high voltage generator. A schematic representation of the process is illustrated in Figure 6-1.

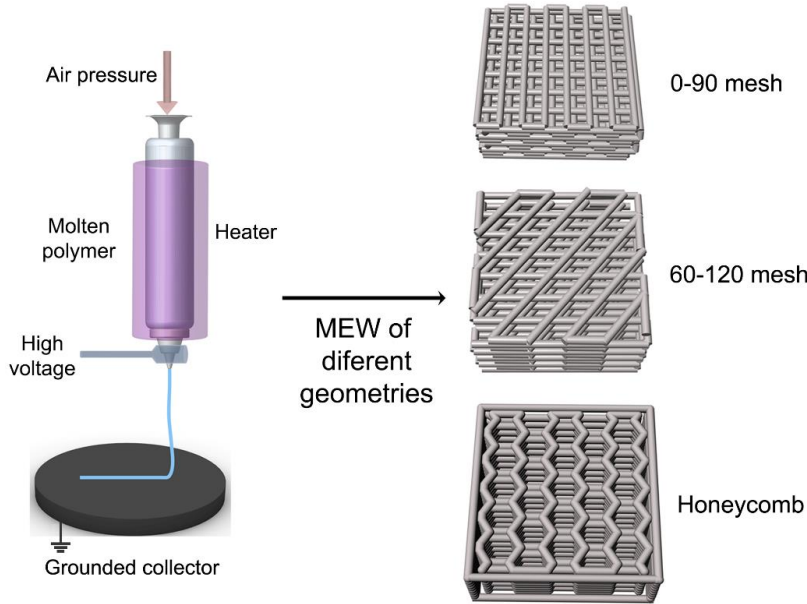


Figure 6-1. A schematic representation of melt electrowriting of structures with different geometries

For each scaffold's design, printing parameters such as feeding pressure, voltage difference, print head speed, and the distance between nozzle tip to the collector were carefully examined to acquire straight and homogeneously deposited fibers. The interdependence of printing parameters on fiber diameter and structural integrity was considered as well. Selected parameters are presented in Table 6-1. Heating temperature was set to 90 °C for all the samples. PCL pellets were poured into the syringe and heated for 2 hours prior printing. Fiber spacing and structural height were 0.8 mm and 1 mm, respectively. Melt electrowritten structures were fabricated at 20 × 20 mm and were cut to 7 × 7 mm pieces using a punch. A challenge for melt electrowriting is to stabilize polymer jet until deposition on the collector, especially for printing large volumes. As the polymer seats on the collector, it interferes with electrical conductivity between collector and nozzle tip. To overcome that

issue, we covered the collector with a flat glass, and it reduced polymer jet instabilities. In addition, for honeycomb structure dynamic printing parameters were selected as shown in Table 6-1. It should be noted that to prevent instable deposition of fiber at the beginning and to reach a balance among processing parameters, printing started after 2 min of polymer extrusion under high voltage.

Table 6-1. Printing parameters for MEW of different geometrical structures

Scaffold type	Printing parameters				
	Printing speed (mm/min)	Feeding pressure (bar)	Nozzle and collector distance (mm)	Acceleration voltage (kV)	Number of layers
0-90 mesh	110	0.4	1.8	4	20
60-120 mesh	130	0.5	2	4	22
Honeycomb	80-95	0.4-0.5	1.7-2.1	4-5	16

6.2.2.1 Sodium hydroxide treatment for enhancing hydrophilicity

Melt electrowritten PCL scaffolds were treated with NaOH to introduce hydroxyl and carboxylate groups to the polymer that would improve their hydrophilicity and simultaneously increase the surface roughness [334]. The scaffolds were immersed in a 1N NaOH solution for 2 h at room temperature and then washed extensively with deionized (DI) water and PBS until the pH of the solution became neutral.

6.2.3 Mechanical testing

Mechanical properties of the PCL scaffolds possessing various geometries were analyzed under uniaxial tensile test using a Zwick/Roell-Z100 universal testing machine (UTM). Rectangular shaped samples ($n=5$) with dimensions of 50×10 mm were cut from a large structure and were analyzed in longitudinal direction. A 200 N load cell with pneumatic grips was equipped for the tests and grip-to-grip distance was set to 35 mm with pre-load of 5 kPa to ensure the straightness of the structure before running the test. Each measurement was done at 2 mm/min until 80% of the maximum force. Elastic moduli of the samples were calculated from the linear region of the engineering stress-strain graph acquired from the test. Hybrid

samples were analyzed directly after crosslinking to prevent their dehydration. To ensure the fixation of hybrid structures to the machine grip, ultrafine sandpapers were used at the attachment point of samples and grips.

6.2.4 Cell-laden hydrogel preparation

Gelatin type B was used as a candidate hydrogel for this study. Gelatin is denatured form of collagen with non-antigenicity and better mechanical and degradation properties compared to collagen [335]. Possessing RGD sequences and resembling natural ECM, it creates an environment which not only provides cell-cell interaction, but also facilitates cell-matrix interaction [336]. A photo initiation process with the presence of Ru and SPS as photoinitiator and crosslinker within visible light range was performed. Gelatin, Ru, and SPS were prepared in PBS at the concentrations of 10 % (wt/vol), 20 mM, and 10 mM, respectively, according to Advanced BioMatrix protocol. It should be noted that higher concentrations of SPS was showed to have no toxic effect on cells if used for crosslinking [337]. Gelatin was first dissolved in autoclaved PBS and mixed at 40 °C for 1 h. Ru and SPS were dissolved in DI water and vortexed thoroughly. All the solutions were sterile filtered using 0.22 µm filter (Minisart).

HSFs were used as skin representative cell type, and at the same time it also induces the formation of capillaries from HUVECs [338]. In fact, fibroblast cells would provide a mechanical support by secretion of their ECM which assist the proliferation and maturation of endothelial cells that eventually lead the vessel formation [339,340]. HUVECs and HSFs were extracted at the number of 1×10^6 cells/mL for both cell types and mixed. Gelatin hydrogel was kept at 37 °C during the whole process. Hydrogel was prepared by addition of Ru and SPS with thorough mixing. Then it was mixed with cell extract with pipetting for a complete mixing.

6.2.5 Hybrid scaffolds preparation

Melt electrowritten scaffolds that were cut and treated with NaOH were sterilized by 15 minutes immersion in ethanol (70%) and 20 minutes of UV exposure for each side. A sterile

mold consisting of series of 7×7 mm and 2 mm height cavities covered with aluminium foil was used for scaffold fabrication. PCL structures were placed in molds of and cell-laden hydrogels were dispensed within each scaffold at the same volume. Directly after casting, hydrogels were photo crosslinked with 2 white LED lamps of 100 W at the distance of 40 cm for 2 minutes. Hybrid scaffolds were then transferred in cell culture plates and stored in a humidified incubator at 37 °C with 5% CO₂ for further analysis. The cells were cocultured in a mixed media of EMEM and basal culture medium with a ratio of 1:1 and every 2 days medium were changed. Figure 6-2 shows a schematic representation of hybrid scaffold fabrication.

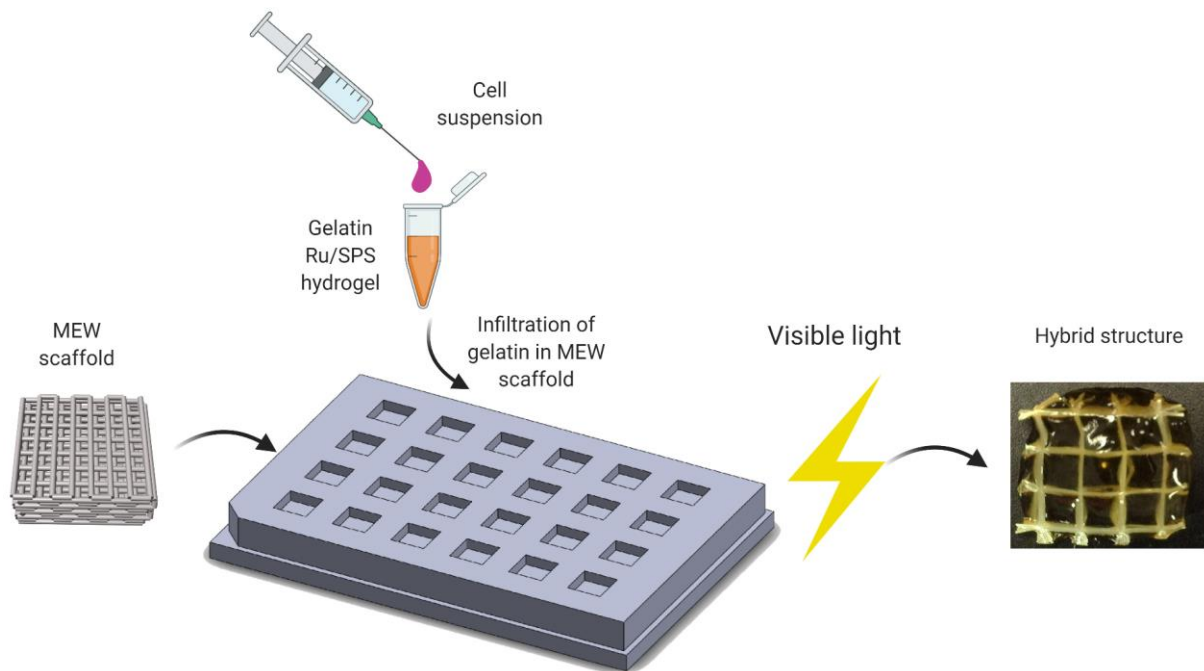


Figure 6-2 Schematic representation of scaffold fabrication; From MEW of PCL scaffold to hybrid structure

6.2.6 Morphological and structural characterization

Morphology of the fabricated structures through MEW was investigated with a Dino Lite digital microscope and a field emission gun scanning electron microscope (FE-SEM, Zeiss Leo Supra VP 35) at accelerating voltage of 4 kV. The samples were coated with gold particles using Cressington 108 sputter coater prior imaging with SEM. The surface roughness

of PCL filaments was also characterized and samples with and without treatment were compared.

6.2.7 Cell viability and morphology

Cellular viability in the hybrid scaffolds at day 1, 3, 7, and 14 were characterized by treating the scaffolds with fluorescent staining kit according to the manufacturer's instruction. Calcein-AM (Invitrogen, green fluorescence) was used to stain live cells appearing in green and propidium iodide (PI) (Invitrogen, red fluorescence) to label dead cells in red. Scaffolds were stained in PBS solution containing Calcein-AM for 30 min at 37 °C followed by a washing step with PBS and treating with PI solution for 5 min at 37 °C and finally washing with PBS.

To observe the morphology of the encapsulated cells, after one week of incubation, they were fixed in 4% paraformaldehyde for 30 min and washed three times with PBS. Cell membranes were permeabilized with 0.1% Triton-X 100 in PBS for 10 min and washed. Samples were stained in red fluorescent Alexa-Fluor 568 phalloidin conjugate (Abcam, UK) for F-actin staining for 1 h at room temperature while protected from light and washed with PBS. Nuclei of the cells were stained with 4',6-diamidino-2-phenylindole (DAPI) for 15 min and washed with PBS. All the procedures took place at room temperature. Subsequently, tiled z-stacks and z-stacks of the structures were captured by a Carl Zeiss LSM 710 laser confocal microscope for observation of live/dead cells and cellular morphologies, respectively. Percentage of viable cells for day 1 were calculated as the following equation:

$$\% \text{ viable cells} = (\text{Number of live cells}/\text{Total cell numbers}) \times 100 \quad (1)$$

6.2.7.1 Statistical analysis

For swelling ratio and cell study test 4 replicates were used. Mechanical tensile test was performed with 5 replicates. Student t-test was carried out in GraphPad Prism 5. Differences were considered significant with a p value of smaller than 0.05. * indicates $P < 0.05$, ** $P < 0.01$, and *** $P < 0.001$. Data are represented as mean \pm standard deviation.

6.2.8 Results and discussion

6.2.8.1 MEW of scaffolds with various geometries

MEW is a benchmark for scaffold fabrication enables to reduce fiber diameter to a few or tens of microns with orderly controlled filament deposition [341]. However, technical challenges are still remained to be addressed and developed for long processes with complex architectures and high layer numbers. To adaptively control the polymer jet during printing, dynamic parameter optimization could be utilized as explained by Jin et al [341]. Here we created tool path planning for three different structures with various geometries aiming to investigate the effect of fibers direction in cellular alignment and morphology which could result in lumen structure formation for vascularization as a critical factor of volumetric structural design.

6.2.8.2 Mechanical analyses of the scaffolds

A uniaxial tensile stress was performed to observe both the geometrical effect and the presence of hydrogel on elastic modulus, and elongation at break. Elastic modulus and elastic energy are of significant importance for the skin tissue substitutes as they will be subjected to axial tensile force and depending on the target location in the body, these properties would vary. The stiffness values of the structures were calculated from the slope of linear region of stress-strain graphs. As explored earlier in a number of studies [15,342], reinforcement effect of fibrous structures for soft network hydrogel is expected. Hence, hydrogel samples were not characterized separately as the control group. Various geometries with and without hydrogel were investigated and the results including the stress-strain graphs, and their elastic moduli are shown in Figure 6-2. Honeycomb and 0-90 mesh structures showed similar mechanical properties compared to 0-60 mesh structure. Their elastic moduli (E), elastic energy (U_{elastic}) which was calculated from the area under the stress-strain curve at linear deformation, and elongation at failure (ϵ_f) are presented in Table 6-2.

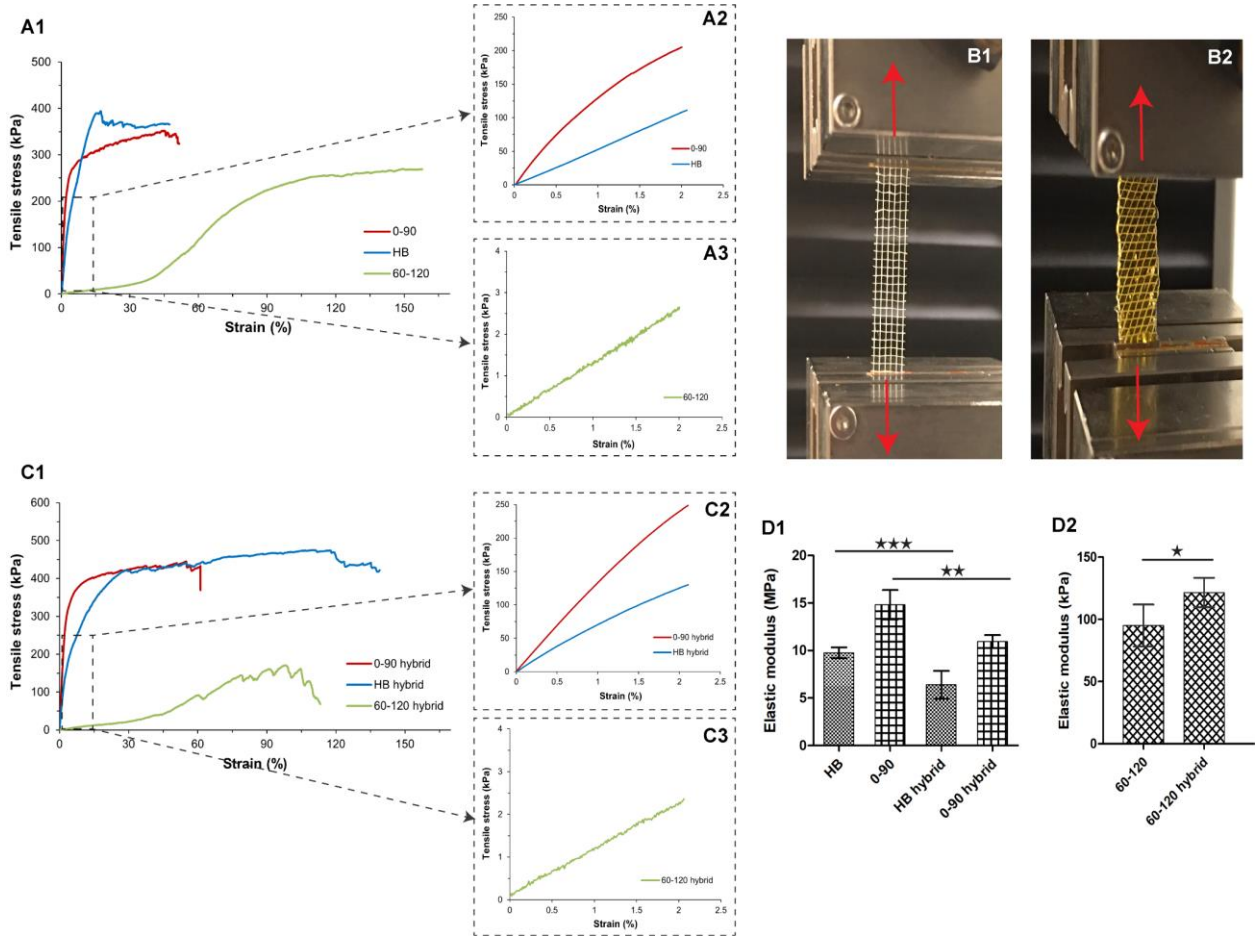


Figure 6-3. Mechanical properties of the fabricated scaffolds. Representative stress-strain curves of scaffolds with different geometries for A) PCL and C) PCL-hydrogel. Insets showing strain values up to 2%. B1) 0-90 scaffold and B2) hybrid 60-120 scaffold under uniaxial strain. D1) and D2) showing elastic modulus values of all the structures

The highest values of elastic modulus were observed in 0-90 mesh, then honeycomb and finally 60-120 had much less stiffness (Figure 6-3-D). A comparison between the young's moduli of samples with different internal architecture implies that those with 0-90 mesh microstructure had the highest elastic moduli, while they failed without experiencing much plastic strain. This could be due to having the fibers fully in the direction of applied load, and the perpendicular joints which restricted further movement and plastic yield of the structure. The same pattern was observed for samples with honeycomb geometry. Although they showed less steep slope in the elastic region (Figure 6-3-A2) that is because of their inclined fibers with respect to the applying force which gives them more stretchability compared to 0-

90 mesh [128]. A rapid increase of stress was observed in 0-90 mesh as their tight fibers were not that flexible in lateral direction (Figure 6-3-A1, -C1) [127]. Moreover, 0-90 mesh entered plastic region in a much slower strain value compared to honeycomb structure. It can be on the basis of the same logic of its structural ability which could withstand more elastic deformation in both elongated direction and perpendicular to elongation [128]. On the other hand, samples with 60-120 mesh structure showed much lower elastic modulus, while withstanding a very large plastic strain up to 120%. This is due to the fact that 60 and 120 degree orientation of fibers with respect to the applied force direction on one hand resulted in gradual rearrangement of the structure in the beginning of loading, while the stretching of the junction points of the fibers in the direction of applied force allowed for more plastic deformation of the structures without significant failure in load bearing fibers. Also, 60-120 mesh yielded at higher strain values in comparison with 0-90 mesh and honeycomb structure. Interestingly, hybrid structure enhanced the plastic deformation of both honeycomb and 0-90 mesh structures (Figure 6-3-D1). In other words, incorporation of hyperelastic hydrogel within the matrix resulted in force distribution from stiff fibers to soft hydrogel that caused more deformation upon failure [123]. In contrast, hybrid sample with 60-120 fiber orientation experienced an elevation in elastic modulus (Figure 6-3-D2). It could be due to the fact that only PCL structure possessed elastic modulus in the same order with hydrogel itself, hence introducing hydrogel within the specific orientation of fibrous structure resulted in load transfer to both soft and hard matrix and subsequently increasing of elastic modulus [343]. Moreover, the failure in plastic region happened at lower strain values for hybrid samples with 60-120 structure. It is speculated that lateral expansion capacity of hydrogel compared to fibrous mesh at plastic region is lower, thus causing the rupture of hybrid structure at lower displacements (Figure 6-3-C1) [9]. Energy of the elastic region was also calculated from the integration of the elastic region of the stress-strain curve from strain zero until it passed the linearity. As the data represents (Table 6-2), elastic energy of 0-90 mesh and honeycomb samples decreased for hybrid forms with the same trend as the elastic modulus values. However, energy stored in 60-120 structure in the elastic region enhanced strongly (almost 5-fold). Indeed, the final mechanical properties of such complex samples are strongly affected by structural properties such as fiber diameter and fiber distancing, porosity, fiber orientations, structural side length, and the number of layers. Therefore, compared with other

studies the results could be different. This variety of properties provides a potential in designing the structures according to the desired application and tissue properties. It should be mentioned that skin is a heterogeneous tissue with a wide range of mechanical properties including elastic modulus, and elongation at failure [336]. Thus, these variety of results could be a benefit for different skin parts of the body.

Table 6-2. Mechanical properties of the scaffolds obtained from tensile test

	Structures					
	Only PCL			PCL/hydrogel		
	0-90	60-120	Honeycomb	0-90	60-120	Honeycomb
E (MPa)	14.54 ± 1.58	0.095 ± 1.31	9.76 ± 0.51	10.95 ± 155	0.12 ± 1.17	6.40 ± 1.32
U _{elastic} (kJ/m ³)	106.10 ± 4.0	7.43 ± 2.1	174.71 ± 3.4	82.33 ± 4.7	37.13 ± 3.6	121.37 ± 5.2
ε _f (%)	51.5 ± 2.8	242 ± 4.4	46.48 ± 2.6	61.2 ± 3.8	113.1 ± 2.4	138.2 ± 4.5

6.2.8.3 Morphological observations of the scaffolds

Scaffolds for cell study and mechanical property characterization were fabricated via MEW and then infiltrated with hydrogel encapsulated with HUVECs and HSFs. Their morphologies and structural integrities were observed with a digital camera and a Dino Lite digital microscope (Figure 6-4).

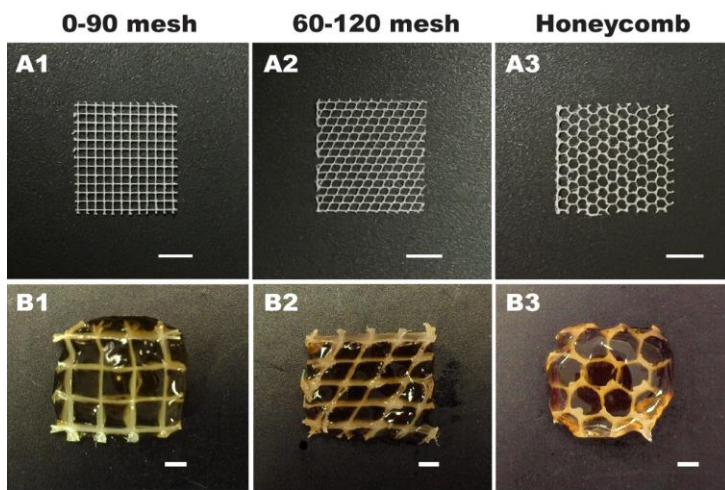


Figure 6-4. Digital images of the scaffolds. A) Melt electrowritten structures before cutting. Scale bars: 5 mm. B) Hybrid structures fabricated by injection of cell-laden hydrogels within the fibrous scaffolds. Scale bars: 1 mm

Furthermore, structural integrities of melt electrowritten samples were analyzed via SEM in a tilted view (Figure 6-5-B) and fiber diameters were calculated by ImageJ software. Reported data is an average of 40 randomly selected fibers from various points of fibers near and far from joint points. Fiber diameter for 0-90 mesh, 60-120 mesh, and honeycomb were 79.81 ± 3.93 , 80.20 ± 6.53 , and 116.11 ± 9.10 , respectively. It should be noted that the honeycomb structure had higher standard deviation value due to its geometrical complication which has several short turns that would cause more changes in filament diameter compared to mesh structures.

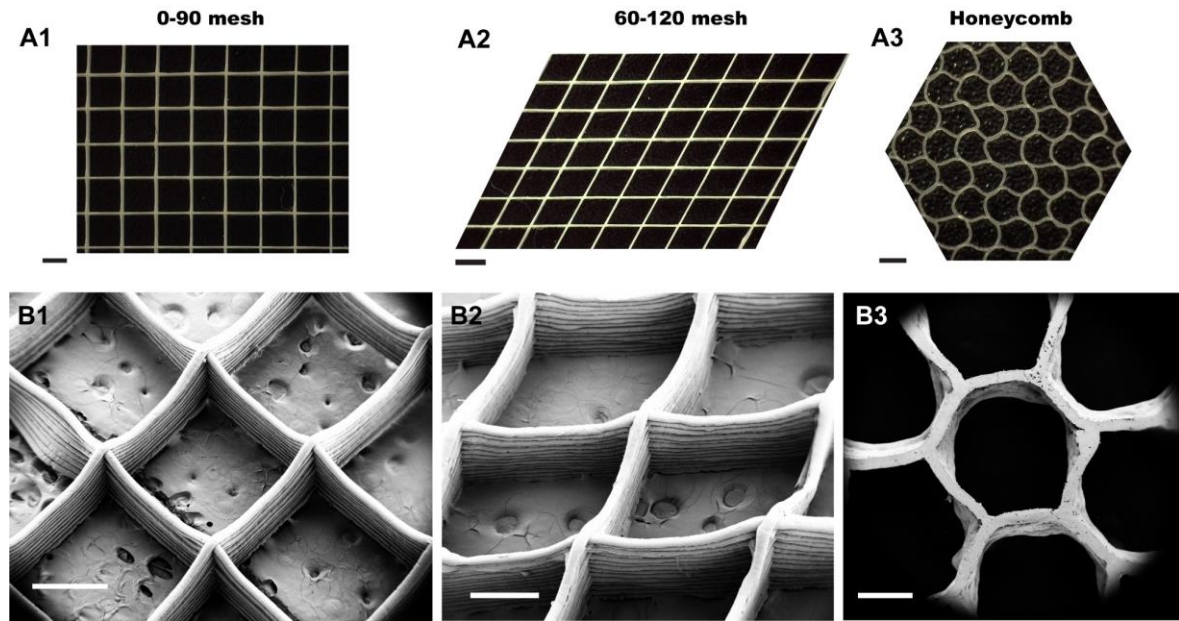


Figure 6-5. Images of the melt electrowritten scaffolds. A) Digital microscopes and B) SEM images. Scale bars in A and B: 1 and 0.5 mm, respectively

6.2.8.4 Cell viability and morphological analysis

To study the effect of geometrical cues and fiber orientations on cellular alignment that would consequently cause the formation of lumen structure as an initial stage of vascularization, 0-90 and 60-120 mesh and a honeycomb structures were melt electrowritten and treated with NaOH to enhance their hydrophilicity. Structures were infiltrated with HUVECs and HSFs encapsulated in gelatin hydrogel in a mold with series of cavities manufactured for this experiment. HUVECs and HSF were selected as representative endothelial cells for vascularization, and dermis abundant cells, respectively. The structures were cultured in a static environment for two weeks and at day 1, 4, 7, and 14 were stained with Calcein-AM/PI assay for live/dead analysis. In addition, at day 7 their cytoskeleton and nuclei were stained with F-actin/DAPI for detailed morphological analysis. Figure 6-5 shows confocal images of the scaffolds stained with Calcein-AM/PI.

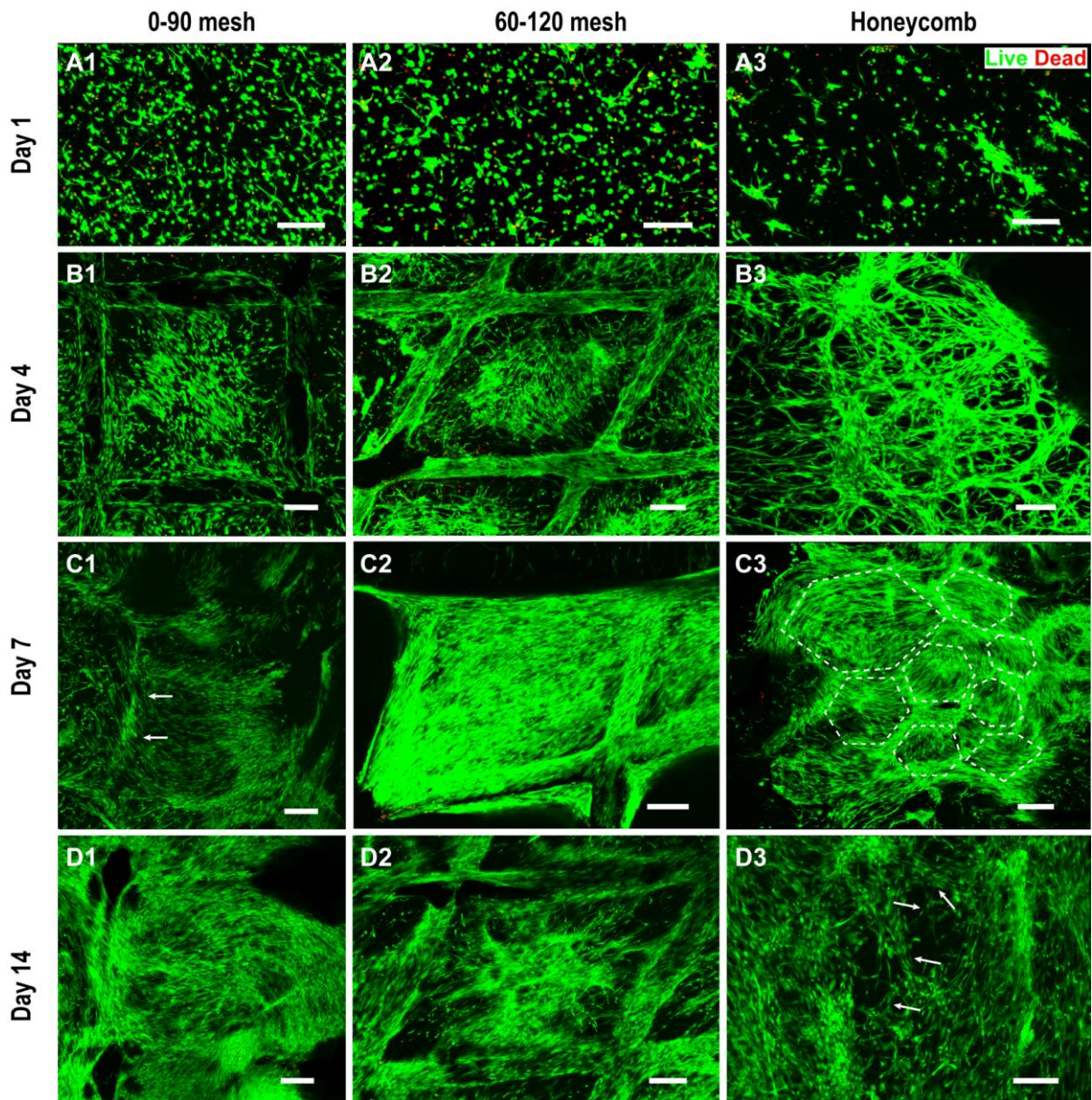


Figure 6-6. Representative confocal images of 0-90 mesh, 60-120 mesh, and honeycomb hybrid scaffolds stained for Calcein-AM (green) and PI (red) at A) day 1, B) day 4, C) day 7, and D) day 14 of incubation. Scale bars are 200 μ m

Cell viability for 0-90 mesh, 60-120 mesh, and honeycomb structure were $83 \pm 2.5\%$, $80 \pm 3.8\%$, and $77 \pm 4.3\%$, respectively. As can be seen from Figure 6-6, after one day of incubation, the number of dead cells dropped to almost less than 5% and cells started to spread throughout the whole structure for all the geometries. The hydrogel environment was cell friendly and soft enough for the cells to start their metabolic activities and spread through

the scaffolds at day 1 (Figure 6-6A). These morphologies would assist HUVECs to start to form a cord-like structure for vessel formation [344]. Cells in the honeycomb structure were not as dispersed as the other two scaffolds at day 1 and they formed small colonies rather than spreading which could be attributed to the higher distance between stiff PCL filaments (Figure 6-6-A3). As expected, one day of incubation is not enough for cells to be guided by morphological cues. But after day 4, they were aligned by the architectures of the ordered scaffolds (Figure 6-6-B&C). It is known that fibroblast cells would like to migrate to a relatively stiff structure to attach and proliferate [345], hence it is speculated that HSFs were mostly attached to the PCL walls (Figure 6-6B) and proliferated faster and could result in formation of cord like structures [339]. By proceeding the incubation time, number of cells increased extremely, and cell alignments were tuned by geometrical factors. After one week of incubation, it is clearly seen that cells started to align on the architecture of ordered scaffolds (Figure 6-6C). However, 0-90 mesh structure did effectively guided cells as on the left vertical length of the PCL filament (Figure 6-6-C1 shown by white arrows) and they formed an inclined direction. This is not the case for the other two structures as the Figure implies (Figure 6-6-C2&C3), the general rhombus can be visualized for 60-120 mesh and in the honeycomb scaffolds the cells were aligned in rounded shape on the PCL fibers. Interestingly, small polygons were also formed within the hydrogel part showed with white dashed polygons in Figure 6-6-C3. This small polygon formation with dense cell population at the sides would subsequently facilitates the cord-like structure formation [327]. At two weeks of incubation, honeycombs structure showed vessel-like structures mostly at hydrogel matrix (pointed with white arrows in Figure 6-6-D3) with some empty spaces which could provide space for vessel formation. It was confirmed that co-culture of cells would facilitate this cord-like formation [344]. Yet, cells in the mesh scaffolds were not guided to any preferred orientations and rather are randomly aligned (Figure 6-6-D1&D2).

To determine geometrical influence of the scaffolds on cellular alignments and morphologies, phalloidin (red)/DAPI (blue) staining were performed at day 7 of incubation. As shown in Figure 6-7, cells on mesh structure with 0-90 degree alignment were mostly spread along the scaffold without any preferred orientation. 60-120 mesh showed more cells on the PCL walls and within the hydrogel part cells were aligned influenced by fiber's angle. However, for the honeycomb structure, cells were spread more selectively with more tubular

structure which could further form vessels. Our results corroborate previously published studies on topographical effect on cellular alignment [327,339]. These results suggest the potential of using honeycomb structure as a scaffold which could facilitate vascularization for skin substitute especially for thick constructs. Although more thorough studies and characterizations are needed to completely prove the potential of a structure which lead the vessel formation such checking with endothelial markers, exploring the effect of fiber diameter, length, and fiber spacing.

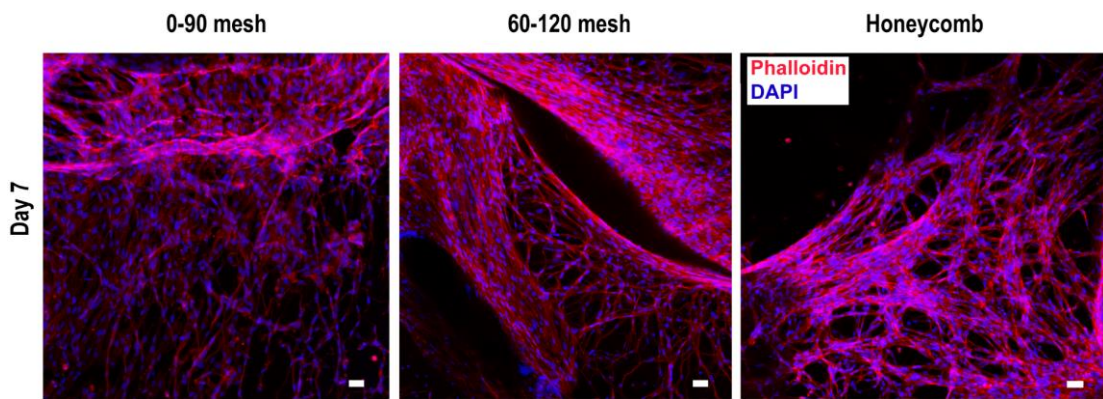


Figure 6-7. Fluorescence images of 0-90 mesh, 60-120 mesh, and honeycomb structures stained for F-actin (phalloidin: red) and nuclei (DAPI: blue) at day 7 of incubation. Scale bars are 50 μm

Based on cellular responses, we could conclude that all the structures provided an environment for the cells with high viability percentage and homogeneous cell distribution through the whole structure. Recently, number of studies with the focus on the geometrical cues on cell morphology for vascularization and tissue formation are increased [128,129,327,339]. However, these studies mainly fabricated small volumetric substitutes in z-direction (at most 300 μm), whereas our confocal image evaluations which were performed in z-stack at high z-increment ($>500 \mu\text{m}$), proved the penetration and infiltration of the cells in z-axis without precipitation at the bottom or floating mostly on the surface of the scaffolds.

Considering the structures height (~1 mm), hydrogel structure allowed penetration of oxygen and nutrient which resulted in cell distribution with high cell number and high metabolic activities. No hydrogel contraction was observed after two weeks of culture, owing to the mechanical support from stiff fibrous PCL.

6.3 Conclusion

Here we aimed to investigate the effect of geometrical hybrid structures on mechanical and cellular behavior of thick skin substitutes. First, we fabricated three PCL structures of 0-90 mesh, 60-120 mesh, and a honeycomb structure via melt electrowriting with 1 mm height. Then gelatin hydrogel with Ru/SPS complex encapsulated with HUVECs and HSFs were infiltrated the porous structures and crosslinked by visible light. Mechanical properties including elastic modulus, elongation at failure and elastic energy were calculated and compared for all the structures. The honeycomb geometry showed high elastic modulus and elastic energy as well as high strain values upon failure. *In vitro* studies revealed successful distribution of cells with high percentage of viability and metabolic activities for all the constructs geometries. Cellular alignment results suggested the potential of honeycomb structure in guiding of co-cultured cells to form vessel-like structures more than the other two mesh structures, followed by 60-120 mesh with less effect on orientation and cord-like formation. These findings could be used as a preliminary study for selection of scaffolds structure for skin tissue substitute which could facilitate vascularization. More characterization is required to confirm the exact effect on vascularization and the effect of more scaffold's properties such as filaments diameter and length, fiber spacing, and several other angles of fiber joints could be investigated for future.

7 Chapter 7: 3D Fiber Reinforced Hydrogel Scaffolds by Melt Electrowriting and Gel Casting as a Hybrid Design for Wound Healing

This chapter was submitted to the journal of Advanced Healthcare Materials as a research article.

Emerging biomanufacturing technologies have revolutionized the field of tissue engineering by offering unprecedent possibilities. Over the past few years, new opportunities arose by combining traditional and novel fabrication techniques, shaping the hybrid designs in biofabrication. One of the potential application fields is skin tissue engineering, in which combination of traditional principles of wound dressing with advanced biofabrication methods could yield more efficient therapies. In this study, we develop a hybrid design of fiber reinforced scaffolds combined with gel casting and asses the efficiency for *in vivo* wound healing applications. For this purpose, three-dimensional fiber meshes produced by melt electrowriting were selectively filled with photocrosslinkable gelatin hydrogel matrices loaded with different growth factor carrier microspheres. Additionally, the influence of inclusion of inorganic bioactive glass particles as a composite fibrous mesh was evaluated. Qualitative evaluation of secondary wound healing criteria and histological analysis showed that hybrid scaffolds containing growth factors and bioactive glass enhanced the healing process significantly, compared to the designs merely providing a fiber reinforced bioactive hydrogel matrix as the wound dressing. This study was aimed at exploring a new application area for melt electrowriting as a powerful tool in fabrication of hybrid therapeutic designs for skin tissue engineering.

7.1 Introduction

Wounds caused by trauma, burns and the diabetics could be intractable to treat or even be fatal [140,346]. Healing is a complex process consists of four consecutive cascaded phases that are generally followed at specific timings and stages [164,347]. The inherent hierarchy of this multiple-stage development will result in restoration of the initial tissue functionality, structural integrity (e.g. formation of extracellular matrix (ECM)), proper migration of keratinocyte and fibroblast cells as well as growth factors [144,348,349]. In the case of delayed chronic or acute wounds, the healing will proceed at a slow rate, and fast wound closure to prevent inflammation mainly causes the connective tissue namely “scar” formation. This will hinder further recovery and in some cases, degradation of ECM will impair the healing process [350,351].

So far, different strategies have been utilized to improve the healing process. A conventional method mostly used for burns is autologous skin grafting which is limited by the weak mechanical strength, vulnerability to infection, sparse donor sites, and creation of additional injury that might require post-surgery treatments [144]. On the other hand, wound dressings or scaffolds would be the alternative candidates for assisting healing process. The rules of thumb in selection of scaffolds for wound healing include the biocompatibility, biodegradability, multifunctionalities to accelerate the healing processes, and the ability to integrate with the host tissue while the mechanical integrity is preserved. In addition, design criterion of scaffold is a three-dimensional (3D) structure with interconnected pores to allow oxygen/nutrition flow and vascularization and at the same time a protective layer to shield the wound [350,352–354]. To meet all these demands, a wide range of biomaterial scaffolds from synthetic or natural sources with different structures and architectures have been investigated [144,164,355,356]. In this respect, hydrogels are a favorable class materials due to their water-rich hydrophilic nature, high porosity allowing rapid oxygen and nutrient through, degradability, and tunable cell/protein absorption [357–360]. Among them, gelatin is a readily available collagen-based biocompatible and biodegradable hydrogel that has been vastly used in tissue engineering applications. Moreover, it shows relatively low antigenicity in comparison with collagen directly derived from an animal source [337,356,361,362]. The high degree of biocompatibility and its chemically rich structure suggest gelatin as a candidate

scaffolding hydrogel. However, weak mechanical properties, reversible thermo-gelling behavior, and rapid degradation rate limit the respective applications [363]. Several approaches were employed to overcome these limiting factors, which are mainly focused on using an additional crosslinking mechanism, including physical, chemical, or photochemical processes [364,365]. However, most of the crosslinking mechanisms are based on the formation of radicals attacking the backbone or pendant groups of polymer chains. Formation and presence of these radicals is often accompanied by increased chemical stress on living cells and enhanced risk of cell death [363,364]. Considering the involved risk of cytotoxicity, there is a trend in the literature to employ more efficient and less harsh crosslinking mechanisms, and to benefit from the rich chemical nature of gelatin with maximized viability of encapsulated cells [323,366,367]. Among them, photo-crosslinking by using low energy (visible) light has gained much attention during recent years [132,321,322,368–370]. This approach can provide rapid crosslinking of gelatin hydrogels while the concerns about the potential damage induced by high-energy light sources like ultraviolet (UV) would be minimized. Photopolymerization reactions involving ruthenium (Ru) metal complexes as photocatalysts are highly efficient with low cytotoxicity, which can be initiated by visible light and progress rapidly in very short times. Previous studies have highlighted the potentials of Ru complexes in crosslinking of gelation scaffolds, while compared to the UV based crosslinking approaches, an improvement in biocompatibility and mechanical properties of hydrogels were observed [320,322,323,371,372]. In addition to gelatin, this approach was also employed in crosslinking of other biomaterials containing tyrosine residues such as fibrinogen, poly(vinyl alcohol), and peptide based hydrogels which showed enhanced bioactivity and mechanical properties [373–376].

Although the cell-friendly nature of soft hydrogels could aid the development of functionalities of cells *in vitro*, the limitations arising from the relatively low mechanical stability of such biomaterials *in vivo* should be addressed. Fabrication of composite materials and structures that can overcome the shortcomings of the individual components and imposing the synergistic effects serves as an efficient route to expand the performance and application window of biomaterials. In such a way, micro- and nanofiber-reinforced hydrogel structures demonstrated enhanced translational potential of hydrogels, as well as improved mechanical and functional properties [15,342,377–379]. Strategies based on enhancement of

the mechanical rigidity of the hydrogels are of special interest, considering the known issues on mechano-biocompatibility of hydrogel biomaterials such as gelatin [363]. To overcome the weak mechanical properties of hydrogels and retain the shape fidelity and integrity, they can be used within a porous polymeric structure from a stiff and at the same time biocompatible material. Composite hybrid structures can resemble and simulate the biological functions of native soft tissues and provide the hierarchical and morphological cues to induce the specific growth and differentiation of cells. Poly caprolactone (PCL) is a synthetic biocompatible and biodegradable polymer with good mechanical properties to mimic the ECM structure and has been used in numerous studies in tissue engineering as well as wound healing applications [164,356,358]. Application of such hybrid design of scaffolds based on a natural biocompatible hydrogel and a thermoplastic polymer mesh would be an interesting approach in wound healing, since the polymeric porous scaffolding architecture can enhance the mechanical properties of the composite structure [122], while the tension forces applied on the skin can be transferred well within the matrix. Melt electrowriting (MEW) as a rapidly growing technique in additive manufacturing, enables the fabrication of porous scaffolds with desired geometries at high resolution [377]. A recent study on hybrid gelatin methacrylate/PCL scaffolds prepared by MEW and gel casting showed that incorporation of PCL microfibers within the hydrogel will significantly enhance the hyperelastic properties [124]. Moreover, the physical restraints provided by the porous scaffold can be used as rough geometrical barriers to induce multifunctionalities within the fabricated scaffolds by local casting of different hydrogels or compositions across different portions of the scaffold. Another level of functionalities of this hybrid design of hydrogel-matrix/thermoplastic-mesh structures can be realized by inclusion of bioactive inorganic materials within the polymer mesh. Commercially available products based on barium containing bioactive glass such as the MIRRAGEN™ Advanced Wound Matrix (ETS Wound care, USA) demonstrated high efficiency in clinical product for treatment of diabetic ulcer. Moreover, polymer composites containing bioactive glass (BG) doped with silver ions (Ag) have also shown enhanced wound healing capacities, presumably due to the antibacterial properties of Ag ions and contributions of Si ions in upregulation of vascular endothelial growth factor (VEGF) expression [200,380]. Moreover, the suitability of MEW process in fabrication of highly ordered polymer matrix composites containing BG have been already demonstrated [381,382].

Within the context of skin tissue engineering, incorporation of biologically active entities like growth factors (GF) can induce specific cellular and biological functionalities throughout the healing process. The proliferation stage of healing is of great importance, since at this level new blood vessels are formed to ease the new tissue development. Previous studies demonstrated that incorporation of VEGF and basic fibroblast growth factor (bFGF) will result in enhanced healing processes, however, the employed strategies for delivery of these biomolecules will significantly determine the outcome.[351,383] Using porous polymeric carriers like gelatin microspheres for delivery of growth factors has been explored in several studies.[384–386] It was reported that direct application of bFGF in a soluble form will not positively contribute in the healing process due to its short *in vivo* life-time [387]. However, the tunable physical and structural properties of drug delivery vehicles would results in adjustable release profiles [384]. In this way, the synchronicity between the rate of delivery and rate of new tissue formation can be tuned by adjusting the physical and chemical properties of the carriers, and their selective geometrical distribution within the scaffold. Well-tuned release profiles of the carriers and the controlled geometrical placement of the vehicles will result in sustained and programmed release behavior depending on the application criteria. In this way, either of sustained or burst release profiles can be achieved depending on the specific applications.

Based on this background, in this study a hybrid design of scaffolds comprising of a gelatin soft hydrogel matrix reinforced with 3D melt electrowritten PCL/PCL-BG meshes was introduced, while the controlled casting of hydrogel within the confining mesh structure resulted in selective, geometrically dependent inclusion of gelatin microspheres (GMS) impregnated with different growth factors. The mechanical and biological properties of the hybrid scaffolds were investigated *in vitro*, and their performance as the potential therapeutic designs were assessed *in vivo*. This study was fundamentally aimed at assessing the potential of hybrid MEW as a novel biofabrication technique in skin tissue engineering.

7.2 Results and Discussion

Melt electrowritten scaffolds could facilitate the spatial control over the distribution of cast hydrogel by providing geometrical constrains throughout a porous architecture. The strategy employed in this study was based on sequential injection of hydrogels with different active

biomolecules within the porous scaffolds prior implantation *in vivo*. Figure 7-1 summarizes the workflow for preparation of the scaffolds. Employing a photocrosslinking mechanism based on visible light aided in formation of physically stable hydrogel matrix shortly after injection, while the thermo-gelling behavior of gelatin was no longer determinant in physical stability of the cast hydrogels. Four different categories of parameters could play significant roles on performance and outcome of *in vivo* implantation in current study, including the ones related to i) geometrical aspects of meshes fabricated by MEW [377] ii) size distribution and degree of crosslinking of GMS [388] iii) the choice of matrix hydrogels [389] and iv) the spatial distribution of impregnated GMS within the scaffolds [390]. There are extensive resources in the literature regarding the details of the application-oriented and fine-tuning of parameters in each of these categories, however addressing all those parameters will result in extreme complexity of the system. Hence, as the proof-of-concept, we employed a minimalistic approach with changing a few process and materials related variables, while the rest were kept at the best-known conditions.

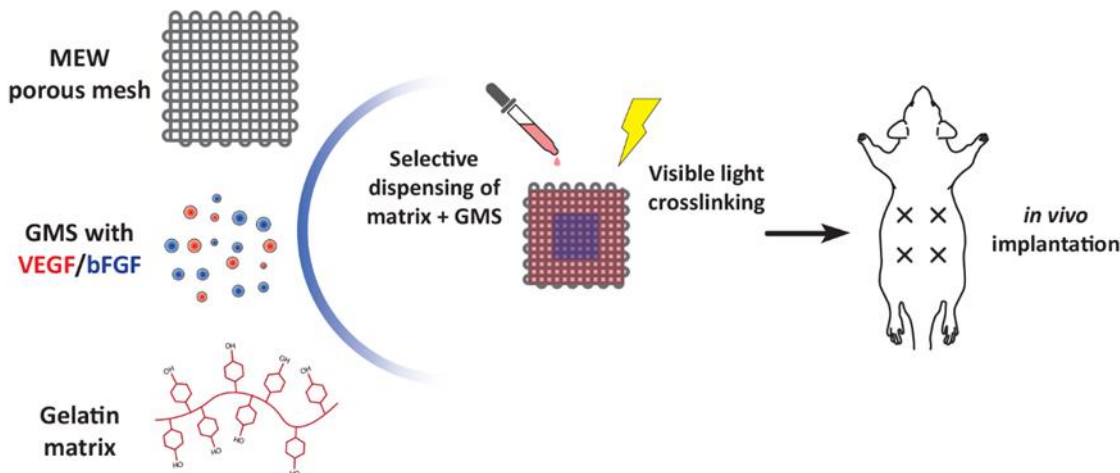


Figure 7-1. Illustration showing an overview of the study. MEW meshes from PCL or PCL/BG were selectively filled with visible light crosslinkable gelatin matrix including growth factor impregnated GMS. Four different types of scaffolds were consequently implanted *in vivo*

7.2.1 Mechanical Properties and swelling behavior

Mechanical properties of three hydrogel matrices and hybrid structures were investigated during tensile loading (details about the nomenclature of the hydrogel matrices and thermoplastic meshes are provided in Experimental sections and Table 7-2). The contribution

of micro- and nano-sized mesh structures in mechanical reinforcement of hydrogels have been highlighted in previous studies [15,342]. It has been proposed that the ordered micro-mesh structure reinforces the hydrogel matrix through load transfer in the direction of loading, lateral expansion/contraction, and also the interconnection points within the mesh structure.[124] Cross-linked Gel-1 matrix behaved as a soft, hyperelastic gel with the Young's modulus of 0.92 ± 0.82 MPa (Figure 7-2A). Moreover, the Gel-1 matrix showed extreme elongation of more than 250%. Incorporation of thermoplastic meshes resulted in significant enhancement of the tensile moduli (5.02 ± 0.95 and 10.95 ± 1.93 MPa for PCL-BG/Gel-1 and PCL/Gel-1, respectively), while limiting the elongation of scaffolds to less than 30% (Figure 7-2A). These results are matching with skin elastic modulus in the literature as stated from 4 to 8 MPa [391,392]. Indeed, this value would vary for skin parts and different mechanical testing also influence the calculated amounts. In addition to the contribution of the mesh structure in efficient load transfer within the hybrid structure, the volume fraction of thermoplastic (i.e. the porosity content of the mesh) plays a significant role in reinforcing mechanism [124]. Since the reinforcing meshes in all hybrid scaffolds shared the same internal design, this factor could be excluded in evaluation and comparison of the mechanical properties of different hybrid structures. In this way, decrease in tensile properties of PCL-BG/Gel-1 scaffolds compared to the ones without BG could be correlated with the presence of domains of stress concentration, which were mainly due to inhomogeneous interface between the hard BG particles and softer PCL matrix [393,394]. This could result in local plasticity of the matrix followed by early failure during loading. The PCL/Gel-1 scaffolds showed significantly higher tensile modulus and ultimate tensile stress compared to PCL-BG/Gel-1, however both faced failure at similar strain values. This observation could be correlated to the geometrical features of both meshes, which resulted in similarities in load transfer within the hybrid scaffold structures. Despite the scale of differences between elastic properties of two hybrid structures, both significantly surpassed Gel-1 hydrogel matrix in terms of elastic properties. Providing a matrix with appropriate mechanical properties is an essential step to enhance the healing process, and sufficient strength and elasticity would assist the tissue regeneration and spatial organization. Hydrogels might be considered as the preferred biocompatible matrices for cells to attach and proliferate, however, lack of mechanical strength led to fabrication of hybrid structures with inclusion of more stiff polymeric materials

[9]. Gel-1 matrix showed a hyperelastic response to tensile deformation with extensive elongation and low tensile modulus. Incorporation of MEW mesh structures resulted in elevation of mechanical rigidity, which can be considered in the range of the native rat skin tissue [395]. Moreover, handling and implantation of such reinforced scaffolds were significantly improved, which resulted in less operational complications. Compatibility between mechanical properties of the tissue and implanted scaffold would aid in progress of tissue-implant integration [396]. The speculated benefits from mechanical compatibility of PCL/Gel-1 and PCL-BG/Gel-1 scaffolds with native rat skin tissue would be more discussed in the next sections.

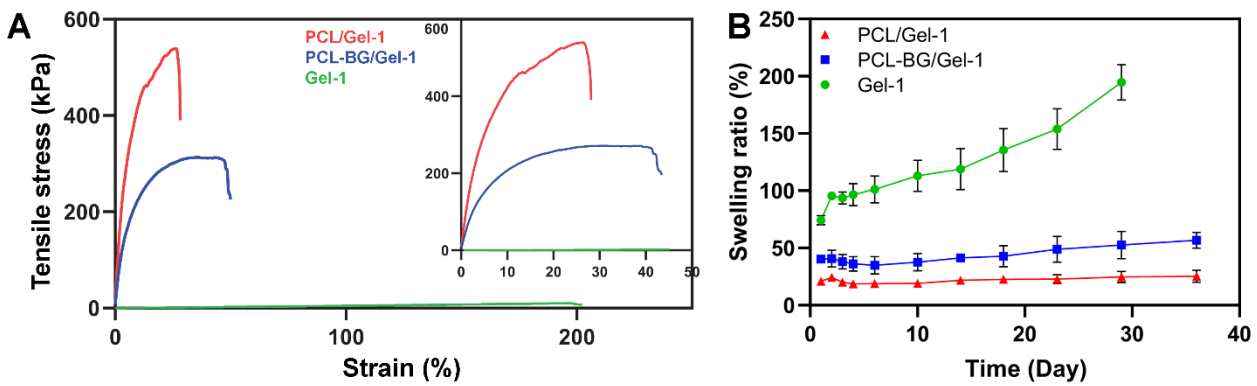


Figure 7-2. A) Tensile properties and B) Swelling behavior at different time intervals in PBS for PCL/Gel-1, PCL-BG/Gel-1 scaffolds and Gel-1 matrix. Inset in (A) showing the slope of tensile behavior in different samples over the magnified percentage strain axis

The swelling ratio can be considered as an indication of materials hydrophilicity/hydrophobicity. An optimum value of swelling is requisite for wound scaffolds to maintain a flexible structure as well as increase its hydrophilic degradation [336]. However, extensive swelling might result in loss of mechanical stability and wound contraction [140]. Figure 7-2B shows the swelling ratios of scaffolds in PBS at different time intervals. Gel-1 matrix showed almost four times more swelling ratio in comparison to the hybrid scaffolds. Incorporation of rigid thermoplastic meshes resulted in restriction of volumetric expansion and stabilized the dimension throughout the whole incubation period in such a way that the swelling ratio of hybrid scaffolds remained almost the same during 35 days, after reaching the initial equilibrium state by 1 day incubation. This stabilization of structure would also

contribute to structural integrity, as the Gel-1 samples were disintegrated after 29 days of incubation. It should be also noted that the hybrid scaffolds containing BG uptook more water, which can be attributed to the lower elastic modulus as well as the increase in wettability [397].

7.2.2 Bioglass characterization

Bioglass powders were observed with FE-SEM and as shown in Figure S7-2A, their sizes were below 50 μm . BG powders were also characterized with an EDS spectrometer equipped with SEM. Elemental percentage obtained from 5 different locations of the samples are represented in Table 7-1 with their theoretical values for synthesis. Structural characterization of BG sample was performed with an XRD diffractometer. The results confirmed the formation of an amorphous structure with no crystalline peak indicating bioactivity of the samples (Figure S7-2B).

Table 7-1. Theoretical and actual values of elements present in the bioglass samples acquired from EDS analysis

Element	Si	Ca	P	Ag
Theoretical %	60	30	8	2
Actual %	55 ± 3.1	26.35 ± 1.3	7.54 ± 1.7	1.54 ± 1.3

7.2.3 *In vitro* cytotoxicity

The biocompatibility of the hybrid PCL/Gel-1, PCL-BG/Gel-1 constructs, and the cast Gel-1 matrix was tested on HDF cells using WST-1 colorimetric assay. The cells treated with extract from PCL/Gel-1 showed no significant decrease in viability, although a slight decrease was observed at the diluted concentrations of 0.4%, 0.8%, and 1.6% (Figure 7-3A). The results of the extracted medium from PCL-BG/Gel-1 also showed the same behavior with a slight decrease at concentrations of 0.4% to 3.1% (Figure 7-3B). However treatment of HDF cells with all the concentrations resulted in cell viability of more than 80% and are considered as non-cytotoxic [337]. Moreover, Gel-1 extract showed no significant decrease in cell

viability compared to the untreated/negative control in all concentrations (Figure 3-7C). The special concerns on the biocompatibility of photocrosslinked gelatin matrices are due to inclusion of SPS and Ru complex, which has been shown to be cytotoxic at high concentrations *in vitro* and *in vivo* [337,373]. However, rapid progress of photocroslinking reaction leads to consumption of more than 99% of cytotoxic persulfate radicals to the non-toxic levels *in vitro* [337]. The same effect was observed, considering the high viability of HDF cells exposed to the extracts of Gel-1 matrices. Moreover, it has been shown that presence of Ru complexes below a certain threshold will not induce any noticeable cytotoxic response *in vitro* and *in vivo* [337,398].

Glutaraldehyde has been extensively used in crosslinking of gelatin hydrogels, however, a proper quenching and washing step should be employed to avoid cytotoxic effects of the crosslinker residues *in vitro*, as well as acute toxicity *in vivo* [399]. Results of cytotoxicity assay showed that the excess amount of glutaraldehyde in GMS were successfully washed away during the synthesis of GMS, and no significant impact on viability of HDF cell were observed.

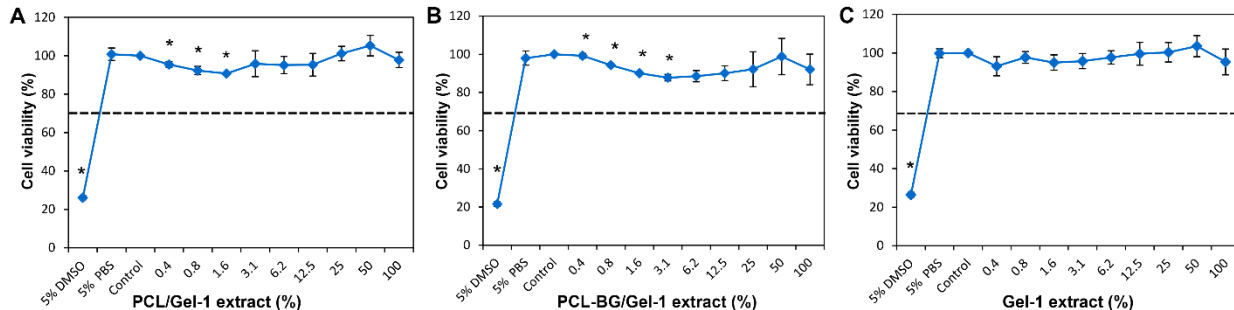


Figure 7-3. Toxicity assay against HDF cells *in vitro* with the extracted media from A) PCL/Gel-1, B) PCL-BG/Gel-1, and C) Gel-1 scaffolds, respectively. Negative controls: fibroblast basal medium and 5% PBS. Positive control: 5% DMSO in culture medium. The components with cell viabilities above 70% (dashed line) are considered as non-toxic

7.2.4 Evaluation of wound healing *in vivo*

7.2.4.1 Gross anatomical evaluation

Wound healing is a complex process consisting of vascularization, epithelialization, fibroblast proliferation and granulation tissue formation in the dermis layer [387,400]. Wound closure and

scar formation during the healing process were monitored and compared with the conditions at Day 0 for each animal (Supplementary Figure S7-1). Wounds treated with PCL/Gel-1 and PCL-BG/Gel-1 scaffolds did not close completely while the wounds treated with hydrogel matrices including GFs were completely integrated with the surrounding tissue with minimum or no visible signs of scar formation. This could be directly correlated to the presence of GF as active biomolecules within the matrix, especially the contributions of bFGF during the healing process. Previous studies showed that delivery of bFGF alone or in combination with other growth factors resulted in accelerated healing by enhancing cell migration and proliferation, granulation tissue formation, re-epithelialization, and angiogenesis, as well as enhanced wound contraction rate [401–404].

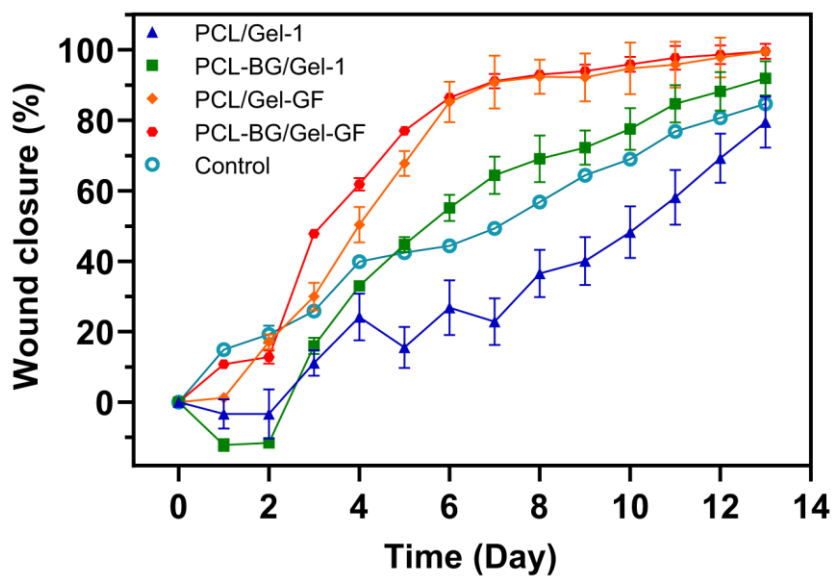


Figure 7-4. Time-dependent variation of the wound closure percentage (mean \pm SD) in wounds treated with different scaffolds versus control

Time-dependent progression of wound closure was monitored during the first two weeks of implantation and the data is presented in Figure 7-4. Control wounds without scaffolds showed 84% reduction in the size of wounds during the monitoring period, with a relatively steady rate of closure. Wounds treated with PCL/Gel-1 scaffolds showed slower rate of wound closure, however, inclusion of BG resulted in a substantial improvement in closure rate compared to both control and PCL/Gel-1 samples. This could be correlated with the antimicrobial properties of

silver doped BG within the scaffolds and also the proposed upregulatory effects of Si ions on expression of VEGF [200,380]. Nevertheless, both scaffold types showed more or less the same behavior as control, in terms of the rate and extent of wound closure. Inclusion of GF within both scaffolds boosted the rate of wound closure, in such a way that wounds treated with either of PCL/Gel-GF or PCL-BG/Gel-GF showed more than 85% reduction in diameter after 6 days, followed by slow steady decrease in wound diameter. The accelerated healing behavior could be correlated to presence of both VEGF and bFGF present within the scaffolds [405]. The slow rate of wound closure observed in PCL/Gel-1 associated with acute inflammatory response and necrotic scar formation. More details on histological evaluation of different samples are provided in the next section.

7.2.4.2 Histological evaluation

Whole wound area was evaluated in terms of secondary wound healing. Seven different evaluation criteria included i) epithelial regeneration, ii) amount of collagen produced, iii and iv) presence of acute and chronic inflammatory cells, v) edema, vi) granulation tissue and vii) integration with environmental tissue, which were evaluated and indexed subjectively and scores as 1: none, 2: mild, 3: moderate, 4: over, and 5: extensive. Wounds were evaluated at two time points, on 7 and 21 days after implantation of scaffolds. Figure 7-5 summarizes the data obtained by subjective evaluation of wound sections.

At the early stage of healing, indexed values on Day 7 corresponding to the presence of acute and chronic inflammatory cells and edema were found to be the most in PCL/Gel-1 wound group and the least in PCL-BG/Gel-GF group. Moreover, incorporation of BG generally resulted in decrease of indices in mentioned categories. While the granulation tissue, epithelial regeneration and fibroblast/collagen ratio did not change significantly between groups, the integration with environmental tissue was the least in PCL/Gel-1 and the most in PCL-BG/Gel-GF groups. Similarly, inclusion of BG contributed positively to healing process and resulted in enhancement of integration with environmental tissue.

At the later stage of healing, indexed values on Day 21 showed the same trend as Day 7 in presence of acute and chronic inflammation and Edema, however the fibroblast/collagen ratio

was significantly higher in scaffolds including GF, contributing in prevention of thick scar tissue formation. Moderate granulation tissue was observed at Day 21 in all groups, and the average extent of epithelial regeneration was not significant between different categories. The integration with environmental tissue in all groups was significantly higher than PCL/Gel-1 group, regardless of presence of GF or BG within the scaffolds. It is worth mentioning that almost whenever a significant difference in indices between PCL/Gel-1 group and the other GF containing groups was observed, PCL-BG/Gel-1 group showed no significant difference compared with the GF containing ones. This observation highlights the role of BG in acceleration of healing process which was mentioned earlier.

Progression of healing process within each scaffold group could be better understood by comparing the corresponding indices in each evaluation criterion between Day 7 and Day 21 in Figure 7-5. All groups showed decreased acute inflammatory signs and edema during the study, but the presence of chronic inflammatory cells did not decrease significantly from Day 7 to Day 21. Excessive formation of granulation tissue was not observed throughout the healing however, the extent of epithelial regeneration was not also significantly enhanced from Day 7 to Day 21. On the other hand, the fibroblast/collagen ratio was significantly increased while its extent was higher in scaffolds containing GF. Moreover, the PCL/Gel-1 group did not show improved integration with environmental tissue, though the wounds treated with either BG or GF had significantly increased integration.

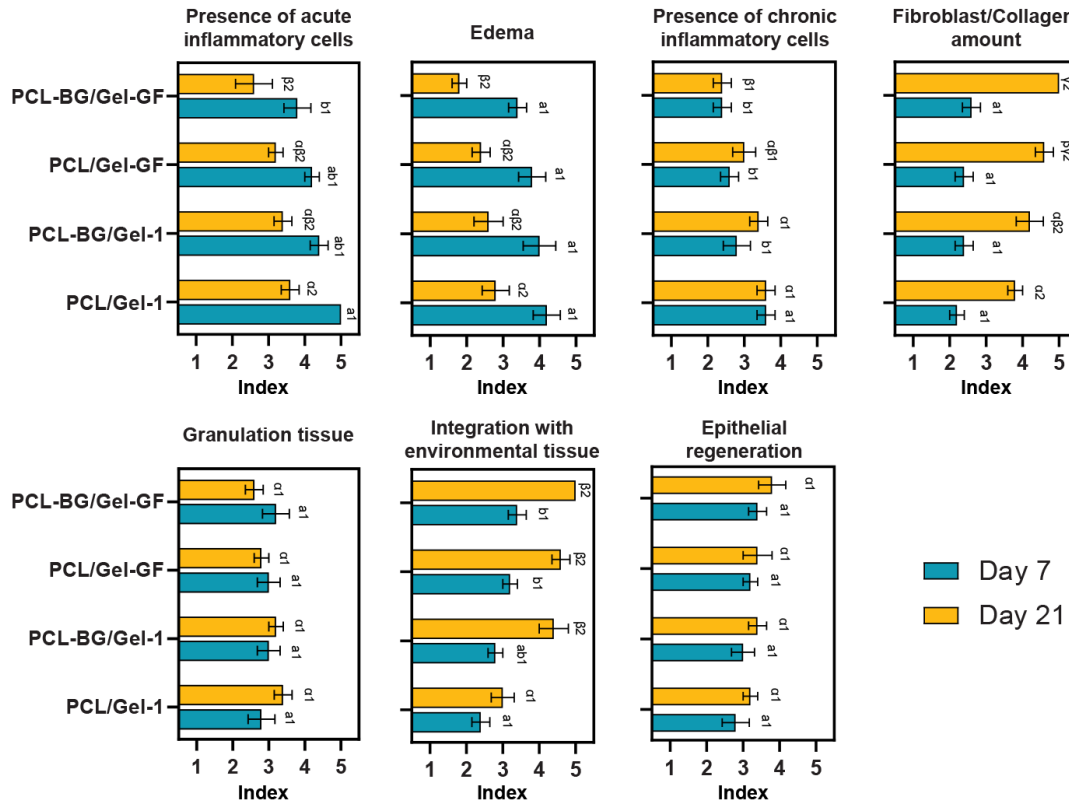


Figure 7-5. Evaluation criteria in secondary wound healing based on histological analysis of different sample groups. Each criterion was indexed subjectively and scores as 1: none, 2: mild, 3: moderate, 4: over, and 5: extensive. Mean values reported with error. Significant differences were denoted as 3 different signs, different Latin letters/Greek letter/numbers show significant difference in comparison with the members of the same categories (scaffold type: Latin letters for Day 7 and Greek letters for Day 21, evaluation date: numbers) ($p<0.05$)

Based on the qualitative evaluation of the scaffolds, PCL-BG/Gel-GF were considered as the most promising hybrid design in terms of inflammatory response and regeneration capacity. In contrast, scaffolds made of PCL/Gel-1 showed intense inflammation and little to no vascularization and granulation tissue formation, eventually expressing intense foreign body reaction. Figure 7-6 shows the H&E stained histological sections of two scaffold types. The presence of fibrinopurulent exudate (hollow star) epithelial regeneration (hollow arrow), granulation tissue (white star) and scaffold fibers (with arrow) are evident (Figure 7-6). On Day 7 in samples from PCL-BG/Gel-GF groups showed better integration with environmental tissue, formation of granulation tissue between fibrinopurulent exudate and increased collagen and fibroblastic proliferation. On the other hand, the PCL/Gel-1 group showed severe fibrin

exudates and hemorrhagic granulation tissue, with considerably low epithelial regeneration and integration with environmental tissue.

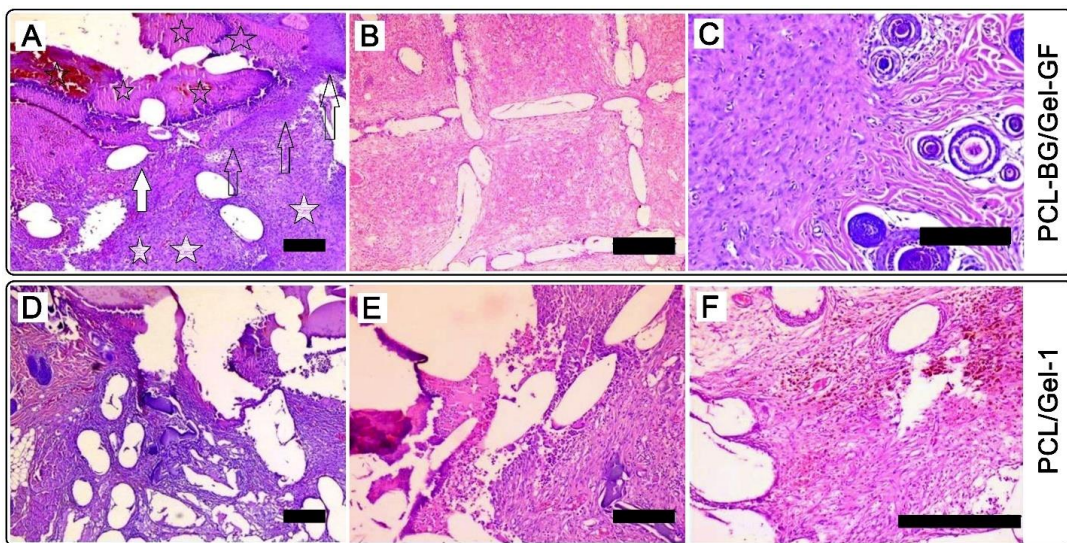


Figure 7-6. Hematoxylin and Eosin (H&E) staining of histological sections of two scaffold groups at Day 7 A-C) PCL-BG/Gel-GF and D-F) PCL/Gel-1. Scale bars: 200 μm . (Hollow star) fibrinopurulent exudate, (hollow arrow) epithelial regeneration, (white star) granulation tissue, (with arrow) scaffold fibers

Development of hypertrophic scar tissue due to excessive granulation tissue formation was not observed in any of the scaffold groups. Histological evaluation of treatment groups on day 21 showed irregular healing of the surface in PCL/Gel-1 (Figure 7-7A). Presence of either BG or growth factors in scaffolds resulted in slightly irregular healing on the surface of wounds treated with both groups (Figure 7-7B and C, respectively). In contrast, wounds treated with PCL-BG/Gel-GF showed regular healing where the lesion area was filled with fibro collagen tissue (Figure 7-7D).

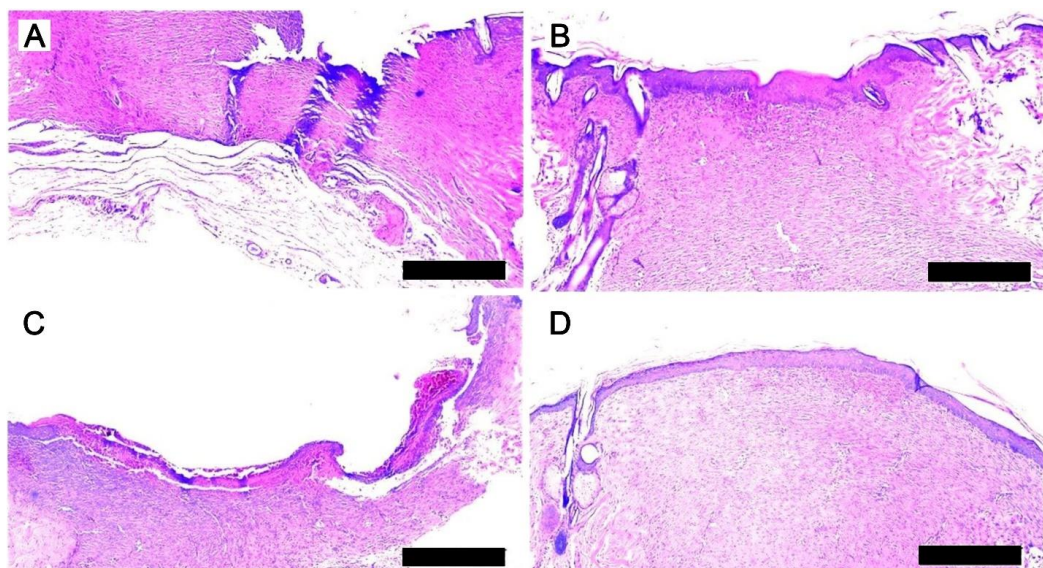


Figure 7-7. Hematoxylin and Eosin (H&E) staining of histological sections of treatment groups A) PCL-Gel-1, B) PCL-BG/Gel-1, C) PCL/Gel-GF and D) PCL-BG/Gel-GF at Day 21. Scale bars: 500 μm

Application of GF in acceleration of wound healing has been vastly explored in considerable number of studies. In contrast, incorporation of bioactive glasses as active therapeutic agents in wound healing is relatively new. In addition to the influence of GF in acceleration of wound healing [383], the observed enhancement of wound healing in scaffolds containing both GF and BG could be attributed to reported activation of genes implicated in the healing process, including VEGF for angiogenesis, bFGF, and vascular cell adhesion protein, as well as the proposed role of BG in modulating the TGF- β pathway [406]. In this paper, the potential of novel biomanufacturing technologies such as MEW in development of hybrid treatment platforms is highlighted.

7.3 Conclusion

This chapter was intended to provide a simple, yet novel example of how the hybrid combination of biomanufacturing technologies could contribute in development of novel and more efficient wound healing strategies. Through selective inclusion of growth factors and bioactive glass, it was demonstrated that the rate of wound closure, as well as secondary

wound healing indices were significantly improved compared to wound groups treated with PCL/Gelatin hybrid scaffolds. *In vitro* data showed that the hybrid scaffolds were cytocompatible and the photocrosslinkable hydrogel matrix did not induce any significant drop in cell viability. Mechanical testing of scaffolds showed a substantial increase in tensile modulus of hybrid structures compared to hydrogel matrix, confirming the role of ordered 3D fibrous matrix in load transfer which can be tuned according to the desired application. The histological examinations of wound tissues during *in vivo* study showed an increase in granulation tissue, fibroblastic proliferation, increase in collagen and regeneration of epithelial cells, in treatment groups with active biomolecules compared to the control group at Day 7 and 21 of the experiments. The findings of this study suggest a great potential in development of hybrid wound healing strategies, while further studies based on altering the design of reinforcing mesh structures, configuration of cast hydrogel matrices, and inclusion of active biomolecules could be performed.

7.4 Experimental sections

7.4.1 Materials

Gelatin type B, glycine, Tween 80, tetraethyl orthosilicate (TEOS) ($\text{Si}(\text{OC}_2\text{H}_5)_4$), silver nitrate ($\text{Ag}(\text{NO}_3)$), triethyl phosphate (TEP), tetrahydrofuran (THF), tris (2,2'-bipyridyl) dichlororuthenium (II) hexahydrate (Ru), Haematoxylin and eosin, and sodium persulfate (SPS) were purchased from Sigma-Aldrich. Glutaraldehyde solution (5.6 M) was obtained from Fluka. Nitric acid (HNO_3) was purchased from Merck. Calcium nitrate tetrahydrate ($\text{Ca}(\text{NO}_3)_2 \cdot 4\text{H}_2\text{O}$) was obtained from Riedel-de-Haen. PCL pellets (CAPA 6400) with a molecular weight of 37,000 g/mol was procured from CAPA, Perstorp Ltd. Human basic fibroblast growth factor (bFGF) and vascular endothelial growth factor (VEGF) were acquired from ProsPec Tany TechnoGene Ltd. Dulbecco's phosphate-buffered saline (DPBS) solutions were obtained from Gibco. PBS tablets were purchased from MP Biomedicals, France. Pen-Strep (10,000 Units/ml penicillin, 10,000 $\mu\text{g}/\text{mL}$ streptomycin) were obtained from Gibco (UK). Cell proliferation reagent WST-1 was purchased from Roche. Fibroblast basal medium (PCS-201-030) and fibroblast growth kit-serum-free (PCS-201-040) were purchased from ATCC.

7.4.2 Fabrication of thermoplastic meshes

7.4.2.1 Synthesis of bioactive glass (BG)

The synthesis of quaternary bioactive glass (BG) with the nominal composition of 60SiO₂-30CaO-8P₂O₅-2Ag₂O (based on mol. %) was performed through an acid-catalyzed sol-gel process. An acidic solution was prepared by mixing 2N nitric acid (3 mL) with 20 mL of deionized (DI) water. TEP (2.8 mL) as the precursor for phosphorus pentoxide (P₂O₅) was added dropwise to the mixture, followed by stirring until reaching a transparent solution. TEOS (2.8 mL) as the precursor for silicon dioxide (SiO₂) was added dropwise and stirred for 30 min until a transparent and homogeneous mixture was acquired. Ca(NO₃)₂.4H₂O (7.2 g) and Ag(NO₃) (0.7 g) as precursors of calcium oxide (CaO) and silver oxide (AgO₂) were added portion-wise. The mixture was stirred for 30 min to allow for the completion of the reaction.

The resulting sol was cast in a glass container and aged in 40 °C for 3 days. The gel was broken into smaller pieces and dried in an oven at 120 °C to remove the residual water. The dried powders were grinded and calcined at 700 °C for 2 h to eliminate the residual nitrates (heating and cooling rates of 10 °C/min and 5 °C/min, respectively).

The resulting sol was cast in a glass container and aged in 40 °C for 3 days. The gel was broken into smaller pieces and dried in an oven at 120 °C to remove the residual water. The dried powders were grinded and calcined at 700 °C for 2 h to eliminate the residual nitrates (heating and cooling rates of 10 °C/min and 5 °C/min, respectively). Final bioglass particles were characterized by X-ray diffractometer (XRD) (Bruker D2 advance, Germany) with a monochromatized Cu-Kα radiation ($\lambda = 1.54184 \text{ \AA}$) generated at 30 kV and 10 mA, at scan rate of 1°/min and step size of 0.02 °. In addition, BG particles were analyzed morphologically and chemically with a field emission gun scanning electron microscopy (FE-SEM, Zeiss Leo Supra VP) at 2 kV accelerating voltage that equipped with energy dispersive X-ray (EDS) spectroscopy. Samples were coated with a thin layer of gold-palladium using Denton Vacuum Desk V to obtain electrical conductivity.

7.4.2.2 Preparation of PCL-bioactive glass composite

The PCL-bioactive glass composite, hereinafter referred to as PCL-BG, was prepared with the PCL:BG ratio of 1:0.75 (wt %) based on the work by Moura *et al.*[200] The required amount of bioactive glass powder was dispersed in THF and stirred for 1 h, followed by high amplitude sonication using a probe sonicator (Q700, QSonica) for 30 min. Afterwards, the proper amount of PCL was added to the suspension while stirring for 30 min followed by 30 min of sonication. At this step, the dispersion was transferred to a wide plate to remove the solvent at room temperature for 24 hours. The remaining solvents were removed by placing the samples in vacuum oven at 40 °C for 3 h.

7.4.2.3 Fabrication of melt electrowritten scaffolds

The 3D meshes of PCL and PCL-BG composite were fabricated by a custom-built melt electrospinning device described elsewhere.[17] The printing parameters were optimized to obtain a straight fiber with a constant diameter. Materials were loaded into a metal syringe and heated to 70 °C by an Arduino Mega microcontroller with two heating elements. The molten polymers were extruded through a nozzle (250 µm, Musashi Engineering Inc., Japan) with the aid of high voltage electrical field supplied between the nozzle and collector (7.5 kV, ES30, Gamma High Voltage Research, FL) and a pneumatic air dispenser (2.8 bars, EFD, Nordson, USA). The printer speed was set to 220 mm/min. The final scaffold mesh was a 10×10 mm cuboid with the height of 3 mm.

7.4.3 GF delivery microparticles and hydrogel matrices

7.4.3.1 Preparation of gelatin microspheres

Gelatin microspheres (GMS) were fabricated by using a water-in-oil emulsion method reported by Tabata *et al* [387,407]. Briefly, 1 g of gelatin type B was dissolved in 10 mL of DI water and heated to 40 °C. Gelatin solution was added dropwise to 350 mL olive oil obtained from local market, while the temperature was kept at 40 °C while being stirred at 550 rpm. The water-in-oil emulsion was stirred for 15 min and then was cooled down in an ice

bath at 10 °C and continuously stirred for 30 min. Chilled acetone (100 mL) was added to the emulsion and the mixture was stirred for 1 hour. The gelatin microspheres were washed with acetone followed by isopropyl alcohol (IPA) and collected by centrifugation (4000 rpm, for 5 min, at 4 °C). The GMS were re-suspended in IPA and were recovered by passing through sieves with mesh size of 63 and 52 µm. The GMS trapped by 52 µm sieve were collected by washing with chilled acetone, centrifuged and air dried at 4 °C overnight. It should be noted that negatively charged gelatin type B with isoelectric point of around 4.7-5.2 was selected as a carrier for bFGF and VEGF with isoelectric points of 9.6 and 7.5, respectively which was proved to have higher loading efficiency [408–410].

An aqueous solution of 2 wt% glutaraldehyde and 0.1 wt% Tween 80 was prepared, and the GMS were crosslinked by immersion in the solution at 4 °C for 12 h. The crosslinked samples were washed with 0.1 wt% Tween 80 aqueous solution followed by centrifugation. The residual glutaraldehyde was removed by washing the GMS in 100 mL of 50 mM glycine aqueous solution containing 0.1 wt% Tween 80 at room temperature for 1 h. The resulting microspheres were washed three times by centrifugation/resuspension in 0.1 wt% Tween 80 aqueous solution at 4000 rpm for 5 min at 4 °C and freeze dried for 3 days to remove the remaining solvents. The morphology of hydrated microspheres was examined by optical microscopy (Nikon, Eclipse ME600). The microspheres were incubated in PBS at 4 °C for 24 h to reach the equilibrium swelling before the morphological observations. The GMS diameters were calculated with ImageJ software and their size distributions are sketched versus their frequencies (Supplementary Figure S7-3).

7.4.3.2 Impregnation of bFGF and VEGF into GMS

The growth factors were loaded into GMS based on a previously established method [385]. Briefly, the solutions of bFGF and VEGF in DPBS were prepared with the concentrations of 50 and 16 ng/µL, respectively. The GMS were impregnated with bFGF and VEGF by addition and through mixing of 15 µL of bFGF solution into 3 mg of freeze-dried GMS, and 45 µL of VEGF solution into 9 mg of freeze-dried GMS, respectively. The impregnated GMS were kept at 4 °C overnight to allow complete loading. By the end of the incubation period, the swelling ratio of the GMS at this stage was considered as 100 % for further calculations. The

volume of GF solutions was intentionally set to be less than the theoretical absorption capacity of dried GMS, to avoid oversaturation and swelling of GMS prior dispersion within the hydrogel matrices. The final mass concentrations of bFGF and VEGF per each scaffold were set as 40 and 16 ng/ μ L, respectively.

7.4.3.3 Hydrogel matrices

Filter-sterilized (0.22 μ m) gelatin type B solution (10% wt/v) was used as the primary matrix ink. Post-crosslinking of the hydrogel matrices including Ru photo-initiator and SPS was adopted from a photochemical process explained and conducted elsewhere [337]. The final concentration of Ru as the photocatalyst and SPS as the quencher in gelatin solution were set to 1 and 20 mM, respectively. Ru and SPS were diluted from the 0.22 μ m filter-sterilized stock aqueous solutions of 25 mM and 1M, respectively. Three types of hydrogel matrices were prepared by proportional mixing of hydrated GMS with primary matrix hydrogel solution (Table 7-2).

Table 7-2. Formulation of different hydrogel matrices

Hydrogel matrix	Primary matrix	GMS+PBS	GMS+bFGF	GMS+VEGF
Gel-1	Gelatin 10% wt/v	*		
Gel-2	Gelatin 10% wt/v		*	
Gel-3	Gelatin 10% wt/v			*

7.4.3.4. Fabrication of hybrid scaffolds

The PCL and PCL-BG melt electrowritten meshes were sterilized using a 240 nm UV lamp prior injection of hydrogel matrices. Hydrogels were injected into the porous meshes with following order. As controls, PCL and PCL-BG meshes were completely filled with Gel-1 hydrogel matrix. For the samples containing growth factors, the inner portion of each scaffold (PCL or PCL-BG) was filled with Gel-2 which included GMS impregnated with bFGF. The peripherals of the same scaffold were fill with Gel-3, containing GMS impregnated with VEGF. A schematic representation of the local distribution of gelatin hydrogel matrices

within a hybrid scaffolds is presented in Figure S7-5. For the purpose of simplicity, the combination of Gel-2 and Gel-3 matrices in the hybrid scaffolds will be referred to as Gel-GF.

The hydrogel matrices were injected within the porous mesh by the aid of a wide-mouth pipette in sterile conditions. Following the casting, the hybrid scaffolds were photo-crosslinked by an array of 3 balanced-white LED lamps with the total power of 150 W from the distance of 30 cm for 1 min. The casting of the hydrogel matrices within the melt spun scaffolds were performed in a square well covered with reflective aluminum foil.

7.4.4 Characterization

7.4.4.1 BG characterization

Bioglass particles were characterized by X-ray diffractometer (XRD) (Bruker D2 advance, Germany) with a monochromatized Cu-K α radiation ($\lambda = 1.54184 \text{ \AA}$) generated at 30 kV and 10 mA, at scan rate of 1°/min and step size of 0.02 °. In addition, BG particles were analyzed morphologically and chemically with a field emission gun scanning electron microscopy (FE-SEM, Zeiss Leo Supra VP) at 2 kV accelerating voltage that equipped with energy dispersive X-ray (EDS) spectroscopy. Samples were coated with a thin layer of gold-palladium using Denton Vacuum Desk V to obtain electrical conductivity.

7.4.4.2 Mechanical testing

Tensile tests were performed using Zwick/Roell-Z100 universal tensile machine (UTM) equipped with 200 N load cells. Hybrid hydrogel/mesh samples were prepared as rectangles with dimensions of 70 mm length, 20 mm width, and 3 mm height. Three samples of PCL/Gel-1, PCL-BG/Gel-1, and Gel-1 where prepared by casting and mechanical testing was conducted with grip-to-grip distance of 30 mm and pre-load of 1kPa. Four replicates of each design were tested. Samples were incubated in PBS overnight prior testing. To make sure the hydrogels will not break before the tests, pneumatic grips were used and at each contact point small piece of filter paper grade 2 was put between grips and sample. Figure S7-4 shows the hydrogel samples holding before and during the mechanical test. The samples were tested in

longitude direction and the speed was set to 1 mm/min for all the experiments and each measurement was automatically stopped by reaching 70% of the maximum force. The force versus displacement data were recorded and the Young's moduli were calculated from the slope of the stress-strain curves in the elastic region.

7.4.4.3 Swelling behavior

The swelling ratio of the scaffolds were measured by incubation in 1x PBS solution at 37 °C under gentle shaking. The PBS medium was prepared by dissolving PBS tablets in MiliQ water. Four replicates of 3 groups of scaffolds, including PCL/Gel-1, PCL-BG/Gel-1, and cast-Gel-1, were prepared with the same conditions mentioned in 4.3.4. Samples were weighed at predetermined time points and the medium was changed every 3 days. The swelling ratio was calculated according to the following equation:

$$\text{Swelling ratio (\%)} = \left[\frac{M_2 - M_1}{M_1} \right] \times 100 \quad (1)$$

where M_1 and M_2 are the mass of the scaffolds before and after soaking in PBS, respectively.

7.4.5 *In vitro* cytotoxicity evaluation

The cytotoxicity of the scaffolds was investigated according to the protocol provided by the international standard ISO 10993-5 with adaptations. Three different samples (PCL/Gel-1, PCL-BG/Gel-1, and Gel-1) were prepared as described in previous sections. Samples were incubated in fibroblast basal media (5-fold volume of the hydrogel matrix) for 66 h at 37°C at 150 rpm. After the incubation period, the liquid portions were taken and filtered using a 0.22 µm filter.

Human dermal fibroblast (HDF, ATCC) cells were cultured in fibroblast basal media containing fibroblast growth kit-serum-free and 1% Pen-Strep. Cultures were maintained at 37°C under the atmosphere containing 5% CO₂. HDF cells were seeded in 96-well plate at 7×10³ cells/well and incubated for 24 h. After the incubation period, the culture media in each

well was replaced with different dilutions of the extracts collected from the samples (100%, 50%, 25%, 12.5%, 6.2%, 3.1%, 1.6%, 0.8% and 0.4%) in fibroblast basal media, and cells were incubated for 24 h. Cultures in fibroblast basal media and 5% PBS were used as the negative controls. 5% DMSO added to the cell culture was used as the positive control. At the end of incubation period, the culture media was removed, and cells were rinsed with PBS. The viability of the cells was determined by performing WST-1 colorimetric assay.

7.4.6 *In vivo* study

All animal experiments used in this study were approved by the Bogazici University animal ethics committee (BAP.12.2013) and conducted at the Vivarium Laboratory of Bogazici University, accredited by AAALAC. The animals were housed in rooms with HEPA filter, temperature of 21 °C and humidity of 50-70%. Light cycle was set to 12 hours light and 12 hours dark. Individually Ventilated Cages (IVC) were used.

7.4.6.1 Implantation of scaffolds

Sprague Dawley rats with the age of 6-9 months were used and each rat was assigned to four different scaffold types (n=8) as the following configuration. PCL/Gel-1 at upper left; PCL-BG/Gel-1 at upper right; PCL/Gel-GF at lower left; and PCL-BG/Gel-GF at lower right. The implantation sites of the scaffolds are shown in Figure S7-6. The wounds were created in the back region by the following procedure. Rats were anaesthetized by injection of a combination of ketamine (80-90 mg/kg) and xylazine (5 mg/kg). After the removal of the furs from the operation area, the animals were placed on a heating pad covered with a sterile sheet to prevent hypothermia. The antisepsis of the operation area was provided by 70% alcohol followed by baticon. Punch biopsy needles (Acuderm Hautstanze, Germany) with a diameter of 8 mm in the back region created circular wounds that descend to the depth of the subcutaneous tissue. The scaffolds were placed in the circular cavities of the wounds. All operations and wound measurements were made under the hood. As post-operative analgesic carprofen was used at 5 mg/kg (s.c.) dosage. Antibiotics have not been systemically used since it was thought to affect the wound healing. Postoperative care period lasted 3 days. In

this period, general nutrition, mobility and advanced infectious disease and pain conditions were monitored. The animals were housed in separate cages and allowed to eat and drink ad libitum.

All the animals were euthanized to determine the progress of wound healing process at one (Group I, n=4) and three (Group II, n=4) weeks after the implantation. Euthanasia was carried out with inhalation of carbon dioxide. For each wound, skin sections were removed for pathological examination in 10% formaldehyde-containing tubes. During the first 14 days of the study, the average diameter of each wound in Group II was measured and normalized to the diameter on Day 0 to calculate the wound closure ratio. Wounds with Identical size and shape without any scaffolds (4 wounds per animal, n=2) were used as control.

7.4.6.2 Macroscopic evaluation of wound closure percentage

The healing process in animals was monitored every day and the wounds size measurements were measure with a caliper and the values were reported in cm. The wound closure percentage was calculated by the following equation:

$$\text{Wound closure \%} = \frac{\text{Area at day (0)} - \text{Area at day (n)}}{\text{Area at day (0)}} \times 100 \quad (6)$$

7.4.6.3 Necropsy and removal of tissues

For detection of wound healing stages, predetermined number of animals were euthanized on day 7 and day 21. For each wound, skin sections were harvested up to the subcutaneous tissue and maintained in tubes containing 10% formaldehyde.

7.4.6.4 Histology

The wound tissues in each group were removed and fixed in 4% formaldehyde/PBS solution (pH 7.4) for 48 h, dehydrated with a graded series of ethanol, embedded in paraffin, and sectioned at 5 microns and mounted on adhesive glass slides. The sections were stained

with haematoxylin and eosin (H&E) following the standard procedures. The stained sections were investigated by an optical microscope (Olympus BX53, Tokyo, Japan).

7.4.6.5 Statistical analysis

The data were analyzed by t-test using at least three replicates and were expressed as mean \pm SD and mean \pm standard error of the mean (SEM) for *in vitro* and *in vivo* studies, respectively. Significant statistical differences for *in vitro* and *in vivo* studies were denoted as $P < 0.01$ and $P < 0.05$, respectively.

7.4.7 Supplementary documents

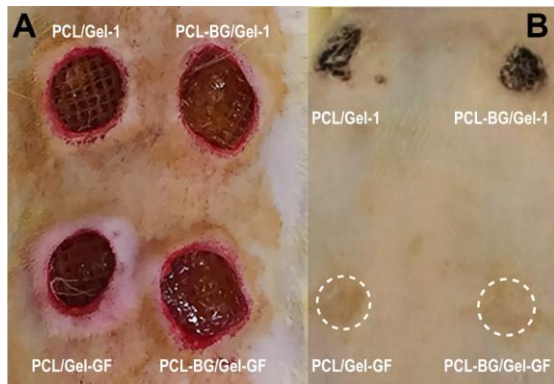


Figure S7- 1. *In vivo* evaluation of the wounds with different scaffolds at A) Day 0, and B) Day 14. Dashed circles represent the healed wounds locations

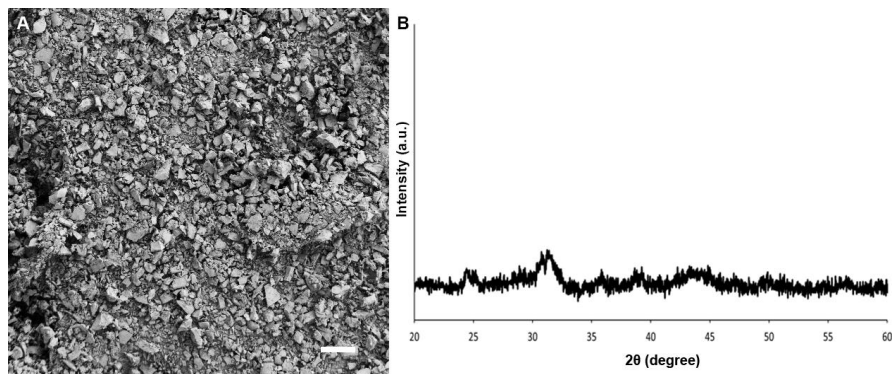


Figure S7-2. Characterization of bioactive glass powders: A) SEM image and B) XRD pattern of synthesized BG powders. Scale bar indicates 100 μm

Figure S7-3A shows an optical micrograph of the gelatin microspheres after crosslinking and one day incubation in PBS at 4 °C. Size distribution of the GMS versus their frequencies are shown at Figure S7-3B.

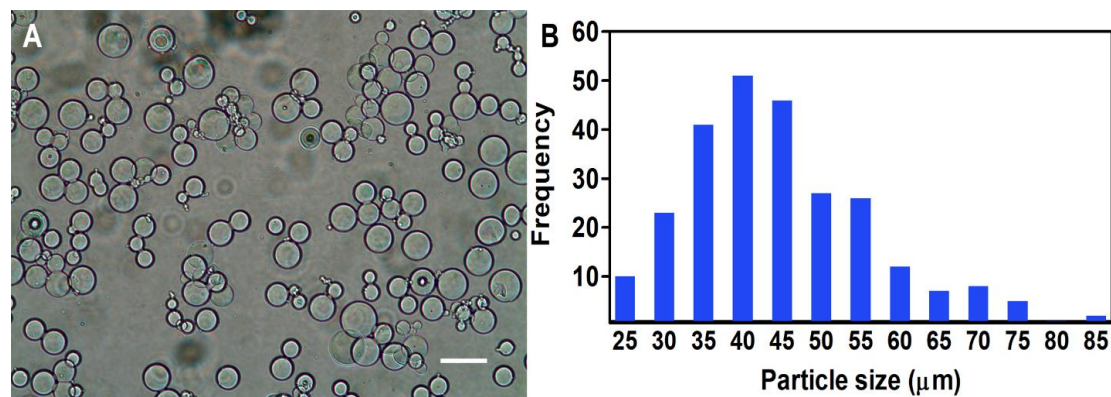


Figure S7-3. A) Optical micrograph of the gelatin microspheres swollen in PBS for 1 day. Scale bare is 100 μm . B) Size distribution of gelatin microspheres diameters in PBS measured by ImageJ

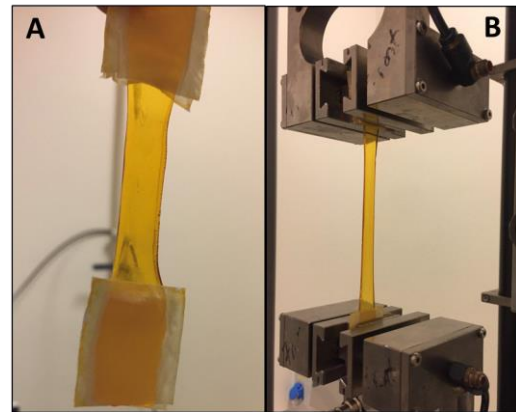


Figure S7-4. Images of gelatin hydrogel sample A) before and B) during tensile test

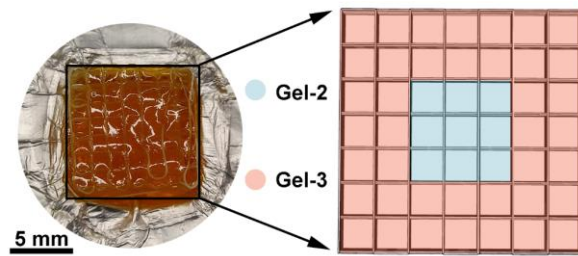


Figure S7-5. Distribution of gelatin matrices in a hybrid scaffold of PCL/Gel-GF

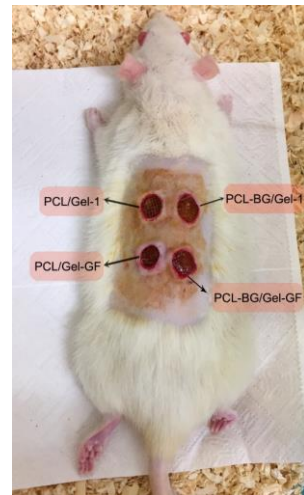


Figure S7-6. Configuration of the implanted scaffolds at Day 0

8 Conclusions and future works

The main theme of this thesis was 3D bioprinting of functionalized hybrid structures for tissue engineering with the focus on skin tissue engineering. To reach this goal, two main techniques of AM including melt electrowriting and extrusion printing was utilized. The findings of this work can be summarized as following:

In the first part a literature review on MEW, its principles, challenges, and potential towards tissue engineering was represented. The combinatory approach of MEW with other printing methods called “hybrid manufacturing” was discussed. In addition, mechanical and biological aspects of hybrid printing including MEW was reviewed as well. In this additive manufacturing technique, the printing parameters strongly affect the deposition of polymer filament. Thus, the operation window criteria were determined through a preliminary study on the effect of printing parameters on fiber diameter and its homogeneity. Furthermore, individual and mutual effects of those parameters were investigated with RSM. The predicted values were validated with experimental data within the confidence intervals. In this sense, these results guided further experiments regarding selection of processing parameters for the desired fiber diameters.

With materials perspective, we focused on physiochemical enhancement of PCL to address its limitations in terms of biocompatibility and degradability for skin tissue engineering applications. It was copolymerized with PPSu and functionalized with silver nitrate to induce its antibacterial properties. The results proved enhanced hydrophilicity and degradability compared to pure PCL with higher antibacterial properties without any toxicity to fibroblast cells. The printability of the final composite was demonstrated via extrusion printing with well-defined 3D mesh structures.

Hydrogel bioprinting is one of the gold standards in biomanufacturing of cell-laden structures. Considering the technical difficulties in adaptation of their physical properties to the process of bioprinting, we developed a composite support-bath for bioprintability of the hydrogels. Among the different complex formulations consisting of Pluronic-Laponite-CaCl₂, the support-bath expressing high recoverability over nozzle motion during printing was selected. Several complex structures were bioprinted using alginate as a sample hydrogel and

final structures possessed adequate shape fidelity without adversely affecting the cell viability. The proposed composite support-bath could be utilized for other bioinks as well.

The influence of geometrical features of hybrid scaffolds on mechanical properties and cellular responses were investigated for structures composed of thermoplastic polymer/hydrogel. Melt electrowriting was used to fabricate PCL mesh structures with 0-90° and 60-120° orientation, and honeycomb patterned constructs. The printing parameters were selected according to the results obtained from the previous chapter. The gelatin hydrogel was infiltrated into the mesh structures and photo-crosslinked in the presence of Ru/SPS as photo-initiator system in visible light without further modifications. Mechanical tensile test results revealed that hybrid honeycomb structure showed synergistic effect with high elastic energies and concurrently high elastic modulus values with more than 100% elongation until break. HSFs and HUVECs were encapsulated in gelatin hydrogel with the purpose of construction of vascularized skin tissue. The honeycomb structure guided cells to form cord-like structures which could be an initial stage of vascular formation. These findings suggest the potential capability of adjusting scaffold's architecture to fine tune biological response for different tissue applications.

The final chapter was designated to manufacturing of hybrid thermoplastic polymer-hydrogel scaffolds for wound healing application. The implemented PCL design with bioactive glass containing silicon, calcium, phosphorus, and silver oxides increased the bioactivity, improved antibacterial properties and stimulated angiogenesis. GMS were synthesized and loaded with growth factors with the aim of providing stability and controlled release from the gelatin. GMS were encapsulated into gelatin hydrogel and selectively casted inside the melt electrowritten PCL-BG mesh structures. *In vivo* implantation of the hybrid scaffolds revealed enhancement in the healing process regarding histological evaluation data such as epithelialization, fibroblast/collagen amount, edema, and integration with environmental tissue as well as the wound closure time.

As future works the following areas of research could be considered:

MEW of thermoplastic polymers with heat resistant bioactive molecules/drugs/additives and their effects on cellular responses could be of great interest, especially by considering the potential of MEW in fabrication of ordered and at the same time delicate porous structures with high surface area. In this respect, guiding the differentiation of stem cells for different tissue types by means of biochemical signals from microfibers could be an interesting area of research. In addition, drugs could also be loaded into carriers including microspheres and nanotubes for sustained release.

The explored methodology for fabrication of hybrid structures produced by MEW and gel casting might be further extended through application of other hydrogels such as GelMA, Matrigel, and collagen, which could potentially offer different biochemical stimuli and inducing diverse regeneration capacities. Moreover, using multi-head printing setups for simultaneous or sequential MEW of thermoplastic polymers and extrusion printing of various hydrogels might provide new opportunities, especially in terms of accurate and local deposition of biomarkers and biochemicals in a delicate fibrous mesh structure. Considering the fabrication limitation of MEW, it could be combined with AM methods could also be a topic of research for the manufacturing of thick structures. In this way, thick hybrid (thermoplastic-hydrogel) structures could be fabricated through MEW-extrusion of polymer and hydrogel, respectively.

More detailed studies on the influence of both architectural design of thermoplastic polymer and biochemical properties of hydrogel could be anticipated regarding mechanical and cellular responses. The architecture of scaffolds could be systematically analyzed, and several factors such as varying fiber diameters, filament distances, and gradient filament distances could be considered. Other parameters related to the hydrogel matrix such as crosslinking density and the resulting stiffness and porosity of hydrogel could be also investigated. Guiding the cellular migration and differentiation pathways through scaffold design and biomechanical cues and in particular, stem cell differentiation, cellular morphogenesis and vascularization would be of great importance.

9 References

- [1] R.D. Pedde, B. Mirani, A. Navaei, T. Styan, S. Wong, M. Mehrali, A. Thakur, N.K. Mohtaram, A. Bayati, A. Dolatshahi-Pirouz, M. Nikkhah, S.M. Willerth, M. Akbari, Emerging Biofabrication Strategies for Engineering Complex Tissue Constructs, *Adv. Mater.* 29 (2017) 1–27. <https://doi.org/10.1002/adma.201606061>.
- [2] D. Howard, L.D. Butterly, K.M. Shakesheff, S.J. Roberts, Tissue engineering: Strategies, stem cells and scaffolds, *J. Anat.* 213 (2008) 66–72. <https://doi.org/10.1111/j.1469-7580.2008.00878.x>.
- [3] F.P.W. Melchels, M.A.N. Domingos, T.J. Klein, J. Malda, P.J. Bartolo, D.W. Hutmacher, Additive manufacturing of tissues and organs, *Prog. Polym. Sci.* 37 (2012) 1079–1104. <https://doi.org/10.1016/j.progpolymsci.2011.11.007>.
- [4] J.K. Placone, A.J. Engler, Recent advances in extrusion-based 3D printing for biomedical applications, *Adv. Healthc. Mater.* 7 (2018) 1701161. <https://doi.org/10.1016/j.physbeh.2017.03.040>.
- [5] U. Jammalamadaka, K. Tappa, Recent advances in biomaterials for 3D printing and tissue engineering, *J. Funct. Biomater.* 9 (2018). <https://doi.org/10.3390/jfb9010022>.
- [6] F. Tourlomousis, H. Ding, D.M. Kalyon, R.C. Chang, Melt Electrospinning Writing Process Guided by a “Printability Number,” *J. Manuf. Sci. Eng.* 139 (2017) 081004. <https://doi.org/10.1115/1.4036348>.
- [7] H. Savoji, B. Godau, M.S. Hassani, M. Akbari, Skin Tissue Substitutes and Biomaterial Risk Assessment and Testing, *Front. Bioeng. Biotechnol.* 6 (2018) 1–18. <https://doi.org/10.3389/fbioe.2018.00086>.
- [8] H.G. Yi, H. Lee, D.W. Cho, 3D printing of organs-on-chips, *Bioengineering* 4 (2017) 10. <https://doi.org/10.3390/bioengineering4010010>.
- [9] J.R. Dias, P.L. Granja, P.J. Bártolo, Advances in electrospun skin substitutes, *Prog. Mater. Sci.* 84 (2016) 314–334. <https://doi.org/10.1016/j.pmatsci.2016.09.006>.
- [10] R.G. Frykberg, J. Banks, Challenges in the Treatment of Chronic Wounds, *Adv. Wound Care* 4 (2015) 560–582. <https://doi.org/10.1089/wound.2015.0635>.
- [11] F. Groeber, M. Holeiter, M. Hampel, S. Hinderer, K. Schenke-Layland, Skin tissue engineering - In vivo and in vitro applications, *Adv. Drug Deliv. Rev.* 63 (2011) 352–366. <https://doi.org/10.1016/j.addr.2011.01.005>.
- [12] D.G. Tamay, T.D. Usal, A.S. Alagoz, D. Yucel, N. Hasirci, V. Hasirci, 3D and 4D printing of polymers for tissue engineering applications, *Front. Bioeng. Biotechnol.* 7 (2019). <https://doi.org/10.3389/fbioe.2019.00164>.
- [13] and N.A.P. Brandon V. Slaughter, Shahana S. Khurshid, Omar Z. Fisher, Ali Khademhosseini, Hydrogels in Regenerative Medicine, *Adv. Mater.* 21 (2009) 3307–3329. <https://doi.org/10.1002/adma.200802106>.
- [14] J.L. Drury, D.J. Mooney, Hydrogels for tissue engineering: Scaffold design variables and

applications, *Biomaterials*. 24 (2003) 4337–4351. [https://doi.org/10.1016/S0142-9612\(03\)00340-5](https://doi.org/10.1016/S0142-9612(03)00340-5).

- [15] F. Afghah, C. Dikyol, M. Altunbek, B. Koc, Biomimicry in bio-manufacturing: Developments in melt electrospinning writing technology towards hybrid biomanufacturing, *Appl. Sci.* 9 (2019) 3540. <https://doi.org/10.3390/app9173540>.
- [16] F. Afghah, M. Ullah, J. Seyyed Monfared Zanjani, P.A. Sut, O. Sen, M. Emanet, B.S. Okan, M. Culha, Y. Menceloglu, M. Yildiz, B. Koc, 3D printing of silver-doped polycaprolactone-poly(propylene succinate) composite scaffolds for skin tissue engineering, *Biomed. Mater.* 15 (2020) 035015. <https://doi.org/10.1088/1748-605X/ab7417>.
- [17] C.B.C.B. Dayan, F. Afghah, B.S.B.S. Okan, M. Yıldız, Y. Menceloglu, M. Culha, B. Koc, Modeling 3D melt electrospinning writing by response surface methodology, *Mater. Des.* 148 (2018) 87–95. <https://doi.org/10.1016/j.matdes.2018.03.053>.
- [18] F. Afghah, M. Altunbek, C. Dikyol, B. Koc, Preparation and characterization of nanoclay-hydrogel composite support-bath for bioprinting of complex structures, *Sci. Rep.* 10 (2020) 5257. <https://doi.org/10.1038/s41598-020-61606-x>.
- [19] G.H. Yang, F. Mun, G.H. Kim, Direct electrospinning writing for producing 3D hybrid constructs consisting of microfibers and macro-struts for tissue engineering, *Chem. Eng. J.* 288 (2016) 648–658. <https://doi.org/10.1016/j.cej.2015.12.047>.
- [20] S. Zaiss, T.D. Brown, J.C. Reichert, A. Berner, Poly(ϵ -caprolactone) scaffolds fabricated by melt electrospinning for bone tissue engineering, *Materials (Basel)*. 9 (2016) 1–15. <https://doi.org/10.3390/ma9040232>.
- [21] P.D. Dalton, M.L. Muerza-Cascante, D.W. Hutmacher, Design and fabrication of scaffolds via melt electrospinning for applications in tissue engineering, *RSC Polym. Chem. Ser.* 2015-Janua (2015) 100–120. <https://doi.org/10.1039/9781849735575-00100>.
- [22] H. Chen, Y. Peng, S. Wu, L.P. Tan, Electrospun 3D fibrous scaffolds for chronic wound repair, *Materials (Basel)*. 9 (2016) 1–12. <https://doi.org/10.3390/ma9040272>.
- [23] C. Intini, L. Elviri, J. Cabral, S. Mros, C. Bergonzi, A. Bianchera, L. Flammini, P. Govoni, E. Barocelli, R. Bettini, M. McConnell, 3D-printed chitosan-based scaffolds: An in vitro study of human skin cell growth and an in-vivo wound healing evaluation in experimental diabetes in rats, *Carbohydr. Polym.* 199 (2018) 593–602. <https://doi.org/10.1016/j.carbpol.2018.07.057>.
- [24] S. Ahn, Y. Kim, H. Lee, G. Kim, A new hybrid scaffold constructed of solid freeform-fabricated PCL struts and collagen struts for bone tissue regeneration: Fabrication, mechanical properties, and cellular activity, *J. Mater. Chem.* 22 (2012) 15901–15909. <https://doi.org/10.1039/c2jm33310d>.
- [25] S.H. Hsu, K.C. Hung, C.W. Chen, Biodegradable polymer scaffolds, *J. Mater. Chem. B*. 4 (2016) 7493–7505. <https://doi.org/10.1039/c6tb02176j>.
- [26] A.A. Zadpoor, J. Malda, Additive Manufacturing of Biomaterials, Tissues, and Organs, *Ann. Biomed. Eng.* 45 (2017) 1–11. <https://doi.org/10.1007/s10439-016-1719-y>.

- [27] S.M. Giannitelli, D. Accoto, M. Trombetta, A. Rainer, Current trends in the design of scaffolds for computer-aided tissue engineering, *Acta Biomater.* 10 (2014) 580–594. <https://doi.org/10.1016/j.actbio.2013.10.024>.
- [28] P. Ahangar, M.E. Cooke, M.H. Weber, D.H. Rosenzweig, Current Biomedical Applications of 3D Printing and Additive Manufacturing, *Appl. Sci.* 9 (2019) 1713. <https://doi.org/10.3390/app9081713>.
- [29] S. Bose, D. Ke, H. Sahasrabudhe, A. Bandyopadhyay, Additive manufacturing of biomaterials, *Prog. Mater. Sci.* 93 (2018) 45–111. <https://doi.org/10.1016/j.pmatsci.2017.08.003>.
- [30] S.S.D. Carter, P.F. Costa, C. Vaquette, S. Ivanovski, D.W. Hutmacher, J. Malda, Additive Biomanufacturing: An Advanced Approach for Periodontal Tissue Regeneration, *Ann. Biomed. Eng.* 45 (2017) 12–22. <https://doi.org/10.1007/s10439-016-1687-2>.
- [31] F. Ning, W. Cong, J. Qiu, J. Wei, S. Wang, Additive manufacturing of carbon fiber reinforced thermoplastic composites using fused deposition modeling, *Compos. Part B Eng.* 80 (2015) 369–378. <https://doi.org/10.1016/j.compositesb.2015.06.013>.
- [32] M.L. Shofner, K. Lozano, F.J. Rodríguez-Macías, E. V. Barrera, Nanofiber-reinforced polymers prepared by fused deposition modeling, *J. Appl. Polym. Sci.* 89 (2003) 3081–3090. <https://doi.org/10.1002/app.12496>.
- [33] D.W. Hutmacher, T. Schantz, I. Zein, K.W. Ng, S.H. Teoh, K.C. Tan, Mechanical properties and cell cultural response of polycaprolactone scaffolds designed and fabricated via fused deposition modeling, *J. Biomed. Mater. Res.* 55 (2001) 203–216. [https://doi.org/10.1002/1097-4636\(200105\)55:2<203::AID-JBM1007>3.0.CO;2-7](https://doi.org/10.1002/1097-4636(200105)55:2<203::AID-JBM1007>3.0.CO;2-7).
- [34] K.W. Lee, S. Wang, B.C. Fox, E.L. Ritman, M.J. Yaszemski, L. Lu, Poly(propylene fumarate) bone tissue engineering scaffold fabrication using stereolithography: Effects of resin formulations and laser parameters, *Biomacromolecules.* 8 (2007) 1077–1084. <https://doi.org/10.1021/bm060834v>.
- [35] T. Boland, T. Xu, B. Damon, X. Cui, Application of inkjet printing to tissue engineering, *Biotechnol. J.* 1 (2006) 910–917. <https://doi.org/10.1002/biot.200600081>.
- [36] J.P. Kruth, G. Levy, F. Klocke, T.H.C. Childs, Consolidation phenomena in laser and powder-bed based layered manufacturing, *CIRP Ann. - Manuf. Technol.* 56 (2007) 730–759. <https://doi.org/10.1016/j.cirp.2007.10.004>.
- [37] D. Li, Y. Xia, Electrospinning of nanofibers: Reinventing the wheel?, *Adv. Mater.* 16 (2004) 1151–1170. <https://doi.org/10.1002/adma.200400719>.
- [38] T. Xu, Z. Liang, B. Ding, Q. Feng, H. Fong, Polymer blend nanofibers containing polycaprolactone as biocompatible and biodegradable binding agent to fabricate electrospun three-dimensional scaffolds/structures, *Polymer (Guildf).* 151 (2018) 299–306. <https://doi.org/10.1016/j.polymer.2018.07.074>.
- [39] T. Xu, Q. Yao, J.M. Miszuk, H.J. Sanyour, Z. Hong, H. Sun, H. Fong, Tailoring weight ratio of PCL/PLA in electrospun three-dimensional nanofibrous scaffolds and the effect on osteogenic differentiation of stem cells, *Colloids Surfaces B Biointerfaces.* 171 (2018)

31–39. <https://doi.org/10.1016/j.colsurfb.2018.07.004>.

- [40] J.M. Miszuk, T. Xu, Q. Yao, F. Fang, J.D. Childs, Z. Hong, J. Tao, H. Fong, H. Sun, Functionalization of PCL-3D electrospun nanofibrous scaffolds for improved BMP2-induced bone formation, *Appl. Mater. Today.* 10 (2018) 194–202. <https://doi.org/10.1016/j.apmt.2017.12.004>.
- [41] T. Xu, J.M. Miszuk, Y. Zhao, H. Sun, H. Fong, Electrospun Polycaprolactone 3D Nanofibrous Scaffold with Interconnected and Hierarchically Structured Pores for Bone Tissue Engineering, *Adv. Healthc. Mater.* 4 (2015) 2238–2246. <https://doi.org/10.1002/adhm.201500345>.
- [42] Q. Yao, J.G.L. Cosme, T. Xu, J.M. Miszuk, P.H.S. Picciani, H. Fong, H. Sun, Three dimensional electrospun PCL/PLA blend nanofibrous scaffolds with significantly improved stem cells osteogenic differentiation and cranial bone formation, *Biomaterials.* 115 (2017) 115–127. <https://doi.org/10.1016/j.biomaterials.2016.11.018>.
- [43] A. Timnak, J.A. Gerstenhaber, K. Dong, Y. El Har-El, P.I. Lelkes, Gradient porous fibrous scaffolds: A novel approach to improving cell penetration in electrospun scaffolds, *Biomed. Mater.* 13 (2018). <https://doi.org/10.1088/1748-605X/aadbbe>.
- [44] M.E. Frohbergh, A. Katsman, G.P. Botta, P. Lazarovici, C.L. Schauer, U.G.K. Wegst, P.I. Lelkes, Electrospun hydroxyapatite-containing chitosan nanofibers crosslinked with genipin for bone tissue engineering, *Biomaterials.* 33 (2012) 9167–9178. <https://doi.org/10.1016/j.biomaterials.2012.09.009>.
- [45] H. Lian, Z. Meng, Melt electrospinning vs. solution electrospinning: A comparative study of drug-loaded poly (ϵ -caprolactone) fibres, *Mater. Sci. Eng. C.* 74 (2017) 117–123. <https://doi.org/10.1016/j.msec.2017.02.024>.
- [46] D. Lukáš, A. Sarkar, L. Martinová, K. Vodsed'álková, D. Lubasová, J. Chaloupek, P. Pokorný, P. Mikeš, J. Chvojka, M. Komárek, Physical principles of electrospinning (electrospinning as a nano-scale technology of the twenty-first century), *Text. Prog.* 41 (2009) 59–140. <https://doi.org/10.1080/00405160902904641>.
- [47] Y. Zhang, H. Ouyang, T.L. Chwee, S. Ramakrishna, Z.M. Huang, Electrospinning of gelatin fibers and gelatin/PCL composite fibrous scaffolds, *J. Biomed. Mater. Res. - Part B Appl. Biomater.* 72 (2005) 156–165. <https://doi.org/10.1002/jbm.b.30128>.
- [48] Q.P. Pham, U. Sharma, A.G. Mikos, Electrospinning of Polymeric Nanofibers for Tissue Engineering Applications: A Review, *Tissue Eng.* 0 (2006) 060509065116001. <https://doi.org/10.1089/ten.2006.12.ft-65>.
- [49] T.D. Brown, P.D. Dalton, D.W. Hutmacher, Melt electrospinning today: An opportune time for an emerging polymer process, *Prog. Polym. Sci.* 56 (2016) 116–166. <https://doi.org/10.1016/j.progpolymsci.2016.01.001>.
- [50] L.H. Zhang, X.P. Duan, X. Yan, M. Yu, X. Ning, Y. Zhao, Y.Z. Long, Recent advances in melt electrospinning, *RSC Adv.* 6 (2016) 53400–53414. <https://doi.org/10.1039/c6ra09558e>.
- [51] D. Sun, C. Chang, S. Li, L. Lin, Near-field electrospinning, *Nano Lett.* 6 (2006) 839–842.

<https://doi.org/10.1021/nl0602701>.

- [52] M. Lee, H.Y. Kim, Toward nanoscale three-dimensional printing: Nanowalls built of electrospun nanofibers, *Langmuir*. 30 (2014) 1210–1214. <https://doi.org/10.1021/la404704z>.
- [53] C.Y. Xu, R. Inai, M. Kotaki, S. Ramakrishna, Aligned biodegradable nanofibrous structure: A potential scaffold for blood vessel engineering, *Biomaterials*. 25 (2004) 877–886. [https://doi.org/10.1016/S0142-9612\(03\)00593-3](https://doi.org/10.1016/S0142-9612(03)00593-3).
- [54] L. Wannatong, A. Sirivat, P. Supaphol, Effects of solvents on electrospun polymeric fibers: Preliminary study on polystyrene, *Polym. Int.* 53 (2004) 1851–1859. <https://doi.org/10.1002/pi.1599>.
- [55] D. Li, G. Ouyang, J.T. McCann, Y. Xia, Collecting electrospun nanofibers with patterned electrodes, *Nano Lett.* 5 (2005) 913–916. <https://doi.org/10.1021/nl0504235>.
- [56] J. Lee, S.Y. Lee, J. Jang, Y.H. Jeong, D.W. Cho, Fabrication of patterned nanofibrous mats using direct-write electrospinning, *Langmuir*. 28 (2012) 7267–7275. <https://doi.org/10.1021/la3009249>.
- [57] F.M. Wunner, M.L. Wille, T.G. Noonan, O. Bas, P.D. Dalton, E.M. De-Juan-Pardo, D.W. Hutmacher, Melt Electrospinning Writing of Highly Ordered Large Volume Scaffold Architectures, *Adv. Mater.* 30 (2018) 1–6. <https://doi.org/10.1002/adma.201706570>.
- [58] H. Zhou, T.B. Green, Y.L. Joo, The thermal effects on electrospinning of polylactic acid melts, *Polymer (Guildf)*. 47 (2006) 7497–7505. <https://doi.org/10.1016/j.polymer.2006.08.042>.
- [59] H. Ding, K. Cao, F. Zhang, R.C. Chang, A fundamental study of charge effects on the melt electrowritten polymer fibers, *Mater. Des.* 178 (2019) 107857. <https://doi.org/10.1016/j.matdes.2019.107857>.
- [60] X. Li, H. Liu, J. Wang, C. Li, Preparation and characterization of poly(ϵ -caprolactone) nonwoven mats via melt electrospinning, *Polymer (Guildf)*. 53 (2012) 248–253. <https://doi.org/10.1016/j.polymer.2011.11.008>.
- [61] J. He, P. Xia, D. Li, Development of melt electrohydrodynamic 3D printing for complex microscale poly (ϵ -caprolactone) scaffolds, *Biofabrication*. 8 (2016). <https://doi.org/10.1088/1758-5090/8/3/035008>.
- [62] G. Hochleitner, T. Jüngst, T.D. Brown, K. Hahn, C. Moseke, F. Jakob, P.D. Dalton, J. Groll, Additive manufacturing of scaffolds with sub-micron filaments via melt electrospinning writing, *Biofabrication*. 7 (2015) 35002. <https://doi.org/10.1088/1758-5090/7/3/035002>.
- [63] O. Bas, E.M. De-Juan-Pardo, M.P. Chhaya, F.M. Wunner, J.E. Jeon, T.J. Klein, D.W. Hutmacher, Enhancing structural integrity of hydrogels by using highly organised melt electrospun fibre constructs, *Eur. Polym. J.* 72 (2015) 451–463. <https://doi.org/10.1016/j.eurpolymj.2015.07.034>.
- [64] J. Lannutti, D. Reneker, T. Ma, D. Tomasko, D. Farson, Electrospinning for tissue

engineering scaffolds, *Mater. Sci. Eng. C*. 27 (2007) 504–509. <https://doi.org/10.1016/j.msec.2006.05.019>.

- [65] T.D. Brown, P.D. Dalton, D.W. Hutmacher, Direct writing by way of melt electrospinning, *Adv. Mater.* 23 (2011) 5651–5657. <https://doi.org/10.1002/adma.201103482>.
- [66] C. Wei, J. Dong, Direct fabrication of high-resolution three-dimensional polymeric scaffolds using electrohydrodynamic hot jet plotting, *J. Micromechanics Microengineering*. 23 (2013). <https://doi.org/10.1088/0960-1317/23/2/025017>.
- [67] D.W. Hutmacher, P.D. Dalton, Melt electrospinning, *Chem. - An Asian J.* 6 (2011) 44–56. <https://doi.org/10.1002/asia.201000436>.
- [68] J. Yong Lak, H. Zhou, Apparatus and method for elevated temperature electrospinning, 7,326,043, 2008.
- [69] F.M. Wunner, S. Florczak, P. Miesczanek, O. Bas, E.M. De-Juan-Pardo, D.W. Hutmacher, *Electrospinning With Polymer Melts – State of the Art and Future Perspectives*, Elsevier Ltd., 2017. <https://doi.org/10.1016/b978-0-12-803581-8.09318-8>.
- [70] S. Sukigara, M. Gandhi, J. Ayutsede, M. Micklus, F. Ko, Regeneration of Bombyx mori silk by electrospinning - Part 1: Processing parameters and geometric properties, *Polymer (Guildf)*. 44 (2003) 5721–5727. [https://doi.org/10.1016/S0032-3861\(03\)00532-9](https://doi.org/10.1016/S0032-3861(03)00532-9).
- [71] C.C. Qin, X.P. Duan, L. Wang, L.H. Zhang, M. Yu, R.H. Dong, X. Yan, H.W. He, Y.Z. Long, Melt electrospinning of poly(lactic acid) and polycaprolactone microfibers by using a hand-operated Wimshurst generator, *Nanoscale*. 7 (2015) 16611–16615. <https://doi.org/10.1039/c5nr05367f>.
- [72] C. Subramanian, S.C. Ugbolue, S.B. Warner, P.K. Patra, The melt electrospinning of polycaprolactone (PCL) ultrafine fibers, *Mater. Res. Soc. Symp.* 1134 (2008). <https://doi.org/10.1557/PROC-1134-BB08-18>.
- [73] S. Naoki, H. Tsutsumi, K. Nakane, T. Ogihara, N. Ogata, Poly(ethylene-co-vinyl alcohol) and Nylon 6/12 Nanofibers Produced by Melt Electrospinning System Equipped with a Line-Like Laser Beam Melting Device, *J. Appl. Polym. Sci.* 116 (2010) 2998–3004. <https://doi.org/10.1002/app>.
- [74] Z. Yang, H. Peng, W. Wang, T. Liu, Crystallization behavior of poly(ϵ -caprolactone)/layered double hydroxide nanocomposites, *J. Appl. Polym. Sci.* 116 (2010) 2658–2667. <https://doi.org/10.1002/app>.
- [75] P.D. Dalton, D. Grafahrend, K. Klinkhammer, D. Klee, M. Möller, Electrospinning of polymer melts: Phenomenological observations, *Polymer (Guildf)*. 48 (2007) 6823–6833. <https://doi.org/10.1016/j.polymer.2007.09.037>.
- [76] N. Detta, T.D. Brown, F.K. Edin, K. Albrecht, F. Chiellini, E. Chiellini, P.D. Dalton, D.W. Hutmacher, Melt electrospinning of polycaprolactone and its blends with poly(ethylene glycol), *Polym. Int.* 59 (2010) 1558–1562. <https://doi.org/10.1002/pi.2954>.
- [77] J. Lyons, C. Li, F. Ko, Melt-electrospinning part I: Processing parameters and geometric

- properties, *Polymer* (Guildf). 45 (2004) 7597–7603. <https://doi.org/10.1016/j.polymer.2004.08.071>.
- [78] T. Jungst, M.L. Muerza-Cascante, T.D. Brown, M. Standfest, D.W. Hutmacher, J. Groll, P.D. Dalton, Melt electrospinning onto cylinders: Effects of rotational velocity and collector diameter on morphology of tubular structures, *Polym. Int.* 64 (2015) 1086–1095. <https://doi.org/10.1002/pi.4948>.
- [79] T.D. Brown, A. Slotosch, L. Thibaudeau, A. Taubenberger, D. Loessner, C. Vaquette, P.D. Dalton, D.W. Hutmacher, Design and fabrication of tubular scaffolds via direct writing in a melt electrospinning mode, *Biointerphases.* 7 (2012) 1–16. <https://doi.org/10.1007/s13758-011-0013-7>.
- [80] T.D. Brown, F. Edin, N. Detta, A.D. Skelton, D.W. Hutmacher, P.D. Dalton, Melt electrospinning of poly(ϵ -caprolactone) scaffolds: Phenomenological observations associated with collection and direct writing, *Mater. Sci. Eng. C.* 45 (2015) 698–708. <https://doi.org/10.1016/j.msec.2014.07.034>.
- [81] J. Fang, L. Zhang, D. Sutton, X. Wang, T. Lin, Needleless melt-electrospinning of polypropylene nanofibres, *J. Nanomater.* 2012 (2012). <https://doi.org/10.1155/2012/382639>.
- [82] K. Morikawa, A. Vashisth, C.J. Grimme, M.J. Green, M. Naraghi, Wire Melt Electrospinning of Thin Polymeric Fibers via Strong Electrostatic Field Gradients, *Macromol. Mater. Eng.* 304 (2019) 1–9. <https://doi.org/10.1002/mame.201800417>.
- [83] N. Mayadeo, K. Morikawa, M. Naraghi, M.J. Green, Modeling of downstream heating in melt electrospinning of polymers, *J. Polym. Sci. Part B Polym. Phys.* 55 (2017) 1393–1405. <https://doi.org/10.1002/polb.24394>.
- [84] Y. Li, X. Wang, S. Yu, Y. Zhao, X. Yan, J. Zheng, M. Yu, S.-Y. Yan, Y.-Z. Long, Bubble Melt Electrospinning for Production of Polymer Microfibers, *Polymers (Basel).* 10 (2018) 1246. <https://doi.org/10.3390/polym10111246>.
- [85] H.Y. Li, M.M. Bubakir, T. Xia, X.F. Zhong, Y.M. Ding, W.M. Yang, Mass production of ultra-fine fibre by melt electrospinning method using umbellate spinneret, *Mater. Res. Innov.* 18 (2014) S4-921-S4-925. <https://doi.org/10.1179/1432891714z.000000000877>.
- [86] A. Hrynevich, B. Elçi, J.N. Haigh, R. McMaster, A. Youssef, C. Blum, T. Blunk, G. Hochleitner, J. Groll, P.D. Dalton, Dimension-Based Design of Melt Electrowritten Scaffolds, *Small.* 14 (2018) 1–6. <https://doi.org/10.1002/smll.201800232>.
- [87] A. Doustgani, E. Ahmadi, Melt electrospinning process optimization of polylactic acid nanofibers, *J. Ind. Text.* 45 (2016) 626–634. <https://doi.org/10.1177/1528083715610297>.
- [88] K. Acatay, E. Simsek, C. Ow-Yang, Y.Z. Menceloglu, Tunable, superhydrophobically stable polymeric surfaces by electrospinning, *Angew. Chemie - Int. Ed.* 43 (2004) 5210–5213. <https://doi.org/10.1002/anie.200461092>.
- [89] C. Boaretti, M. Roso, A. Lorenzetti, M. Modesti, Synthesis and process optimization of electrospun PEEK-sulfonated nanofibers by response surface methodology, *Materials (Basel).* 8 (2015) 4096–4117. <https://doi.org/10.3390/ma8074096>.

- [90] A. Patnaik, R.D. Anandjiwala, An optimized melt spinning process to increase the productivity of nanofiber materials, *J. Ind. Text.* 45 (2016) 1026–1037. <https://doi.org/10.1177/1528083714551439>.
- [91] S.X. Yu, J. Zheng, X. Yan, X.X. Wang, G. Di Nie, Y.Q. Tan, J. Zhang, K.Y. Sui, Y.Z. Long, Morphology control of PLA microfibers and spheres via melt electrospinning, *Mater. Res. Express.* 5 (2018). <https://doi.org/10.1088/2053-1591/aab9f4>.
- [92] E. Zhmayev, H. Zhou, Y.L. Joo, Modeling of non-isothermal polymer jets in melt electrospinning, *J. Nonnewton. Fluid Mech.* 153 (2008) 95–108. <https://doi.org/10.1016/j.jnnfm.2007.11.011>.
- [93] Y. Shen, Q. Liu, B. Deng, P. Yao, S. Xia, Experimental study and prediction of the diameter of melt-electrospinning polypropylene fiber, *Fibers Polym.* 17 (2016) 1227–1237. <https://doi.org/10.1007/s12221-016-6303-4>.
- [94] A. Youssef, S.J. Hollister, P.D. Dalton, Additive manufacturing of polymer melts for implantable medical devices and scaffolds, *Biofabrication.* 9 (2017). <https://doi.org/10.1088/1758-5090/aa5766>.
- [95] B.L. Farrugia, T.D. Brown, Z. Upton, D.W. Hutmacher, P.D. Dalton, T.R. Dargaville, Dermal fibroblast infiltration of poly(ϵ -caprolactone) scaffolds fabricated by melt electrospinning in a direct writing mode, *Biofabrication.* 5 (2013) 025001. <https://doi.org/10.1088/1758-5082/5/2/025001>.
- [96] M.L. Muerza-Cascante, A. Shokohmand, K. Khosrotehrani, D. Haylock, P.D. Dalton, D.W. Hutmacher, D. Loessner, Endosteal-like extracellular matrix expression on melt electrospun written scaffolds, *Acta Biomater.* 52 (2017) 145–158. <https://doi.org/10.1016/j.actbio.2016.12.040>.
- [97] J. Ko, N.K. Mohtaram, F. Ahmed, A. Montgomery, M. Carlson, P.C.D. Lee, S.M. Willerth, M.B.G. Jun, Fabrication of poly (ϵ -caprolactone) microfiber scaffolds with varying topography and mechanical properties for stem cell-based tissue engineering applications, *J. Biomater. Sci. Polym. Ed.* 25 (2014) 1–17. <https://doi.org/10.1080/09205063.2013.830913>.
- [98] M. Castilho, D. Feyen, M. Flandes-Iparraguirre, G. Hochleitner, J. Groll, P.A.F. Doevedans, T. Vermonden, K. Ito, J.P.G. Sluijter, J. Malda, Melt Electrospinning Writing of Poly-Hydroxymethylglycolide-co- ϵ -Caprolactone-Based Scaffolds for Cardiac Tissue Engineering, *Adv. Healthc. Mater.* 6 (2017) 1–9. <https://doi.org/10.1002/adhm.201700311>.
- [99] Y. Qin, L. Cheng, Y. Zhang, X. Chen, X. Wang, X. He, W. Yang, Y. An, H. Li, Efficient preparation of poly(lactic acid) nanofibers by melt differential electrospinning with addition of acetyl tributyl citrate, *J. Appl. Polym. Sci.* 135 (2018) 42–45. <https://doi.org/10.1002/app.46554>.
- [100] H. Xu, M. Yamamoto, H. Yamane, Melt electrospinning: Electrodynamics and spinnability, *Polymer (Guildf).* 132 (2017) 206–215. <https://doi.org/10.1016/j.polymer.2017.11.006>.

- [101] J.E. Sanders, S.E. Lamont, A. Karchin, S.L. Golledge, B.D. Ratner, Fibro-porous meshes made from polyurethane micro-fibers: Effects of surface charge on tissue response, *Biomaterials*. 26 (2005) 813–818. <https://doi.org/10.1016/j.biomaterials.2004.03.030>.
- [102] X.F. Wang, Z.M. Huang, Melt-electrospinning of PMMA, *Chinese J. Polym. Sci. (English Ed.* 28 (2010) 45–53. <https://doi.org/10.1007/s10118-010-8208-9>.
- [103] R. Nayak, I.L. Kyratzis, Y.B. Truong, R. Padhye, L. Arnold, Melt-electrospinning of polypropylene with conductive additives, *J. Mater. Sci.* 47 (2012) 6387–6396. <https://doi.org/10.1007/s10853-012-6563-3>.
- [104] F. Chen, G. Hochleitner, T. Woodfield, J. Groll, P.D. Dalton, B.G. Amsden, Additive Manufacturing of a Photo-Cross-Linkable Polymer via Direct Melt Electrospinning Writing for Producing High Strength Structures, *Biomacromolecules*. 17 (2016) 208–214. <https://doi.org/10.1021/acs.biomac.5b01316>.
- [105] S. Bertlein, G. Hochleitner, M. Schmitz, J. Tessmar, M. Raghunath, P.D. Dalton, J. Groll, Permanent Hydrophilization and Generic Bioactivation of Melt Electrowritten Scaffolds, *Adv. Healthc. Mater.* 1801544 (2019) 1801544. <https://doi.org/10.1002/adhm.201801544>.
- [106] G. Hochleitner, J.F. Hümmer, R. Luxenhofer, J. Groll, High definition fibrous poly(2-ethyl-2-oxazoline) scaffolds through melt electrospinning writing, *Polymer (Guildf.)*. 55 (2014) 5017–5023. <https://doi.org/10.1016/j.polymer.2014.08.024>.
- [107] S. Florczak, T. Lorson, T. Zheng, M. Mrlik, D.W. Hutmacher, M.J. Higgins, R. Luxenhofer, P.D. Dalton, Melt electrowriting of electroactive poly(vinylidene difluoride) fibers, *Polym. Int.* 68 (2019) 735–745. <https://doi.org/10.1002/pi.5759>.
- [108] M.L. Muerza-Cascante, D. Haylock, D.W. Hutmacher, P.D. Dalton, Melt Electrospinning and Its Technologization in Tissue Engineering, *Tissue Eng. Part B Rev.* 21 (2015) 187–202. <https://doi.org/10.1089/ten.teb.2014.0347>.
- [109] F.M. Wunner, S. Eggert, J. Maartens, O. Bas, P.D. Dalton, E.M. De-Juan-Pardo, D.W. Hutmacher, Design and Development of a Three-Dimensional Printing High-Throughput Melt Electrowriting Technology Platform, *3D Print. Addit. Manuf.* 6 (2018) 82–90. <https://doi.org/10.1089/3dp.2017.0149>.
- [110] K.F. Eichholz, D.A. Hoey, Mediating human stem cell behaviour via defined fibrous architectures by melt electrospinning writing, *Acta Biomater.* 75 (2018) 140–151. <https://doi.org/10.1016/j.actbio.2018.05.048>.
- [111] R. McMaster, C. Hoefner, A. Hrynevich, C. Blum, M. Wiesner, K. Wittmann, T.R. Dargaville, P. Bauer-Kreisel, J. Groll, P.D. Dalton, T. Blunk, Tailored Melt Electrowritten Scaffolds for the Generation of Sheet-Like Tissue Constructs from Multicellular Spheroids, *Adv. Healthc. Mater.* March (2019) 1801326. <https://doi.org/10.1002/adhm.201801326>.
- [112] G. Hochleitner, F. Chen, C. Blum, P.D. Dalton, B. Amsden, J. Groll, Melt electrowriting below the critical translation speed to fabricate crimped elastomer scaffolds with non-linear extension behaviour mimicking that of ligaments and tendons, *Acta Biomater.* 72 (2018) 110–120. <https://doi.org/10.1016/j.actbio.2018.03.023>.

- [113] J. Zeng, H. Wang, Y. Lin, J. Zhang, F. Liang, F. Fang, F. Yang, P. Wang, Z. Zhu, X. Chen, X. Chen, Z. Wang, N. Cai, Y. Tang, P. Wu, Fabrication of microfluidic channels based on melt-electrospinning direct writing, *Microfluid. Nanofluidics.* 22 (2018) 23. <https://doi.org/10.1007/s10404-018-2043-7>.
- [114] E. Schnell, K. Klinkhammer, S. Balzer, G. Brook, D. Klee, P. Dalton, J. Mey, Guidance of glial cell migration and axonal growth on electrospun nanofibers of poly- ϵ -caprolactone and a collagen/poly- ϵ -caprolactone blend, *Biomaterials.* 28 (2007) 3012–3025. <https://doi.org/10.1016/j.biomaterials.2007.03.009>.
- [115] A. Fuchs, A. Youssef, A. Seher, G. Hochleitner, P.D. Dalton, S. Hartmann, R.C. Brands, U.D.A. Müller-Richter, C. Linz, Medical-grade polycaprolactone scaffolds made by melt electrospinning writing for oral bone regeneration - A pilot study in vitro, *BMC Oral Health.* 19 (2019) 1–11. <https://doi.org/10.1186/s12903-019-0717-5>.
- [116] D. Yan, J. Jones, X. Yuan, X. Xu, J. Sheng, J.C.M. Lee, G. Ma, Q. Yu, Plasma treatment of random and aligned electrospun PCL nanofibers, *J. Med. Biol. Eng.* 33 (2013) 171–178. <https://doi.org/10.5405/jmbe.1072>.
- [117] N. Abbasi, S. Soudi, N. Hayati-Roodbari, M. Dodel, M. Soleimani, The effects of plasma treated electrospun nanofibrous poly (ϵ -caprolactone) Scaffolds with different orientations on mouse embryonic stem cell proliferation, *Cell J.* 16 (2014) 245–254.
- [118] A.P. Hollander, S.C. Dickinson, W. Kafienah, Stem cells and cartilage development: Complexities of a simple tissue, *Stem Cells.* 28 (2010) 1992–1996. <https://doi.org/10.1002/stem.534>.
- [119] M. de Ruijter, A. Ribeiro, I. Dokter, M. Castilho, J. Malda, Simultaneous Micropatterning of Fibrous Meshes and Bioinks for the Fabrication of Living Tissue Constructs, *Adv. Healthc. Mater.* 8 (2019). <https://doi.org/10.1002/adhm.201800418>.
- [120] P.A. Levett, F.P.W. Melchels, K. Schrobbach, D.W. Hutmacher, J. Malda, T.J. Klein, A biomimetic extracellular matrix for cartilage tissue engineering centered on photocurable gelatin, hyaluronic acid and chondroitin sulfate, *Acta Biomater.* 10 (2014) 214–223. <https://doi.org/10.1016/j.actbio.2013.10.005>.
- [121] P.M. Kharkar, K.L. Kiick, A.M. Kloxin, Designing degradable hydrogels for orthogonal control of cell microenvironments, *Chem. Soc. Rev.* 42 (2013) 7335–7372. <https://doi.org/10.1039/c3cs60040h>.
- [122] J. Visser, F.P.W.W. Melchels, J.E. Jeon, E.M. van Bussel, L.S. Kimpton, H.M. Byrne, W.J.A.A. Dhert, P.D. Dalton, D.W. Hutmacher, J. Malda, Reinforcement of hydrogels using three-dimensionally printed microfibres, *Nat. Commun.* 6 (2015) 1–10. <https://doi.org/10.1038/ncomms7933>.
- [123] O. Bas, E.M. De-Juan-Pardo, C. Meinert, D. D'Angella, J.G. Baldwin, L.J. Bray, R.M. Wellard, S. Kollmannsberger, E. Rank, C. Werner, T.J. Klein, I. Catelas, D.W. Hutmacher, Biofabricated soft network composites for cartilage tissue engineering., *Biofabrication.* 9 (2017) 025014. <https://doi.org/10.1088/1758-5090/aa6b15>.
- [124] M. Castilho, G. Hochleitner, W. Wilson, B. Van Rietbergen, P.D. Dalton, J. Groll, J.

Malda, K. Ito, Mechanical behavior of a soft hydrogel reinforced with three-dimensional printed microfibre scaffolds, *Sci. Rep.* 8 (2018) 1–10. <https://doi.org/10.1038/s41598-018-19502-y>.

- [125] O. Bas, S. Lucarotti, D.D. Angella, N.J. Castro, C. Meinert, F.M. Wunner, E. Rank, G. Vozzi, T.J. Klein, I. Catelas, E.M. De-Juan-Pardo, D.W. Hutmacher, Rational design and fabrication of multiphasic soft network composites for tissue engineering articular cartilage: A numerical model-based approach, *Chem. Eng. J.* 340 (2018) 15–23. <https://doi.org/10.1016/j.cej.2018.01.020>.
- [126] M. Castilho, V. Mouser, M. Chen, J. Malda, K. Ito, Bi-layered micro-fibre reinforced hydrogels for articular cartilage regeneration, *Acta Biomater.* (2019). <https://doi.org/10.1016/j.actbio.2019.06.030>.
- [127] O. Bas, D. D'Angella, J.G. Baldwin, N.J. Castro, F.M. Wunner, N.T. Saidy, S. Kollmannsberger, A. Reali, E. Rank, E.M. De-Juan-Pardo, D.W. Hutmacher, An Integrated Design, Material, and Fabrication Platform for Engineering Biomechanically and Biologically Functional Soft Tissues, *ACS Appl. Mater. Interfaces.* 9 (2017) 29430–29437. <https://doi.org/10.1021/acsami.7b08617>.
- [128] M. Castilho, A. van Mil, M. Maher, C.H.G. Metz, G. Hochleitner, J. Groll, P.A. Doevedans, K. Ito, J.P.G. Sluijter, J. Malda, Melt Electrowriting Allows Tailored Microstructural and Mechanical Design of Scaffolds to Advance Functional Human Myocardial Tissue Formation, *Adv. Funct. Mater.* 1803151 (2018) 1–10. <https://doi.org/10.1002/adfm.201803151>.
- [129] N.T. Saidy, F. Wolf, O. Bas, H. Keijdener, D.W. Hutmacher, P. Mela, E.M. De-Juan-Pardo, Biologically Inspired Scaffolds for Heart Valve Tissue Engineering via Melt Electrowriting, *Small.* 1900873 (2019) 1–15. <https://doi.org/10.1002/smll.201900873>.
- [130] D. Loessner, A. Rockstroh, A. Shokoohmand, B.M. Holzapfel, F. Wagner, J. Baldwin, M. Boxberg, B. Schmalfeldt, E. Lengyel, J.A. Clements, D.W. Hutmacher, A 3D tumor microenvironment regulates cell proliferation, peritoneal growth and expression patterns, *Biomaterials.* 190–191 (2019) 63–75. <https://doi.org/10.1016/j.biomaterials.2018.10.014>.
- [131] D.W. Hutmacher, F. Wagner, L.C. Martine, B.M. Holzapfel, C. Theodoropoulos, O. Bas, F.M. Savi, E.M. De-Juan-Pardo, D.W. Hutmacher, Periosteum tissue engineering in an orthotopic in vivo platform, *Biomaterials.* 121 (2017) 193–204. <https://doi.org/10.1016/j.biomaterials.2016.11.016>.
- [132] S. Pahoff, C. Meinert, O. Bas, L. Nguyen, T.J. Klein, D.W. Hutmacher, Effect of gelatin source and photoinitiator type on chondrocyte redifferentiation in gelatin methacryloyl-based tissue-engineered cartilage constructs, *J. Mater. Chem. B.* 7 (2019) 1761–1772. <https://doi.org/10.1039/c8tb02607f>.
- [133] N. Schaefer, D. Janzen, E. Bakirci, A. Hrynevich, P.D. Dalton, C. Villmann, 3D Electrophysiological Measurements on Cells Embedded within Fiber-Reinforced Matrigel, *Adv. Healthc. Mater.* 1801226 (2019) 1801226. <https://doi.org/10.1002/adhm.201801226>.
- [134] L. Thibaudeau, A. V. Taubenberger, B.M. Holzapfel, V.M. Quent, T. Fuehrmann, P. Hesami, T.D. Brown, P.D. Dalton, C.A. Power, B.G. Hollier, D.W. Hutmacher, A tissue-

engineered humanized xenograft model of human breast cancer metastasis to bone, *Dis. Model. Mech.* 7 (2014) 299–309. <https://doi.org/10.1242/dmm.014076>.

- [135] S. Bertlein, D. Hikimoto, G. Hochleitner, J. Hügger, T. Jungst, M. Matsusaki, M. Akashi, J. Groll, Development of Endothelial Cell Networks in 3D Tissues by Combination of Melt Electrospinning Writing with Cell-Accumulation Technology, *Small.* 14 (2018) 1–7. <https://doi.org/10.1002/smll.201701521>.
- [136] G.H. Kim, S.H. Ahn, H.J. Lee, S. Lee, Y. Cho, W. Chun, A new hybrid scaffold using rapid prototyping and electrohydrodynamic direct writing for bone tissue regeneration, *J. Mater. Chem.* 21 (2011) 19138–19143. <https://doi.org/10.1039/c1jm13712c>.
- [137] A. Fuchs, A. Youssef, A. Seher, S. Hartmann, R.C. Brands, U.D.A. Müller-Richter, A.C. Kübler, C. Linz, A new multilayered membrane for tissue engineering of oral hard- and soft tissue by means of melt electrospinning writing and film casting – An in vitro study, *J. Cranio-Maxillofacial Surg.* 47 (2019) 695–703. <https://doi.org/10.1016/j.jcms.2019.01.043>.
- [138] S.H. Park, T.G. Kim, H.C. Kim, D.Y. Yang, T.G. Park, Development of dual scale scaffolds via direct polymer melt deposition and electrospinning for applications in tissue regeneration, *Acta Biomater.* 4 (2008) 1198–1207. <https://doi.org/10.1016/j.actbio.2008.03.019>.
- [139] N.K. Mohtaram, J. Ko, C. King, L. Sun, N. Muller, M.B.G. Jun, S.M. Willerth, Electrospun biomaterial scaffolds with varied topographies for neuronal differentiation of human-induced pluripotent stem cells, *J. Biomed. Mater. Res. - Part A.* 103 (2015) 2591–2601. <https://doi.org/10.1002/jbm.a.35392>.
- [140] S.P. Zhong, Y.Z. Zhang, C.T. Lim, Tissue scaffolds for skin wound healing and dermal reconstruction, *Wiley Interdiscip. Rev. Nanomedicine Nanobiotechnology.* 2 (2010) 510–525. <https://doi.org/10.1002/wnan.100>.
- [141] N. Cubo, M. Garcia, J.F. Del Cañizo, D. Velasco, J.L. Jorcano, 3D bioprinting of functional human skin: Production and in vivo analysis, *Biofabrication.* 9 (2017) 015006. <https://doi.org/10.1088/1758-5090/9/1/015006>.
- [142] M.A. Mofazzal Jahromi, P. Sahandi Zangabad, S.M. Moosavi Basri, K. Sahandi Zangabad, A. Ghamarypour, A.R. Aref, M. Karimi, M.R. Hamblin, Nanomedicine and advanced technologies for burns: Preventing infection and facilitating wound healing, *Adv. Drug Deliv. Rev.* 123 (2018) 33–64. <https://doi.org/10.1016/j.addr.2017.08.001>.
- [143] K.A. Rieger, N.P. Birch, J.D. Schiffman, Designing electrospun nanofiber mats to promote wound healing-a review, *J. Mater. Chem. B.* 1 (2013) 4531–4541. <https://doi.org/10.1039/c3tb20795a>.
- [144] J. Liao, Y. Jia, B. Wang, K. Shi, Z. Qian, Injectable Hybrid Poly(ϵ -caprolactone)- b - poly(ethylene glycol)- b -poly(ϵ -caprolactone) Porous Microspheres/Alginate Hydrogel Cross-linked by Calcium Gluconate Crystals Deposited in the Pores of Microspheres Improved Skin Wound Healing, *ACS Biomater. Sci. Eng.* 4 (2018) 1029–1036. <https://doi.org/10.1021/acsbiomaterials.7b00860>.

- [145] S.P. Tarassoli, Z.M. Jessop, A. Al-Sabah, N. Gao, S. Whitaker, S. Doak, I.S. Whitaker, Skin tissue engineering using 3D bioprinting: An evolving research field, *J. Plast. Reconstr. Aesthetic Surg.* 71 (2018) 615–623. <https://doi.org/10.1016/j.bjps.2017.12.006>.
- [146] C. Wei, J. Dong, Hybrid hierarchical fabrication of three-dimensional scaffolds, *J. Manuf. Process.* 16 (2014) 257–263. <https://doi.org/10.1016/j.jmapro.2013.10.003>.
- [147] J. Visser, B. Peters, T.J. Burger, J. Boomstra, W.J.A. Dhert, F.P.W. Melchels, J. Malda, Biofabrication of multi-material anatomically shaped tissue constructs, *Biofabrication*. 5 (2013). <https://doi.org/10.1088/1758-5082/5/3/035007>.
- [148] A. Nadernezhad, N. Khani, G.A. Skvortsov, B. Toprakhisar, E. Bakirci, Y. Menceloglu, S. Unal, B. Koc, Multifunctional 3D printing of heterogeneous hydrogel structures, *Sci. Rep.* 6 (2016) 1–12. <https://doi.org/10.1038/srep33178>.
- [149] J.E. Trachtenberg, J.K. Placone, B.T. Smith, C.M. Piard, M. Santoro, D.W. Scott, J.P. Fisher, A.G. Mikos, Extrusion-Based 3D Printing of Poly(propylene fumarate) in a Full-Factorial Design, *ACS Biomater. Sci. Eng.* 2 (2016) 1771–1780. <https://doi.org/10.1021/acsbiomaterials.6b00026>.
- [150] S. V. Murphy, A. Atala, 3D bioprinting of tissues and organs, *Nat. Biotechnol.* 32 (2014) 773–785. <https://doi.org/10.1038/nbt.2958>.
- [151] L. Shor, S. Güceri, R. Chang, J. Gordon, Q. Kang, L. Hartsock, Y. An, W. Sun, Precision extruding deposition (PED) fabrication of polycaprolactone (PCL) scaffolds for bone tissue engineering, *Biofabrication*. 1 (2009). <https://doi.org/10.1088/1758-5082/1/1/015003>.
- [152] R. Cornock, S. Beirne, B. Thompson, G.G. Wallace, Coaxial additive manufacture of biomaterial composite scaffolds for tissue engineering, *Biofabrication*. 6 (2014). <https://doi.org/10.1088/1758-5082/6/2/025002>.
- [153] M.A. Woodruff, D.W. Hutmacher, The return of a forgotten polymer - Polycaprolactone in the 21st century, *Prog. Polym. Sci.* 35 (2010) 1217–1256. <https://doi.org/10.1016/j.progpolymsci.2010.04.002>.
- [154] I. Armentano, M. Dottori, E. Fortunati, S. Mattioli, J.M. Kenny, Biodegradable polymer matrix nanocomposites for tissue engineering: A review, *Polym. Degrad. Stab.* 95 (2010) 2126–2146. <https://doi.org/10.1016/j.polymdegradstab.2010.06.007>.
- [155] S. Bi, B. Tan, J.L. Soule, M.J. Sobkowicz, Enzymatic degradation of poly (butylene succinate-co-hexamethylene succinate), *Polym. Degrad. Stab.* 155 (2018) 9–14. <https://doi.org/10.1016/j.polymdegradstab.2018.06.017>.
- [156] B. Tan, S. Bi, K. Emery, M.J. Sobkowicz, Bio-based poly(butylene succinate-co-hexamethylene succinate) copolymers with tunable thermal and mechanical properties, *Eur. Polym. J.* 86 (2017) 162–172. <https://doi.org/10.1016/j.eurpolymj.2016.11.017>.
- [157] S. PAPADIMITRIOU, D.N. BIKIARIS, K. CHRISSAFIS, K.M. PARASKEVOPOULOS, S. MOURTAS3, Synthesis, Characterization, and Thermal Degradation Mechanism of Fast Biodegradable PPSu/PCL Copolymers, *Wiley Intersci.* 45 (2007) 5076–5090. <https://doi.org/10.1002/pola.22250>.

- [158] G.Z. Papageorgiou, D.N. Bikaris, Crystallization and melting behavior of three biodegradable poly(alkylene succinates). A comparative study, *Polymer* (Guildf). 46 (2005) 12081–12092. <https://doi.org/10.1016/j.polymer.2005.10.073>.
- [159] D.N. Bikaris, G.Z. Papageorgiou, D.S. Achilias, E. Pavlidou, A. Stergiou, Miscibility and enzymatic degradation studies of poly(ϵ -caprolactone)/poly(propylene succinate) blends, *Eur. Polym. J.* 43 (2007) 2491–2503. <https://doi.org/10.1016/j.eurpolymj.2007.03.051>.
- [160] M. Zamani, M.P. Prabhakaran, S. Ramakrishna, Advances in drug delivery via electrospun and electrosprayed nanomaterials, *Int. J. Nanomedicine*. 8 (2013) 2997–3017. <https://doi.org/10.2147/IJN.S43575>.
- [161] M.S. Kumar, S. Kirubanandan, R. Sripriya, P.K. Sehgal, Triphala Incorporated Collagen Sponge-A Smart Biomaterial for Infected Dermal Wound Healing, *J. Surg. Res.* 158 (2010) 162–170. <https://doi.org/10.1016/j.jss.2008.07.006>.
- [162] I. Romano, M. Summa, J.A. Heredia-Guerrero, R. Spanó, L. Ceseracciu, C. Pignatelli, R. Bertorelli, E. Mele, A. Athanassiou, Fumarate-loaded electrospun nanofibers with anti-inflammatory activity for fast recovery of mild skin burns, *Biomed. Mater.* 11 (2016). <https://doi.org/10.1088/1748-6041/11/4/041001>.
- [163] X. Hu, S. Liu, G. Zhou, Y. Huang, Z. Xie, X. Jing, Electrospinning of polymeric nanofibers for drug delivery applications, *J. Control. Release*. 185 (2014) 12–21. <https://doi.org/10.1016/j.jconrel.2014.04.018>.
- [164] M.R. Mohammadi, S. Rabbani, S.H. Bahrami, M.T. Joghataei, F. Moayer, Antibacterial performance and in vivo diabetic wound healing of curcumin loaded gum tragacanth/poly(ϵ -caprolactone) electrospun nanofibers, *Mater. Sci. Eng. C*. 69 (2016) 1183–1191. <https://doi.org/10.1016/j.msec.2016.08.032>.
- [165] Z. Li, C. Chong, Y. Wang, P.M. Maitz, U. Simanainen, An electrospun scaffold loaded with anti-androgen receptor compound for accelerating wound healing, *Burn. Trauma*. 1 (2013) 95. <https://doi.org/10.4103/2321-3868.118935>.
- [166] E.A.T. Vargas, N.C. do Vale Baracho, J. de Brito, A.A.A. de Queiroz, Hyperbranched polyglycerol electrospun nanofibers for wound dressing applications, *Acta Biomater.* 6 (2010) 1069–1078. <https://doi.org/10.1016/j.actbio.2009.09.018>.
- [167] 3 J.C. Knowles I. Ahmed, 1 D. Ready, 2 M. Wilson, Antimicrobial effect of silver-doped phosphate-based glasses, *Wiley Intersci.* 79 (2006). <https://doi.org/10.1002/jbm.a.30808>.
- [168] K.M. Fromm, B. Giese, S. Eckhardt, J. Gagnon, M. Priebe, P.S. Brunetto, Nanobio Silver: Its Interactions with Peptides and Bacteria, and Its Uses in Medicine, *Chem. Rev.* 113 (2013) 4708–4754. <https://doi.org/10.1021/cr300288v>.
- [169] M.A. Fonder, G.S. Lazarus, D.A. Cowan, B. Aronson-Cook, A.R. Kohli, A.J. Mamelak, Treating the chronic wound: A practical approach to the care of nonhealing wounds and wound care dressings, *J. Am. Acad. Dermatol.* 58 (2008) 185–206. <https://doi.org/10.1016/j.jaad.2007.08.048>.
- [170] M. Radisic, L. Yang, J. Boublík, R.J. Cohen, R. Langer, L.E. Freed, G. Vunjak-Novakovic, Medium perfusion enables engineering of compact and contractile cardiac

tissue, Am. J. Physiol. - Hear. Circ. Physiol. 286 (2004) 507–516. <https://doi.org/10.1152/ajpheart.00171.2003>.

- [171] G. Zhao, S.E. Stevens, Multiple parameters for the comprehensive evaluation of the susceptibility of *Escherichia coli* to the silver ion, BioMetals. 11 (1998) 27–32. <https://doi.org/10.1023/A:1009253223055>.
- [172] B. Le Ouay, F. Stellacci, Antibacterial activity of silver nanoparticles: A surface science insight, Nano Today. 10 (2015) 339–354. <https://doi.org/10.1016/j.nantod.2015.04.002>.
- [173] M. Rai, A. Yadav, A. Gade, Silver nanoparticles as a new generation of antimicrobials, Biotechnol. Adv. 27 (2009) 76–83. <https://doi.org/10.1016/j.biotechadv.2008.09.002>.
- [174] M.S. Sumitha, K.T. Shalumon, V.N. Sreeja, R. Jayakumar, S. V. Nair, D. Menon, Biocompatible and antibacterial nanofibrous poly(ϵ -caprolactone)-nanosilver composite scaffolds for tissue engineering applications, J. Macromol. Sci. Part A Pure Appl. Chem. 49 (2012) 131–138. <https://doi.org/10.1080/10601325.2012.642208>.
- [175] Y.-H. Lin, J.-H. Lin, S.-H. Wang, T.-H. Ko, G.-C. Tseng, Evaluation of silver-containing activated carbon fiber for wound healing study: In vitro and in vivo , J. Biomed. Mater. Res. Part B Appl. Biomater. 100B (2012) 2288–2296. <https://doi.org/10.1002/jbm.b.32800>.
- [176] T. Patrício, M. Domingos, A. Gloria, P. Bárto, Characterisation of PCL and PCL/PLA scaffolds for tissue engineering, Procedia CIRP. 5 (2013) 110–114. <https://doi.org/10.1016/j.procir.2013.01.022>.
- [177] M.E. Hoque, D.W. Hutmacher, W. Feng, S. Li, M.H. Huang, M. Vert, Y.S. Wong, Fabrication using a rapid prototyping system and in vitro characterization of PEG-PCL-PLA scaffolds for tissue engineering, J. Biomater. Sci. Polym. Ed. 16 (2005) 1595–1610. <https://doi.org/10.1163/156856205774576709>.
- [178] R. Fang, E. Zhang, L. Xu, S. Wei, Electrospun PCL/PLA/HA based nanofibers as scaffold for osteoblast-like cells, J. Nanosci. Nanotechnol. 10 (2010) 7747–7751. <https://doi.org/10.1166/jnn.2010.2831>.
- [179] Q. Ou-Yang, B. Guo, J. Xu, Preparation and Characterization of Poly(butylene succinate)/Polylactide Blends for Fused Deposition Modeling 3D Printing, ACS Omega. 3 (2018) 14309–14317. <https://doi.org/10.1021/acsomega.8b02549>.
- [180] A. Nadernezhad, O.S. Caliskan, F. Topuz, F. Afghah, B. Erman, B. Koc, Nanocomposite Bioinks Based on Agarose and 2D Nanosilicates with Tunable Flow Properties and Bioactivity for 3D Bioprinting, ACS Appl. Bio Mater. 2 (2019) 796–806. <https://doi.org/10.1021/acsabm.8b00665>.
- [181] A. Kaplan, G. Akalin Ciftci, H.M. Kutlu, Cytotoxic, anti-proliferative and apoptotic effects of silver nitrate against H-ras transformed 5RP7, Cytotechnology. 68 (2016) 1727–1735. <https://doi.org/10.1007/s10616-015-9922-5>.
- [182] M.A. Al-Omair, Synthesis of antibacterial silver-poly(ϵ -caprolactone)-methacrylic acid graft copolymer nanofibers and their evaluation as potential wound dressing, Polymers (Basel). 7 (2015) 1464–1475. <https://doi.org/10.3390/polym7081464>.

- [183] T. Elzein, M. Nasser-Eddine, C. Delaite, S. Bistac, P. Dumas, FTIR study of polycaprolactone chain organization at interfaces, *J. Colloid Interface Sci.* 273 (2004) 381–387. <https://doi.org/10.1016/j.jcis.2004.02.001>.
- [184] L. Zheng, C. Li, D. Zhang, G. Guan, Y. Xiao, D. Wang, Multiblock copolymers composed of poly(butylene succinate) and poly(1,2-propylene succinate): Effect of molar ratio of diisocyanate to polyester-diols on crosslink densities, thermal properties, mechanical properties and biodegradability, *Polym. Degrad. Stab.* 95 (2010) 1743–1750. <https://doi.org/10.1016/j.polymdegradstab.2010.05.016>.
- [185] Y.K. Sung, D.K. Song, Synthesis and characterization of new biodegradable polymers for biomodeling and biomedical applications, *Macromol. Symp.* 224 (2005) 239–252. <https://doi.org/10.1002/masy.200550621>.
- [186] P. Parcheta, J. Datta, Structure analysis and thermal degradation characteristics of bio-based poly(propylene succinate)s obtained by using different catalyst amounts, *J. Therm. Anal. Calorim.* 130 (2017) 197–206. <https://doi.org/10.1007/s10973-017-6376-3>.
- [187] L. Zheng, C. Li, W. Huang, X. Huang, D. Zhang, G. Guan, Y. Xiao, D. Wang, Synthesis of high-impact biodegradable multiblock copolymers comprising of poly(butylene succinate) and poly(1,2-propylene succinate) with hexamethylene diisocyanate as chain extender, *Polym. Adv. Technol.* 22 (2011) 279–285. <https://doi.org/10.1002/pat.1530>.
- [188] C. De Kesel, C. Lefèvre, J.B. Nagy, C. David, Blends of polycaprolactone with polyvinylalcohol: A DSC, optical microscopy and solid state NMR study, *Polymer (Guildf).* 40 (1999) 1969–1978. [https://doi.org/10.1016/S0032-3861\(98\)00253-5](https://doi.org/10.1016/S0032-3861(98)00253-5).
- [189] Y. Sun, M. Matsumoto, M. Haruki, S.I. Kihara, S. Takishima, Molecular weight dependence of the crystallization of the polycarbonate induced by supercritical CO₂, *J. Supercrit. Fluids.* 113 (2016) 144–149. <https://doi.org/10.1016/j.supflu.2016.03.025>.
- [190] S.K. Singh, A.K. Matta, R.U. Rao, K.N.S. Suman, V. Rambabu, Preparation and Characterization of Biodegradable PLA/PCL Polymeric Blends, *Procedia Mater. Sci.* 6 (2014) 1266–1270. <https://doi.org/10.1016/j.mspro.2014.07.201>.
- [191] S. Wojtyła, P. Klama, T. Baran, Is 3D printing safe? Analysis of the thermal treatment of thermoplastics: ABS, PLA, PET, and nylon, *J. Occup. Environ. Hyg.* 14 (2017) D80–D85. <https://doi.org/10.1080/15459624.2017.1285489>.
- [192] W. Jamróz, J. Szafraniec, M. Kurek, R. Jachowicz, 3D Printing in Pharmaceutical and Medical Applications – Recent Achievements and Challenges, *Pharm. Res.* 35 (2018) 176. <https://doi.org/10.1007/s11095-018-2454-x>.
- [193] W.H. Traub, B. Leonhard, Brief reports heat stability of the antimicrobial activity of sixty-two antibacterial agents, *J. Antimicrob. Chemother.* 35 (1995) 149–154.
- [194] O. Svahn, E. Björklund, Thermal stability assessment of antibiotics in moderate temperature and subcritical water using a pressurized dynamic flow-through system, *Int. J. Innov. Appl. Stud. ISSN.* 11 (2015) 2028–9324. <http://www.ijias.issr-journals.org/>.
- [195] M. Kim, G. Kim, Electrospun PCL/phlorotannin nanofibres for tissue engineering: Physical properties and cellular activities, *Carbohydr. Polym.* 90 (2012) 592–601.

<https://doi.org/10.1016/j.carbpol.2012.05.082>.

- [196] V.M. Pathak, Navneet, Review on the current status of polymer degradation: a microbial approach, *Bioresour. Bioprocess.* 4 (2017) 15. <https://doi.org/10.1186/s40643-017-0145-9>.
- [197] I. Grigoriadou, N. Nianias, A. Hoppe, Z. Terzopoulou, D. Bikaris, J. Will, J. Hum, J.A. Roether, R. Detsch, A.R. Boccaccini, Evaluation of silica-nanotubes and strontium hydroxyapatite nanorods as appropriate nanoadditives for poly(butylene succinate) biodegradable polyester for biomedical applications, *Compos. Part B Eng.* 60 (2014) 49–59. <https://doi.org/10.1016/j.compositesb.2013.12.015>.
- [198] L.M. Orozco-Castellanos, A. Marcos-Fernández, A. Martínez-Richa, Hydrolytic degradation of poly(ϵ -caprolactone) with different end groups and poly(ϵ -caprolactone-co- γ -butyrolactone): Characterization and kinetics of hydrocortisone delivery, *Polym. Adv. Technol.* 22 (2011) 430–436. <https://doi.org/10.1002/pat.1531>.
- [199] M. Gigli, M. Fabbri, N. Lotti, R. Gamberini, B. Rimini, A. Munari, Poly(butylene succinate)-based polyesters for biomedical applications: A review, *Eur. Polym. J.* 75 (2016) 431–460. <https://doi.org/10.1016/j.eurpolymj.2016.01.016>.
- [200] D. Moura, M.T. Souza, L. Liverani, G. Rella, G.M. Luz, J.F. Mano, A.R. Boccaccini, Development of a bioactive glass-polymer composite for wound healing applications, *Mater. Sci. Eng. C* 76 (2017) 224–232. <https://doi.org/10.1016/j.msec.2017.03.037>.
- [201] Z. Bai, Y. Liu, T. Su, Z. Wang, Effect of hydroxyl monomers on the Enzymatic degradation of poly(ethylene succinate), poly(butylene succinate), and poly(hexylene succinate), *Polymers (Basel)*. 10 (2018) 90. <https://doi.org/10.3390/polym10010090>.
- [202] L. Tan, Y. Chen, W. Zhou, H. Nie, F. Li, X. He, Novel poly(butylene succinate-co-lactic acid) copolyesters: Synthesis, crystallization, and enzymatic degradation, *Polym. Degrad. Stab.* 95 (2010) 1920–1927. <https://doi.org/10.1016/j.polymdegradstab.2010.04.010>.
- [203] J. Peña, T. Corrales, I. Izquierdo-Barba, A.L. Doadrio, M. Vallet-Regí, Long term degradation of poly(ϵ -caprolactone) films in biologically related fluids, *Polym. Degrad. Stab.* 91 (2006) 1424–1432. <https://doi.org/10.1016/j.polymdegradstab.2005.10.016>.
- [204] R.D. Turner, J.R. Wingham, T.E. Paterson, J. Shepherd, C. Majewski, Use of silver-based additives for the development of antibacterial functionality in Laser Sintered polyamide 12 parts, *Sci. Rep.* 10 (2020) 1–11. <https://doi.org/10.1038/s41598-020-57686-4>.
- [205] G. Hochleitner, A. Youssef, A. Hrynevich, J.N. Haigh, T. Jungst, J. Groll, P.D. Dalton, Fibre pulsing during melt electrospinning writing, *BioNanoMaterials*. 17 (2016) 159–171. <https://doi.org/10.1515/bnm-2015-0022>.
- [206] N. Khani, A. Nadernezhad, P. Bartolo, B. Koc, Hierarchical and spatial modeling and bio-additive manufacturing of multi-material constructs, *CIRP Ann. - Manuf. Technol.* 66 (2017) 229–232. <https://doi.org/10.1016/j.cirp.2017.04.132>.
- [207] C. Mota, D. Puppi, F. Chiellini, E. Chiellini, Additive manufacturing techniques for the production of tissue engineering constructs, *J. Tissue Eng. Regen. Med.* 9 (2015) 174–190. <https://doi.org/10.1002/term.1635>.

- [208] C. Colosi, M. Costantini, A. Barbetta, M. Dentini, Microfluidic bioprinting of heterogeneous 3d tissue constructs, *Methods Mol. Biol.* 1612 (2017) 369–380. https://doi.org/10.1007/978-1-4939-7021-6_26.
- [209] J. Ko, N.K. Mohtaram, P.C.D. Lee, S.M. Willerth, M.B. Jun, Parametric Studies of Melt Electrospinning Poly ε (caprolactone) Fibers for Tissue Engineering Applications, *Proc. 8th Int. Conf. MicroManufacturing.* (2013) 526–531. <https://minds.wisconsin.edu/bitstream/handle/1793/65300/0015.pdf?sequence=1>.
- [210] D.W. Hutmacher, M. Sittiger, M. V. Risbud, Scaffold-based tissue engineering: Rationale for computer-aided design and solid free-form fabrication systems, *Trends Biotechnol.* 22 (2004) 354–362. <https://doi.org/10.1016/j.tibtech.2004.05.005>.
- [211] R. Deng, Y. Liu, Y. Ding, P. Xie, L. Luo, W. Yang, Melt electrospinning of low-density polyethylene having a low-melt flow index, *J. Appl. Polym. Sci.* 114 (2009) 166–175. <https://doi.org/10.1002/app.29864>.
- [212] H. Chen, A.D.B.F.B. Malheiro, C. Van Blitterswijk, C. Mota, P.A. Wieringa, L. Moroni, Direct Writing Electrospinning of Scaffolds with Multidimensional Fiber Architecture for Hierarchical Tissue Engineering, *ACS Appl. Mater. Interfaces.* 9 (2017) 38187–38200. <https://doi.org/10.1021/acsami.7b07151>.
- [213] O.S. Yördem, M. Papila, Y.Z. Menceloğlu, Effects of electrospinning parameters on polyacrylonitrile nanofiber diameter: An investigation by response surface methodology, *Mater. Des.* 29 (2008) 34–44. <https://doi.org/10.1016/j.matdes.2006.12.013>.
- [214] H.M. Khanlou, B.C. Ang, S. Talebian, M.M. Barzani, M. Silakhori, H. Fauzi, Multi-response analysis in the processing of poly (methyl methacrylate) nano-fibres membrane by electrospinning based on response surface methodology: Fibre diameter and bead formation, *Meas. J. Int. Meas. Confed.* 65 (2015) 193–206. <https://doi.org/10.1016/j.measurement.2015.01.014>.
- [215] N. Bu, Y. Huang, Y. Duan, Z. Yin, Process Optimization of Mechano-Electrospinning by Response Surface Methodology, *J. Nanosci. Nanotechnol.* 14 (2014) 3464–3472. <https://doi.org/10.1166/jnn.2014.8659>.
- [216] V. Beachley, X. Wen, Effect of electrospinning parameters on the nanofiber diameter and length, *Mater. Sci. Eng. C.* 29 (2009) 663–668. <https://doi.org/10.1016/j.msec.2008.10.037>.
- [217] N. Ogata, S. Yamaguchi, N. Shimada, G. Lu, T. Iwata, K. Nakane, T. Ogihara, Poly(lactide) nanofibers produced by a melt-electrospinning system with a laser melting device, *J. Appl. Polym. Sci.* 104 (2007) 1640–1645. <https://doi.org/10.1002/app.25782>.
- [218] S. Sukigara, M. Gandhi, J. Ayutsede, M. Micklus, F. Ko, Regeneration of Bombyx mori silk by electrospinning. Part 2. Process optimization and empirical modeling using response surface methodology, *Polymer (Guildf).* 45 (2004) 3701–3708. <https://doi.org/10.1016/j.polymer.2004.03.059>.
- [219] M. Ahmadipourroudposht, E. Fallahiarezoudar, N.M. Yusof, A. Idris, Application of response surface methodology in optimization of electrospinning process to fabricate

- (ferrofluid/polyvinyl alcohol) magnetic nanofibers, *Mater. Sci. Eng. C*. 50 (2015) 234–241. <https://doi.org/10.1016/j.msec.2015.02.008>.
- [220] D.C. Montgomery, *Design and Analysis of Experiments Eighth Edition*, 2013. <https://doi.org/10.1198/tech.2006.s372>.
- [221] J.-Y. Park, W.-G. Shim, I.-H. Lee, Modeling and optimization of electrospun polyvinylacetate (PVAc) nanofibers by response surface methodology (RSM)., *J. Nanosci. Nanotechnol.* 11 (2011) 1359–63. <https://doi.org/10.1166/jnn.2011.3420>.
- [222] M. Yazdanpanah, M. Khanmohammadi, R. Mehdinavaz Aghdam, K. Shabani, M. Rajabi, Optimization of electrospinning process of poly(vinyl alcohol) via response surface methodology (RSM) based on the central composite design, *Curr. Chem. Lett.* 3 (2014) 175–182. <https://doi.org/10.5267/j.ccl.2014.5.001>.
- [223] M. Essalhi, M. Khayet, C. Cojocaru, P. Arribas, Response Surface Modeling and Optimization of Electrospun Nanofiber Membranes, *Open Nanosci. J.* 7 (2013) 8–17. <https://doi.org/10.2174/1874140101307010008>.
- [224] S.Y. Gu, J. Ren, G.J. Vancso, Process optimization and empirical modeling for electrospun polyacrylonitrile (PAN) nanofiber precursor of carbon nanofibers, *Eur. Polym. J.* 41 (2005) 2559–2568. <https://doi.org/10.1016/j.eurpolymj.2005.05.008>.
- [225] J.M. Lyons, *Melt-electrospinning of Thermoplastic Polymers: An Experimental and Theoretical Analysis*, Drexel University, 2004.
- [226] Y. Liu, R. Deng, M. Hao, H. Yan, W. Yang, Orthogonal Design Study on Factors Effecting on Fibers Diameter of Melt Electrospinning, *Polym. Eng. Sci.* 50 (2010) 2074–8. <https://doi.org/10.1002/pen.21753>.
- [227] X. Li, H. Liu, J. Liu, J. Wang, C. Li, Preparation and Experimental Parameters Analysis of Laser Melt Electrospun Poly(L-lactide) Fibers Via Orthogonal Design, *Polym. Eng. Sci.* 52 (2012) 1964–7. <https://doi.org/10.1002/pen.23138>.
- [228] G. Xie, Z. Chen, S. Ramakrishna, Y. Liu, Orthogonal design preparation of phenolic fiber by melt electrospinning, *J. Appl. Polym. Sci.* 132 (2015). <https://doi.org/10.1002/app.42574>.
- [229] S. V. Fridrikh, J.H. Yu, M.P. Brenner, G.C. Rutledge, Controlling the Fiber Diameter during Electrospinning, *Phys. Rev. Lett.* 90 (2003) 4. <https://doi.org/10.1103/PhysRevLett.90.144502>.
- [230] A.K. Sood, R.K. Ohdar, S.S. Mahapatra, Parametric appraisal of mechanical property of fused deposition modelling processed parts, *Mater. Des.* 31 (2010) 287–295. <https://doi.org/10.1016/j.matdes.2009.06.016>.
- [231] M. Balachandran, S. Devanathan, R. Muraleekrishnan, S.S. Bhagawan, Optimizing properties of nanoclay-nitrile rubber (NBR) composites using Face Centred Central Composite Design, *Mater. Des.* 35 (2012) 854–862. <https://doi.org/10.1016/j.matdes.2011.03.077>.
- [232] S.H. Tan, R. Inai, M. Kotaki, S. Ramakrishna, Systematic parameter study for ultra-fine

- fiber fabrication via electrospinning process, *Polymer (Guildf)*. 46 (2005) 6128–6134. <https://doi.org/10.1016/j.polymer.2005.05.068>.
- [233] B. Guillotin, A. Souquet, S. Catros, M. Duocastella, B. Pippenger, S. Bellance, R. Bareille, M. Rémy, L. Bordenave, J. Amédée j, F. Guillemot, Laser assisted bioprinting of engineered tissue with high cell density and microscale organization, *Biomaterials*. 31 (2010) 7250–7256. <https://doi.org/10.1016/j.biomaterials.2010.05.055>.
- [234] I.T. Ozbolat, M. Hospodiuk, Current advances and future perspectives in extrusion-based bioprinting, *Biomaterials*. 76 (2016) 321–343. <https://doi.org/10.1016/j.biomaterials.2015.10.076>.
- [235] H.W. Kang, S.J. Lee, I.K. Ko, C. Kengla, J.J. Yoo, A. Atala, A 3D bioprinting system to produce human-scale tissue constructs with structural integrity, *Nat. Biotechnol.* 34 (2016) 312–319. <https://doi.org/10.1038/nbt.3413>.
- [236] Y. Jin, A. Compaan, W. Chai, Y. Huang, Functional Nanoclay Suspension for Printing-Then-Solidification of Liquid Materials, *ACS Appl. Mater. Interfaces*. 9 (2017) 20057–20066. <https://doi.org/10.1021/acsami.7b02398>.
- [237] Y. Matsuzaki, K. John, T. Shoji, T. Shinoka, The Evolution of Tissue Engineered Vascular Graft Technologies: From Preclinical Trials to Advancing Patient Care, *Appl. Sci.* 9 (2019) 1274. <https://doi.org/10.3390/app9071274>.
- [238] A. McCormack, C.B. Highley, N.R. Leslie, F.P.W. Melchels, 3D Printing in Suspension Baths: Keeping the Promises of Bioprinting Afloat, *Trends Biotechnol.* xx (2020) 1–10. <https://doi.org/10.1016/j.tibtech.2019.12.020>.
- [239] P. Datta, B. Ayan, I.T. Ozbolat, Bioprinting for vascular and vascularized tissue biofabrication, *Acta Biomater.* 51 (2017) 1–20. <https://doi.org/10.1016/j.actbio.2017.01.035>.
- [240] C.J. Wu, A.K. Gaharwar, B.K. Chan, G. Schmidt, Mechanically tough Pluronic F127/Laponite nanocomposite hydrogels from covalently and physically cross-linked networks, *Macromolecules*. 44 (2011) 8215–8224. <https://doi.org/10.1021/ma200562k>.
- [241] F. Topuz, A. Nadernezhad, O.S. Caliskan, Y.Z. Menceloglu, B. Koc, Nanosilicate embedded agarose hydrogels with improved bioactivity, *Carbohydr. Polym.* 201 (2018) 105–112. <https://doi.org/10.1016/j.carbpol.2018.08.032>.
- [242] C.W. Peak, J. Stein, K.A. Gold, A.K. Gaharwar, Nanoengineered Colloidal Inks for 3D Bioprinting, *Langmuir*. 34 (2018) 917–925. <https://doi.org/10.1021/acs.langmuir.7b02540>.
- [243] T.G. Mezger, *The Rheology Handbook* (2nd Ed.), Vincentz. (2006) 180.
- [244] O. Jeon, Y. Bin Lee, H. Jeong, S.J. Lee, D. Wells, E. Alsborg, Individual cell-only bioink and photocurable supporting medium for 3D printing and generation of engineered tissues with complex geometries, *Mater. Horizons*. (2019). <https://doi.org/10.1039/c9mh00375d>.
- [245] Howard A. Barnes, *A Handbook of Elementary Rheology*, The University of Wales Institute of Non-Newtonian Fluid Mechanics, 2000.

- [246] H. Ding, R. Chang, Printability Study of Bioprinted Tubular Structures Using Liquid Hydrogel Precursors in a Support Bath, *Appl. Sci.* 8 (2018) 403. <https://doi.org/10.3390/app8030403>.
- [247] T. Bhattacharjee, S.M. Zehnder, K.G. Rowe, S. Jain, R.M. Nixon, W.G. Sawyer, T.E. Angelini, Writing in the granular gel medium, *Sci. Adv.* 1 (2015) e1500655. <https://doi.org/10.1126/sciadv.1500655>.
- [248] T.J. Hinton, Q. Jallerat, R.N. Palchesko, J.H. Park, M.S. Grodzicki, H.J.H.-J. Shue, M.H. Ramadan, A.R. Hudson, A.W. Feinberg, Three-dimensional printing of complex biological structures by freeform reversible embedding of suspended hydrogels, *Sci Adv.* 1 (2015) 1–10. <https://doi.org/10.1126/sciadv.1500758>.
- [249] D.F. Duarte Campos, A. Blaeser, M. Weber, J. Jäkel, S. Neuss, W. Jahnens-Decent, H. Fischer, Three-dimensional printing of stem cell-laden hydrogels submerged in a hydrophobic high-density fluid, *Biofabrication*. 5 (2013). <https://doi.org/10.1088/1758-5082/5/1/015003>.
- [250] Y. Jin, A. Compaan, T. Bhattacharjee, Y. Huang, Granular gel support-enabled extrusion of three-dimensional alginate and cellular structures, *Biofabrication*. 8 (2016) 025016. <https://doi.org/10.1088/1758-5090/8/2/025016>.
- [251] Y. Jin, W. Chai, Y. Huang, Printability study of hydrogel solution extrusion in nanoclay yield-stress bath during printing-then-gelation biofabrication, *Mater. Sci. Eng. C*. 80 (2017) 313–325. <https://doi.org/10.1016/j.msec.2017.05.144>.
- [252] T.J. Hinton, A. Hudson, K. Pusch, A. Lee, A.W. Feinberg, 3D Printing PDMS Elastomer in a Hydrophilic Support Bath via Freeform Reversible Embedding, *ACS Biomater. Sci. Eng.* 2 (2016) 1781–1786. <https://doi.org/10.1021/acsbiomaterials.6b00170>.
- [253] A.K. Grosskopf, R.L. Truby, H. Kim, A. Perazzo, J.A. Lewis, H.A. Stone, Viscoplastic Matrix Materials for Embedded 3D Printing, *ACS Appl. Mater. Interfaces*. 10 (2018) 23353–23361. <https://doi.org/10.1021/acsami.7b19818>.
- [254] A.M. Compaan, K. Song, Y. Huang, Gellan Fluid Gel as a Versatile Support Bath Material for Fluid Extrusion Bioprinting, *ACS Appl. Mater. Interfaces*. 11 (2019) 5714–5726. <https://doi.org/10.1021/acsami.8b13792>.
- [255] T. Bhattacharjee, S.M. Zehnder, K.G. Rowe, S. Jain, R.M. Nixon, W.G. Sawyer, T.E. Angelini, Writing in the granular gel medium, *Sci. Adv.* 1 (2015) e1500655. <https://doi.org/10.1126/sciadv.1500655>.
- [256] C.B. Highley, C.B. Rodell, J.A. Burdick, Direct 3D Printing of Shear-Thinning Hydrogels into Self-Healing Hydrogels, *Adv. Mater.* 27 (2015) 5075–5079. <https://doi.org/10.1002/adma.201501234>.
- [257] J. Jiang, C. Li, J. Lombardi, R.H. Colby, B. Rigas, M.H. Rafailovich, J.C. Sokolov, The effect of physiologically relevant additives on the rheological properties of concentrated Pluronic copolymer gels, *Polymer (Guildf.)*. 49 (2008) 3561–3567. <https://doi.org/10.1016/j.polymer.2008.05.038>.
- [258] D.B. Kolesky, R.L. Truby, A.S. Gladman, T.A. Busbee, K.A. Homan, J.A. Lewis, 3D

bioprinting of vascularized, heterogeneous cell-laden tissue constructs, *Adv. Mater.* 26 (2014) 3124–3130. <https://doi.org/10.1002/adma.201305506>.

- [259] M. Rocca, A. Fragasso, W. Liu, M.A. Heinrich, Y.S. Zhang, Embedded Multimaterial Extrusion Bioprinting, *SLAS Technol.* 23 (2018) 154–163. <https://doi.org/10.1177/2472630317742071>.
- [260] C.J. Wu, G. Schmidt, Thermosensitive and dissolution properties in nanocomposite polymer hydrogels, *Macromol. Rapid Commun.* 30 (2009) 1492–1497. <https://doi.org/10.1002/marc.200900163>.
- [261] K. Haraguchi, R. Farnworth, A. Ohbayashi, T. Takehisa, Compositional effects on mechanical properties of nanocomposite hydrogels composed of poly(*N,N*-dimethylacrylamide) and clay, *Macromolecules.* 36 (2003) 5732–5741. <https://doi.org/10.1021/ma034366i>.
- [262] C.W. Chang, A. Van Spreeuwel, C. Zhang, S. Varghese, PEG/clay nanocomposite hydrogel: A mechanically robust tissue engineering scaffold, *Soft Matter.* 6 (2010) 5157–5164. <https://doi.org/10.1039/c0sm00067a>.
- [263] I. Boucenna, L. Royon, P. Colinart, M.A. Guedea-Boudeville, A. Mourchid, Structure and thermorheology of concentrated pluronic copolymer micelles in the presence of laponite particles, *Langmuir.* 26 (2010) 14430–14436. <https://doi.org/10.1021/la102744c>.
- [264] H. Tomás, C.S. Alves, J. Rodrigues, Laponite®: A key nanoplatform for biomedical applications?, *Nanomedicine Nanotechnology, Biol. Med.* 14 (2018) 2407–2420. <https://doi.org/10.1016/j.nano.2017.04.016>.
- [265] A.K. Gaharwar, L.M. Cross, C.W. Peak, K. Gold, J.K. Carrow, A. Brokesh, K.A. Singh, 2D Nanoclay for Biomedical Applications: Regenerative Medicine, Therapeutic Delivery, and Additive Manufacturing, *Adv. Mater.* 31 (2019) 1–28. <https://doi.org/10.1002/adma.201900332>.
- [266] J.L. Dávila, M.A. D'Ávila, Laponite as a rheology modifier of alginate solutions: Physical gelation and aging evolution, *Carbohydr. Polym.* 157 (2017) 1–8. <https://doi.org/10.1016/j.carbpol.2016.09.057>.
- [267] P.I. Au, S. Hassan, J. Liu, Y.K. Leong, Behaviour of laponite gels: Rheology, ageing, pH effect and phase state in the presence of dispersant, *Chem. Eng. Res. Des.* 101 (2015) 65–73. <https://doi.org/10.1016/j.cherd.2015.07.023>.
- [268] S. Jatav, Y.M. Joshi, Chemical stability of Laponite in aqueous media, *Appl. Clay Sci.* 97–98 (2014) 72–77. <https://doi.org/10.1016/j.clay.2014.06.004>.
- [269] V. Castelletto, I.A. Ansari, I.W. Hamley, Influence of added clay particles on the structure and rheology of a hexagonal phase formed by an amphiphilic block copolymer in aqueous solution, *Macromolecules.* 36 (2003) 1694–1700. <https://doi.org/10.1021/ma021396x>.
- [270] A. Pek-Ing, L. Yee-Kwong, Surface chemistry and rheology of Laponite dispersions - Zeta potential, yield stress, ageing, fractal dimension and pyrophosphate, *Appl. Clay Sci.* 107 (2015) 36–45. <https://doi.org/10.1016/j.clay.2015.01.033>.

- [271] M. Ehrbar, A. Sala, P. Lienemann, A. Ranga, K. Mosiewicz, A. Bittermann, S.C. Rizzi, F.E. Weber, M.P. Lutolf, Elucidating the role of matrix stiffness in 3D cell migration and remodeling, *Biophys. J.* 100 (2011) 284–293. <https://doi.org/10.1016/j.bpj.2010.11.082>.
- [272] S. Krishnamoorthy, B. Noorani, C. Xu, Effects of encapsulated cells on the physical-mechanical properties and microstructure of gelatin methacrylate hydrogels, *Int. J. Mol. Sci.* 20 (2019). <https://doi.org/10.3390/ijms20205061>.
- [273] M. Ahearne, Introduction to cell – hydrogel mechanosensing, *R. Soc. Interface* (2014) 20130038. <https://doi.org/10.1098/rsfs.2013.0038>.
- [274] K. Yang, Z. Liu, J. Wang, W. Yu, Stress bifurcation in large amplitude oscillatory shear of yield stress fluids, *J. Rheol. (N. Y. N. Y.)* 62 (2018) 89–106. <https://doi.org/10.1122/1.4986062>.
- [275] Q. He, W. Yu, Y. Wu, C. Zhou, Shear induced phase inversion of dilute smectic liquid crystal/polymer blends, *Soft Matter* 8 (2012) 2992–3001. <https://doi.org/10.1039/c2sm06963f>.
- [276] A.K. Gaharwar, P.J. Schexnailder, B.P. Kline, G. Schmidt, Assessment of using Laponite® cross-linked poly(ethylene oxide) for controlled cell adhesion and mineralization, *Acta Biomater.* 7 (2011) 568–577. <https://doi.org/10.1016/j.actbio.2010.09.015>.
- [277] P.B. Laxton, J.C. Berg, Relating clay yield stress to colloidal parameters, *J. Colloid Interface Sci.* 296 (2006) 749–755. <https://doi.org/10.1016/j.jcis.2005.09.061>.
- [278] N. Sakairi, M. Kobayashi, Y. Adachi, Effects of salt concentration on the yield stress of sodium montmorillonite suspension, *J. Colloid Interface Sci.* 283 (2005) 245–250. <https://doi.org/10.1016/j.jcis.2004.08.181>.
- [279] B. Ruzicka, E. Zaccarelli, A fresh look at the Laponite phase diagram, *Soft Matter*. 7 (2011) 1268–1286. <https://doi.org/10.1039/c0sm00590h>.
- [280] A. Sheikhi, S. Afewerki, R. Oklu, A.K. Gaharwar, A. Khademhosseini, Effect of ionic strength on shear-thinning nanoclay-polymer composite hydrogels, *Biomater. Sci.* 6 (2018) 2073–2083. <https://doi.org/10.1039/c8bm00469b>.
- [281] K. Sun, S.R. Raghavan, Thermogelling aqueous fluids containing low concentrations of pluronic F127 and laponite nanoparticles, *Langmuir*. 26 (2010) 8015–8020. <https://doi.org/10.1021/la904907b>.
- [282] A. Nelson, T. Cosgrove, Small-angle neutron scattering study of adsorbed pluronic tri-block copolymers on laponite, *Langmuir*. 21 (2005) 9176–9182. <https://doi.org/10.1021/la050680p>.
- [283] P.J. Lu, J.C. Conrad, H.M. Wyss, A.B. Schofield, D.A. Weitz, Fluids of clusters in attractive colloids, *Phys. Rev. Lett.* 96 (2006) 1–4. <https://doi.org/10.1103/PhysRevLett.96.028306>.
- [284] Y. Jin, Y. Shen, J. Yin, J. Qian, Y. Huang, Nanoclay-Based Self-Supporting Responsive Nanocomposite Hydrogels for Printing Applications, *ACS Appl. Mater. Interfaces*. 10

(2018) 10461–10470. <https://doi.org/10.1021/acسامی.8b00806>.

- [285] S.J. Song, J. Choi, Y.D. Park, S. Hong, J.J. Lee, C.B. Ahn, H. Choi, K. Sun, Sodium Alginate Hydrogel-Based Bioprinting Using a Novel Multinozzle Bioprinting System, *Artif. Organs.* 35 (2011) 1132–1136. <https://doi.org/10.1111/j.1525-1594.2011.01377.x>.
- [286] A. Nelson, T. Cosgrove, Dynamic light scattering studies of poly(ethylene oxide) adsorbed on laponite: Layer conformation and its effect on particle stability, *Langmuir.* 20 (2004) 10382–10388. <https://doi.org/10.1021/la049323p>.
- [287] J. Park, S.C. Jana, Mechanism of exfoliation of nanoclay particles in epoxy-clay nanocomposites, *Annu. Tech. Conf. - ANTEC, Conf. Proc.* 2 (2003) 1438–1442. <https://doi.org/10.1021/ma021509c>.
- [288] F. Karimi, N. Taheri Qazvini, R. Namivandi-Zangeneh, Fish gelatin/Laponite biohybrid elastic coacervates: A complexation kinetics-structure relationship study, *Int. J. Biol. Macromol.* 61 (2013) 102–113. <https://doi.org/10.1016/j.ijbiomac.2013.06.054>.
- [289] Y. Luo, A. Lode, M. Gelinsky, Direct plotting of three-dimensional hollow fiber scaffolds based on concentrated alginate pastes for tissue engineering, *Adv. Healthc. Mater.* 2 (2013) 777–783. <https://doi.org/10.1002/adhm.201200303>.
- [290] Y. Yu, Y. Zhang, J.A. Martin, I.T. Ozbolat, Evaluation of cell viability and functionality in vessel-like bioprintable cell-laden tubular channels, *J. Biomech. Eng.* 135 (2013) 1–9. <https://doi.org/10.1115/1.4024575>.
- [291] T. Distler, F. Ruther, A.R. Boccaccini, R. Detsch, Development of 3D Biofabricated Cell Laden Hydrogel Vessels and a Low-Cost Desktop Printed Perfusion Chamber for In Vitro Vessel Maturation, *Macromol. Biosci.* 19 (2019). <https://doi.org/10.1002/mabi.201900245>.
- [292] F. Ruther, T. Distler, A.R. Boccaccini, R. Detsch, Biofabrication of vessel-like structures with alginate di-aldehyde—gelatin (ADA-GEL) bioink, *J. Mater. Sci. Mater. Med.* 30 (2019). <https://doi.org/10.1007/s10856-018-6205-7>.
- [293] K. Dubbin, A. Tabet, S.C. Heilshorn, Quantitative criteria to benchmark new and existing bio-inks for cell compatibility, *Biofabrication.* 9 (2017). <https://doi.org/10.1088/1758-5090/aa869f>.
- [294] G. Gao, H. Kim, B.S. Kim, J.S. Kong, J.Y. Lee, B.W. Park, S. Chae, J. Kim, K. Ban, J. Jang, H.J. Park, D.W. Cho, Tissue-engineering of vascular grafts containing endothelium and smooth-muscle using triple-coaxial cell printing, *Appl. Phys. Rev.* 6 (2019). <https://doi.org/10.1063/1.5099306>.
- [295] Y. Jin, W. Chai, Y. Huang, Fabrication of Stand-Alone Cell-Laden Collagen Vascular Network Scaffolds Using Fugitive Pattern-Based Printing-Then-Casting Approach, *ACS Appl. Mater. Interfaces.* 10 (2018) 28361–28371. <https://doi.org/10.1021/acسامی.8b09177>.
- [296] Y. Wang, X. Huang, Y. Shen, R. Hang, X. Zhang, Y. Wang, X. Yao, B. Tang, Direct writing alginate bioink inside pre-polymers of hydrogels to create patterned vascular networks, *J. Mater. Sci.* 54 (2019) 7883–7892. <https://doi.org/10.1007/s10853-019-03447-2>.

- [297] Z. Zhang, Y. Jin, J. Yin, C. Xu, R. Xiong, K. Christensen, B.R. Ringeisen, D.B. Chrisey, Y. Huang, Evaluation of bioink printability for bioprinting applications, *Appl. Phys. Rev.* 5 (2018). <https://doi.org/10.1063/1.5053979>.
- [298] M. Suzanne, H. Steller, Shaping organisms with apoptosis, *Cell Death Differ.* 20 (2013) 669–675. <https://doi.org/10.1038/cdd.2013.11>.
- [299] J. Burak, K.P. Grela, J. Pluta, B. Karolewicz, D.M. Marciniak, Impact of sterilisation conditions on the rheological properties of thermoresponsive pluronic f-127-based gels for the ophthalmic use, *Acta Pol. Pharm. - Drug Res.* 75 (2018) 471–481.
- [300] B. Zhang, L. Gao, L. Ma, Y. Luo, H. Yang, Z. Cui, 3D Bioprinting: A Novel Avenue for Manufacturing Tissues and Organs, *Engineering.* 5 (2019) 777–794. <https://doi.org/10.1016/j.eng.2019.03.009>.
- [301] J.H. Kim, Y.J. Seol, I.K. Ko, H.W. Kang, Y.K. Lee, J.J. Yoo, A. Atala, S.J. Lee, 3D Bioprinted Human Skeletal Muscle Constructs for Muscle Function Restoration, *Sci. Rep.* 8 (2018) 1–15. <https://doi.org/10.1038/s41598-018-29968-5>.
- [302] R.B. Diego, M.P. Olmedilla, A.S. Aroca, J.L.G. Ribelles, M.M. Pradas, M.S. Sanchez, Acrylic scaffolds with interconnected spherical pores and controlled hydrophilicity, *J. Mater. Sci.* 40 (2005) 4881–4887. <https://doi.org/10.1007/s10853-005-3885-4>.
- [303] Q.L. Loh, C. Choong, Three-dimensional scaffolds for tissue engineering applications: Role of porosity and pore size, *Tissue Eng. - Part B Rev.* 19 (2013) 485–502. <https://doi.org/10.1089/ten.teb.2012.0437>.
- [304] E.J. Chong, T.T. Phan, I.J. Lim, Y.Z. Zhang, B.H. Bay, S. Ramakrishna, C.T. Lim, Evaluation of electrospun PCL/gelatin nanofibrous scaffold for wound healing and layered dermal reconstitution, *Acta Biomater.* 3 (2007) 321–330. <https://doi.org/10.1016/j.actbio.2007.01.002>.
- [305] C.O. Crosby, J. Zoldan, Mimicking the physical cues of the ECM in angiogenic biomaterials, *Regen. Biomater.* 6 (2019) 61–73. <https://doi.org/10.1093/rb/rbz003>.
- [306] P.A.J. Kolarsick, M.A. Kolarsick, C. Goodwin, Anatomy and Physiology of the Skin, *Oncol. Nurs. Soc.* 3 (2011) 203–213. <https://doi.org/10.1097/JDN.0b013e3182274a98>.
- [307] M. Rimann, E. Bono, H. Annaheim, M. Bleisch, U. Graf-Hausner, Standardized 3D Bioprinting of Soft Tissue Models with Human Primary Cells, *J. Lab. Autom.* 21 (2016) 496–509. <https://doi.org/10.1177/2211068214567146>.
- [308] V. Lee, G. Singh, J.P. Trasatti, C. Bjornsson, X. Xu, T.N. Tran, S.S. Yoo, G. Dai, P. Karande, Design and fabrication of human skin by three-dimensional bioprinting, *Tissue Eng. - Part C Methods.* 20 (2014) 473–484. <https://doi.org/10.1089/ten.tec.2013.0335>.
- [309] L. Koch, A. Deiwick, S. Schlie, S. Michael, M. Gruene, V. Coger, D. Zychlinski, A. Schambach, K. Reimers, P.M. Vogt, B. Chichkov, Skin tissue generation by laser cell printing, *Biotechnol. Bioeng.* 109 (2012) 1855–1863. <https://doi.org/10.1002/bit.24455>.
- [310] H.E. Abaci, Z. Guo, A. Coffman, B. Gillette, W.H. Lee, S.K. Sia, A.M. Christiano, Human Skin Constructs with Spatially Controlled Vasculature Using Primary and iPSC-

Derived Endothelial Cells, *Adv. Healthc. Mater.* 5 (2016) 1800–1807. <https://doi.org/10.1002/adhm.201500936>.

- [311] A.K. Miri, A. Khalilpour, B. Cecen, S. Maharjan, S.R. Shin, A. Khademhosseini, Multiscale bioprinting of vascularized models, *Biomaterials*. 198 (2019) 204–216. <https://doi.org/10.1016/j.biomaterials.2018.08.006>.
- [312] W. Zhu, X. Qu, J. Zhu, X. Ma, S. Patel, J. Liu, P. Wang, C.S.E. Lai, M. Gou, Y. Xu, K. Zhang, S. Chen, Direct 3D bioprinting of prevascularized tissue constructs with complex microarchitecture, *Biomaterials*. 124 (2017) 106–115. <https://doi.org/10.1016/j.biomaterials.2017.01.042>.
- [313] Z. Hadisi, T. Walsh, S.M. Hossein Dabiri, A. Seyfoori, B. Godeau, G. Charest, D. Fortin, M. Akbari, 3D printing for the future of medicine, *J. 3D Print. Med. Ahead of P* (2020). <https://doi.org/10.2217/3dp-2019-0010>.
- [314] W.C. Yan, P. Davoodi, S. Vijayaventaraman, Y. Tian, W.C. Ng, J.Y.H. Fuh, K.S. Robinson, C.H. Wang, 3D bioprinting of skin tissue: From pre-processing to final product evaluation, *Adv. Drug Deliv. Rev.* 132 (2018) 270–295. <https://doi.org/10.1016/j.addr.2018.07.016>.
- [315] L. Cui, J. Li, Y. Long, M. Hu, J. Li, Z. Lei, H. Wang, R. Huang, X. Li, Vascularization of LBL structured nanofibrous matrices with endothelial cells for tissue regeneration, *RSC Adv.* 7 (2017) 11462–11477. <https://doi.org/10.1039/c6ra26931a>.
- [316] J. Rouwkema, A. Khademhosseini, Vascularization and Angiogenesis in Tissue Engineering: Beyond Creating Static Networks, *Trends Biotechnol.* 34 (2016) 733–745. <https://doi.org/10.1016/j.tibtech.2016.03.002>.
- [317] L.J. Pourchet, A. Thepot, M. Albouy, E.J. Courtial, A. Boher, L.J. Blum, C.A. Marquette, Human Skin 3D Bioprinting Using Scaffold-Free Approach, *Adv. Healthc. Mater.* 6 (2017) 1–8. <https://doi.org/10.1002/adhm.201601101>.
- [318] B.S. Kim, G. Gao, J.Y. Kim, D.W. Cho, 3D Cell Printing of Perfusionable Vascularized Human Skin Equivalent Composed of Epidermis, Dermis, and Hypodermis for Better Structural Recapitulation of Native Skin, *Adv. Healthc. Mater.* 8 (2019) 1801019. <https://doi.org/10.1002/adhm.201801019>.
- [319] T. Baltazar, J. Merola, C. Catarino, C.B. Xie, N.C. Kirkiles-Smith, V. Lee, S. Hotta, G. Dai, X. Xu, F.C. Ferreira, W.M. Saltzman, J.S. Pober, P. Karande, Three Dimensional Bioprinting of a Vascularized and Perfusible Skin Graft Using Human Keratinocytes, Fibroblasts, Pericytes, and Endothelial Cells, *Tissue Eng. Part A*. 26 (2020) 227–238. <https://doi.org/10.1089/ten.tea.2019.0201>.
- [320] K.S. Lim, B.J. Klotz, G.C.J. Lindberg, F.P.W. Melchels, G.J. Hooper, J. Malda, D. Gawlitza, T.B.F. Woodfield, Visible Light Cross-Linking of Gelatin Hydrogels Offers an Enhanced Cell Microenvironment with Improved Light Penetration Depth, *Macromol. Biosci.* 9 (2019) 1900098. <https://doi.org/10.1002/mabi.201900098>.
- [321] S. Bertlein, G. Brown, K.S. Lim, T. Jungst, T. Boeck, T. Blunk, J. Tessmar, G.J. Hooper, T.B.F. Woodfield, J. Groll, Thiol–Ene Clickable Gelatin: A Platform Bioink for Multiple

- [322] K.S. Lim, B.S. Schon, N. V. Mekhileri, G.C.J. Brown, C.M. Chia, S. Prabakar, G.J. Hooper, T.B.F. Woodfield, New Visible-Light Photoinitiating System for Improved Print Fidelity in Gelatin-Based Bioinks, *ACS Biomater. Sci. Eng.* 2 (2016) 1752–1762. <https://doi.org/10.1021/acsbiomaterials.6b00149>.
- [323] P. Xiao, J. Zhang, F. Dumur, M.A. Tehfe, F. Morlet-Savary, B. Graff, D. Gigmes, J.P. Fouassier, J. Lalevée, Visible light sensitive photoinitiating systems: Recent progress in cationic and radical photopolymerization reactions under soft conditions, *Prog. Polym. Sci.* 41 (2015) 32–66. <https://doi.org/10.1016/j.progpolymsci.2014.09.001>.
- [324] D.A. Fancy, T. Kodadek, Chemistry for the analysis of protein-protein interactions: Rapid and efficient cross-linking triggered by long wavelength light, *Proc. Natl. Acad. Sci. U. S. A.* 96 (1999) 6020–6024. <https://doi.org/10.1073/pnas.96.11.6020>.
- [325] R. Levato, T. Jungst, R.G. Scheuring, T. Blunk, J. Groll, J. Malda, From Shape to Function: The Next Step in Bioprinting, *Adv. Mater.* 32 (2020). <https://doi.org/10.1002/adma.201906423>.
- [326] J.M. Sobral, S.G. Caridade, R.A. Sousa, J.F. Mano, R.L. Reis, Three-dimensional plotted scaffolds with controlled pore size gradients: Effect of scaffold geometry on mechanical performance and cell seeding efficiency, *Acta Biomater.* 7 (2011) 1009–1018. <https://doi.org/10.1016/j.actbio.2010.11.003>.
- [327] T. Yao, P.A. Wieringa, H. Chen, C. Amit, P. Samal, S. Giselbrecht, M.B. Baker, L. Moroni, Fabrication of a self-assembled honeycomb nanofibrous scaffold to guide endothelial morphogenesis, *Biofabrication.* 12 (2020) 045001. <https://doi.org/10.1088/1758-5090/ab9988>.
- [328] P.L. Lewis, R.M. Green, R.N. Shah, 3D-printed gelatin scaffolds of differing pore geometry modulate hepatocyte function and gene expression, *Acta Biomater.* 69 (2018) 63–70. <https://doi.org/10.1016/j.actbio.2017.12.042>.
- [329] S. Van Bael, Y.C. Chai, S. Truscello, M. Moesen, G. Kerckhofs, H. Van Oosterwyck, J.P. Kruth, J. Schrooten, The effect of pore geometry on the in vitro biological behavior of human periosteum-derived cells seeded on selective laser-melted Ti6Al4V bone scaffolds, *Acta Biomater.* 8 (2012) 2824–2834. <https://doi.org/10.1016/j.actbio.2012.04.001>.
- [330] Q. Zhang, H. Lu, N. Kawazoe, G. Chen, Pore size effect of collagen scaffolds on cartilage regeneration, *Acta Biomater.* 10 (2014) 2005–2013. <https://doi.org/10.1016/j.actbio.2013.12.042>.
- [331] F.S.L. Bobbert, A.A. Zadpoor, Effects of bone substitute architecture and surface properties on cell response, angiogenesis, and structure of new bone, *J. Mater. Chem. B.* 5 (2017) 6175–6192. <https://doi.org/10.1039/c7tb00741h>.
- [332] M. Nikkhah, N. Eshak, P. Zorlutuna, N. Annabi, M. Castello, K. Kim, A. Dolatshahi-Pirouz, F. Edalat, H. Bae, Y. Yang, A. Khademhosseini, Directed endothelial cell morphogenesis in micropatterned gelatin methacrylate hydrogels, *Biomaterials.* 33 (2012)

9009–9018. <https://doi.org/10.1016/j.biomaterials.2012.08.068>.

- [333] Y. Zhu, Y. Cao, J. Pan, Y. Liu, Macro-alignment of electrospun fibers for vascular tissue engineering, *J. Biomed. Mater. Res. - Part B Appl. Biomater.* 92 (2010) 508–516. <https://doi.org/10.1002/jbm.b.31544>.
- [334] A. Cipitria, A. Skelton, T.R. Dargaville, P.D. Dalton, D.W. Hutmacher, Design, fabrication and characterization of PCL electrospun scaffolds - A review, *J. Mater. Chem.* 21 (2011) 9419–9453. <https://doi.org/10.1039/c0jm04502k>.
- [335] R. Tutar, A. Motealleh, A. Khademhosseini, N.S. Kehr, Functional Nanomaterials on 2D Surfaces and in 3D Nanocomposite Hydrogels for Biomedical Applications, *Adv. Funct. Mater.* 1904344 (2019) 1904344. <https://doi.org/10.1002/adfm.201904344>.
- [336] J.R. Dias, S. Baptista-Silva, A. Sousa, A.L. Oliveira, P.J. Bárto, P.L. Granja, Biomechanical performance of hybrid electrospun structures for skin regeneration, *Mater. Sci. Eng. C.* (2018). <https://doi.org/10.1016/J.MSEC.2018.08.050>.
- [337] C.M. Elvin, T. Vuocolo, A.G. Brownlee, L. Sando, M.G. Huson, N.E. Liyou, P.R. Stockwell, R.E. Lyons, M. Kim, G.A. Edwards, G. Johnson, G.A. McFarland, J.A.M. Ramshaw, J.A. Werkmeister, A highly elastic tissue sealant based on photopolymerised gelatin, *Biomaterials.* 31 (2010) 8323–8331. <https://doi.org/10.1016/j.biomaterials.2010.07.032>.
- [338] M.N. Nakatsu, R.C.A. Sainson, J.N. Aoto, K.L. Taylor, M. Aitkenhead, S. Pérez-del-Pulgar, P.M. Carpenter, C.C.W. Hughes, Angiogenic sprouting and capillary lumen formation modeled by human umbilical vein endothelial cells (HUVEC) in fibrin gels: The role of fibroblasts and Angiopoietin-1, *Microvasc. Res.* 66 (2003) 102–112. [https://doi.org/10.1016/S0026-2862\(03\)00045-1](https://doi.org/10.1016/S0026-2862(03)00045-1).
- [339] A.A. Szklanny, L. Debbi, U. Merdler, D. Neale, A. Muñiz, B. Kaplan, S. Guo, J. Lahann, S. Levenberg, High-Throughput Scaffold System for Studying the Effect of Local Geometry and Topology on the Development and Orientation of Sprouting Blood Vessels, *Adv. Funct. Mater.* 30 (2020) 1–13. <https://doi.org/10.1002/adfm.201901335>.
- [340] M. Potente, H. Gerhardt, P. Carmeliet, Basic and therapeutic aspects of angiogenesis, *Cell.* 146 (2011) 873–887. <https://doi.org/10.1016/j.cell.2011.08.039>.
- [341] Y. Jin, Q. Gao, C. Xie, G. Li, J. Du, J. Fu, Y. He, Fabrication of heterogeneous scaffolds using melt electrospinning writing: Design and optimization, *Mater. Des.* 185 (2020) 108274. <https://doi.org/10.1016/j.matdes.2019.108274>.
- [342] A.L. Butcher, G.S. Offeddu, M.L. Oyen, Nanofibrous hydrogel composites as mechanically robust tissue engineering scaffolds, *Trends Biotechnol.* 32 (2014) 564–570. <https://doi.org/10.1016/J.TIBTECH.2014.09.001>.
- [343] A.M. van Genderen, K. Jansen, M. Kristen, J. van Duijn, Y. Li, C.C.L. Schuurmans, J. Malda, T. Vermonden, J. Jansen, R. Masereeuw, M. Castilho, Topographic Guidance in Melt-Electrowritten Tubular Scaffolds Enhances Engineered Kidney Tubule Performance, *SSRN Electron. J.* (2020) 3683606. <https://doi.org/10.2139/ssrn.3683606>.
- [344] F. Shahabipour, R.K. Oskuee, H. Dehghani, M.A. Shokrgozar, G.E. Aninwene, S.

Bonakdar, Cell-cell interaction in a coculture system consisting of CRISPR/Cas9 mediated GFP knock-in HUVECs and MG-63 cells in alginate-GelMA based nanocomposites hydrogel as a 3D scaffold, *J. Biomed. Mater. Res. - Part A*. 108 (2020) 1596–1606. <https://doi.org/10.1002/jbm.a.36928>.

- [345] H. El-Mohri, Y. Wu, S. Mohanty, G. Ghosh, Impact of matrix stiffness on fibroblast function, *Mater. Sci. Eng. C*. 74 (2017) 146–151. <https://doi.org/10.1016/j.msec.2017.02.001>.
- [346] S. Guo, L.A. DiPietro, Critical review in oral biology & medicine: Factors affecting wound healing, *J. Dent. Res.* 89 (2010) 219–229. <https://doi.org/10.1177/0022034509359125>.
- [347] M.E. Smithmyer, L.A. Sawicki, A.M. Kloxin, Hydrogel scaffolds as in vitro models to study fibroblast activation in wound healing and disease, *Biomater. Sci.* 2 (2014) 634–650. <https://doi.org/10.1039/c3bm60319a>.
- [348] J. Sapudom, X. Wu, M. Chkolnikov, M. Ansorge, U. Anderegg, T. Pompe, Fibroblast fate regulation by time dependent TGF- β 1 and IL-10 stimulation in biomimetic 3D matrices, *Biomater. Sci.* 5 (2017) 1858–1867. <https://doi.org/10.1039/c7bm00286f>.
- [349] Y.S. Kim, D.K. Sung, W.H. Kong, H. Kim, S.K. Hahn, Synergistic effects of hyaluronate-epidermal growth factor conjugate patch on chronic wound healing, *Biomater. Sci.* 6 (2018) 1020–1030. <https://doi.org/10.1039/c8bm00079d>.
- [350] M. Flanagan, *Wound Healing and Skin Integrity: Principles and Practice*, Wiley-Blackwell, 2013.
- [351] G.C. Gurtner, S. Werner, Y. Barrandon, M.T. Longaker, Wound repair and regeneration, *Nature*. 453 (2008) 314–321. <https://doi.org/10.1038/nature07039>.
- [352] M. Liu, G. Luo, Y.Y. Wang, R. Xu, Y.Y. Wang, W. He, J. Tan, M. Xing, J. Wu, Nano-silver-decorated microfibrous eggshell membrane: Processing, cytotoxicity assessment and optimization, antibacterial activity and wound healing, *Sci. Rep.* 7 (2017) 1–14. <https://doi.org/10.1038/s41598-017-00594-x>.
- [353] J. Rnjak-Kovacina, S.G. Wise, Z. Li, P.K.M.M. Maitz, C.J. Young, Y. Wang, A.S. Weiss, Electrospun synthetic human elastin:collagen composite scaffolds for dermal tissue engineering, *Acta Biomater.* 8 (2012) 3714–3722. <https://doi.org/10.1016/j.actbio.2012.06.032>.
- [354] M. Berthet, Y. Gauthier, C. Lacroix, B. Verrier, C. Monge, Nanoparticle-Based Dressing: The Future of Wound Treatment?, *Trends Biotechnol.* 35 (2017) 770–784. <https://doi.org/10.1016/j.tibtech.2017.05.005>.
- [355] Z. Yuan, J. Zhao, W. Zhu, Z. Yang, B. Li, H. Yang, Q. Zheng, W. Cui, Ibuprofen-loaded electrospun fibrous scaffold doped with sodium bicarbonate for responsively inhibiting inflammation and promoting muscle wound healing in vivo, *Biomater. Sci.* 2 (2014) 502–511. <https://doi.org/10.1039/c3bm60198f>.
- [356] X. Yang, J. Yang, L. Wang, B. Ran, Y. Jia, L. Zhang, G. Yang, H. Shao, X. Jiang, Pharmaceutical Intermediate-Modified Gold Nanoparticles: Against Multidrug-Resistant

Bacteria and Wound-Healing Application via an Electrospun Scaffold, ACS Nano. 11 (2017) 5737–5745. <https://doi.org/10.1021/acsnano.7b01240>.

- [357] X. Wang, T. Coradin, C. Hélary, Modulating inflammation in a cutaneous chronic wound model by IL-10 released from collagen-silica nanocomposites: Via gene delivery, Biomater. Sci. 6 (2018) 398–406. <https://doi.org/10.1039/c7bm01024a>.
- [358] K. Kataria, A. Gupta, G. Rath, R.B. Mathur, S.R. Dhakate, In vivo wound healing performance of drug loaded electrospun composite nanofibers transdermal patch, Int. J. Pharm. 469 (2014) 102–110. <https://doi.org/10.1016/j.ijpharm.2014.04.047>.
- [359] Y. Wo, E.J. Brisbois, R.H. Bartlett, M.E. Meyerhoff, Recent advances in thromboresistant and antimicrobial polymers for biomedical applications: just say yes to nitric oxide (NO), Biomater. Sci. 4 (2016) 1161–1183. <https://doi.org/10.1039/c6bm00271d>.
- [360] D. Chimene, R. Kaunas, A.K. Gaharwar, Hydrogel Bioink Reinforcement for Additive Manufacturing: A Focused Review of Emerging Strategies, Adv. Mater. 32 (2020) 1–22. <https://doi.org/10.1002/adma.201902026>.
- [361] A.O. Elzoghby, Gelatin-based nanoparticles as drug and gene delivery systems: Reviewing three decades of research, J. Control. Release. 172 (2013) 1075–1091. <https://doi.org/10.1016/j.jconrel.2013.09.019>.
- [362] B.J. Klotz, D. Gawlitza, A.J.W.P. Rosenberg, J. Malda, F.P.W. Melchels, Gelatin-Methacryloyl Hydrogels: Towards Biofabrication-Based Tissue Repair, Trends Biotechnol. 34 (2016) 394–407. <https://doi.org/10.1016/j.tibtech.2016.01.002>.
- [363] M.E. Hoque, T. Nuge, T.K. Yeow, N. Nordin, R.G.S. V Prasad, Gelatin Based Scaffolds for Tissue Engineering – a Review, Polym. Res. J. 9 (2015) 1935–2530.
- [364] S. Gorgieva, Vanja Kokol, Collagen-vs. gelatine-based biomaterials and their biocompatibility review and perspectives, Intech Open. 2 (2011) 64. <https://doi.org/10.5772/32009>.
- [365] E. Hoch, T. Hirth, G.E.M. Tovar, K. Borchers, Chemical tailoring of gelatin to adjust its chemical and physical properties for functional bioprinting, J. Mater. Chem. B. 1 (2013) 5675–5685. <https://doi.org/10.1039/c3tb20745e>.
- [366] R.F. Pereira, P.J. Bartolo, 3D bioprinting of photocrosslinkable hydrogel constructs, J. Appl. Polym. Sci. 132 (2015). <https://doi.org/10.1002/app.42458>.
- [367] R.F. Pereira, C.C. Barrias, P.J. Bártolo, P.L. Granja, Cell-instructive pectin hydrogels crosslinked via thiol-norbornene photo-click chemistry for skin tissue engineering, Acta Biomater. 66 (2018) 282–293. <https://doi.org/10.1016/j.actbio.2017.11.016>.
- [368] T. Mazaki, Y. Shiozaki, K. Yamane, A. Yoshida, M. Nakamura, Y. Yoshida, D. Zhou, T. Kitajima, M. Tanaka, Y. Ito, T. Ozaki, A. Matsukawa, A novel, visible light-induced, rapidly cross-linkable gelatin scaffold for osteochondral tissue engineering, Sci. Rep. 4 (2014) 1–10. <https://doi.org/10.1038/srep04457>.
- [369] A. Hoshikawa, Y. Nakayama, T. Matsuda, H. Oda, K. Nakamura, K. Mabuchi, Encapsulation of Chondrocytes in Photopolymerizable Styrenated Gelatin for Cartilage

Tissue Engineering, Tissue Eng. 12 (2006) 2333–2341.
<https://doi.org/10.1089/ten.2006.12.2333>.

- [370] X. Yang, M. Mohseni, O. Bas, C. Meinert, E.J. New, N.J. Castro, Type II Photoinitiator and Tuneable Poly(Ethylene Glycol)-Based Materials Library for Visible Light Photolithography, Tissue Eng. - Part A. 26 (2020) 292–304.
<https://doi.org/10.1089/ten.tea.2019.0282>.
- [371] P.Y. Zhang, P.P. Xu, Z.J. Xia, J. Wang, J. Xiong, Y.Z. Li, Combined treatment with the antibiotics kanamycin and streptomycin promotes the conjugation of Escherichia coli, FEMS Microbiol. Lett. 348 (2013) 149–156. <https://doi.org/10.1111/1574-6968.12282>.
- [372] P. Müller, K. Brettel, [Ru(bpy)₃]²⁺ as a reference in transient absorption spectroscopy: Differential absorption coefficients for formation of the long-lived 3MLCT excited state, Photochem. Photobiol. Sci. 11 (2012) 632–636. <https://doi.org/10.1039/c2pp05333k>.
- [373] C.M. Elvin, A.G. Brownlee, M.G. Huson, T.A. Tebb, M. Kim, R.E. Lyons, T. Vuocolo, N.E. Liyou, T.C. Hughes, J.A.M.M. Ramshaw, J.A. Werkmeister, The development of photochemically crosslinked native fibrinogen as a rapidly formed and mechanically strong surgical tissue sealant, Biomaterials. 30 (2009) 2059–2065.
<https://doi.org/10.1016/j.biomaterials.2008.12.059>.
- [374] Y. Ding, Y. Li, M. Qin, Y. Cao, W. Wang, Photo-cross-linking approach to engineering small tyrosine-containing peptide hydrogels with enhanced mechanical stability, Langmuir. 29 (2013) 13299–13306. <https://doi.org/10.1021/la4029639>.
- [375] K.S. Lim, M.H. Alves, L.A. Poole-Warren, P.J. Martens, Covalent incorporation of non-chemically modified gelatin into degradable PVA-tyramine hydrogels, Biomaterials. 34 (2013) 7097–7105. <https://doi.org/10.1016/j.biomaterials.2013.06.005>.
- [376] P. Atienza-Roca, D. Kieser, X. Cui, B. Bathish, Y. Ramaswamy, G.J. Hooper, A. Clarkson, J. Rnjak-Kovacina, P. Martens, L. Wise, T.B. Woodfield, K.S. Lim, Visible Light Mediated PVA-Tyramine Hydrogels for Covalent Incorporation and Tailorable Release of Functional Growth Factors, Biomater. Sci. (2020).
<https://doi.org/10.1039/D0BM00603C>.
- [377] T.M. Robinson, D.W. Hutmacher, P.D. Dalton, The Next Frontier in Melt Electrospinning: Taming the Jet, Adv. Funct. Mater. (2019) 1904664.
<https://doi.org/10.1002/adfm.201904664>.
- [378] M. Setayeshmehr, E. Esfandiari, M. Rafieinia, B. Hashemibeni, A. Taheri-Kafrani, A. Samadikuchaksaraei, D.L. Kaplan, L. Moroni, M.T. Joghataei, Hybrid and Composite Scaffolds Based on Extracellular Matrices for Cartilage Tissue Engineering, Tissue Eng. Part B Rev. 25 (2019) 202–224. <https://doi.org/10.1089/ten.teb.2018.0245>.
- [379] S. Xu, L. Deng, J. Zhang, L. Yin, A. Dong, Composites of electrospun-fibers and hydrogels: A potential solution to current challenges in biological and biomedical field, J. Biomed. Mater. Res. Part B Appl. Biomater. 104 (2016) 640–656.
<https://doi.org/10.1002/jbm.b.33420>.
- [380] L. Kong, Z. Wu, H. Zhao, H. Cui, J. Shen, J. Chang, H. Li, Y. He, Bioactive Injectable

Hydrogels Containing Desferrioxamine and Bioglass for Diabetic Wound Healing, ACS Appl. Mater. Interfaces. (2018) acsami.8b09191. <https://doi.org/10.1021/acsami.8b09191>.

- [381] G. Hochleitner, M. Kessler, M. Schmitz, A.R. Boccaccini, J. Teßmar, J. Groll, J. Teßmar, J. Groll, Melt electrospinning writing of defined scaffolds using polylactide-poly(ethylene glycol) blends with 45S5 bioactive glass particles, Mater. Lett. 205 (2017) 257–260. <https://doi.org/10.1016/J.MATLET.2017.06.096>.
- [382] N.C. Paxton, J. Ren, M.J. Ainsworth, A.K. Solanki, J.R. Jones, M.C. Allenby, M.M. Stevens, M.A. Woodruff, Rheological Characterization of Biomaterials Directs Additive Manufacturing of Strontium-Substituted Bioactive Glass/Polycaprolactone Microfibers, Macromol. Rapid Commun. 40 (2019) 1900019. <https://doi.org/10.1002/marc.201900019>.
- [383] S.Werner, R. Grose, Regulation of wound healing by growth factors and cytokines, Physiol. Rev. 83 (2003) 835–870.
- [384] M.T. Poldervaart, H. Gremmels, K. Van Deventer, J.O. Fledderus, F.C. Öner, M.C. Verhaar, W.J.A.A. Dhert, J. Alblas, Prolonged presence of VEGF promotes vascularization in 3D bioprinted scaffolds with defined architecture, J. Control. Release. 184 (2014) 58–66. <https://doi.org/10.1016/j.jconrel.2014.04.007>.
- [385] X.H. Zhu, Y. Tabata, C.-H. Wang, Y.W. Tong, Delivery of basic fibroblast growth factor from gelatin microsphere scaffold for the growth of human umbilical vein endothelial cells, Tissue Eng. - Part A. 14 (2008). <https://doi.org/10.1089/ten.tea.2007.0346>.
- [386] S.C.G. Leeuwenburgh, J. Jo, H. Wang, M. Yamamoto, J.A. Jansen, Y. Tabata, Mineralization , Biodegradation , and Drug Release Behavior of Gelatin/Apatite Composite Microspheres for Bone Regeneration, Biomacromolecules. 11 (2010) 2653–2659. <https://doi.org/10.1021/bm1006344>.
- [387] K. Kawai, S. Suzuki, Y. Tabata, Y. Ikada, Accelerated tissue regeneration through incorporation of basic fibroblast growth factor-impregnated gelatin microspheres into artificial dermis, Biomaterials. 21 (2000) 489–499. [https://doi.org/http://dx.doi.org/10.1016/S0142-9612\(99\)00207-0](https://doi.org/http://dx.doi.org/10.1016/S0142-9612(99)00207-0).
- [388] D.L. Elbert, Liquid--liquid two-phase systems for the production of porous hydrogels and hydrogel microspheres for biomedical applications: a tutorial review, Acta Biomater. 7 (2011) 31–56.
- [389] J. Koehler, F.P. Brandl, A.M. Goepfertich, Hydrogel wound dressings for bioactive treatment of acute and chronic wounds, Eur. Polym. J. 100 (2018) 1–11.
- [390] U. Park, K. Kim, Multiple growth factor delivery for skin tissue engineering applications, Biotechnol. Bioprocess Eng. 22 (2017) 659–670.
- [391] X. Dai, K. Kathiria, Y.C. Huang, Electrospun fiber scaffolds of poly (glycerol-dodecanoate) and its gelatin blended polymers for soft tissue engineering, Biofabrication. 6 (2014). <https://doi.org/10.1088/1758-5082/6/3/035005>.
- [392] K. A, L. A, Mechanical Behaviour of Skin: A Review, J. Mater. Sci. Eng. 5 (2016). <https://doi.org/10.4172/2169-0022.1000254>.

- [393] J.J. Blaker, S.N. Nazhat, A.R. Boccaccini, Development and characterisation of silver-doped bioactive glass-coated sutures for tissue engineering and wound healing applications, *Biomaterials*. 25 (2004) 1319–1329. <https://doi.org/10.1016/j.biomaterials.2003.08.007>.
- [394] L. Liverani, J. Lacina, J.A. Roether, E. Boccardi, M.S. Killian, P. Schmuki, D.W. Schubert, A.R. Boccaccini, Incorporation of bioactive glass nanoparticles in electrospun PCL/chitosan fibers by using benign solvents, *Bioact. Mater.* 3 (2018) 55–63. <https://doi.org/10.1016/j.bioactmat.2017.05.003>.
- [395] H. Joodaki, M.B. Panzer, Skin mechanical properties and modeling: A review, *Proc. Inst. Mech. Eng. Part H J. Eng. Med.* 232 (2018) 323–343. <https://doi.org/10.1177/0954411918759801>.
- [396] H.M. Powell, S.T. Boyce, Engineered human skin fabricated using electrospun collagen-PCL blends: Morphogenesis and mechanical properties, *Tissue Eng. - Part A*. 15 (2009) 2177–2187. <https://doi.org/10.1089/ten.tea.2008.0473>.
- [397] B.A. Allo, S. Lin, K. Mequanint, A.S. Rizkalla, Role of bioactive 3D hybrid fibrous scaffolds on mechanical behavior and spatiotemporal osteoblast gene expression, *ACS Appl. Mater. Interfaces*. 5 (2013) 7574–7583. <https://doi.org/10.1021/am401861w>.
- [398] S. Laïb, B.H. Fellah, A. Fatimi, S. Quillard, C. Vinatier, O. Gauthier, P. Janvier, M. Petit, B. Bujoli, S. Bohic, P. Weiss, The in vivo degradation of a ruthenium labelled polysaccharide-based hydrogel for bone tissue engineering, *Biomaterials*. 30 (2009) 1568–1577. <https://doi.org/10.1016/j.biomaterials.2008.11.031>.
- [399] R.O. Beauchamp, M.B.G. St Clair, T.R. Fennell, D.O. Clarke, K.T. Morgan, F.W. Karl, A critical review of the toxicology of glutaraldehyde, *Crit. Rev. Toxicol.* 22 (1992) 143–174. <https://doi.org/10.3109/10408449209145322>.
- [400] I. Pastar, O. Stojadinovic, N.C. Yin, H. Ramirez, A.G. Nusbaum, A. Sawaya, S.B. Patel, L. Khalid, R.R. Isseroff, M. Tomic-Canic, Epithelialization in Wound Healing: A Comprehensive Review, *Adv. Wound Care.* 3 (2014) 445–464. <https://doi.org/10.1089/wound.2013.0473>.
- [401] Y. Liu, S. Cai, X.Z. Shu, J. Shelby, G.D. Prestwich, Release of basic fibroblast growth factor from a crosslinked glycosaminoglycan hydrogel promotes wound healing, *Wound Repair Regen.* 15 (2007) 245–251.
- [402] K. Mizuno, K. Yamamura, K. Yano, T. Osada, S. Saeki, N. Takimoto, T. Sakurai, Y. Nimura, Effect of chitosan film containing basic fibroblast growth factor on wound healing in genetically diabetic mice, *J. Biomed. Mater. Res. Part A An Off. J. Soc. Biomater. Japanese Soc. Biomater. Aust. Soc. Biomater. Korean Soc. Biomater.* 64 (2003) 177–181.
- [403] S. Ogino, N. Morimoto, M. Sakamoto, C. Jinno, Y. Sakamoto, T. Taira, S. Suzuki, Efficacy of the dual controlled release of HGF and bFGF impregnated with a collagen/gelatin scaffold, *J. Surg. Res.* 221 (2018) 173–182. <https://doi.org/10.1016/j.jss.2017.08.051>.

- [404] H.-X. Shi, C. Lin, B.-B. Lin, Z.-G. Wang, H.-Y. Zhang, F.-Z. Wu, Y. Cheng, L.-J. Xiang, D.-J. Guo, X. Luo, others, The anti-scar effects of basic fibroblast growth factor on the wound repair in vitro and in vivo, *PLoS One.* 8 (2013).
- [405] P. Losi, E. Briganti, C. Errico, A. Lisella, E. Sanguinetti, F. Chiellini, G. Soldani, Fibrin-based scaffold incorporating VEGF-and bFGF-loaded nanoparticles stimulates wound healing in diabetic mice, *Acta Biomater.* 9 (2013) 7814–7821.
- [406] S. Naseri, W.C. Lepry, S.N. Nazhat, Bioactive glasses in wound healing: hope or hype?, *J. Mater. Chem. B.* 5 (2017) 6167–6174. <https://doi.org/10.1039/C7TB01221G>.
- [407] Y.M.K.K.H.Y.T.I.Ka.K.M. Tabata, Yasuhiko; Ikada, Surfactant-free preparation of biodegradable hydrogel microspheres for protein release, *J. Bioact. Compat. Polym.* 14 (1999) 371–384. <https://doi.org/10.1177/088391159901400501>.
- [408] S. Young, M. Wong, Y. Tabata, A.G. Mikos, Gelatin as a delivery vehicle for the controlled release of bioactive molecules, *J. Control. Release.* 109 (2005) 256–274. <https://doi.org/10.1016/j.jconrel.2005.09.023>.
- [409] C. Claaßen, L. Sewald, G. Tovar, K. Borchers, Controlled Release of Vascular Endothelial Growth Factor from Heparin-Functionalized Gelatin Type A and Albumin Hydrogels, *Gels.* 3 (2017) 35. <https://doi.org/10.3390/gels3040035>.
- [410] X. Li, C. Ma, X. Xie, H. Sun, X. Liu, Pulp regeneration in a full-length human tooth root using a hierarchical nanofibrous microsphere system, *Acta Biomater.* 35 (2016) 57–67. <https://doi.org/10.1016/j.actbio.2016.02.040>.